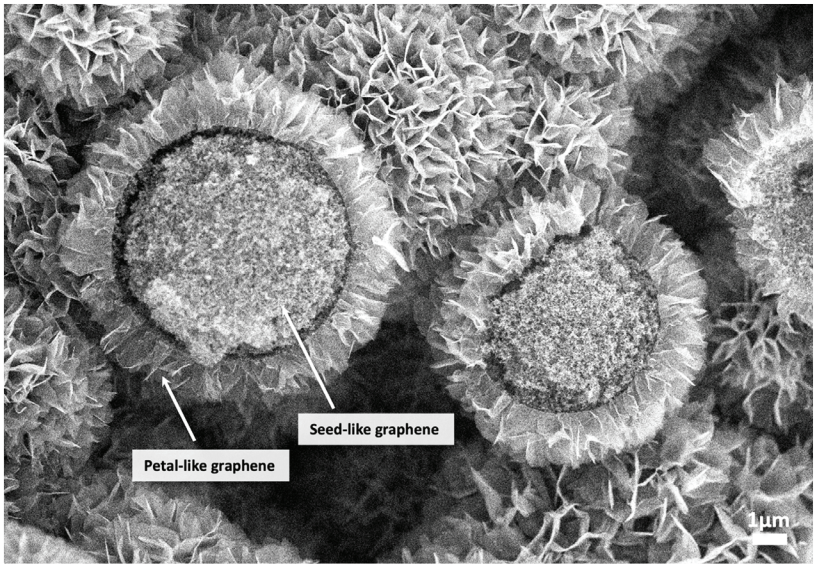

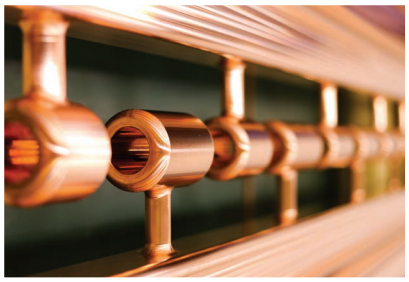

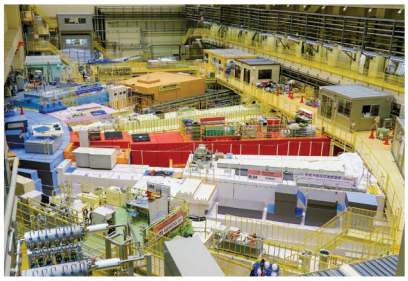

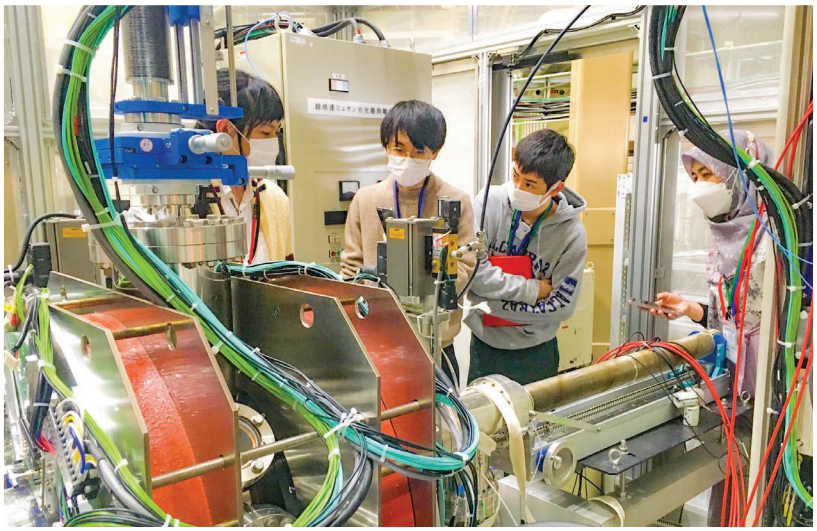

J-PARC

ANNUAL REPORT 2022

Vol.2: Materials and Life Science Experimental Facility

MLF ANNUAL REPORT

Cover photographs

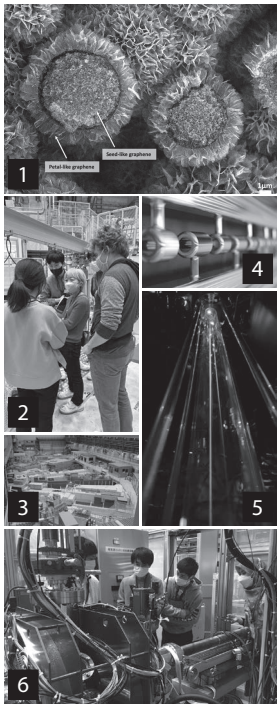

1 : The SEM image of a nanosized graphene flower produced by the hot isostatic pressing treatment. Development of this new material is in progress to enhance neutron intensity below cold neutrons.

2 : The 6th Neutron and Muon School.

3 : MLF Experimental Hall-1 in October 2022.

4 : An interdigital H-mode drift tube linear accelerator (IH-DTL) for the J-PARC muon g−2/EDM experiment. Drift tubes made of oxygen-free copper are monolithically machined.

5 : Plasma fluorescence produced by laser.
This is the plasma fluorescence produced when the Kr gas used as a wavelength conversion medium is ionized in the process of generating intense vacuum ultraviolet coherent light for Ultra-slow Muon generation.

6 : The 6th Neutron and Muon School.

J-PARC MLF
Materials and Life Science Division
J-PARC Center
https://mlfinfo.jp/en

J-PARC was jointly constructed and is now operated by the High Energy Accelerator Research Organization (KEK) and the Japan Atomic Energy Agency (JAEA).

Comprehensive Research Organization for Science and Society
https://neutron.cross.or.jp/en

J-PARC 23-02

Preface

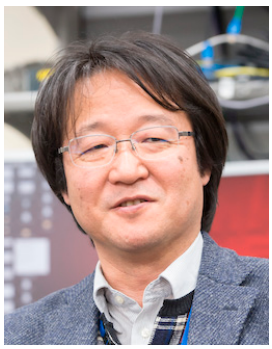

Toshiya Otomo
Division Head of Materials and Life Science Division, MLF

In 2022, beam power of 830 kW with high operational efficiency of over 90% was reached for the first time in the user program. 21 neutron beamlines and 7 muon areas were operated. Despite that, the soaring electricity costs affected the beam time, J-PARC reviewed the operation schedule upon the approval of a supplementary budget and decided to elongate the MLF user operation until March 14. The user program was operated for a total of 146 days, although 159 days were originally planned, and 418 general user proposals were conducted.

Over 250 papers were published, such as a structural study of new flexible and tough super elastic alloy with promising use in Biomedical Applications, asteroid explorer Hayabusa2, initial analysis revealing the formation and evolution of the carbonaceous asteroid Ryugu, nondestructive two-dimensional quantitative analysis of degradation of the charging capacity of Lithium-ion secondary batteries and discovering the hidden order of the Mo and Nb atoms in disordered $Ba_7Nb_4MoO_{20}$ crystals.

As part of the process to establish a stable operation, the target vessel replacement process was re-examined, and the tritium release was successfully reduced. Also, the preparation of the spare muon target (the third muon rotating target) advanced and will be completed in 2023.

The SEOP system as a spin polarizer on BL23 has been set and finally the on-beam commissioning with a polarized neutron beam has begun. Constructing the world's first muon accelerator on the H2 area of the H-line was approved by the Nuclear Regulatory Authority ("GENSHIRYOKU-KISEI-CHOU"). The RFQ and IH-DTL, by which ultra-slow muons are accelerated to 4.3 MeV, will be installed in the H2 area. They act as the front stage of the 212 MeV linear accelerators.

Events in 2022 were held in a hybrid mode of in-person and internet meetings: one of them was the annual meeting of neutron industrial application at Akihabara with 300 participants. This annual meeting was held to merge the outcomes from the MLF and Japan Research Reactor - 3 (JRR-3) of JAEA. The 11th International Workshop on Sample Environment at Scattering Facilities (ISSE) was held at Nasu and the 6th Neutron and Muon School (NM-school) was held as KEK-IINAS (Inter-Institution Network for Accelerator Science) School at Tokai (https://mlfinfo.jp/sp/school/6th-nms/). Workshops were held for neutron sources with ESS (online capability), for commissioning with the ESS & J-PARC collaboration, for the accelerator system and neutron/muon target system with ISIS and for the neutron source system with SNS.

In November 2022, the border control of Japan restored almost completely the rules from the time before COVID-19. The number of foreign users is gradually reaching the previous level and various activities now take place as before. We will continue to improve the environment so that more and more excellent results will be produced in the MLF.

Materials and Life Science Division, Japan Proton Accelerator Research Complex
https://mlfinfo.jp/en

Preface

Mitsuhiro Shibayama
Director, CROSS

The Comprehensive Research Organization of Science and Society (CROSS), a partner institution of the Materials and Life Science Experimental Facility (MLF), is honored to release the J-PARC MLF ANNUAL REPORT 2022 (MLF-AR2022), which includes sections on R&D Highlights, Neutron Sources, Neutron Science, Muon Science and more. The Neutron Science Center of the CROSS is a registered organization of the J-PARC's Specific Neutron Beamline Facility, appointed by the Japanese government in 2011. It supports the activities of the 7 public beamlines of the MLF (BL01 4SEASONS, BL02 DNA, BL11 PLANET, BL15 TAIKAN, BL17 SHARAKU, BL18 SENJU, and BL22 RADEN), and provides high-quality user support to the MLF users, both academic and industrial researchers, and promotes the use of the facility.

In FY2022, the neutron beam at the MLF was stably operated, which ensured highly reliable machine operation. The total numbers of short term neutron proposals submitted and accepted in the two proposal rounds in FY2022 were 614 and 286, respectively, and those for the Public Beamlines were 285 and 123, respectively. As of the outcome, 200 scientific papers (excluding proceedings) were published from the MLF in 2022, 74 of which were from the Public Beamlines. The details are included in the Research and Development Highlights collected in this volume. The numbers of press releases were 20 from the MLF and 5 from the Public Beamlines. These numbers illustrate the high activities of the Public Beamlines as well as the MLF, which have been used by a wide range of users from the academia and various industries. The special program for new users "New User Promotion (NUP)", which started in 2016, was also operated in 2022, and 9 NUP neutron users conducted experiments at the MLF.

Regarding public relations, in FY2020, a unified consultation service named "J-JOIN", operated by the J-PARC MLF, Ibaraki Pref., JRR-3 (JAEA and the University of Tokyo), and the CROSS, welcomed potential users. (https://jrr3ring.jaea.go.jp/jjoin/index_en.php).

I hope that this Annual Report would provide useful information about the current status of the MLF operations and recent scientific achievements, the technical R&D reports, and so on. On behalf of the CROSS, I sincerely welcome your visit to the MLF.

Neutron Science and Technology Center, Comprehensive Research Organization for Science and Society
https://neutron.cross.or.jp/en

Contents

Research and Development Highlights

Neutron Source

Neutron Science

Muon Science

MLF Safety

MLF Operations in 2022

Organization Chart

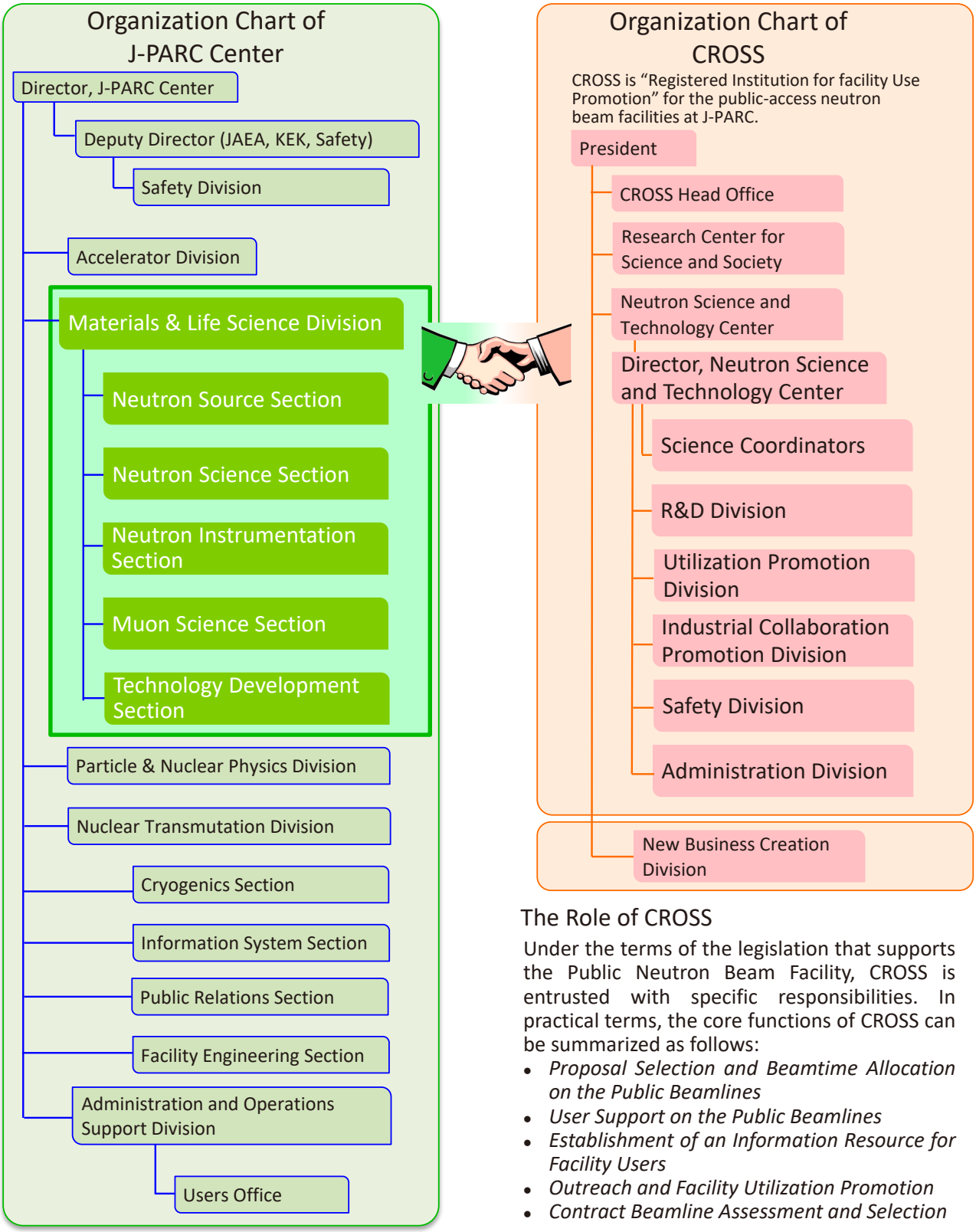

The Role of CROSS

Under the terms of the legislation that supports the Public Neutron Beam Facility, CROSS is entrusted with specific responsibilities. In practical terms, the core functions of CROSS can be summarized as follows:

- *Proposal Selection and Beamtime Allocation on the Public Beamlines*
- *User Support on the Public Beamlines*
- *Establishment of an Information Resource for Facility Users*
- *Outreach and Facility Utilization Promotion*
- *Contract Beamline Assessment and Selection*

J-PARC Map

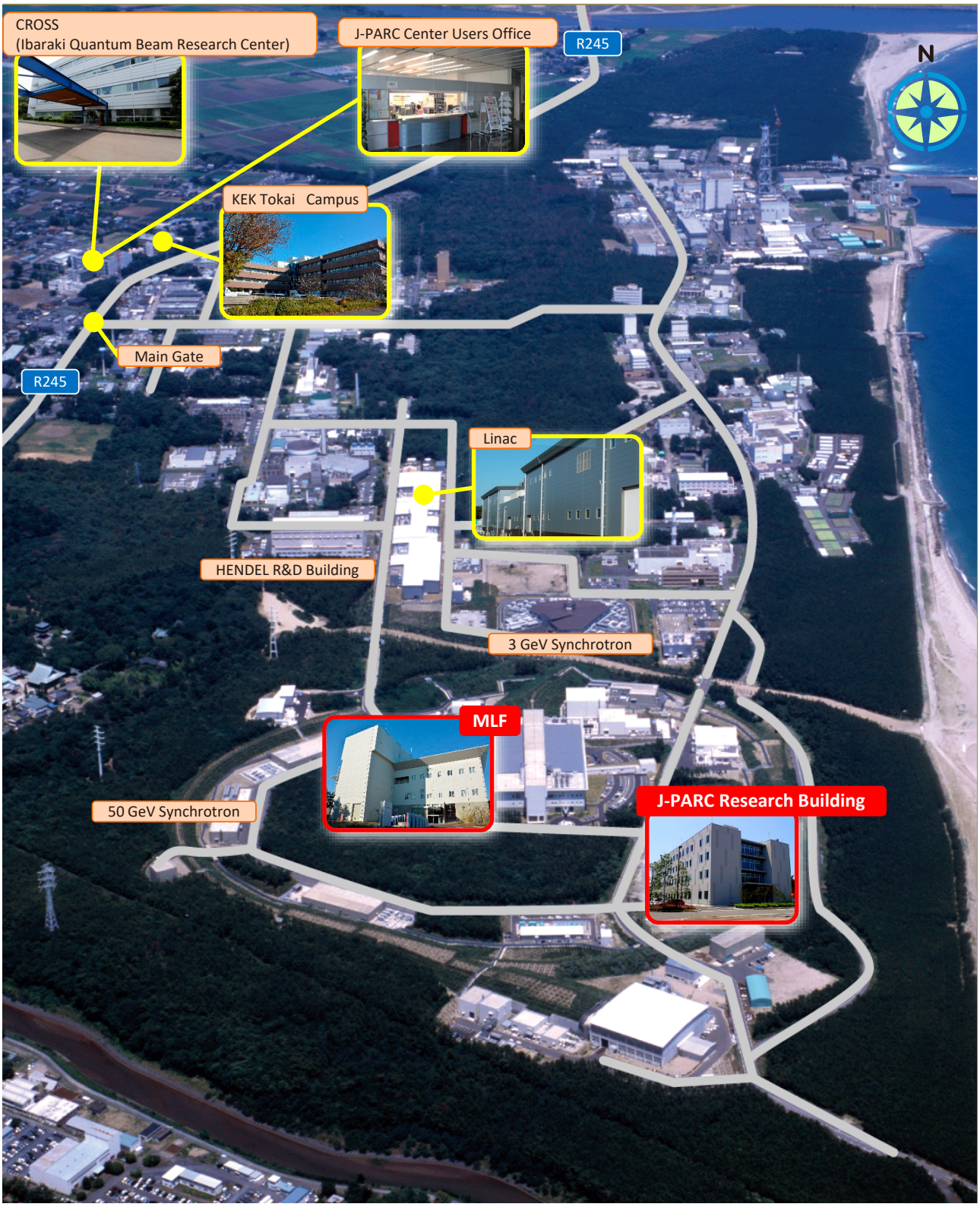
CROSS
(Ibaraki Quantum Beam Research Center)
J-PARC Center Users Office
R245
N
KEK Tokai Campus
Main Gate
R245
Linac
HENDEL R&D Building
3 GeV Synchrotron
MLF
J-PARC Research Building
50 GeV Synchrotron

Muon and Neutron Instruments

Muon Source

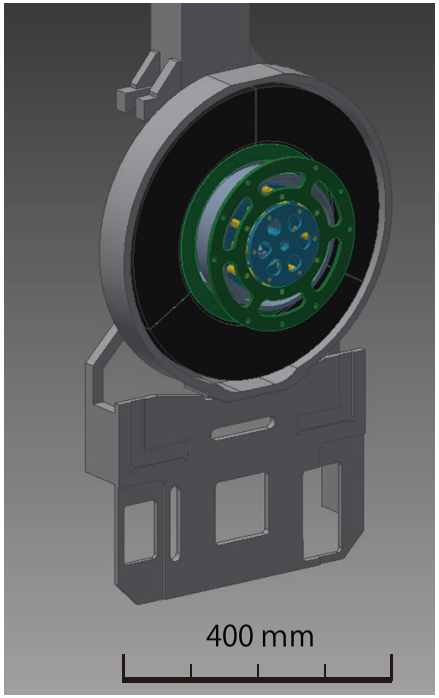

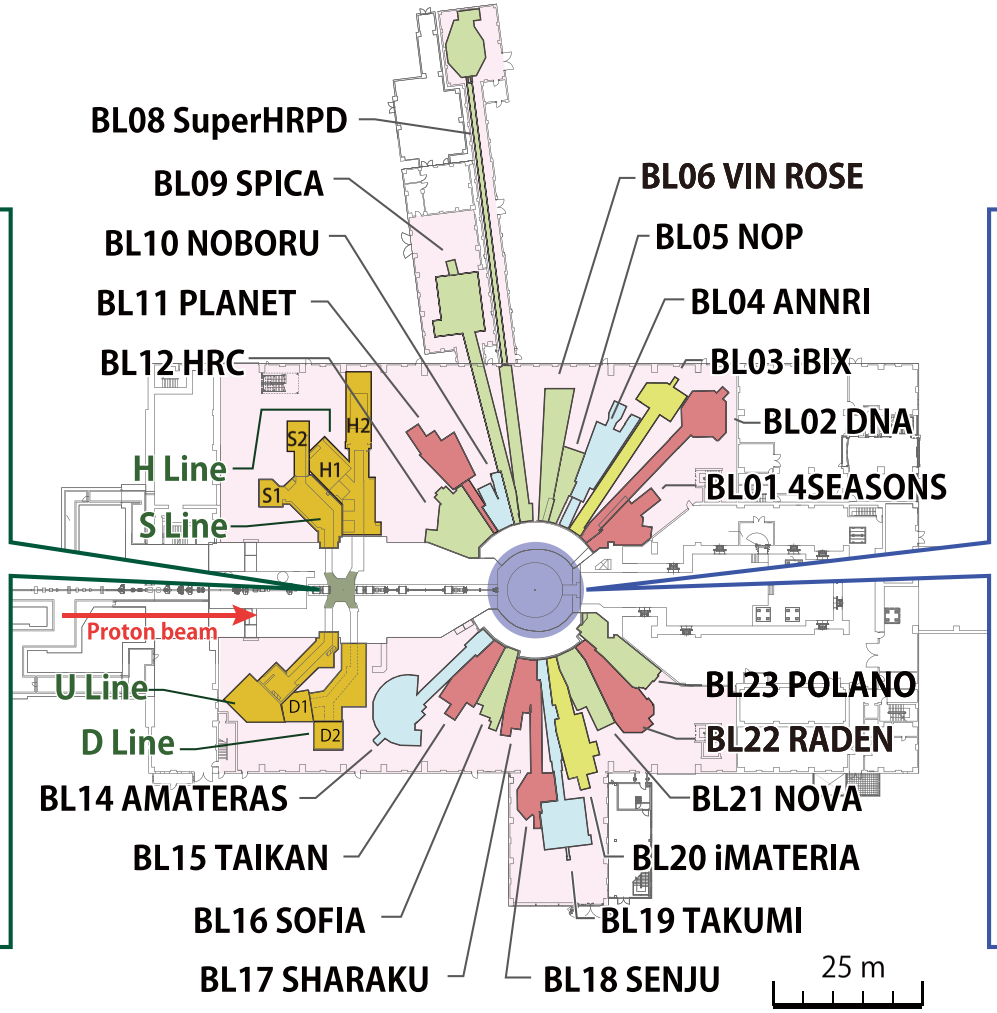

Neutron Source

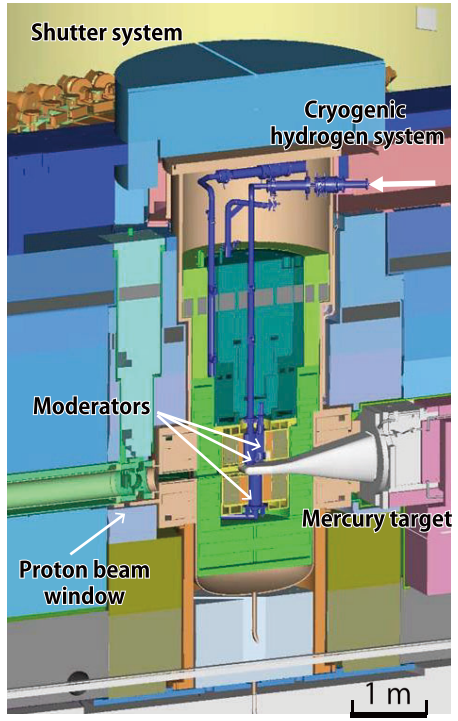

Muon Instruments

Neutron Instruments

JAEA

KEK

Public beam lines

Ibaraki Pref.

As of March 2023

Research and Development Highlights

Atomic Distribution and Local Structure in Ice VII from in situ Neutron Diffraction

1. Introduction

Water (H_2O or D_2O) is one of the simplest molecules but is also known for the anomalous diversity in crystalline polymorphs, which number 20 to date. Ice VII is one of the high-pressure phases, which is stable at temperatures higher than 273 K at 3 GPa. Ice VII is a hydrogen-disordered phase in which water molecules randomly orient. It transforms to ice VIII below 273 K [1]. Ice VIII is an ordered counterpart which has an oxygen sublattice identical to ice VII, but the orientations of water molecules align in a certain manner.

In ice structures, each water molecule is connected to four neighbouring water molecules *via* hydrogen bonds in tetrahedral geometry. Hence, the structure of ice VII is often described by a cubic model in which oxygen forms BCC sublattice and hydrogens are located on the vertices of oxygen-centred tetrahedra. This simple "single-site model" reproduces the diffraction patterns well and is widely adopted. On the other hand, it is also known to result in physically unreasonable water geometry such as too short covalently-bonded OD (0.89 Å [2]) compared to those in ice VIII (0.97 Å [2, 3]). This discrepancy comes from the too-simplified description with tetrahedral symmetry.

More reasonable "multi-site models" have been proposed to describe the structure of ice VII. In these models, the hydrogens are located away from a straight line between adjacent oxygens [4, 5]. Oxygen positions were modelled mainly in two ways: displacements towards <111> [5] or <100> [2]. Displacements along <100> imply that ice VII favours local structures similar to ice VIII, while displacements along <111> imply the opposite. A computational study supported the <100> model but also claimed the insufficiency of the simple models with discrete atom sites [6]. In the present study, we investigated the disordered structure of ice VII from *in-situ* neutron diffraction combined with the maximum entropy method (MEM) and pair distribution function (PDF) analyses [7].

2. Experimental

The powder diffraction experiments were performed at the BL11 (PLANET) beamline [8] using the MITO system [9] for *pT* control. Powder samples of deuterated ice VII were obtained *via* solid-solid phase transitions, which provide fine powder samples suitable for structure analyses. Deuterated samples (D) are used to avoid the incoherent scattering from light hydrogen (H). Diffraction patterns of ice VII were collected at 2.2 GPa and temperatures of 298 K and 274 K. A powder diffraction pattern of ice VIII was also collected at 2.2 GPa and 274 K for comparison in PDF analysis. The sample pressures were estimated from the equation of state of ice VII and VIII themselves [10].

3. Atomic distribution from MEM analysis

Based on the principle of maximum entropy, the MEM analysis derives the most probable distribution $\rho(r)$ by maximising the information entropy under constraints on the observed structure factors $F_o(\boldsymbol{k})$ and their uncertainties $\sigma F_o(\boldsymbol{k})$. The MEM analysis is often called "model-free" analysis in comparison to the conventional parameter refinements of presumed structure models such as the Rietveld analysis.

The obtained MEM result (Fig. 1) shows the elongated feature of oxygen distribution along <111> direction, consistent with Nelmes' work [5]. At the same time, the distribution has a tetrahedral shape rather than a tetrapodal one, which suggests that the oxygen distribution

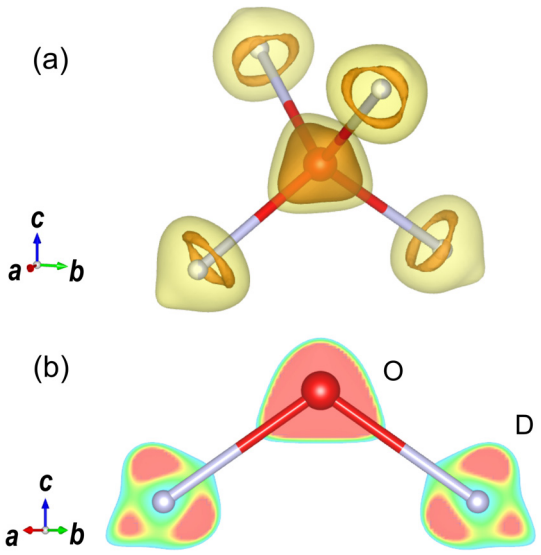

Figure 1. Distribution of scattering-length density in ice VII derived at 298 K and 2.2 GPa. (b) indicates the cross sections of (a) on the (110) plane. The oxygens and deuteriums are illustrated as those in the single-site model with O-D = 0.97 Å, as in the water molecule, and ∠DOD = 109.47° for comparison. Density decreases from red to blue colour.

also includes the components along <100>.

The deuterium has density maxima aside from the <111> axis, as reported in the previous studies [4, 5]. On the other hand, the distribution is not localised at discrete points but has a ring-like feature. Moreover, the distribution is elongated along <111>. These features cannot be described in the conventional models with ellipsoidal atom sites, but their physicochemical origin is not clear yet.

4. Local structure from PDF analysis

We also derived local structure information from PDF analysis. The MEM analysis only deals with Bragg peaks assuming a periodic structure, resulting in an averaged structure within the unit cell. In the PDF analysis, the interatomic correlation is obtained from the back Fourier transformation of the structure factor $S(Q)$ without the assumption of the periodicity.

The obtained PDF $G(r)$ shows the consistency of intramolecular structures between ice VII and VIII (Fig. 2). The covalently-bonded OD bond distances are estimated to have similar values: 0.9662 (5) for ice VII and 0.9658 (5) Å for ice VIII. These findings are in contrast to the Rietveld result with OD = 0.9163 (5) Å for ice VII and 0.9681 (8) Å for ice VIII. On the other hand, ice VII and VIII differ in the intermolecular region. This is consistent with the MEM result and a computational study suggesting that the ice-VII-like is no longer dominant at the temperature close to the phase boundary [11].

5. Future plans

Various experiments suggested the crossover in dominant dynamic processes in ice VII at approximately 10 GPa from molecular rotation to proton translation ([12] and references therein). Such cross-over would be related to the structural changes upon compression, such as the shortening of intermolecular distances and accompanying steric hindrance. High-pressure *in-situ* diffraction techniques will lead to comprehensive pictures of the anomalous physical properties of ice VII.

References

[1] E. Whalley et al., J. Chem. Phys. **45**, 3976 (1966).
[2] W. F. Kuhs et al., J. Chem. Phys. **81**, 3612 (1984).
[3] J. D. Jorgensen et al., J. Chem. Phys. **81**, 3211 (1984).
[4] J. D. Jorgensen and T. G. Worlton, J. Chem. Phys. **83**, 329 (1985).
[5] R. J. Nelmes et al., Phys. Rev. Lett. **81**, 2719 (1998).
[6] C. Knight and S. J. Singer, J. Phys. Chem. A **113**, 12433 (2009).
[7] K. Yamashita, et al., Proc. Natl. Acad. Sci. **119**, 1 (2022).
[8] T. Hattori et al., Nucl. Instruments Methods Phys. Res. **780**, 55 (2015).
[9] K. Komatsu et al., High Press. Res. **33**, 208 (2013).
[10] S. Klotz et al., Phys. Rev. B **95**, 174111 (2017).
[11] K. Umemoto et al., Chem. Phys. Lett. **499**, 236 (2010).
[12] R. Yamane et al., Phys. Rev. B **104**, 214304 (2021).

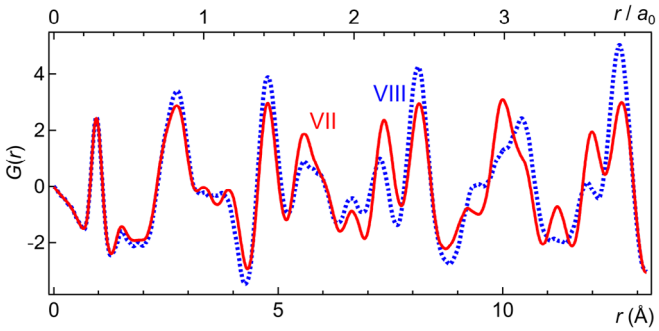

Figure 2. Pair distribution functions $G(r)$ of ice VII and VIII obtained at 274 K and 2.2 GPa. The abscissa on top is normalised interatomic distance by lattice parameter $a_0 = 3.346632$ (13) Å of ice VII, determined from the Rietveld analysis.

K. Yamashita[1,#], K. Komatsu[1], S. Klotz[2], O. Fabelo[3], M. T. Fernández-Díaz[3], J. Abe[4], S. Machida[4], T. Hattori[5], T. Irifune[6], T. Shinmei[6], K. Sugiyama[7], T. Kawamata[7], and H. Kagi[1]

[1]Geochemical Research Center, Graduate School of Science, The University of Tokyo; [2]Institut de Minéralogie, de Physique des Matériaux et de Cosmochimie, Sorbonne Université; [3]Institut Laue-Langevin; [4]Neutron Science and Technology Center, CROSS; [5]Neutron Science Section, Materials and Life Science Division, J-PARC Center; [6]Geodynamics Research Center, Ehime University; [7]Institute for Materials Research, Tohoku University [#]Present address: Institute of Physical Chemistry, University of Innsbruck

Study on Large Elastic Deformation in Bulk Metal by *In Situ* Neutron Diffraction

1. Introduction

The metals and alloys used in our everyday life are mostly crystalline, capable of elastic deformation as the bonds between atoms can be temporarily expanded or contracted by external forces. Theoretically, a maximum elastic strain in the order of 10% is predicted for most metal crystals under a uniaxial stress, but in practical bulk metallic materials, the elastic strain is usually below 0.5% due to defects. The stress-strain relationship of bulk metals in this small elastic deformation region is generally linear and follows the well-known Hooke's law.

Metals with a large capacity for elastic deformation can store mechanical energy due to their ability to undergo substantial reversible strain, making them good candidates for applications in mechanical vibration systems, sports equipment, medical devices, and more. It is known that downscaling is effective in achieving large elastic strains in metal crystals. For instance, when metal samples are reduced to microscale or nanoscale, as in the case of whiskers or nanowires, the generation of dislocations is suppressed, and they are known to exhibit ultra-high yield strengths and elastic strains up to 4%~7%, close to the theoretical values. However, scaling up metals to bulk dimensions, such as exceeding 1 mm^3, has proven difficult to achieve large elastic strains. Until now, only a few titanium-based alloys known as gum metals [1] and certain high-entropy alloys [2] have been reported to have large elastic strains, but these strains are only about 2%. In a recent study, we have discovered that a BCC-structured Heusler-type bulk copper alloy exhibits a substantial giant elastic strain exceeding 4.3% at room temperature [3]. This paper introduces the investigation of its origins through *in situ* neutron diffraction experiments.

2. Experimental

The alloy with a chemical composition of $Cu_{69}Al_{17}Mn_{14}$ (at%) was prepared by induction melting from pure elements. The ingot was then hot rolled and subjected to cyclic heat treatment [4], by which single-crystal sheets with length over several centimeters could be obtained. Tensile tests on the single crystals at room temperature were conducted in conjunction with neutron diffraction measurements. The neutron diffraction experiments were carried out using the Engineering Materials Diffractometer BL19 "TAKUMI" installed at the Materials and Life Science Experimental Facility (MLF) of the J-PARC (Japan Proton Accelerator Research Complex). This instrument is a time-of-flight (TOF) neutron diffraction diffractometer using powerful pulsed neutrons, capable of simultaneously measuring diffraction profiles existing over a wide range of lattice plane spacings. *In situ* neutron diffraction experiments during uniaxial deformation can simultaneously measure the lattice plane spacings in the loading direction (LD) and the transverse direction (TD) by positioning the detectors at ±90° to the incident beam and setting up the testing machine so that the load axis is horizontal at 45° [5].

3. Results and discussion

The alloy shows a giant elastic anisotropy [6], as shown in Fig. 1a. The Zener ratio is very large at 11.1, and the Young's modulus along <100> direction is very small at 23.2 GPa based on the calculation results from elastic constants. Figure 1b shows the stress-strain curve for a single-crystal sample stretched along <100> direction at room temperature. Upon unloading the applied stress, it was found that the sample fully recovered its original shape. The reversible strain in this process reached 4.31%, which is about an order of magnitude larger than the elastic strain values of most practical bulk metallic materials, including steels. The initial Young's modulus along the <100> direction was found to be approximately 24 GPa. Additionally, the stress hysteresis in the loading-unloading loop is zero, indicating that essentially no work is dissipated. Moreover, with the increase of applied stress, the slope of the stress-strain curve becomes smaller, indicating a significant elastic softening phenomenon.

When the phenomenon of large reversible strain without stress hysteresis was initially discovered, it was assumed to be due to the contribution of local stress-induced martensitic transformation. To investigate the nature of this phenomenon, *in situ* neutron diffraction measurement was conducted. The changes in the two-dimensional diffraction profiles of LD and TD accompanying the load-unloading tensile deformation are shown in Figs. 2a and 2b, respectively. The maximum applied stress was set at 580 MPa to prevent damage to the sample. The diffraction profiles were demonstrated to change continuously and reversibly with the

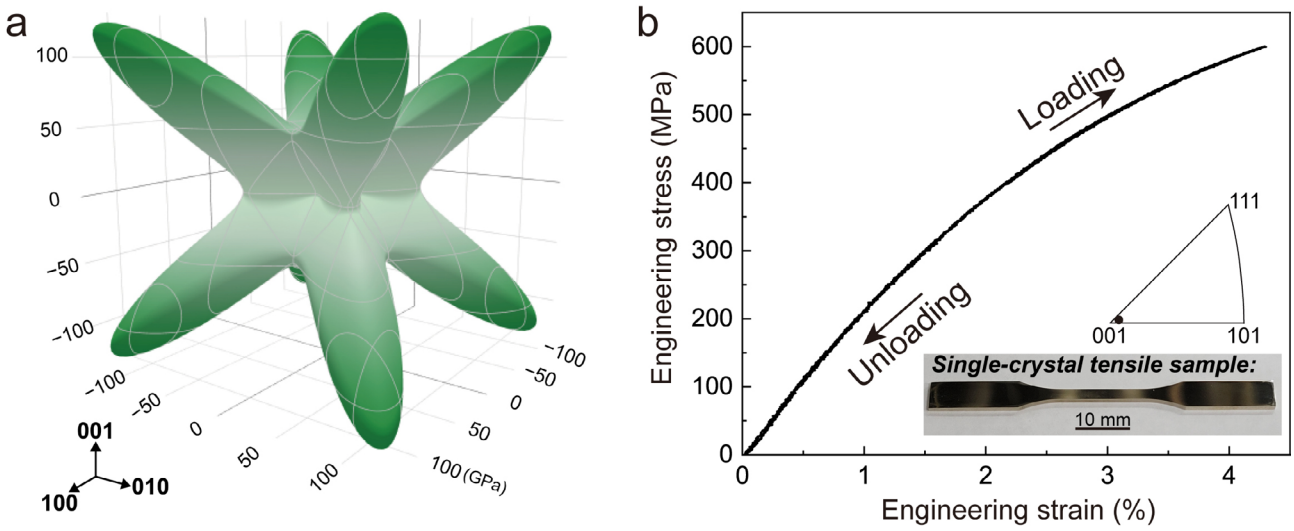

Figure 1. (a) The crystal orientation dependence of Young's modulus, where a giant elastic anisotropy can be referred; (b) The loading-unloading tensile stress-strain curve for a <100> single crystal obtained at room temperature.

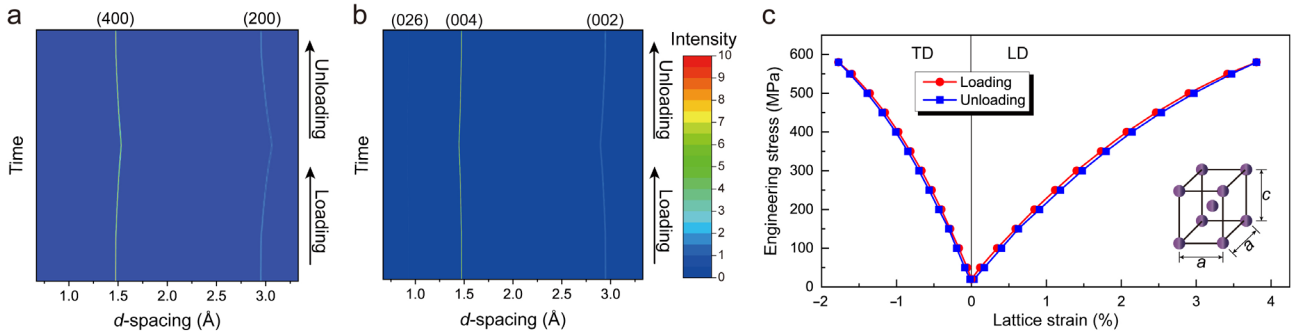

Figure 2. (a) Two-dimensional neutron diffraction patterns in the LD; (b) Two-dimensional diffraction patterns in the TD; (c) Lattice strain as a function of engineering stress.

application and release of stress in both LD and TD. In the wide range of interplanar spacing *d*-spacing from 0.67 Å to 3.33 Å, no other diffraction patterns were detected during the measurement, revealing that neither phase transformation nor phase decomposition occurred during the reversible deformation.

To quantitatively evaluate the atomic-level structural changes during reversible deformation, one-dimensional diffraction patterns corresponding to the (400) plane in LD and the (004) plane in TD were extracted, and the lattice strains were then obtained. Figure 2c plots the lattice strain, which is the rate of change of interplanar spacing relative to the initial value before loading, against the applied stress. The engineering stress-lattice strain curve for LD shows a shape similar to the macroscopic stress-strain curve shown in Fig. 1b. The maximum reversible lattice strain in LD at 580 MPa stress is large at 3.81%, which closely matches the strain of 3.83% macroscopically measured with an extensometer.

The results of the neutron diffraction experiments reveal that the nature of the large reversible strain in the Cu-Al-Mn alloy is a true elastic deformation, where reversible lattice strains occur while maintaining the parent phase. This is independent of the "pseudoelastic deformation" caused by martensitic transformation, which is characteristic of the shape memory alloys.

4. Summary and future perspectives

This paper presented results from *in situ* neutron diffraction experiments applied to the study of the dynamic deformation behavior of metallic materials, using the Cu-Al-Mn alloy as an example of a material exhibiting significant elastic strain. Bulk Cu-Al-Mn alloy, which shows large elastic strain, possesses superior elastic properties in terms of elastic deformation capacity and Young's modulus compared to conventional bulk

metallic materials. This suggests a wide range of potential applications for high-performance springs, sealing materials, and precision machinery. We hope that these results will encourage the development of new materials capable of large elastic strain and the invigoration of research using *in situ* neutron diffraction experiments from both fundamental and practical perspectives.

References

[1] T. Saito et al., Science, **300** 464 (2003).
[2] Q. F. He et al., Nature, **602** 251 (2022).
[3] S. Xu et al., Nat. Commun., **13** 5307 (2022).
[4] T. Omori et al., Science, **341** 1500 (2013).
[5] https://mlfinfo.jp/en/bl19/
[6] S. Xu, Ph.D. thesis, Tohoku University (2020).

S. Xu[1], T. Odaira[1], X. Xu[1], T. Omori[1], T. Kawasaki[2], S. Harjo[2], and R. Kainuma[1]
[1]*Department of Materials Science, Tohoku University;* [2]*Neutron Science Section, Materials and Life Science Division, J-PARC Center*

Effect of Hydrogen on Evolution of Deformation Microstructure in 2Mn-0.1C Ferritic Steel

1. Introduction

Deterioration of the mechanical properties of metals and alloys by hydrogen is known as hydrogen embrittlement. Hydrogen-related quasi-cleavage (QC) fracture, one of the typical fracture modes of hydrogen embrittlement, occurs along a non-cleavage plane in a transgranular manner. We previously found that the QC fracture propagated parallel to {011} planes both in martensitic steel and ferritic steel [1, 2]. These results suggested that the mechanism of the QC fracture is closely related to plastic deformation because {011} plane corresponds to the slip plane in body-centered cubic (BCC) crystals. Therefore, further study on the effect of hydrogen on plastic deformation is needed to understand the mechanism of the QC fracture.

In this study, we characterized the evolution of the deformation microstructure in a hydrogen-charged steel with ferrite microstructure [3].

2. Experimental

A 2Mn-0.1C (mass%) steel with ferrite (87%) and pearlite (13%) phases was used in this study. Sheet-type tensile test specimens with a gauge length of 10 mm, a width of 5 mm, and a thickness of 1 mm were cathodically pre-charged with hydrogen in an aqueous solution (3% NaCl + 3 g L^{-1} NH_4SCN) at a current density of 5 A m^{-2}. Uniaxial tensile tests were performed at a strain rate of 8.3×10^{-6} s^{-1}, at ambient temperature under hydrogen concurrent-charging condition (same as the pre-charging condition). Some of the tensile tests were stopped and the specimens were unloaded at strain amounts of 3%, 11.5%, 20%, and 24% corresponding to the end of the Lüders deformation, the middle point of work hardening, the ultimate tensile strength, and prior to the final rupture, respectively.

The tensile-tested and unloaded specimens at strain amounts of 3%–20% were analyzed by neutron diffraction using BL19 "TAKUMI" in J-PARC. From the obtained neutron diffraction profiles, the dislocation densities and the fractions of screw/edge dislocations were evaluated by a convolutional multiple whole profile (CMWP) fitting proposed by Ungar [4]. The microstructures of the tensile-tested and neutron-diffraction-measured specimens were characterized by scanning transmission electron microscopy (STEM). TEM is very useful in characterizing the dislocation morphology, character, and density. However, the disadvantage of TEM is the limited observation area. In contrast, we can obtain bulk average information from neutron diffraction. Using TEM and neutron diffraction together, we characterized the deformation microstructure from bulk to nanoscale.

3. Results and discussion

Figure 1(a) shows the nominal stress–nominal strain curves and dislocation densities. Although the total elongation of the hydrogen-charged specimen (red, 27%) is much smaller than that of the uncharged specimen (black, 48%), the dislocation densities are hardly affected by the presence of hydrogen at the corresponding strain amounts. We note that a certain amount of dislocation that forms cell boundaries is excluded in Fig. 1 because their elastic strain fields mutually cancel each other. Figure 1(b) shows the fractions of screw/edge dislocations estimated from the neutron diffraction

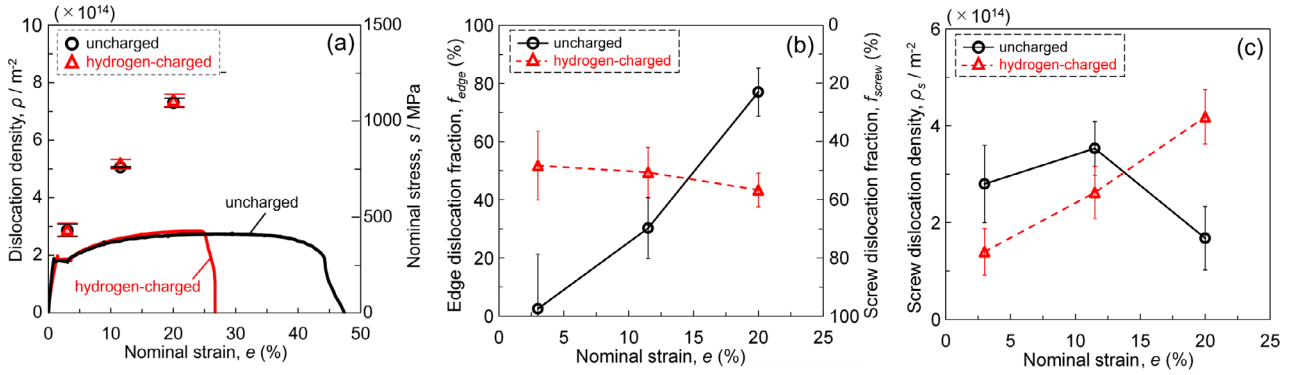

Figure 1. (a) Nominal stress–nominal strain curves and dislocation densities, (b) fractions of screw and edge dislocations, (c) screw dislocation densities of the uncharged specimens (black, circle marks) and the hydrogen-charged specimens (red, triangle marks) [3].

analysis. The left and right axes indicate the fractions of the edge and screw components, respectively. In the uncharged specimens (black circle marks), almost all of the dislocations were screw-type at the initial stage of deformation (e = 3%), and the fraction of the edge component increased monotonically with increasing strain. In contrast, in the hydrogen-charged specimens (red triangle marks), almost equal fractions of screw/edge components were present and did not vary greatly with the strain amount. From the dislocation density data (Fig. 1(a)) and the fractions of the dislocations (Fig. 1(b)), we calculated the individual densities of each type of dislocations. Figure 1(c) shows the changes in the screw dislocation density with strain amount. We found that the screw dislocation density in the hydrogen-charged specimen was much higher than that of the uncharged specimen at the later stage of deformation (e = 20%).

Figures 2(a, d) show low-magnification STEM images of the dislocation morphologies in the uncharged and hydrogen-charged specimens, respectively, at e = 3%. The dislocations are linear in the uncharged specimen, while they are curved and tangled in the hydrogen-charged specimen. To further investigate the deformation microstructure, the nature of the dislocations was characterized. Figures 2(b, e) show high-magnification STEM images of the deformed microstructure in the uncharged and hydrogen-charged specimens, respectively, at e = 3%. Figures 2(c, f) are the schematic illustrations of the dislocation configurations in (b, e), respectively, where the Burgers vectors of the dislocations determined by the $\boldsymbol{g} \cdot \boldsymbol{b} = 0$ invisibility criterion are represented by different colors. In the uncharged specimen, almost all the observed dislocation loops elongated parallel to their Burgers vectors, suggesting that they have a large screw component. On the other hand, in the hydrogen-charged specimen, many dislocations have a large edge component as indicated by arrows in Fig. 2(f). Accordingly, the results demonstrated that the fractions of screw/edge dislocations estimated from the neutron diffraction analysis (Fig. 1(b)) were consistent with the real dislocation nature observed by STEM. We also confirmed that the fraction of each dislocation component was consistent between neutron diffraction and STEM at e = 20%.

It is widely accepted that in BCC transition metals, edge dislocations have greater mobility than screw dislocations because of the higher Peierls potential of screw dislocations, leading to screw-segment-elongated dislocation loops at the initial stage of deformation [5]. This is consistent with the present microstructure in the uncharged specimen. On the other hand, in the hydrogen-charged specimen, many edge-segment-elongated dislocation loops were observed. Thus, the results strongly suggest that the relative velocity of screw dislocation to edge dislocation was increased by hydrogen. Itakura et al. [6] performed first-principles calculations and reported that hydrogen reduced the activation energy for kink-pair nucleation, which led to a

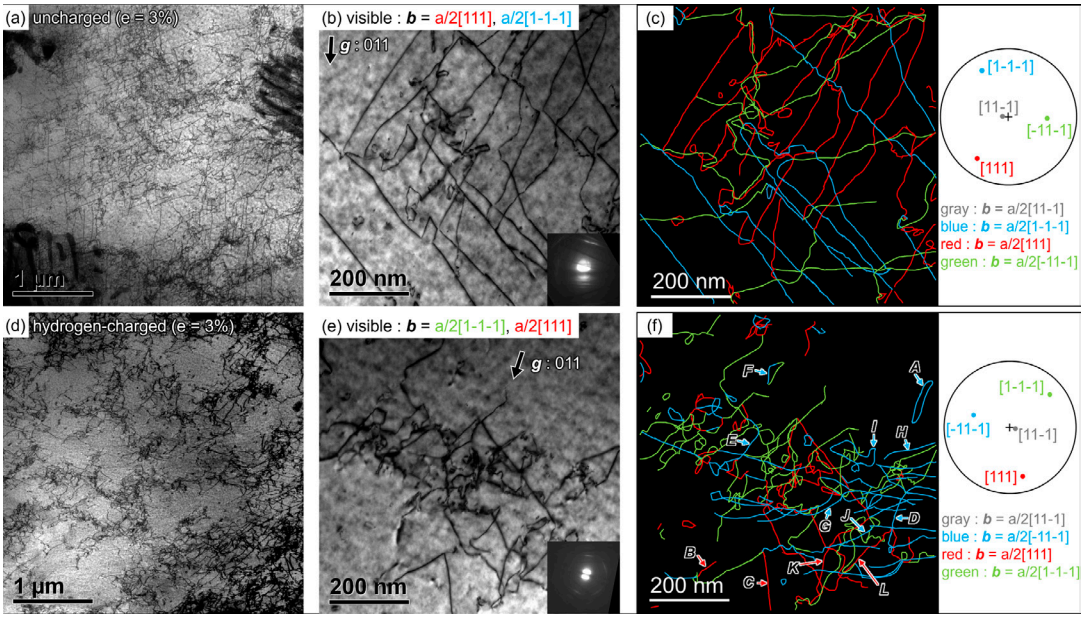

Figure 2. (a, d) low-magnification and (b, e) high-magnification STEM images of the dislocation morphologies under two-beam conditions ($\boldsymbol{g}$ = 011) at a strain amount of 3%. (c, f) Schematic illustrations of the dislocation configurations corresponding (b, e), respectively, where the Burgers vectors of the dislocations determined by contrast analysis are represented by different colors [3]. (a–c) and (d–f) show the uncharged and hydrogen-charged specimens, respectively.

decrease in the critical shear stress for screw dislocation motion. In addition, using molecular dynamics simulations, Matsumoto et al. [7] reported that the motion of edge dislocations was significantly damped by hydrogen. Therefore, we can consider that the tangled dislocation morphology in the hydrogen-charged specimen resulted from the frequent cutting of screw dislocations due to the increase in their relative velocity.

At a strain amount of 24%, well-developed dislocation cell structures, the so-called low energy dislocation structures (LEDS), were observed both in the uncharged and hydrogen-charged specimens. The statistical distributions of LEDS size (d_{LEDS}) and misorientation of LEDS boundaries (θ_{LEDS}) are summarized in Fig. 3(a, b), respectively. The d_{LEDS} was smaller and θ_{LEDS} was larger in the hydrogen-charged specimen than those in the uncharged specimen, suggesting that the amount of dislocation constituting LEDS boundaries was larger in the hydrogen-charged specimen. As explained previously, a certain amount of dislocation constituting the LEDS boundaries was not involved in the dislocation densities derived from the neutron diffraction analysis (Fig. 1(a)). Therefore, the amount of excluded dislocation in the neutron diffraction analysis should be larger in the hydrogen-charged specimen and the density of total dislocations (existing outside the LEDS boundaries and constituting LEDS boundaries) was higher in the hydrogen-charged specimen.

4. Conclusions

In this study, the effect of hydrogen on the evolution of the deformation microstructure in 2Mn-0.1C steel mainly composed of ferrite microstructure was systematically investigated. We found that the densities of the total dislocations (existing outside the LEDS boundaries and constituting LEDS boundaries) were higher in the hydrogen-charged specimens. In addition, we conclude that hydrogen increases the relative mobility of screw dislocations to edge dislocation, leading to the frequent cutting of screw dislocations and tangled dislocation morphology.

5. Acknowledgements

This study was financially supported by JSPS KAKENHI (JP19J21267, JP15H04158, JP19H02459, and JP20K21083) and the Elements Strategy Initiative for Structural Materials (ESISM). The neutron diffraction experiment at the J-PARC was performed under a user program (Proposal No. 2018A0051).

References

[1] A. Shibata et al., Mater. Sci. and Technol., **33** 1524 (2017).
[2] K. Okada et al., Int. J Hydro. Ener., **43** 11298 (2018).
[3] K. Okada et al., Acta Mater., **225** 117549 (2022).
[4] T. Ungar et al., J Appl. Cryst., **32** 992 (1999).
[5] D. Caillard, Acta Mater., **58** 3439 (2010).
[6] M. Itakura et al., Acta Mater., **61** 6857 (2013).
[7] R. Matsumoto et al, Int. ISIJ, **62** 2402 (2022).

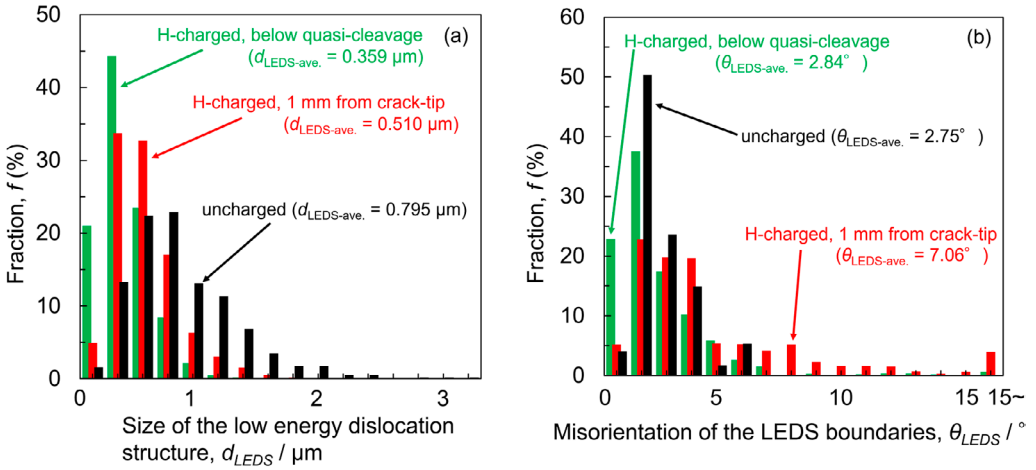

Figure 3. Statistical distribution of (a) LEDS size (d_{LEDS}) and (b) misorientation of LEDS boundaries (θ_{LEDS}) of the microstructures at a strain amount of 24% [3]. The red, green, and black bars indicate areas 1 mm from the crack tip in the hydrogen-charged specimen, just beneath the quasi-cleavage surface in the hydrogen-charged specimen, and the uncharged specimen, respectively.

K. Okada[1,2], A. Shibata[1,3], W. Gong[3,4], and N. Tsuji[2,3]

[1]Research Center for Structural Materials, NIMS; [2]Department of Materials Science and Engineering, Kyoto University; [3]Elements Strategy Initiative for Structural Materials (ESISM), Kyoto University; [4]Neutron Science Section, Materials and Life Science Division, J-PARC Center

High-Pressure Synthesis of Transition-Metal Oxyhydrides with Double Perovskite Structures

1. Introduction

Transition-metal Oxyhydrides crystallizing in perovskite-type and related structures often exhibit high performances regarding ionic conductivity and catalyzing ammonia synthesis owing to the low valence and large negative redox potential of H^- (–2.25 eV) [1–4]. Because such performances are improved with increasing H^- content, the development of oxyhydrides containing large amounts of H^- is crucial.

Known perovskite transition-metal oxyhydrides are represented by the general formula $ABO_{3-x}H_x$, where A is an alkaline earth metal and B is an early transition metal such as Ti, V, and Cr. To ensure charge neutrality, the number of hydride ions can be increased by decreasing the valency of the transition-metal ions at the B site, as observed for $BaTiO_{3-x}H_x$ [5]. However, it is difficult to increase *x* to values above 1 when using early transition metals because they are mostly stable in trivalent and tetravalent states.

To explore a transition-metal oxyhydride with high H^- content, the reduction of the total cation valence would be helpful. Thus, we focused on double-perovskite-type structures ($A_2B'B''X_6$), which comprise corner-sharing octahedra as in the ABO_3 perovskite, but with two types of B cations arranged in two distinct octahedral sites (rock-salt-type order). Various combinations of B′ and B″ metals are allowed within a range of tolerance factors [7]. For instance, the tolerance factor of $Ba_2NaM(O,H)_6$ (M = an early transition metal) is approximately 1 owing to the ionic radii of its constituent ions. In this study, we successfully synthesized four new oxyhydrides with double perovskite structures with different B″ atoms, namely $Ba_2NaVO_3H_3$, $Ba_2NaVO_{2.4}H_{3.6}$, $Ba_2NaCrO_{2.2}H_{3.8}$, and $Ba_2NaTiO_3H_3$ [7].

2. Experimental

Polycrystalline samples of $Ba_2NaVO_3H_3$, $Ba_2NaVO_{2.4}H_{3.6}$, $Ba_2NaCrO_3H_3$, and $Ba_2NaTiO_3H_3$ were synthesized by a solid-state reaction under high pressure. The molar ratio of these starting materials was stoichiometric, except for the 2 molar excess of NaH. A mixture of these reagents was ground thoroughly in an Ar-filled glovebox and placed in a NaCl capsule, which was placed in a pyrophyllite cell with a graphite heater. The cell was compressed to a pressure of 4 GPa using a cubic anvil press, heated for 1 h at 825°C, and then quenched to room temperature before releasing the pressure. The obtained sample was washed with 0.1 molar NH_4Cl/MeOH to remove residual NaH. Powder XRD measurements were performed using a SmartLab (Rigaku) with CuKα1 radiation selected by a Johansson-type monochromator with a Ge(111) crystal. Time-of-flight powder ND measurements were performed using a neutron total scattering spectrometer (NOVA) installed in the Japan Proton Accelerator Research Complex (MLF J-PARC). Powder diffraction data were collected at room temperature using a vanadium holder with a diameter of 3 mm. The crystal structure was determined by the simultaneous refinement of the XRD and ND data by the Rietveld method using the Jana2006 program [8]. The chemical compositions of the products were examined by EDX analysis (JSM-IT100). Thermogravimetric measurements were carried out by heating powder samples at a rate of 10 K min^{-1} under flowing oxygen atmosphere using Bruker TG-DTA 2020SA. The electronic charge densities of $Ba_2NaTiO_3H_3$ and $BaTiO_{2.5}H_{0.5}$ were obtained using first-principles DFT calculations implemented in the WIEN2k code [9].

3. Results and discussion

First, we will discuss $Ba_2NaVO_3H_3$. Elemental analysis by EDX for the obtained sample reveals that the molar ratio of Ba:Na:V was 2:1:1. To determine the precise crystal structure and chemical composition of the product, we carried out structural analyses using XRD and neutron diffraction (ND) data based on a structural model of the double-perovskite structure (Fig. 1). Two assumptions were made: (1) the anion sites are randomly occupied by O^{2-} and H^-, and (2) V and Na are ordered in a rock-salt-type manner at the octahedral sites. As shown in Fig. 2, fittings of both data were satisfactory and converged with reasonably small *R* factors (R_{wp} = 7.47% and R_p = 5.52% for XRD; R_{wp} = 1.05% and R_p = 0.83% for ND). We examined the possibility of site mixing among the Na and V sites and found that both atoms are highly ordered with a mixing of less than 1%. This is likely due to the large differences between the ionic radii and valences of Na^+ (1.02 Å) and V^{4+} (0.58 Å). The refined chemical composition is $Ba_2NaVO_{2.996(4)}H_{3.004(4)}$; this gives a tetravalent state for V, which agrees with the average valence of V in the starting materials. Thermogravimetric analysis of the sample under oxygen flow shows a weight

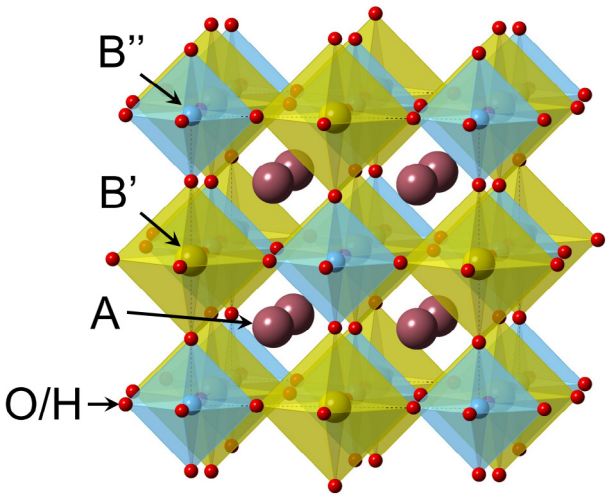

Figure 1. Crystal structure of double-perovskite oxyhydrides $A_2B'B''(O, H)_6$.

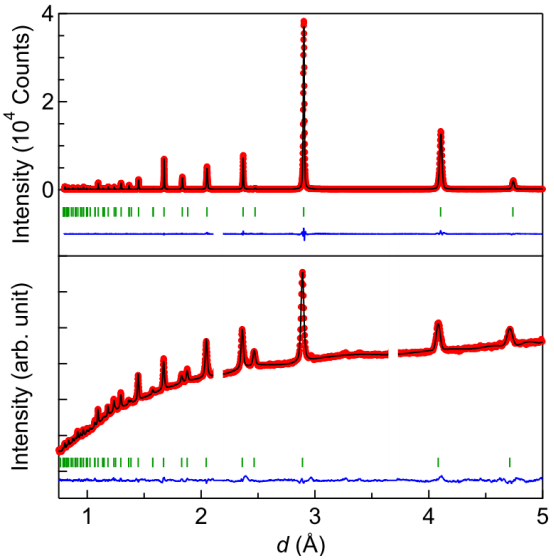

Figure 2. Powder XRD pattern (upper) and powder neutron diffraction (ND) pattern (lower) of $Ba_2NaVO_3H_3$ analyzed by the Rietveld method. The observed (red marks), calculated (black line), and difference (blue line) profiles are shown, together with the positions of the Bragg reflections represented by the green ticks.

increase of 7.36%, which is consistent with this chemical composition.

We also attempted to synthesize vanadium oxyhydrides with higher hydride contents. The synthesis yielded a double-perovskite phase. Our structural analyses of the XRD and ND data revealed the formation of a double perovskite oxyhydride with a chemical composition of $Ba_2NaVO_{2.400(5)}H_{3.600(5)}$. Furthermore, we found that not only vanadium but also chromium and titanium formed oxyhydrides with double-perovskite structures. The syntheses yielded double-perovskite phases with chemical compositions of $Ba_2NaCrO_{2.238(9)}H_{3.762(9)}$ and $Ba_2NaTiO_3H_3$. For the latter compound, our structural refinements revealed nearly 7% anti-site mixing between Na and Ti.

Owing to the high hydride contents, newly discovered $Ba_2NaM(O,H)_6$ have a covalent bonding nature of the M–H bonds. To compare that of $Ba_2NaM(O,H)_6$ and known perovskite oxyhydrides $BaM(O,H)_3$, two-dimensional electronic charge densities for $Ba_2NaTiO_3H_3$ and $BaTiO_{2.5}H_{0.5}$ were visualized by DFT calculations using atomic positions obtained from structural analyses. Figures 3 represent the contour plots of the electronic charge densities around the Ti, O, and H sites, in which the semi-core states, such as Ti-3s and -3p, were removed to obtain a meaningful picture of the chemical bonds. In each compound, there is a certain electron

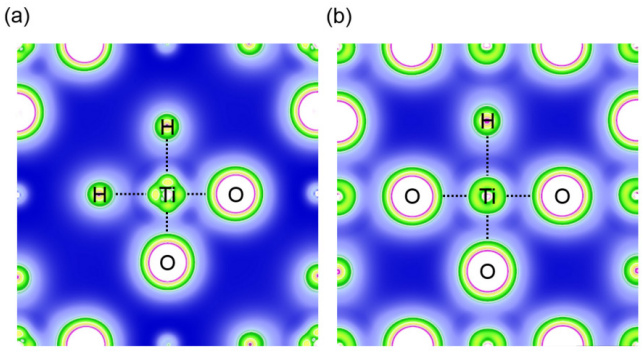

Figure 3. Two-dimensional contour plots of the electronic charge densities of (a) $Ba_2NaTiO_3H_3$ and (b) $BaTiO_{2.5}H_{0.5}$ in the (100) plane.

charge density around H, which is indicative of a hydride anion. The non-spherical charge distribution around Ti in $Ba_2NaTiO_3H_3$ clearly shows the noticeable covalent nature of the Ti–H and Ti–O bonds in the double-perovskite oxyhydride. This covalent nature of the Ti–H bonds is reduced in $BaTiO_{2.5}H_{0.5}$, with fewer hydrides, as evidenced by the almost spherical charge density around Ti.

4. Conclusion

We synthesized successfully four new oxyhydrides, $Ba_2NaM(O,H)_6$ (M = Ti, V, Cr) with double-perovskite structures via high-pressure synthesis. Structural analyses of the XRD and ND data showed that Na and M are highly ordered in a rock-salt-type structure. The hydride species occupy a maximum of 63% of the anion sites in $Ba_2NaCrO_{2.2}H_{3.8}$, which is the highest amount reported thus far for known transition-metal oxyhydrides with perovskite-related structures. Owing to this high hydride content, the M–(O,H) bonds have significant covalent nature confirmed by DFT calculations. We believe that these oxyhydrides could provide a new platform for hydride chemistry.

References

[1] T. Yajima et al., *J. Am. Chem. Soc.*, **134**, 8782-8785 (2012).
[2] G. Kobayashi et al., *Science*, **351**, 1314-1317 (2016).
[3] T. Yajima et al., *Nat. Chem.*, **7**, 1017 (2015).
[4] Y. Tang et al., *Adv. Ener. Mater.*, **8**, 1801772 (2018).
[5] Y. Kobayashi et al., *Nat. Mater.*, **11**, 507-511 (2012).
[6] S. Vasala et al., *Prog. Solid State Ch.*, **43**, 1-36 (2015).
[7] T. Yajima et al., *Inorg. Chem.* **61**, 2010-2016 (2022).
[8] V. Petricek et al., *Z. Kristallogr. -Cryst. Mater.* **229**, 345 (2014).
[9] P. Blaha et al., Technische Universität Wien: Vienna, Austria, (2001).

T. Yajima[1,2], K. Takahashi[2], H. Nakajima[2], T. Honda[3,4], K. Ikeda[3,4], T. Otomo[3,4], and Z. Hiroi[2]
[1]*Graduate School of Engineering, Nagoya University;* [2]*Institute for Solid State Physics, University of Tokyo;* [3]*Neutron Science Section, Materials and Life Science Division, J-PARC Center;* [4]*Institute of Materials Structure Science, KEK*

The Ion Dynamics in $Li_{10}GeP_2S_{12}$ Investigated by Quasi-Elastic Neutron Scattering Measurements

1. Introduction

The performances of current Li-ion batteries could potentially be enhanced through the development of all-solid-state Li batteries, where Li^+ conductors are used as solid electrolytes to replace conventional organic liquid electrolytes [1]. For the ideal design of Li^+ conductors, it is important to understand the correlation between microscopic and macroscopic motions (e.g., microscopic = Li^+ jumping between neighboring sites; macroscopic = long-range Li^+ migration). This study [2] reports the application of the quasi-elastic neutron scattering (QENS) measurement to characterize the lithium diffusive behavior in a well-known superionic conductor, $Li_{10+x}Ge_{1+x}P_{2-x}S_{12}$ (LGPS) [3]. The microscopic diffusivity obtained by analysis of the QENS spectra is compared with reported values [4, 5] measured by pulse-field gradient nuclear magnetic resonance (PFG-NMR) for relatively long-range Li^+ migration, to highlight the fact that QENS provides the local dynamic behavior for the Li^+ species present in bulk crystals. In addition, QENS is used to measure the $Li_9P_3S_9O_3$ (LiPSO) phase [6], which is a structural derivative of LGPS, but exhibits an ionic conductivity two orders of magnitude lower than that of LGPS. As a result, the dynamic parameters of the two phases can be compared, and any differences in their conductivities can be rationalized.

2. Description of materials and methods

Figure 1A shows the crystal structure frameworks of LGPS and LiPSO [7, 8]. For LGPS, the structure consists of a scaffold composed of PS_4 and $[P/Ge]S_4$ tetrahedral units. Through these tetrahedral units Li sites are widely distributed forming connected sites along the *c*-axis, which is considered as a Li migration pathway. The LiPSO crystal possesses similar structural features, except that its tetrahedral units are PS_4 and $P[S/O]_4$, and its unit cell volume is smaller than that of LGPS.

The phase-pure LGPS and LiPSO samples were synthesized according to previous reports [3, 8]. In synthesis, Li was substituted into ^7Li to avoid neutron absorption. The sample compositions and the reported ionic conductivity at room temperature are summarized in Table 1, together with the physical values determined by the present QENS study. The QENS spectra were recorded at the BL02 beamline (DNA at MLF/J-PARC), which is a TOF-type near-backscattering spectrometer equipped with a high-resolution Si crystal analyzer. Measurements were performed with an energy resolution of 3.6 eV in the temperature (*T*) range between 150 and 614 K, and the instrument resolution function was measured at 150 K, where no QENS signal was observed. Data were collected within an energy transfer range from −40 to 100 μeV and a *Q* range of 0.1–1.9 $Å^{-1}$.

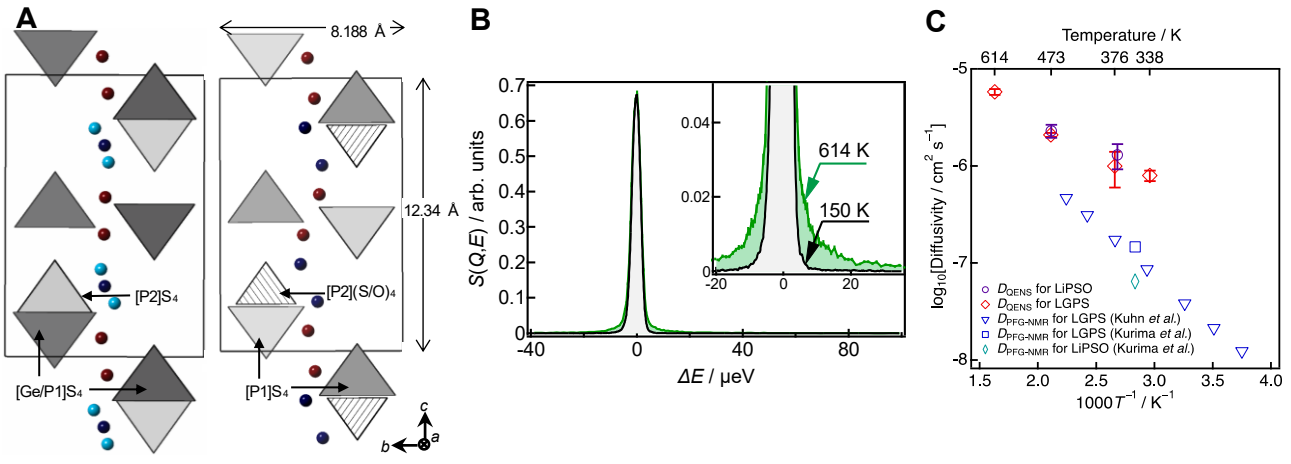

Figure 1. QENS study of LGPS and LiPSO. (**A**) Tetrahedral structural units and lithium site distributions along the *c*-axis for LGPS (left) and LiPSO (right). For the lithium sites, only those located along the *c*-axis are displayed for clarity. The black rectangle indicated for each phase represents the scale of the unit cell. The lattice parameters for LiPSO at 473 K are indicated. (**B**) Normalized scattering spectra *S*(*Q*, *E*) for LGPS. The inset shows an amplification of the quasi-elastic region. (**C**) Arrhenius plots of the diffusivities measured using the QENS and PFG-NMR techniques [4, 5] for LGPS and LiPSO. Reproduced with permission [2]. Copyright 2022, the American Chemical Society.

Table 1. Sample information, dynamic parameters for Li^+ diffusion, and details for the mobile Li^+ fractions for LGPS and LiPSO at different measurement temperatures.

Sample (composition)	σ_{RT} /mS cm^{-1}	T /K	L_{QENS} or r_{QENS} /Å [a]	τ_{QENS} /ps	D_{QENS} /10^{-6} cm^2 s^{-1}	Mobile fraction 1− EISF [b]
LGPS ($^7Li_{10.05}Ge_{1.05}P_{1.95}S_{12}$)	12	338	2.4 ± 0.13	117 ± 5.8	0.8 ± 0.09	0.14 ± 0.020
		376	2.6 ± 0.50	111 ± 29.1	1.0 ± 0.43	0.29 ± 0.056
		473	2.8 ± 0.08	62 ± 2.3	2.1 ± 0.13	0.40 ± 0.031
		614	3.3 ± 0.10	31 ± 1.5	5.8 ± 0.41	0.48 ± 0.004
LiPSO ($^7Li_9P_3S_9O_3$)	<0.1	373	4.5 ± 0.31	–	1.3 ± 0.38	0.12 ± 0.005
		473	4.9 ± 0.22	–	2.3 ± 0.35	0.25 ± 0.004

[a] L_{QENS} represents the jump distance for LGPS, and r_{QENS} indicates the radius of the sphere for Li^+ diffusion in LiPSO.
[b] The mobile fraction was obtained from the elastic incoherent structure factor (: EISF).

Here, Q represents the magnitude of the scattering vector expressed by $Q = k_i - k_f$, where k_i and k_f denote the wavevector of the incident and the scattered neutrons, respectively. The intensity of the spectra was integrated over a separate Q step. The step size ranged from 0.1 to 0.15 Å^{-1}, depending on the Q range.

3. Analysis of QENS spectra

Figure 1B shows the normalized scattering spectra $S(Q, E)$ of LGPS at 150 and 614 K as a function of the energy transfer ΔE μeV between the incident and scattered neutrons at a representative scattering vector Q = 0.33 Å^{-1}. Compared with the resolution function observed at 150 K, clear quasi-elastic broadening was detected at 614 K with a sufficiently low background. This result implies that the recorded QENS signal, which is due to the relaxation process of the Li ion, is statistically relevant and worthy of further analysis.

The QENS spectra were fitted with a combination of a delta function, a Lorentz function, and a constant background, which were convoluted with the resolution function, in order to obtain an elastic incoherent structure factor (EISF), and half width at half maximum (Γ) of the Lorentz function. The former was calculated from coefficients of the delta and Lorentz function to estimate the immobile species ratio for all Li ions present in the compound.

For LGPS, the obtained Q-dependences of Γ were found to fit well using the Chudley–Elliott model [9], which is a diffusion model that assumes a jump-diffusion process. The fitting analysis provided the jump distance L_{QENS} and the residence time τ_{QENS}. From these parameters the diffusion coefficient (D_{QENS}) was calculated.

For LiPSO, the Chudley-Elliott model was not applicable to the Q dependence of Γ. Thus, the obtained EISF was analyzed using an alternative model in which the mobile species diffuse in a restricted space of a characteristic radius r_{QENS}. The r_{QENS} value ($2r_{QENS}$ ~10 Å) obtained from Q-dependence of EISF was used to derive D_{QENS} from the Γ–Q dependence [10–12].

4. Discussion

The physical values determined by the present QENS analysis are summarized in Table 1. Figure 1C compares the D_{QENS} (/10^{-6} cm^2 s^{-1}) values with those measured by PFG-NMR ($D_{PFG\text{-}NMR}$ /10^{-6} cm^2 s^{-1}) techniques in previous studies [4, 5].

Herein, the difference in the reported conductivity between LGPS (>10 mS cm^{-1}) and LiPSO (<0.1 mS cm^{-1})[3, 8] can be rationalized by two factors indicated by QENS: (1) an impediment that blocks Li ion migration at a spatial scale below 10 Å, and (2) the number of Li ions participating in the conduction process. More specifically, the first factor was indicated by the Γ–Q relationships obtained for LGPS and LiPSO. The former was well described by the translational motion of Li^+ without restriction over the Q/Å^{-1} range of 0–2, corresponding to a value of d > 3.1 Å. In contrast, the translational motion model was applicable to the latter only in the cases where 1 < Q/Å^{-1} < 2 (i.e., 3.1 < d/Å < 6.3), while outside this range, the inside sphere diffusion model was more suitable with a sphere diameter $2r_{QENS}$ of ~10 Å (corresponding to the size of single unit cell of LiPSO with a = 8.1876 Å and c = 12.3415 Å at 473 K). These differences in the Γ–Q relationships for the two materials indicate that the migration of Li ions in LiPSO is more impeded at certain unit cell sizes (~10 Å) than in the case of LGPS. This was considered partly due to the crystal structure difference between LGPS and LiPSO, the anion distribution (Fig. 1A). The anion site is evenly occupied by sulfur in LGPS, but is unevenly occupied in LiPSO due to the oxygen partially occupying the anion sites. In the unit cell for LiPSO there is one pair of PO_4 and PS_2O_2 tetrahedral units or two PSO_3 units, potentially attracting Li

ions [8], and thereby trapping mobile ions around the tetrahedral unit, and eventually impeding Li migration across several unit cells. The oxygen distribution in the LiPSO may be the reason for the fact that Li^+ diffusion over a range longer than the unit cell size was more restricted for LiPSO than for LGPS, as indicated by our QENS analysis. This finding is consistent with the diffusivity evaluated by PFG-NMR, which represents the macroscopic diffusivity to a greater extent than the QENS technique [13]. More specifically, the $D_{PFG\text{-}NMR}$ value for LiPSO (i.e., 6.4×10^{-2} at 353 K) was found to be lower than that of LGPS (i.e., 15×10^{-2} at 353 K), while the D_{QENS} value for LiPSO (i.e., 1.3 ± 0.38 at 373 K for $d < 10$ Å) was determined to be slightly larger than that of LGPS (1.0 ± 0.43 at 376 K for $d > 3.1$ Å).

The second factor responsible for the conductivity difference between LiPSO and LGPS involves the number of Li ions contributing to the conduction process. More specifically, the mobile lithium fraction estimated for LiPSO was lower than that for LGPS; in the estimation based on EISF, the mobile fractions of the Li ions at 473 K were 0.40 ± 0.03 for LGPS and 0.25 ± 0.004 for LiPSO (see Table 1). Based on these values, the volumetric concentrations of mobile Li ions were calculated to be 13.4 and 9.04 mol L^{-1} for LGPS and LiPSO at 473 K, respectively. It was therefore apparent that a larger number of mobile Li ions were present in LGPS, and so in combination with its higher macroscopic diffusivity over the micrometer scale, this factor contributes to its higher conductivity when compared to that of LiPSO.

5. Conclusions

In this study, we successfully observed short-length ionic motion in lithium-ion systems and established the relationship between such motion and ionic conduction for both LGPS and LiPSO. The diffusivity obtained by PFG-NMR was smaller than that obtained by QENS measurements, indicating that any factors acting to impede the diffusivity only become evident during longer-scale ionic migration, especially for the case of LiPSO. Moreover, the mobile fraction of Li ions also influenced the conductivity. Thus, the present study demonstrates that QENS measurements on sulfide fast ionic conductors can allow elucidation of the dynamic behavior of ions, which is linked to the conductivity of the material.

References

[1] K. Takada, Acta Mater., 61, (2013) 759.
[2] S. Hori, et al., J. Phys. Chem. C, 126, (2022) 9518.
[3] N. Kamaya, et al., Nat. Mater., 10, (2011) 682.
[4] A. Kuhn, et al., Energy Environ. Sci., 6, (2013) 3548.
[5] A. Kurima, et al., Abstract of the 55th Battery Symposium in Japan, (2014).
[6] K. Takada, et al., Solid State Ionics, 176, (2005) 2355.
[7] T. Yajima, et al., J. Mater. Chem. A, 9, (2021) 11278.
[8] M. Xu, et al., Inorg Chem, 61, (2022) 52.
[9] C. T. Chudley, et al., Proc. Phys. Soc., 77, (1961) 353.
[10] F. Volino, et al., Mol. Phys., 41, (1980) 271.
[11] K. Ito, et al., J. Phys. Chem. C, 125, (2021) 21645.
[12] V. Kuznetsov, et al., Phys Chem Chem Phys, 23, (2021) 7961.
[13] M. J. Klenk, et al., Solid State Ionics, 312, (2017) 1.

S. Hori[1], R. Kanno[1], O. Kwon[2], Y. Kato[3], T. Yamada[4], M. Matsuura[4], M. Yonemura[5], T. Kamiyama[5], K. Shibata[6], and Y. Kawakita[6]
[1]Institute of Innovative Research, Tokyo Institute of Technology; [2]Interdisciplinary Graduate School of Science and Engineering, Tokyo Institute of Technology; [3]Toyota Motor Europe; [4]Neutron Science and Technology Center, CROSS; [5]Neutron Science Division (KENS), Institute of Materials Structure Science, KEK; [6]J-PARC Center, Japan Atomic Energy Agency

Impact of Na Concentration on the Phase Transition Behavior and H^- Conductivities in the Ba-Li-Na-H-O Oxyhydride System

1. Introduction

Hydrogen transport in solids has received much attention due to expectation for electrochemical applications, including fuel cells and batteries. In the field, proton (H^+) conduction has been almost the only choice, but recently, the use of hydride ion (H^-) is becoming a new trend. Owing to its basic characteristics, such as mono-valence and large polarizability, H^- could be considered a promising charged carrier for fast conduction. We especially focus on K_2NiF_4-type oxyhydride as a platform of H^- conducting materials and have reported $La_{2-x-y}Sr_{x+y}LiH_{1-x+y}O_{3-y}$ in 2016 [1], followed by Ln_2LiHO_3 (Ln = La, Pr, Nd) [2], and Ba_2MHO_3 (M = Sc, Y) [3].

Recently, we found a new member, $Ba_{1.75}LiH_{2.7}O_{0.9}$, hereafter called BLHO [4], wherein a sizable number of vacancies in Ba-, H-, and O-sites form a long-range ordering at room temperature (β-BLHO, space group $Pnm2_1$). Upon heating, a successive order-disorder phase transition to γ-BLHO (space group $Pnma$) at 300°C, followed by to δ-BLHO (space group $I4/mmm$) at 360°C, triggered a drastic increase in ionic conductivity reaching over 10^{-2} S/cm without being influenced by the temperature. Such a non-trivial, so-called "superionic conduction" state was firstly observed in the H^- conduction.

In this study, we attempted to stabilize the superionic phase by partial Na substitution for Li (Na-BLHO). By using high-intensity and high-resolution neutron diffraction experiments, the impact of the chemical substitution on the phase transition behavior and the ionic conducting property were investigated.

2. Experiment

Powder samples of nominal composition $Ba_2Li_{1-x}Na_xH_3O$ (x = 0.2, 0.4, and 0.6) were synthesized by the high-pressure method, and post annealing process in an H_2 gas-filled SUS container (0.42 MPa) provided a highly vacant compositions.

Temperature-controlled powder synchrotron X-ray diffraction measurements were performed at BL02B2 at SPring-8 [5]. Powder neutron diffraction data at room temperature and 427°C for samples loaded into a cylindrical vanadium cell (radius = 6 mm, height = 55 mm) were collected using time-of-flight (TOF) diffractometers (SPICA(BL09) and NOVA(BL21)) at J-PARC. The collected profiles were analyzed by the Rietveld method using the RIETAN-FP program [6] for the X-ray diffraction data and the Z-Rietveld program [7] for the neutron diffraction data. Ionic conductivity of the Na-BLHO was measured by electrochemical impedance spectroscopy (EIS) under H_2 gas flow at 200–350°C, with an applied frequency range from 0.1 Hz to 35 MHz. The obtained impedance spectra were fitted with electrical equivalent circuits using the EC-Lab software.

3. Results and discussion

SXRD profiles revealed that, with increasing Na content x, the points of phase transitions were lowered. In response to that trend, the high conductivity region (≥10^{-2} S/cm) was expanded to lower temperatures, as shown in the Arrhenius plot, Fig. 1. In addition, the $x \geq 0.4$ samples showed an increase in conductivity

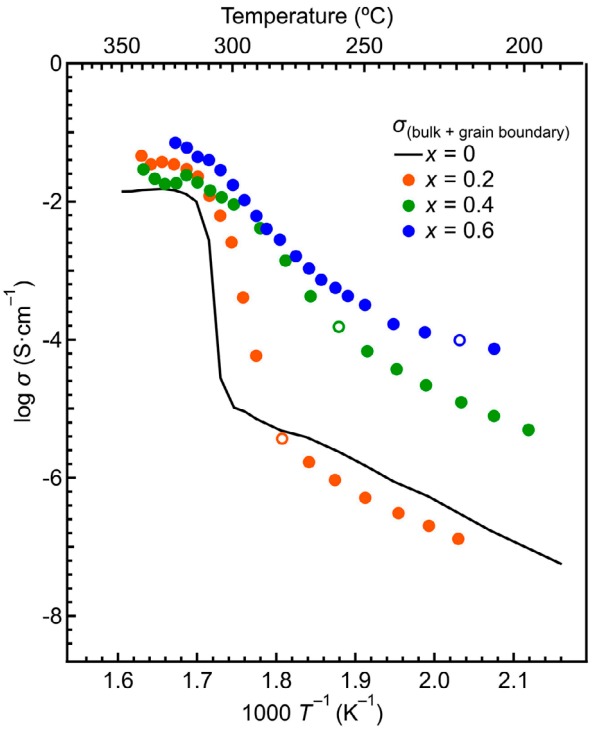

Figure 1. Temperature dependencies of the total (bulk and grain boundary contributions) conductivity for each composition in Na-BLHO, together with that of BLHO [4]. The unfilled circles show the inflection points of the Arrhenius plots, the β-γ transition temperature estimated from the temperature-controlled synchrotron X-ray diffraction.

more than 100 times also at low temperature region (< 300°C), compared to the pristine BLHO. The slope on the Arrhenius plots of discontinuous transitions to the high conductivity region became shallower with increasing *x*, implying that the transition nature was changed by Na doping.

To investigate the impact of Na on the phase transition, the crystal structures for $x = 0.2$, and 0.4 were evaluated using neutron diffraction. Figure 2a shows the fitting profile of Rietveld refinement for the data of $x = 0.4$ collected using SPICA at room temperature. The refinement result converges using a structure model based on the β-BLHO [4], indicating that the similar superlattice structure is maintained (Fig. 2b). The refined composition of $Ba_{1.60(3)}Li_{0.6}Na_{0.4}H_{2.25(3)}O_{0.959(8)}$ has more vacancies than that of $Ba_{1.75}LiH_{2.7}O_{0.9}$ ($x = 0$), especially in the occupancies of Ba and H_{eq} sites. Furthermore, as shown in Fig. 2c, a contrast in the occupancy (g(Ba) = 0.74-0.85, and $g(H_{eq})$ = 0.65-0.76) weakens, meaning that the crystal structure at room temperature is closer to the high conductive γ-phase [4] in which H^- and vacancies are disordered. This is consistent with the results of enhanced conductivity for $x \geq 0.4$ at < 300°C. On the other hand, $x = 0.2$ has almost the same ordering manner with β-BLHO. Such a trend in vacancy ordering could result in a difference in conductivity at low temperatures.

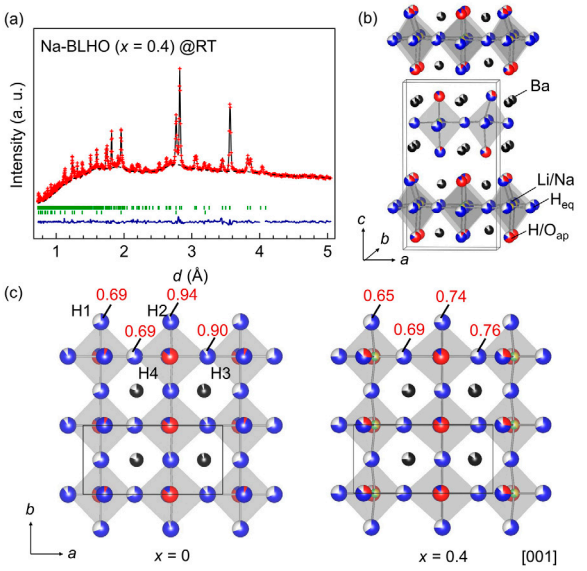

Figure 2. a) Rietveld refinement profile of neutron diffraction data collected at RT for Na-BLHO (x = 0.4) using SPICA. b) Refined crystal structure of x = 0.4. c) Comparison in vacancy distributions of equatorial H^-sites between BLHO (x = 0) and x = 0.4 projected along the [001] direction. The crystal structures were drawn using VESTA software [9].

4. Conclusion

We succeeded in expanding the "superionic conduction" state appeared by order/disorder transition in BLHO to lower temperatures by Na doping [8]. With the increase of the Na content *x*, the phase transition points were lowered and high conductivity over 10^{-2} S/cm was achieved at 300°C. Furthermore, for $x \geq 0.4$, the conductivity below 300°C was also enhanced more than 100 times compared to the pristine BLHO, that is attributed to a decrease in the degree of vacancy orderings in Ba/V_{Ba} and H_{eq}/V_H at even the orthorhombic phase at room temperature.

References

[1] G. Kobayashi et al. Science, **351** 1314 (2016).
[2] Y. Iwasaki et al. J. Mater. Chem. A, **6** 23457 (2018).
[3] F. Takeiri et al. Inorg. Chem., **58** 4431 (2019); H. Nawaz et al. Chem. Commun., **56** 10373 (2020).
[4] F. Takeiri et al. Nat. Mater., **21** 325 (2022).
[5] S. Kawaguchi et al. Rev. Sci. Instrum., **88** 085111 (2017).
[6] F. Izumi et al. Solid State Phenom., **130** 15 (2007).
[7] R. Oishi et al. Nucl. Instrum. Methods Phys. Res. Sect. A, **600** 94 (2009).
[8] K. Okamoto et al. Adv. Sci., **10** 2203541 (2022).
[9] K. Momma et al. J. Appl. Cystallogr., **44** 1272 (2009).

K. Okamoto[1], F. Takeiri[2], and G. Kobayashi[2,3]
[1]*Institute for Materials Research, Tohoku University;* [2]*Cluster for Pioneering Research (CPR), RIKEN;* [3]*Department of Electrical Engineering and Bioscience, Waseda University*

Tracer diffusion coefficient measurements in solid-state electrolytes through neutron radiography

1. Introduction

All-solid-state batteries (ASSBs) have been an attractive technology for higher reliability and higher energy density in comparison to ordinary Li-ion batteries. However, due to the low ionic conductivity of solid-state electrolytes (SSEs) which is a key component to the ASSBs, the performance of ASSBs is less than ideal. One way to mitigate such problem is to heterogeneously dope the SSEs with dielectric particles (i.e., composite SSEs) [1].

Originally discovered in halide-based SSEs, it was believed that space charge layers facilitating ionic conduction can be formed at particle/SSE interfaces, leading to significant increase in overall ionic conductivity once an optimum particle/SSE interface distribution is achieved [1]. Although researchers have been focused on halide-based SSEs during early stage, this strategy has been successfully applied to the oxide-based SSEs by Onishi *et. al*., where a 2-fold enhancement in room-temperature conductivity has been observed when $LaPO_4$ particles were added to $Li_{1.7}Al_{0.3}Ti_{1.7}(PO_4)_3$ (LATP) SSEs [2, 3].

Due to the different defect chemistries inherent to LATP-based SSEs in comparison to the halides, the ionic conductivity enhancement mechanism might be different from our previous understanding. Therefore, it is quintessential to measure the Li diffusion coefficient of LATP-based composite SSEs from multiple scales in order to understand how the dielectric particle dispersion technique enhances the mass transport behavior.

By utilizing the significant difference in neutron cross sections between ^{7}Li and ^{6}Li, neutron radiography has been proven a viable technique in measuring the diffusion coefficients of Li-ion-conductive materials on macroscopic scale [4]. In this study, tracer diffusion experiments at 300 to 500°C were conducted on ^{7}Li LATP and composite SSEs with ^{6}Li as tracer species. The diffusion of ^{6}Li was observed through neutron radiography at RADEN BL22 at J-PARC MLF. This allows calculation of the sample tracer diffusion coefficients, the results of which were then compared with conclusions from other works.

2. Material and methods

The ^{7}Li LATP and LATP-$LaPO_4$ composite samples were synthesized through ordinary solid-state reaction method [2]. The sintered samples were in cuboid shape (approx. 6 × 6 × 8 mm) and polished until mirror finish was obtained on a 6 mm × 6 mm face. In tracer diffusion experiment, saturated $^6LiNO_3$ aqueous solution was applied to the polished surface. The samples were then annealed at 300 to 500°C for 20 to 30 min (in a tubular furnace within the beamline), after which the samples were cooled to room temperature and subjected to neutron radiography observation. The annealing + neutron radiography process was repeated 4-6 times until the total annealing time (i.e., diffusion time) reached 80 to 180 min.

During the experiment at RADEN BL22 at J-PARC MLF, the sample was configured 18 m away from the beam source, accepting a white beam (with fast neutrons removed by a T0 chopper). The samples were placed on an aluminum sample holder which is directly attached onto the protective aluminum plate of the scintillator to maximize resolution. A 50 μm ^{6}LiF/ZnS scintillator was employed to capture the transmitted neutrons. The converted photons were then sampled by a water-cooled CCD camera (Andor Technology Ltd.). During each neutron radiography, 5 consecutive images were taken with 3 min exposure time for each image. For each measurement, an average intensity image of the 5 images were calculated to mitigate the gamma noise and beam intensity fluctuation. The 'averaged' image was then divided by the open beam image to obtain the spatially resolved transmission of the samples.

3. Result and discussion

Typical neutron radiographs (transmission) before and after the diffusion experiment are shown in Fig. 1. Since the LATP and LATP-$LaPO_4$ composite samples consist of species with relatively small neutron cross sections (^{7}Li, Al, Ti, P, O, and La), the presence of ^{6}Li can contribute to a significant drop in transmitted neutron flux, thereby producing a dark contrast on the neutron radiographs. At locations further away from the surface where ^{6}Li was applied (x = 0 plane), the contrast from ^{6}Li becomes weaker. The length of the diffusion (diffusion distance) also increases as the diffusion time is increased. It is therefore assumed that the diffusion is a semi-finite 1-dimensional diffusion. The result also demonstrates a straightforward way of visualizing Li mass transportation at macroscopic scale.

Quantitatively, the Beer-Lamberts law can be

combined with the semi-finite solution to the Fick's second law (fixed amount of ^{6}Li at surface), which gives:

$$-\ln(I/I_0) = M\cdot(4\pi Dt)^{-1/2}\cdot\exp(-x^2/4Dt) \quad (1)$$

where M is the total amount of diffusing species, D is the tracer diffusion coefficient, t is diffusion time, x is the position where the specific I/I_0 is observed, I/I_0 is the neutron transmission at local that is spatially averaged along y direction. By assuming M and D are constant, equation 1 describes the neutron transmission as a function of position. Since t is a known quantity, equation 1 allows calculation of tracer diffusion coefficients from the intensity profiles of the neutron radiographs through non-linear fitting, as demonstrated by Fig. 2.

The measured tracer diffusion coefficients are

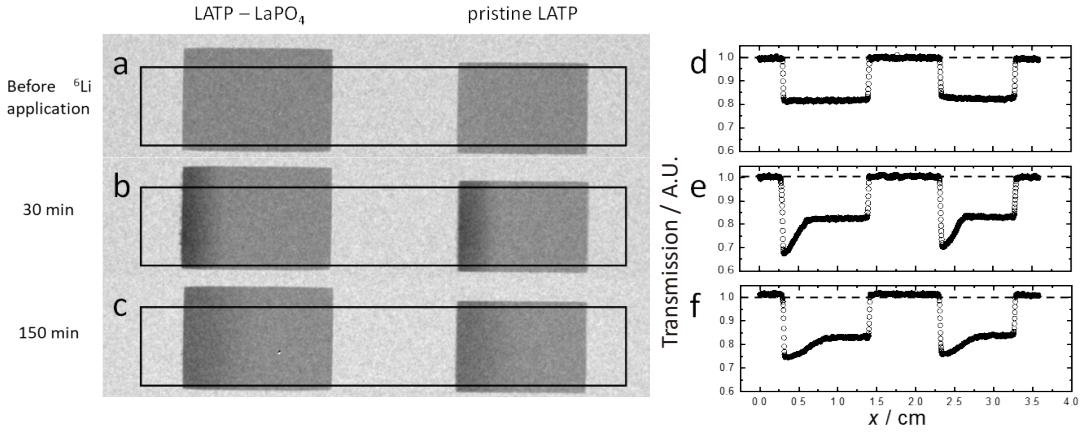

Figure 1. Typical transmitted neutron images of LATP – $LaPO_4$ composite (left) and pristine LATP (right) samples (a) before application of $^6LiNO_3$, (b) applied with $^6LiNO_3$ followed by annealing at 300°C for 30 min, and (c) annealing at 300°C for 150 min. Plots (d)–(f) are intensity profiles corresponding to the selected rectangle areas in (a)–(c). Used with authors' permission from ref. [5].

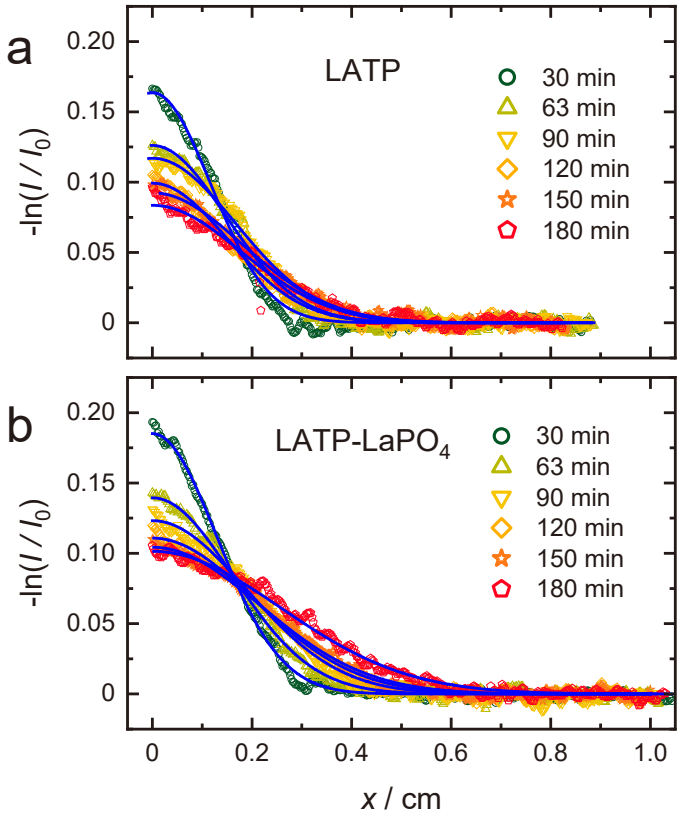

Figure 2. Diffusion profile of (a) pristine LATP and (b) LATP – $LaPO_4$ composite samples after diffusion at 300°C. Fit results basing on the Fick's second law are also given by blue curves. Used with authors' permission from ref. [5].

summarized in Table 1 and are compared with chemical diffusion coefficients from other works in Fig. 3 (converted from ionic conductivities through Nernst-Einstein relation). The diffusion coefficient of LATP – $LiPO_4$ measured through neutron radiography is comparable to the chemical diffusion coefficient calculated from the result of Onishi's work [2], but that of the pristine LATP measured in this work as well as by other works show a lower consistency. This might be due to different sample preparation methods employed in different works which leads to various impurity content or humidity at LATP grain boundaries that affects the overall Li mobility.

The activation energy measured in this work also falls within the reported range (0.15 – 0.3 eV) [7-9]. It

Table 1 Tracer diffusion coefficient of lithium ion in LATP and LATP – $LaPO_4$ composite obtained by tracer diffusion - neutron radiography experiments

Temperature t / °C	Diffusion coefficient, D^* / 10^{-6} $cm^2 \cdot s^{-1}$	
	pristine LATP	LATP – $LaPO_4$ composite
300	1.71 (20)	2.95 (14)
350	2.60 (12)	3.22 (19)
400	2.88 (16)	3.53 (53)
450	-	4.97 (27)
500	4.48 (37)	7.63 (25)

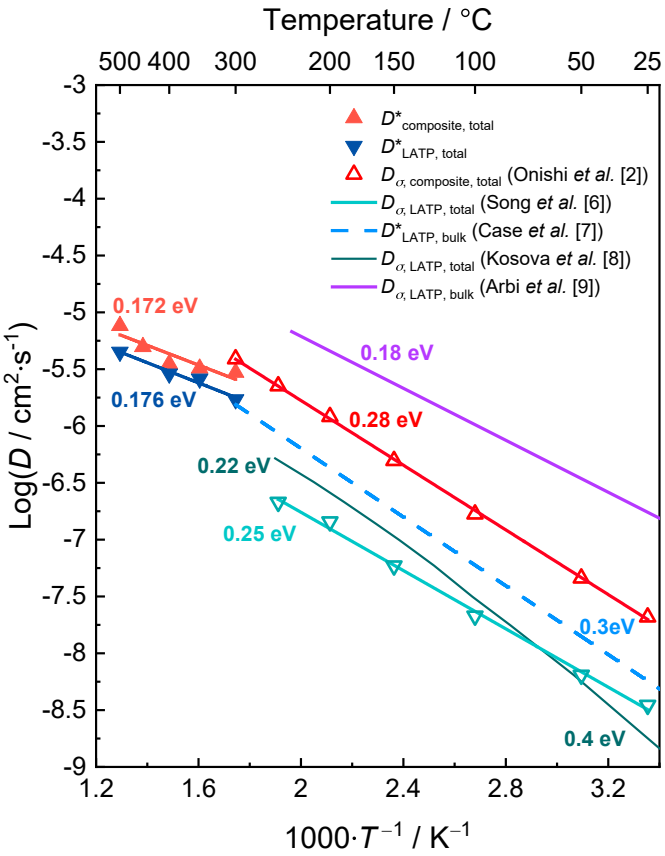

Figure 3. Arrhenius plots of the tracer diffusion coefficients of pristine LATP (▼) and LATP – $LaPO_4$ composite (▲). The conductivity diffusion coefficients for LATP – $LaPO_4$ composite (△) and pristine LATP (▽) are obtained from conductivities measured in previous works using Nernst-Einstein equation [2, 6]. The blue dash line is the bulk tracer diffusion coefficient in pristine LATP simulated by Case *et al.* [7], the dark cyan and purple solid lines are total and bulk conductivity diffusion coefficients, respectively in pristine LATP, which are converted from the conductivity measured by Kosova *et al.* and Arbi *et al.* through Nernst-Einstein equation [8, 9]. Adapted with authors' permission from ref. [5].

is also worth noting that the activation energy for the LATP – $LaPO_4$ composite at 300 – 500°C is relatively close to that of the pristine sample, which indicates that the bulk diffusion is the dominant mechanism in both samples at 300 – 500°C, coinciding with the observation in Kosova's work [8]. This also explains the similar diffusion coefficients for LATP and LATP – $LaPO_4$ composite measured in this work: as the bulk diffusion becomes the dominant mechanism at high temperatures, contribution from grain boundary and $LaPO_4$ / LATP interface become much less obvious. The results confirms the speculation that dielectric particle dispersion enhancement for SSEs is more suitable at room temperatures rather than high temperatures [10].

4. Perspectives

This work demonstrated that the neutron radiography is an effective and non-destructive way of diffusion coefficient measurement for Li-ion conductors. It also shows a possibility for *in-situ* visualizations of Li mass transport within ASSBs with thick electrolytes. In this case, the oxide-based solid-state electrolyte samples were annealed at 300 to 500°C in order to accelerate the Li diffusion and thereby reduce the time cost. Since the ASSBs are mostly operating at room temperature where the Li mobility is significantly lower, conducting such experiment under room temperature will take much longer times. Nevertheless, this method is proven to be an effective way of characterizing overall diffusion coefficients in SSEs with engineered microstructures.

However, the limitation of the diffusion experiment should also be addressed. The presented work modeled the ^6Li diffusion with the semi-finite solution of the Fick's second law, where the ^6Li is assumed to be a dimensionless thin film with finite concentration and diffuses toward the other end of the sample. However, in cases where an excessive amount of ^6Li was applied to the sample surface, redistribution of ^6Li within the thick ^6Li layer can disrupt the diffusion behavior of the ^6Li diffusion in the sample, since the excessive ^6Li that are not initially available can migrate to the sample surface during later process, contributing to an underestimation of the Li diffusion coefficient. On the other hand, if the samples are porous, permeation of $LiNO_3$ solution can contribute to a significant overestimation of diffusion coefficient at early stages of the diffusion. Such complication should be fully considered and controlled through modification of experiment and sample preparation such that macroscopic diffusion coefficients can be measured with higher accuracies.

References

[1] J. Maier, *Chem. Mater.,* **26** (2014) 348-360.
[2] H. Onishi, *et. al.*, *Electrochemistry*. **84** (2016) 967-970.
[3] F. Song, *et. al.*, *J. Alloy Compd.*, **853** (2021) 157089.
[4] S. Takai, *et. al*, *Solid State Ionics*, **256** (2014) 93-96.
[5] F. Song, *et. al.*, *Solid State Ionics*, **377** (2022) 115873.
[6] F. Song, *et. al.*, *Materials*, **14** (2021) 3502.
[7] D. Case, *et. al.*, *Solid State Ionics*, **346** (2020) 115192.
[8] N.V. Kosova, *et. al.*, *Ionics*, **14** (2008) 303-311.
[9] K. Arbi, *et. al.*, *Inorg. Chem.*, **52** (2013) 9290-9296.
[10] J. Maier, *Prog. Solid State Chem.*, **13** (1995) 171-263.

F. Song[1], H. Hayashida[2], T. Kai[1], T. Shinohara[1], T. Yabutsuka[3], T. Yao[4], and S. Takai[3]
[1]Neutron Science Section, Materials and Life Science Division, J-PARC Center; [2]Neutron Science and Technology Center, CROSS; [3]Graduate School of Energy Science, Kyoto University; [4]Kyoto University

Ionomer Distribution of N-Doped Carbon Surfaces

1. Introduction

To meet the demand for more affordable fuel cell electric vehicles, it is necessary to reduce the Pt loading in the catalyst layer of polymer electrolyte fuel cells (PEFCs). Ott et al. [1] proposed a method involving NH_3 treatment to modify the carbon support used in the catalyst layer of PEFCs. They demonstrated that the modified N-doped carbon resulted in a more uniform ionomer distribution in the catalyst layer and improved the PEFC performance. Therefore, to understand the influence of ionomers on the PEFC performance, it would be interesting to explore the effect of the surface modification on the ionomer adsorption behavior. We evaluated the interfacial structure of ionomers on N-doped carbon surfaces using the neutron reflectivity (NR) technique and discussed the influence of surface properties on the ionomer adsorption [2].

2. Experiment

The deposition of carbon thin films (50 nm) on Si wafers was performed by magnetron sputtering. The as-deposited carbon films (Film C) were first treated with concentrated HNO_3 at 70°C for 2 h, and then rinsed three times with ultrapure water. The oxidized carbon films (Film O) were then heated in a tube furnace with NH_3/Ar gas at 200°C, 400°C and 600°C, for 2 h. The obtained carbon films were designated as Film N200, N400, and N600 at the respective treatment temperatures. On the top of the carbon films, ionomer thin films (30 nm) were prepared by spin-coating a Nafion ionomer dispersion at 2000 rpm for 30 s. The Nafion ionomer dispersion was diluted to 1 wt% with 1-propanol. The thin films were annealed at 120°C for 1 h in a vacuum oven. NR measurements were performed at BL17 SHARAKU in J-PARC MLF (Japan Proton Accelerator Research Complex, Material and Life Science Experimental Facility). Neutron pulses of 25 Hz were generated with a wavelength band of 0.2 nm < λ < 0.88 nm. NR profiles were obtained at reflection angles of 0.3, 0.7, 1.6, and 3.5°, covering a q-range of 0.07–3.0 nm^{-1}. The magnitude of the scattering vector q was defined as $4\pi\sin\theta/\lambda$, where θ is the incident angle. All measurements were performed at room temperature (22°C) with two scattering contrasts on the same system using H_2O/D_2O vapor for double contrast measurements. A saturated KCl in H_2O/D_2O was used to maintain the vapor condition.

3. Results and discussion

Figure 1 shows NR curves of the ionomer thin films obtained at H_2O/D_2O vapor. The observed fringes in the NR curves arise from the interference of reflections at the interfaces within the thin films. The shape of the fringes at q = 0.55 nm^{-1} exhibited variations between Films C–O and Films N200–N600, indicating changes in the interfacial structures associated with the ionomer on the N-doped carbon surfaces. First, the NR curves of the thin films obtained under H_2O vapor were analyzed to determine the structural parameters of the carbon and ionomer layers, including thickness, scattering length density (SLD), and interfacial roughness. Subsequently, the NR curves collected under D_2O vapor were fitted using the parameters determined from the H_2O vapor fits.

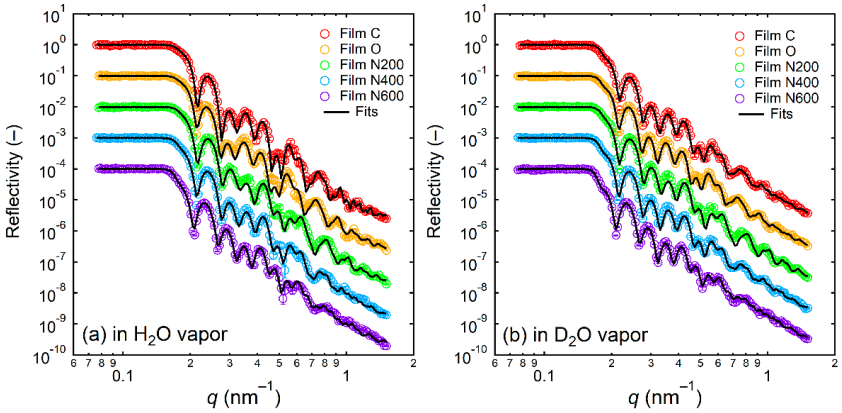

Figure 1. Experimental NR data and the corresponding fits (solid lines) of Nafion ionomer thin films obtained under (a) H_2O and (b) D_2O vapors. The NR curves have been vertically offset (×10^{-1}, ×10^{-2}, ×10^{-3}, and ×10^{-4} for Films O, N200, N400, and N600, respectively) to aid visualization. Copyright 2022, American Chemical Society.

In the fits, only the SLDs of the ionomer layers were fitted as variables, while the other parameters were fixed.

Figures 2a–e show the SLD profiles of the ionomer thin films under H_2O/D_2O vapor as a function of vertical distance from the carbon surfaces. These SLD profiles showed a SLD variation with the vertical distance, indicating fluctuations in the density and/or composition of the ionomers and water in the thin films. The SLD profiles under D_2O vapor were subtracted from those under H_2O vapor to determine the water volume fraction in the thin films (Figs. 2f–j). Based on the obtained water volume fraction, the ionomer volume fraction was evaluated under certain constraints [2]. The NR analysis revealed an "ionomer adsorption layer" at the carbon-ionomer interface. The hydrophobic carbon surface (Film C) had a higher volume fraction of ionomer adsorption layer than the hydrophilic carbon surface (Film O). The difference may be due to the breakdown of ionomer aggregates and the adsorption of the ionomer backbone onto the hydrophobic carbon surface by the hydrophobic interaction [3]. Moreover, the thickness and volume fraction of the ionomers in the adsorption layer increased after NH_3 treatment (Films N200–N600). The wettability of N-doped carbon surfaces exhibited hydrophilic nature as well as Film O. It is worth noting that the ionomer adsorption behavior was different in hydrophilic oxidized and N-doped carbon thin films in wet conditions. Yang et al. [4] reported that the ζ-potential of carbon black was changed from −1.28 to +74.2 mV after introducing nitrogen functional groups into the carbon. The positive charge derived from the ionization of the N-doped carbon surface is sufficient to attract the negatively charged SO_3^- groups in the side chains of the ionomers via the Coulombic interaction. The strong electrostatic interaction induces a thick and dense ionomer adsorption layer form at the ionomer-carbon interface.

4. Conclusion

We conducted modification on a carbon surface by NH_3 treatment to investigate the ionomer distribution on these modified surfaces using the NR technique. The results support the idea that introducing nitrogen into carbon supports can promote the formation of a dense ionomer layer at the ionomer-carbon interface.

References

[1] S. Ott et al., Nat. Mater. **19** 77 (2020).
[2] W. Yoshimune, et al., ACS Appl. Mater. Interfaces **14** 53744 (2022).
[3] T. Mashio, et al., J. Phys. Chem. C **114** 13739 (2010).
[4] F. Yang, et al., ACS Appl. Mater. Interfaces **9** 6530 (2017).

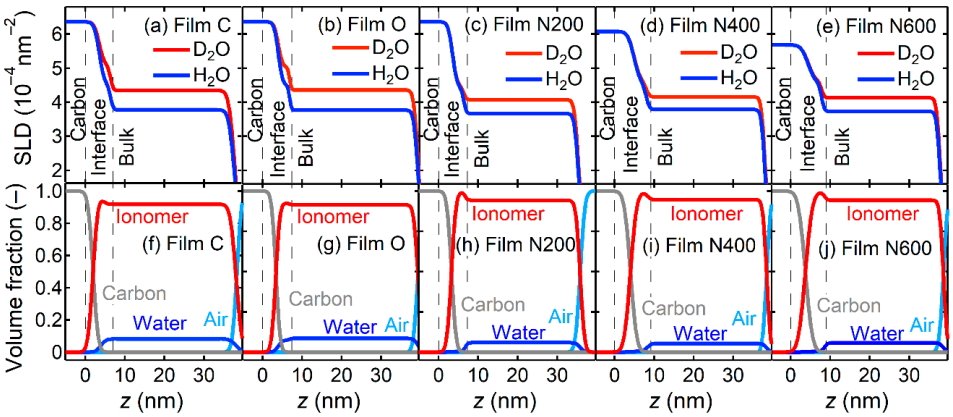

Figure 2. (a–e) SLD profiles of Nafion ionomer thin films as a function of vertical distance from the carbon surfaces *z* obtained under H_2O (blue) and D_2O vapors (red). (f–j) Volume fractions of the components of the ionomer thin films. Gray, red, blue, and light blue lines represent carbon, the ionomer, water, and air, respectively. Copyright 2022, American Chemical Society.

W. Yoshimune[1], N. Kikkawa[1], H. Yoneyama[1], N. Takahashi[1], S. Minami[1], Y. Akimoto[1], T. Mitsuoka[1], H. Kawaura[1], M. Harada[1], N. L. Yamada[2,3], and H. Aoki[2,3]

[1]*Toyota Central R&D Labs., Inc.;* [2]*Neutron Science Section, Materials and Life Science Division, J-PARC Center;* [3]*Institute of Materials Structure Science, KEK*

Interfacial Structure and Tribological Property of Adsorbed Layer Formed by Organic Friction Modifier

1. Introduction

In recent years, engine oil has been increasingly low-viscosity in order to achieve further fuel efficiency in automobiles. However, low viscosity engine oil tends to cause oil film breakage, which increases the risk of seizure in addition to increased friction and wear in the sliding parts. Molybdenum dithiocarbamate (MoDTC) and Zinc Dialkyldithiophosphate (ZnDTP) are generally used as lubricating additives to engine oils to reduce friction by forming a 'tribofilm' on the sliding surfaces under high temperature and high pressure, thereby reducing friction and wear [1, 2]. However, MoDTC and ZnDTP cause problems, such as additive-derived metal sludge, clogging of oil filters, and catalyst poisoning for exhaust gas treatment due to the presence of phosphorus and sulfur. Therefore, development of organic friction modifiers that do not contain metal, such as phosphorus and sulfur, is underway [3–5].

In this study, we focus on dibasic acid ester derivatives, which are one of the organic friction modifiers. In a high-speed reciprocating friction and wear test conducted in a previous study, these dibasic acid ester derivatives were reported to have the same friction reduction effect as glycerol monooleate (GMO) at room temperature and the same wear durability as ZnDTP and phosphate ester amine salts even at high temperature [6]. On the other hand, there has been no sufficient study on how these additives form adsorption layers on metal surfaces and contribute to the improvement of friction and wear properties. In this study, the interfacial structure of the adsorbed molecular film formed on the iron surface by dibasic acid ester derivatives was evaluated by neutron reflectometry, and the macrotribological properties of each additive comprising the derivative were evaluated [7]. The relationship between the structure and tribological properties of adsorbed molecular films was finally discussed.

2. Samples

The dibasic acid ester derivative, succinic acid monooleyl dimethyl laurylamine salt (SA-DA, Fig. 1(a)), was the target of this study. The constituent acid was monooleoyl succinate (C18: 1SA) and the amine was dimethyl laurylamine (C12DA). In the neutron reflectometry study, SA-DA with all hydrogen atoms deuterated should ideally be used, but since it was difficult to obtain

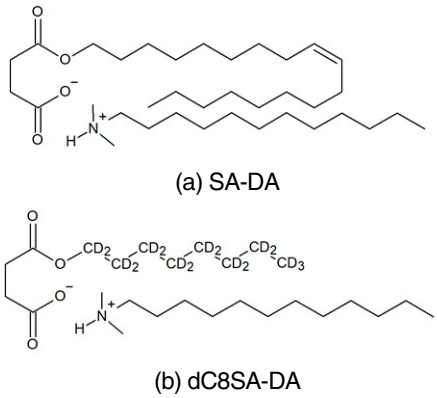

Figure 1. The chemical structures of the dibasic acid ester derivatives prepared for the study.

deuterated molecules of both C18: 1SA and C12DA, the oleyl chain of C18: 1SA was substituted with a deuterated octane chain in the present study. Therefore, we prepared a derivative (dC8SA-DA, Fig. 1(b)) by combining the deuterated monooctane succinate (dC8SA) with deuterated octane (C12DA). Polyalphaolefin (PAO) was used as the base oil, and the sample oil was a mixture of the dibasic acid ester derivative at a concentration of 0.1 mass%.

3. Neutron reflectometry

The neutron reflectometry experiments were conducted using the BL16 SOFIA, a time-of-flight neutron reflectometer installed at the MLF J-PARC. An iron-coated silicon block was set in a holder, and reflectivity profiles were obtained from the interface of iron and sample oil. First, the sample oil was put in a liquid cell in the holder and the reflectivity profiles were measured. In addition, the reflectivity profiles were measured after heating at 50°C for 30 minutes, and again after heating at 100°C for 30 minutes. The obtained reflectivity profiles and the scattering length density profiles estimated by the optimum fitting on the Parratt's theory are shown in Fig. 2 [7]. In this measurement, the C12DA, which is a component of dC8SA-DA, is not deuterated as is the case with PAO. Therefore, the thickness and density of the adsorbed layer formed by dC8SA-DA were estimated from the thickness and film density of the adsorbed layer formed by dC8SA, which constitutes the derivative. Figure 2 shows that the thickness of the adsorbed layer formed by dC8SA-DA on the iron surface at room temperature was about 2.0 nm, with a graft density of

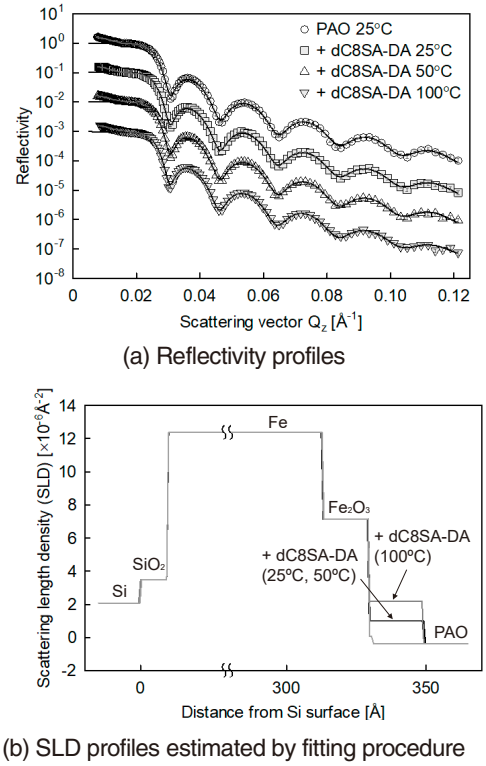

Figure 2. Neutron reflectometry results for the interface between iron surface and sample oil [7].

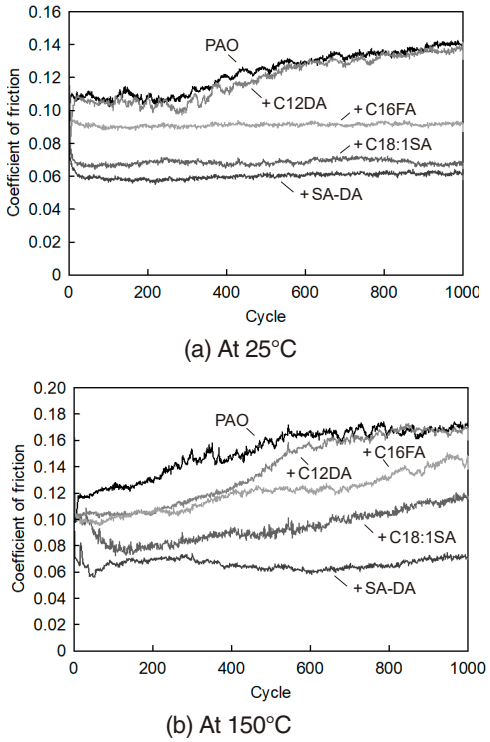

Figure 3. Typical friction behaviours of sample oils containing each additive [7].

26%. The thickness and graft density remained almost unchanged when the temperature was increased to 50°C, but the graft density increased to 47% when the temperature was increased to 100°C. This indicates that the dibasic acid ester derivatives form dense adsorption layers, especially at high temperatures.

4. Friction tests

To evaluate the macrotribological properties of the adsorbed layers formed by the various additives, friction tests were conducted using balls and discs made of bearing steel (AISI 52100). Typical friction behaviours of sample oils containing each additive are shown in Fig. 3. Palmitic acid, a common type of oiliness additive, was also added as a reference OFM here (shown as C16FA). When SA-DA was used, the behavior of the coefficient of friction was stable and smaller than that of the other additives. In addition, the wear amount was also significantly lower than that of the other additives. Combined with the results of neutron reflectometry, SA-DA formed a dense adsorption layer on the iron surface, which suppressed friction and wear. Furthermore, not only does the coefficient of friction decrease rapidly with the number of friction cycles due to the properties of the amine additive, but that additional friction also produces succinate-derived metallic soap, which in turn produces a sustained low-friction effect. These results provide useful guidelines for the development of effective additives in the future, and in particular, the combination with the neutron reflectometry was shown to be extremely effective in elucidating the mechanism.

References

[1] J. Zhang and H. A. Spikes, Tribology Letters, **63** 2 1 (2016).
[2] W. Shen, T. Hirayama, N. Yamashita et al., Tribology International, **167** 107365 (2022).
[3] M. Desaker, X. He et al., ACS Applied Materials & Interfaces, **9** 10 9118 (2017).
[4] B. M. Fry, M. Y. Chui et al., Tribology International, **151** 106438 (2020).
[5] Y. Song, K. Fukuzawa, T. Hirayama et al., Macromolecules, **56** 5 1954 (2023).
[6] Y.Shimizu, Tribology Monthly Magazine, 400 **22** (2020) (in Japanese).
[7] N. Yamashita, T. Hirayama, N. L. Yamada et al., Tribology Online, **17** 4 246 (2022).

T. Hirayama[1], N. Yamashita[1], and N. L. Yamada[2]
[1]*Dept. of Mechanical Engineering and Science, Kyoto University;* [2]*Institute of Materials Structure Science, KEK*

Mobile Water Near Poly(ethylene oxide) at Physiological Temperature

1. Introduction

The macroscopic properties of synthetic polymers are greatly varied by the choice of functional groups in the main and side chains. Appropriate placement of hydrophilic and hydrophobic functional groups can control the position of water molecules around the polymer chain and the state of hydrogen bonding. These properties allow findings from basic science research to be applied and used as advanced functional materials in a variety of medical applications.

Poly(2-methoxyethyl acrylate) (PMEA)[1] (Fig. 1a) is utilized in the inner wall coating of the circuit of the extracorporeal membrane oxygenation (ECMO), known as Covit-19 medical devices. The full picture of the mechanism of its superiority over other materials is not yet clear, and research is underway by various methodologies as a major topic of a research grant (Aquatic Functional Materials [2]). The research outcomes will advance the fundamental science of water on material surfaces and design greater materials.

We are studying water dynamics in the vicinity of matter via incoherent neutron quasi-elastic scattering (QENS) using BL02 at the J-PARC MLF. BL02 provides a broad energy range of dynamics and a high signal-to-noise ratio, enabling us to obtain even a tiny amount of dynamics information. By replacing H in substances other than water with deuterium (D), which has a low incoherent scattering capability, the motion of substances with high incoherent scattering capability of light hydrogen (H) can be evaluated. Therefore, the combination of fully deuterated polymer and light water can selectively extract information on the motion of water in the material. Conversely, the combination of a polymer with regular hydrogen and heavy water can provide information on the polymer chain dynamics.

The side chains of PMEA have hydrophilic structures such as poly(ethylene oxide) (PEO). Here, we focused on the dynamics of water near the polymer chains at 37°C using PEO (Fig. 1b). PEO is known to form eutectic with water at lower water content or lower temperature. In this study, we evaluated the dynamics properties of mobile water interacting with PEO chains at 37°C.

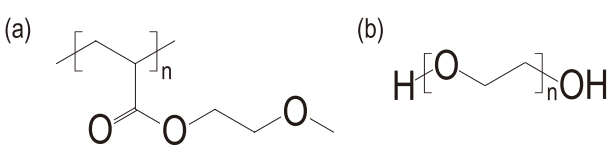

Figure 1. Chemical structure of (a) PMEA, and (b) PEO.

2. Experimental procedures

Perdeuterated PEO (dPEO, Polymer Source Inc., Mn: 17000 g/mol, Mw/Mn: 1.07), protiated PEO (hPEO, Polymer Source Inc., Mn: 16000 g/mol, Mw/Mn: 1.05) were used as received. Milli-Q water (H_2O) and D_2O (deuteration ≥ 99.96%, Aldrich) were added to the dried dPEO and hPEO. The ratios of water molecules to ethylene oxide, n_{water}/n_{EO} was prepared to be 0, 0.3, 0.5, 1.1, 2.2, and 4.0 for the hPEO + D_2O samples, and 0, 0.3, 0.4, 0.9, 1.8, and 3.2 for the hPEO + D_2O samples.

The samples were cast on a Nb foil [3], were folded then shaped into cylinders and set in an Al cell. The QENS measurements were performed with BL02 [4] at 500 kW beam power operation. The scattering vector, Q [Å^{-1}] range was $0.125 < Q < 1.875$. The energy resolutions were 3.6 and 12 μeV in the energy transfer E [μeV] ranges of $-20 < E < 50$ and $-40 < E < 1000$ respectively. The exposure time was approximately 3 h. The sample temperature was 37°C [5].

3. Results and discussion

The dynamic structure factor $S(Q, E)$ of the dPEO + H_2O sample exhibited an increase in H_2O mobility with increasing water content [5]. We could fit the QENS profiles by the sum of three terms, a delta function and two Lorentz functions (eq. 1).

$$S(Q, E) = R(Q, E) \otimes [A_{\text{immobile}}(Q)\ \delta(Q, E) + A_{\text{slow}}(Q)\ L_{\text{slow}}(\Gamma_{\text{slow}}, E) + A_{\text{fast}}(Q)\ L_{\text{fast}}(\Gamma_{\text{fast}}, E)] + B_g, \quad (1)$$

where L, R, δ, $A(Q)$, Γ, and B_g are the Lorentz function, the instrumental resolution function, the delta function, a coefficient of the delta or the Lorentz function, HWHM of the Lorentz function, and a constant background, respectively. The delta function represents the immobile component in BL02 that is longer than the sub-nanosecond order. The Q^2 dependence of D_{slow} and D_{fast} was followed by the jump diffusion model [6]: $\Gamma = DQ^2/(1 + DQ^2\tau_0)$, where D and τ_0 are the diffusion coefficient and mean residence time, respectively.

The D of the fast mode water were of the same order of magnitude as that of the bulk water [7], and those of

the slow mode water were an order of magnitude smaller than those of the fast mode water (Fig. 2a). Compared to the dynamics of PEO obtained from the experiments by hPEO+D_2O samples, the mobility of the polymer chains increased abruptly with the addition of water to the dried polymer and increased with the increase of water content and was equivalent in order to D_{slow}. This provides evidence of an interaction between the PEO chains and the hydration water molecules.

Figure 2b shows the n_{water}/n_{EO} dependence of τ_0. The maximum values of τ_0 of the slow mode water were obtained at $n_{water}/n_{EO} \sim 1$. These behaviors may be attributed to the length of the hydrogen bonding in the water network, which is close to the O–O distance in the PEO chain [8].

In the n_{water}/n_{EO} range of 0.3 to 4.0, the ratios of $A_{immobile}$, A_{slow}, and A_{fast} did not change significantly, approximately in the order of 5, 65, and 30%. 'Immobile water' corresponds to water that interacts strongly with PEO, 'slow water' interacts moderately well with PEO, and 'fast water' is free water that interacts with PEO but is closest to bulk water. Thus, a large amount of mobile water exists around PEO, interacting with the polymer chain. The terahertz time-domain spectroscopy results also revealed that in the n_{water}/n_{EO} range of 1–2, the ratio of water to total water interacting with PEO is approximately 60%, which is comparable to the QENS analysis results [5].

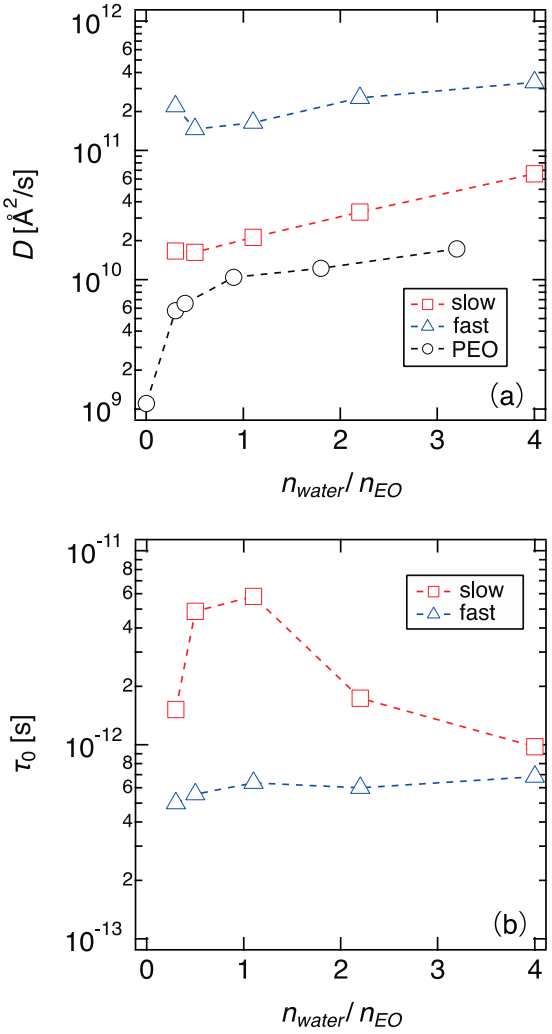

Figure 2. The n_{water}/n_{EO} dependence of D for slow mode water (square), fast mode water (triangle), and PEO chain (circle). (b) The n_{water}/n_{EO} dependence of τ_0 for slow mode water (squares) and fast mode water (triangles) [5].

4. Summary

QENS revealed that at physiological temperatures, under low water content, significant amounts of mobile water are interacting with PEO. Although PEO has no side chains, polymer chains with side chains, such as PMEA, deuteration of the main chain or part of the side chains can be approached into a detailed depiction.

Acknowledgements

The neutron experiments were conducted by proposal Nos. 2018B0235 and 2020A0221. This work was supported by Grants-in-Aid for Scientific Research on Innovative Areas Nos. JP19H05717 and JP19H05720.

References

[1] M. Tanaka et al., Biomaterials, **21** 1471 (2000).
[2] https://www.aquatic-functional-materials.org
[3] T. Tominaga et al., J. Appl. Cryst., **54** 1631 (2021).
[4] K. Shibata et al., JPS Conf. Proc., B 036022 (2015).
[5] T. Tominaga et al., J. Phys. Chem. B, 126, 1758 (2022).
[6] M. Bée, Quasielastic Neutron Scattering (Adam Hilger: Bristol, England, 1988).
[7] T. Yamada et al., J. Phys. Chem. B, **115** 13563 (2011).
[8] A. Maconnachie et al., Polymer **19** 33 (1978).

T. Tominaga[1], M. Hishida[2], D. Murakami[3], Y. Fujii[4], M. Tanaka[5], and H. Seto[6]
[1]*Neutron Science and Technology Center, CROSS;* [2]*Department of Chemistry, Faculty of Science, Tokyo University of Science;* [3]*Faculty of Humanity-Oriented Science and Engineering, Kindai University;* [4]*Graduate School of Engineering, Mie University;* [5]*Institute for Materials Chemistry and Engineering, Kyushu University;* [6]*Neutron Science Section, Materials and Life Science Division, J-PARC Center, Institute of Materials Structure Science, KEK*

Monitoring of Rapid Morphological Changes by Photo-Irradiation in Micelles by *in situ* SANS

1. Introduction

Photo-induced rapid control of molecular assemblies formed by surfactants, such as micelles and vesicles can be applied in the controlled release and delivery of drugs or active components (Fig. 1(a)) [1]. A variety of photoresponsive surfactants based on photochromic compounds (e.g., azobenzene and spiropyran) have been synthesized and characterized. However, conventional photoresponsive molecular assemblies require minutes to hours of photo-irradiation for significant changes in the properties. For promising applications, the response by light irradiation needs to be fast and to occur at an arbitrary moment.

To achieve rapid control of surfactant self-assembly, we focused on the lophine dimer (LPD) as a photochromic moiety. The LPD molecules quickly dissociate into two lophyl radicals and are recovered by a thermal recombination reaction (Fig. 1(b)). However, this recombination is extremely slow due to the free diffusion of the radical species. Abe et al. reported that the reaction rate is significantly enhanced by inhibiting diffusion of the radicals when two lophine moieties are connected through a linker [2]. Our group also reported the rapid recombination in micelles formed by surfactants as a confined space to inhibit free diffusion of the radicals [3–5].

In this study, we investigated the effects of micelle volumes as a reaction site on the recombination rate of the lophyl radicals by using small-angle neutron scattering (SANS) measurements. Furthermore, we examined the morphological changes in the micelles, formed by amphiphilic LPD derivatives by using an *in situ* SANS system.

2. Effects of the micelle volumes on recombination reaction of the lophyl radicals

The recombination reaction of lophyl radicals produced from LPD by ultraviolet (UV) light irradiation is significantly enhanced when LPD molecules are solubilized and incorporated in the micelle formed by surfactants. It is expected that the inner space of the micelle confines the radicals in the nano space and enhances the recombination of the radicals. In this study, we examined the relationship between the micelle volumes and the recombination rates (Fig. 2) [6].

For this, an LPD derivative with triethylene glycol

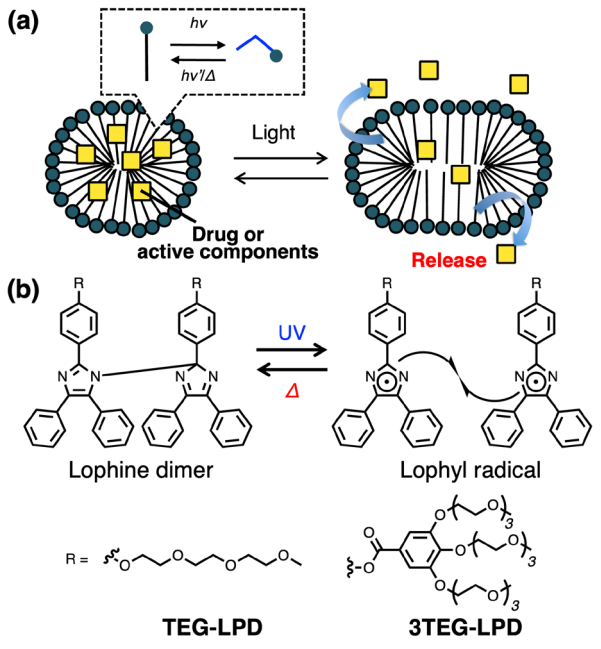

Figure 1. Schematic image of controlled release with a photoresponsive molecular assembly (a) and photochromism of the lophine dimer derivatives (b).

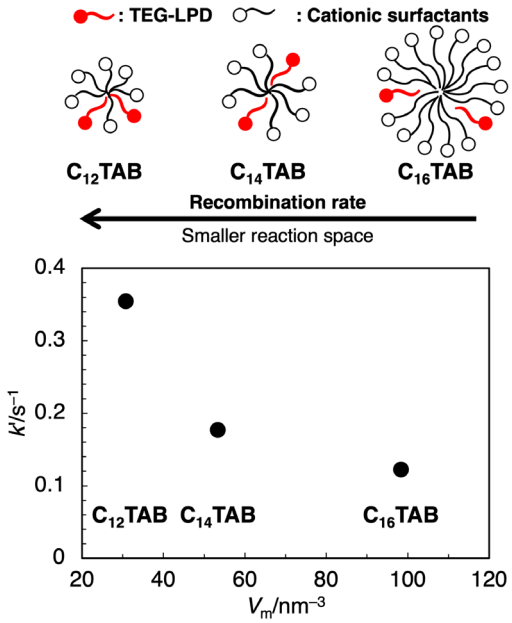

Figure 2. Schematic of micellar structures formed between **TEG-LPD** and cationic surfactants and apparent reaction rates of recombination of the lophyl radicals (*k'*) vs. the volume of the micelle with different alkyl chain length of cationic surfactants.

monomethyl ether groups (TEG) (**TEG-LPD**, Fig. 1(b)) was solubilized into micelle solutions prepared using cationic surfactants bearing alkyl chains of various lengths (C_{12}TAB, C_{14}TAB, or C_{16}TAB). To reveal the morphology and size of the micelles, we performed SANS measurements (0.5 mM **TEG-LPD**/50 mM surfactant in D_2O) with the small and wide angle neutron scattering instrument TAIKAN (BL-15) installed at the MLF in J-PARC. The SANS data could be well fitted using a uniform prolate ellipsoid model interacting through a screened Coulomb potential. With increasing alkyl chain length, both the long radius (R_a) and short radius (R_b) increased, and so did the volume of the individual micelles (V_m). From these results, the inner volumes of micelles as a reaction space of the recombination can be tuned by selection of the surfactants.

Next, we examined the apparent recombination rates (k') of the lophyl radicals in these micelles as a UV/vis absorption spectroscopy and plotted the k' against micelle volume V_m according obtained by SANS analysis (Fig. 2). The recombination was enhanced in micelles with smaller inner volumes. To see a clear trend for this assumption, we calculated the free volume per lophyl radical in the micelle (V_f) according to V_m. This value indicates that the C_{12}TAB micelle has the smallest volume for diffusion of the lophyl radicals, which is consistent with this trend. From these results, it becomes clear that the confined space of micelles is useful for enhancing and tuning of the photochromic reaction of LPD.

3. *in situ* SANS measurement for photo-induced rapid morphological changes in the micelle

Next, we examined the morphological changes in micelles formed by an amphiphilic LPD derivative (**3TEG-LPD**) upon UV light irradiation. However, conventional lab-scale analytical techniques for colloidal particles (e.g., light scattering and laser diffraction) have problems with obtaining precise information about the structures of molecular assemblies by high time resolution and overlapping optical systems for photochromic reactions and analysis. To overcome the problems, we developed an *in situ* SANS system (TAIKAN, MLF, J-PARC) by installing a lamp and a UV/Vis absorption spectrometer to monitor the morphology of the micelles and the photochromic reaction of the LPD moiety of **3TEG-LD** (Fig. 3) [7,8]. Figure 4(a) shows the SANS profiles of **3TEG-LPD** in D_2O. The experimental data were well fitted using a uniform prolate ellipsoid model with a long radius (r_a) of ~47 Å and a short radius (r_b) of ~28 Å [9]. After UV irradiation, the long radius increased to ~70 Å.

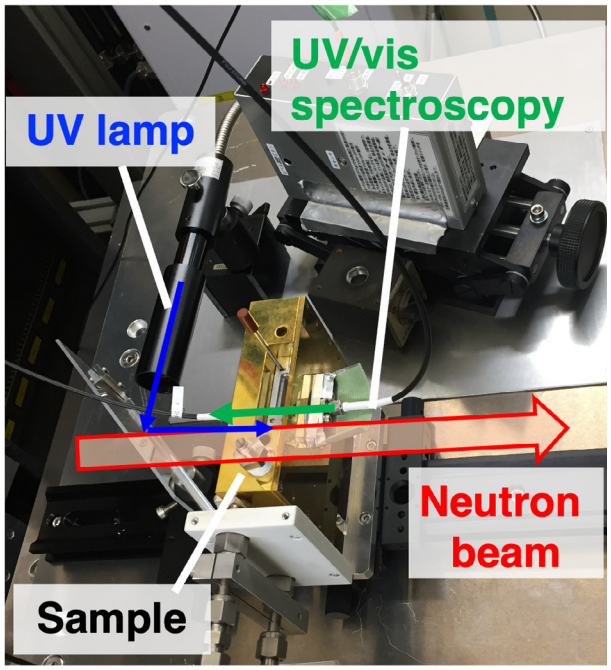

Figure 3. Picture of *in-situ* SANS system.

This indicated that UV irradiation induced elongation of the longer axis of the micelles because of photo-induced morphological changes in the molecular structures between the dimer and monomer forms.

To see the time course of morphological changes in the SANS profile, the integrated scattering intensity in the q-region of 0.01–0.05 $Å^{-1}$ during cycles of 2 min UV irradiation followed by 4 min standing in the dark was plotted against the time, as shown in Fig. 4(b). This revealed that the elongation of the elliptical micelles was completed after 60 s of irradiation and reversed after 60 s of standing in the dark. UV/Vis absorption spectra were collected simultaneously during the SANS measurements. As shown in Fig. 4(c), a new absorption band deriving from the lophyl radical was observed at 580 nm during UV irradiation. The change in the absorption at 580 nm during the irradiation cycle revealed that morphological changes in the micelles and photochromism of LPD occurred without a time lag within the analytical time resolution (Fig. 4(b) and 4(c)). From these results, we have successfully observed rapid morphological changes in the LPD micelles by the developed *in-situ* SANS system.

4. Conclusion

Recombination of lophyl radicals produced from a lophine dimer with UV light irradiation was significantly enhanced in the surfactant micelle as a confined nano space. SANS measurements revealed the detailed

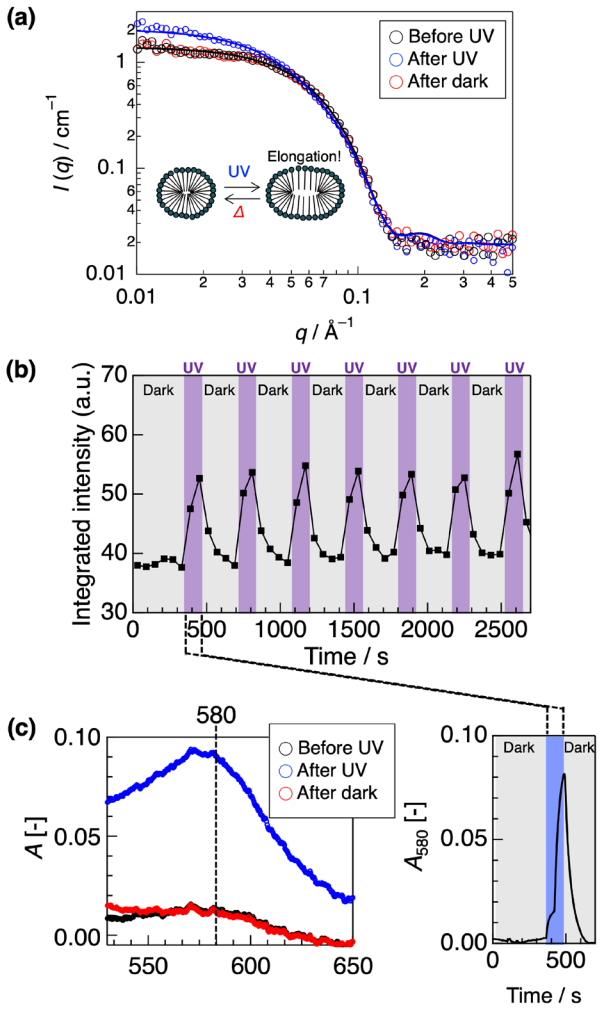

Figure 4. (a) SANS profiles of 10 mM **3TEG-LPD** in D_2O before and after 2 min UV irradiation and 4 min standing in the dark. (b) The integrated scattering intensity of the SANS profiles of **3TEG-LPD** in the *q*-region of 0.01–0.05 Å^{-1} during cycles of UV irradiation and standing in the dark. (c) UV/Vis absorption spectra before and after UV irradiation and standing in the dark (left), and the temporal changes in absorption at 580 nm during the cycle using an *in-situ* UV/Vis absorption spectrometer (right).

micelle structures as a reaction site and their effect on the recombination rate. With the decrease in the micelle volume, the recombination rate increased. This is because in a smaller space, the lophyl radicals easily collide and rapidly recombine themselves. Furthermore, we examined the photo-induced morphological changes in the micelle, formed by an amphiphilic LPD derivative. An *in-situ* SANS system, developed at the small and wide angle neutron scattering instrument TAIKAN at the MLF in J-PARC revealed that the LPD micelle is rapidly and reversibly elongated during UV light irradiation in the order of seconds and the speed of the morphological changes exceeds the conventional photoresponsive molecular assemblies. From these results, the SNAS technique (particularly, *in situ* set-up) is suitable for stimuli-responsive materials.

5. Future plans

We enabled the observation of photo-induced rapid morphological changes in the micelles by the developed *in-situ* SANS systems. Recently, the structural analysis of the LPD micelles with a time scale of 500 ms was realized by stroboscopic SANS [10]. In the future, we will change the time resolution to ~10 ms and enable the understating of the dynamics of morphological changes in the properties of photoresponsive molecular assemblies.

References

[1] M. Akamatsu et al., Chem. Lett., **52**, 573 (2023).
[2] Y. Kishimoto et al., J. Am. Chem. Soc., **131**, 4227 (2009).
[3] M. Akamatsu et al., Chem. Lett., **47**, 113 (2018).
[4] M. Akamatsu et al., J. Oleo. Sci., **68**, 659 (2019).
[5] M. Akamatsu et al., Chem. Commun., **55**, 9769 (2019).
[6] M. Akamatsu et al., Colloids Surfaces A Physicochem. Eng. Asp., **638**, 128319 (2022).
[7] Y. Sakaguchi et al., JPS Conf. Proc. JPS Conf. Proc., **33**, 011100 (2021).
[8] H. Iwase et al., J. Appl. Cryst., **56**, 110 (2023).
[9] M. Akamatsu et al., Sci. Rep., **11**, 10754 (2021).
[10] H. Iwase et al., Langmuir, **39**, 12357 (2023).

M. Akamatsu[1,2], H. Iwase[3], K. Kobayashi[2], T. Morita[2], R. Tanaka[2], Y. Sakaguchi[3], K. Sakai[2], and H. Sakai[2]
[1]*Faculty of Engineering, Tottori University;* [2]*Faculty of Science and Technology, Tokyo University of Science;* [3]*Neutron Science and Technology Center, CROSS*

High-resolution Neutron Structure Reveals the Non-planarity of Peptide bonds

1. Introduction

Proteins are polymers composed of α-amino acids, interconnected through peptide bonds. The dihedral angles of main chain, known as φ and ψ, are restricted to energetically favorable regions, serving as parameters in Ramachandran plots for assessing the accuracy of structure refinement. Due to the double-bond character of the peptide bond, the dihedral angle, ω, between the C-N bond is typically 180° in its trans form or 0° in its cis form. Traditional understanding dictates that the six atoms involved in the peptide bond lie on the same plane. However, high-resolution X-ray crystallography has revealed inconsistencies in the distortion of peptide bonds, dependent on the values of φ and ψ [1–3]. Despite the advancements in high-resolution X-ray structural determination, refining the coordinates of amide protons remains a significant challenge. In protein structure refinement, the coordinates of hydrogen atoms are constrained using a riding model, which assumes that hydrogen atoms ride on their parent atoms. This means that the position of a hydrogen atom is determined based on the knowledge about the chemical bond between the hydrogen and its attached heavier atoms. Neutron crystallography is highly effective for direct observation of the hydrogen atoms. Through our efforts, we were able to obtain neutron data with an impressive resolution of 1.2 Å for the oxidized structure of the high-potential iron-sulfur protein (HiPIP) from *Thermochromatium tepidum*. This resolution allowed for the refinement of the coordinates of amide protons without the geometric constraints [4].

2. Experiments

We carried out the crystallization of HiPIP employing a solution prepared from deuterated reagents and heavy water, yielding deuterium-substituted crystals. Neutron diffraction data were collected utilizing the IBARAKI Biological Crystal Diffractometer (iBIX) at BL03 in J-PARC MLF. X-ray diffraction data were collected at the Photon Factory BL5A using ADSC Q315r detector. For the structural refinement, we used neutron (1.2 Å resolution) and X-ray data (0.66 Å resolution). The data-to-parameter ratio in the neutron data was adequate to modify the crystallographic parameters for amide protons, prompting us to refine their coordinates without geometric constraints. This was appropriated for deuterium atoms with occupancies exceeding 0.60, and for protium atoms with occupancies exceeding 0.75. The final R_{work} and R_{free} values were 7.41% and 8.15%, respectively, for the X-ray data, and 15.4% and 16.8%, respectively, for the neutron data.

3. Results and Discussion

As a result of X/N refinement, electron density and neutron scattering length density can be observed independently for each atom, and a density map that clearly shows the polarization of hydrogen atoms can be obtained (Fig. 1). The neutron data is of sufficient quality to determine the accurate positions of hydrogen atoms. In the case of typical hydrogen bond, the interaction is often characterized by an acceptor-donor dyad. Nonetheless, alternative configurations of hydrogen bond exist, which consists of multiple donors or

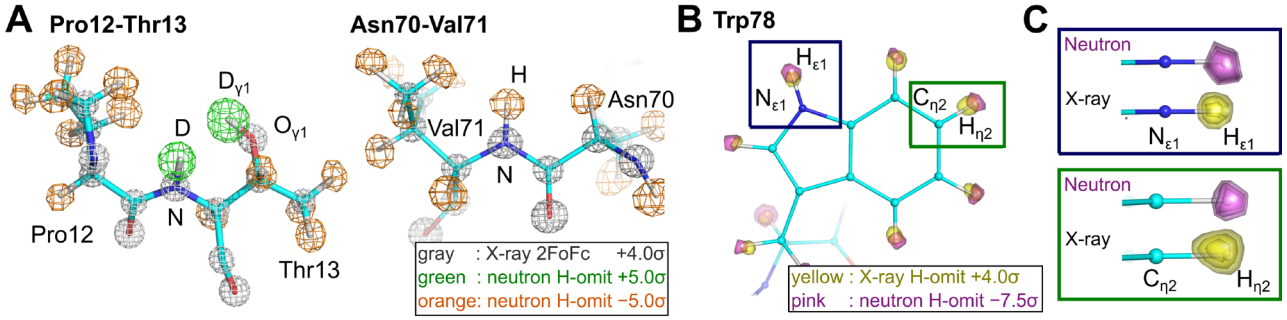

Figure 1. (A) Density map between Pro12 and Thr13 and Asn70 and Val71. (B) Difference between the electron and neutron scattering length density map of indole ring of Trp78. (C) Close-up view of $N_{ε1}$– $H_{ε1}$ and $C_{η2}$– $H_{η2}$ of Trp78 [4].

acceptors, and it is called a bifurcated hydrogen bond. In single-acceptor hydrogen bonds, the angular relationships among the donor, hydrogen, and acceptor (denoted as ∠DH…A) frequently deviate from the riding models, often displaying increased angles (Fig. 2A). The nuclei of amide protons have a pronounced propensity to orient themselves toward acceptor atoms. In contrast, the bifurcated bond paradigm reveals a distinct pattern: certain amide protons are conspicuously displaced from proximate acceptor atoms (Fig. 2B). This observation underscores the significance of bidirectional electrostatic forces in influencing the spatial positioning of atoms involved in hydrogen bonding, a compelling demonstration.

Historically, affirmations of the planarity of peptide bonds have relied on non-hydrogen atoms, due to a deficit of structural insights for the amide proton. Here, we focus on the dihedral angle of the $H_i - N_i - C_{i-1} = O_{i-1}$ plane (where "*i*" denotes residue number) as ω′. The planarity associated with a double bond, which implies a dominance of sp^2 hybrid orbitals, can be evaluated using the pyramidalization angle, denoted as θ [5]. For carbon (θ_C), these angles range between –5° and 5°, reflecting the consistent maintenance of the sp^2 orbital arrangement in the C = O double bond (Fig. 3A). On the other hand, the pyramidalization angle of amide nitrogen (θ_N)

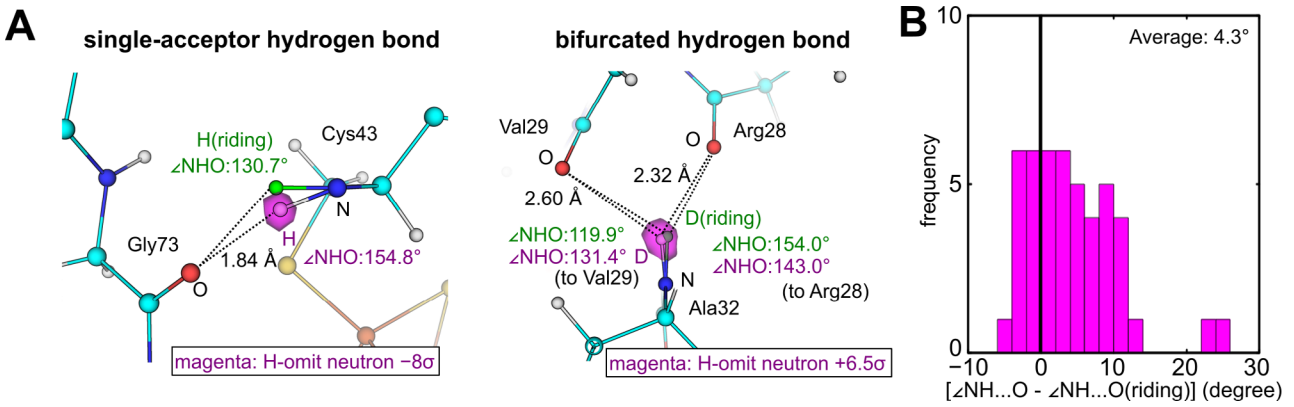

Figure 2. (A) Deviation of the amide proton from peptide plane in single-acceptor hydrogen bond (left) and bifurcated hydrogen bond (right). (B) Histogram of the frequency of differences in donor-hydrogen acceptor angles in single-acceptor hydrogen bonds between the experimentally refined model and the riding model. (This figure is modified from reference [4].)

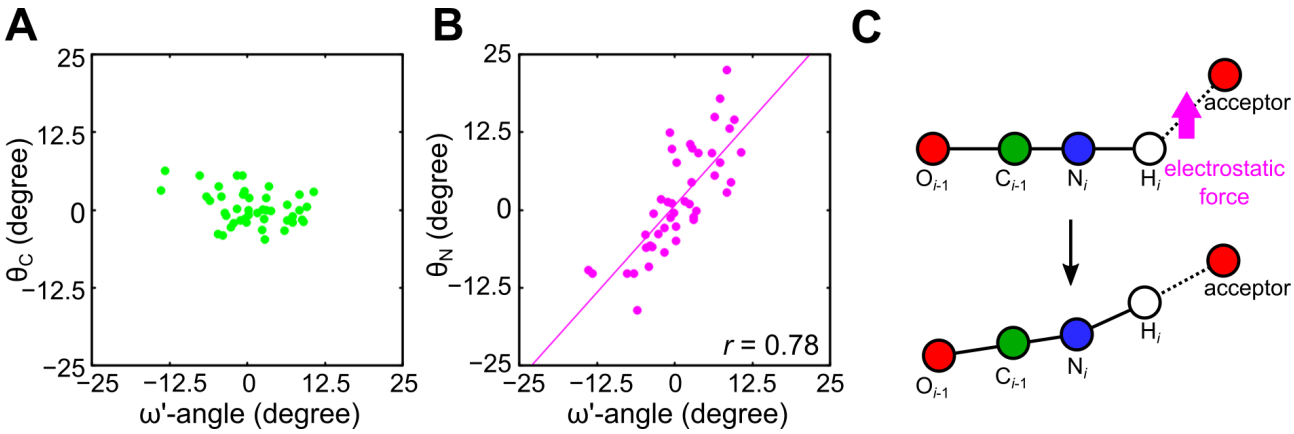

Figure 3. (A) Scatter plot of θ_C against ω′ angle. (B) Scatter plot of θ_N against the ω′ angle. Linear regression is shown as a solid line. (C) Side-view schematic of the peptide bond. The attraction of the amide proton by the acceptor atom shifts the $H_i - N_i - C_{i-1} = O_{i-1}$ plane [4].

spans a broad range from –25° to 20° (Fig. 3B). Such data clearly suggest that the tendency of amide nitrogens to assume a pyramidal shape is triggered when amide protons are drawn to acceptors due to electrostatic forces. This disrupts the inherent planarity of the $H_i - N_i - C_{i-1} = O_{i-1}$ (Fig. 3C). These insights suggest that this plane is susceptible to alterations by electronic influences, potentially causing deviations from the peptide bond planarity.

References

[1] D. S. Berkholz et al., Proc. Natl. Acad. Sci. USA, **109**, 449 (2012).
[2] R. Improta et al., PLOS ONE, **6**, e24533 (2011).
[3] L. Esposite et al., J. Mol. Biol., **347**, 483 (2005).
[4] Y. Hanazono et al., Sci. Adv., **8**, eabn2276 (2022).
[5] G. N. Ramachandran and A. S. Kolaskar, Biochim. Biophys. Acta, **303**, 385 (1973).

Y. Hanazono[1], Y. Hirano[2,3], K. Takeda[4], K. Kusaka[5], T. Tamada[2,3], and K. Miki[4]
[1]Medical Research Institutes, Tokyo Medical and Dental University; [2]Institute for Quantum Life Science, National Institutes for Quantum Science and Technology; [3]Graduate School of Science, Chiba University; [4]Graduate School of Science, Kyoto University; [5]Neutron Science and Technology Center, CROSS

Excitations in the Ordered and Paramagnetic States of Honeycomb Magnet $Na_2Co_2TeO_6$

1. Introduction

The spin-1/2 Kitaev honeycomb model is a booming direction to search for quantum spin liquids, where spins are highly frustrated due to bond-directional Ising interactions [1]. In the past decade, the materialization of this model has been focused on iridium and ruthenium compounds [2], with Na_2IrO_3 and α-$RuCl_3$ being two most promising candidates [3, 4]. Recently, cobalt-based honeycomb materials were proposed to be another category of compounds for the realization of Kitaev model [5, 6]. Among a series of candidates, $Na_2Co_2TeO_6$ shows intriguing magnetism and similar thermodynamic properties with α-$RuCl_3$ [7, 8], which therefore has attracted a lot of attention. However, its leading exchange interactions remain elusive due to a lack of knowledge on the full excitation spectrum. For example, previous inelastic neutron scattering (INS) studies on powder samples have pointed to diversifying sets of parameters [8-11], which puts its relevance to the Kitaev physics under hot debate. To resolve this problem, we performed an INS experiment on high-quality $Na_2Co_2TeO_6$ single crystals with the 4SEASONS spectrometer.

2. Spin waves in the ordered state

In the magnetically ordered state, sharp spin waves can be clearly resolved. Figure 1(a) presents the lowest-energy spin wave branch at 5 K along high-symmetric lines in the two-dimensional Brillouin zone. This branch reaches the same energy minimum (~1 meV) at both the M (0.5, 0) and Γ (0, 0) points. There are two possible magnetic ground states of $Na_2Co_2TeO_6$: one is a zigzag structure [Fig. 1(d)] [9, 12, 13], which has C_3-related domains in a macroscopic sample; another is a triple-q structure [Fig. 1(e)] [14] formed by the vector sum of all C_3-related zigzag structures. However, if the zigzag state were driven by Kitaev interactions, the spin waves would reach their band minimum at the M point, and become higher-energy flat modes near the Γ point [15, 16], which is different from different from our observation. The observation of the same spin wave energy at the M

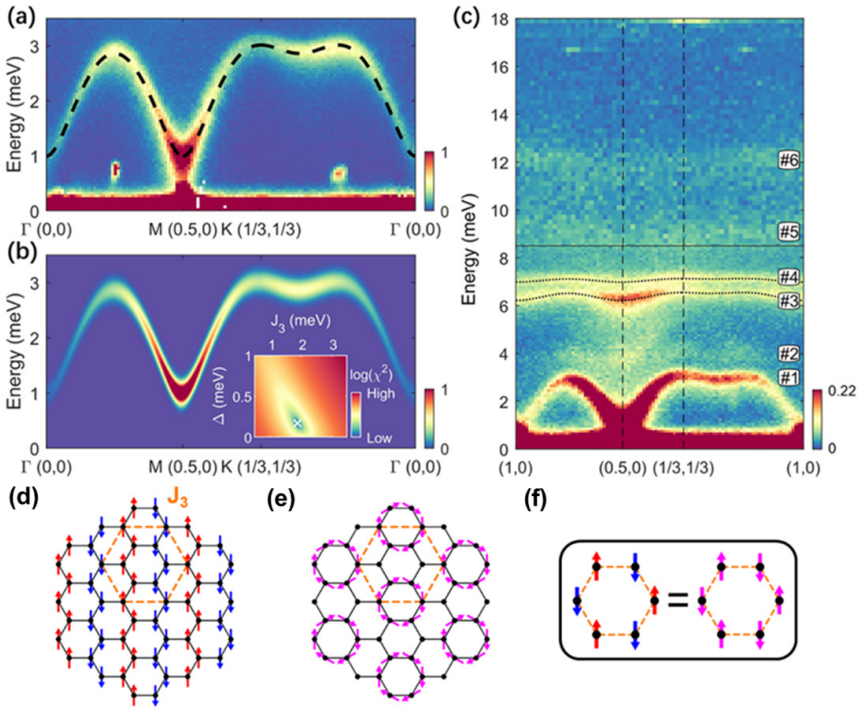

Figure 1. (a) Low-energy spin waves along high-symmetric lines of the Brillouin zone at 5 K. The dashed curve is the fitted dispersion. (b) Calculated spin waves with a J_3-Δ model. Inset shows the goodness of fit. (c) Full spin-wave spectrum at 5 K. Data are averaged over the entire covered L-range and all presented intensities are converted to absolute units with phonon scattering. (d) Zigzag order in the honeycomb lattice (only one zigzag domain is shown). The dashed orange lines show the J_3 connection. (e) Triple-q order in the honeycomb lattice. (f) Highlight of the emerging honeycomb lattice with Néel order from (a) and (b).

and Γ points therefore supports either a zigzag structure driven primarily by competing Heisenberg terms or a triple-q magnetic structure.

Although the powder averaged excitation spectrum has been widely discussed in the context of an exchange Hamiltonian with Kitaev interaction, we find the lowest-energy spin wave can be adequately described by an effective model with only third-nearest-neighbor antiferromagnetic (AFM) coupling (J_3) and gap-opening (Δ) terms:

$$H = J_3 \sum_{\langle\langle\langle i,j\rangle\rangle\rangle} \mathbf{S}_i \cdot \mathbf{S}_j - \Delta \sum_i (\mathbf{S}_i \cdot \hat{\mathbf{n}}_i)^2 .$$

The model has an effective Néel order on each of the four J_3-linked (enlarged honeycomb) sublattices [Fig. 1(d) and (e)], and $\hat{\mathbf{n}}_i$ denotes the ordered spin direction at site i. We fit the observed dispersion [Fig. 1(a)] with linear spin wave theory. The best-fit parameters are J_3 = 1.896(9) meV and Δ = 0.170(6) meV, which also reproduce the observed intensities very well [Fig. 1(b)]. Under this J_3-Δ model, the two possible magnetic structures (zigzag and triple-q) are completely equivalent [Fig. 1(f)], which accounts for why they cannot be distinguished by most experiments up to date.

At higher energy, we can further identify at least five spin wave branches [Fig. 1(c)]. The dispersions of the two branches between 6 meV and 8 meV (#3 and #4) are very clear, which can also be well captured by respective J_3-Δ models [dashed curves in Fig. 1(c)]. From a structural point of view, the cobalt hexagons in $Na_2Co_2TeO_6$ centered around tellurium atoms, whose spatially extended d orbitals may naturally promote electron hopping and further-neighbor coupling.

3. Diffuse scattering in the paramagnetic state

Upon warming above T_N ~ 27 K, the spin waves disappear, yet the finite-energy dynamics persist far above T_N [Fig. 2(a)]. These paramagnetic fluctuations are weakly structured in energy but strongly structured in **Q**: intensities are concentrated around the M points of the Brillouin zone [Fig. 2(b)], indicative of instability towards the ordering at low temperature. This **Q**-structure can be modeled by the equal-time spin correlation function, which in effect considers scattering interference from a hexagonal unit. There are two kinds of spin arrangements in the hexagonal unit [Fig. 2(c)], in accord with the two magnetic structures. The calculated patterns based on both spin arrangements are consistent with the experiment data [Fig. 2(d) and (e)]. A common characteristic of them is that the AFM J_3 coupling always connects opposite spins, reminding us of J_3's fingerprint on the most pronounced spin waves in the ordered state.

4. Conclusion

We have successfully mapped out the magnetic excitations over the 2D Brillouin zone and studied their temperature dependence in conjunction with thermodynamics. In the ordered state, sharp spin waves contribute the most spectrum weight. With linear spin-wave theory, we find that a third-nearest-neighbor Heisenberg interaction alone provides a highly accurate effective description of the low-energy spin waves. Moreover, we find paramagnetic scattering persists well above the ordering temperature, which can be accounted for

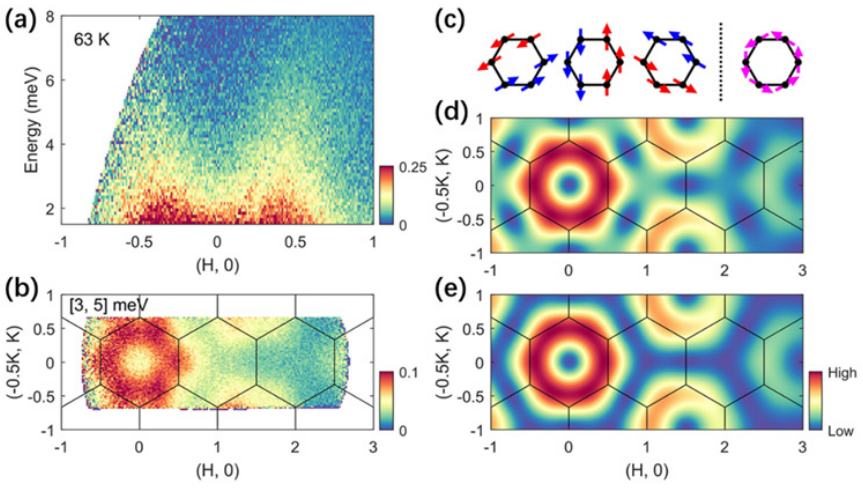

Figure 2. (a) Paramagnetic fluctuations at 63 K plotted along (H, 0) direction. (b) Constant energy cut around 4 meV in the (H, K) plane. (c) Two zigzag-type spin arrangements in a hexagon. (d) and (e) Calculated paramagnetic scattering patterns based on the spin arrangements in (c).

by equal-time magnetic structure factors of a hexagonal cluster. Our results shed light on the closely competing interactions and instabilities in $Na_2Co_2TeO_6$ and provide new insights on designing Kitaev materials in general. This work was published in [17].

References

[1] A. Kitaev, Ann. Phys. **321**, 2 (2006).
[2] Takagi et al. Nat. Rev. Phys. **1**, 264 (2019).
[3] Singh et al. Phys. Rev. B **82**, 064412 (2010).
[4] Plumb et al. Phys. Rev. B **90**, 041112(R) (2014).
[5] Liu et al. Phys. Rev. B **97**, 014407 (2018).
[6] Sano et al. Phys. Rev. B **97**, 014408 (2018).
[7] Yao et al. Phys. Rev. B **101**, 085120 (2020).
[8] Lin et al. Nat. Commun. **12**, 5559 (2021).
[9] Samarakoon et al. Phys. Rev. B **104**, 184415 (2021).
[10] Kim et al. J. Phys. Condens. Matter **34**, 045802 (2022).
[11] Sanders et al. Phys. Rev. B **106**, 014413 (2022).
[12] Lefrançois et al. Phys. Rev. B **94**, 214416 (2016).
[13] Bera et al. Phys. Rev. B **95**, 094424 (2017).
[14] Chen et al. Phys. Rev. B **103**, L180404 (2021).
[15] Banerjee et al. Nat. Mater. **15**, 733 (2016).
[16] Chaloupka et al. Phys. Rev. Lett. **110**, 097204 (2013).
[17] Yao et al. Phys. Rev. Lett. **129**, 147202 (2022).

W. Yao[1], K. Iida[2], K. Kamazawa[2], and Y. Li[1]
[1]*International Center for Quantum Materials, School of Physics, Peking University;* [2]*Neutron Science and Technology Center, CROSS*

Crystal Electric Field Level Scheme Behind Giant Magnetocaloric Effect for Hydrogen Liquefaction

1. Introduction

Magnetic refrigeration, which is known as a cooling method using a magnetic field, has been actively researched so far mainly for application to near room temperature or extremely low temperatures below 1 K [1]. On the other hand, recently, magnetic refrigeration in the intermediate temperature range (on the order of several tens of K) has been attracting attention as a new cooling method for efficiently cooling liquid hydrogen [2]. Magnetic refrigeration for the purpose of hydrogen liquefaction requires efficient cooling in the temperature range from the hydrogen liquefaction temperature of 20 K to around 77 K (assuming precooling with liquid nitrogen). In magnetic refrigeration, the magnetic entropy change (ΔS_M) of a magnetic material when a magnetic field is excited or demagnetized is an important factor in developing an efficient magnetic refrigeration system.

For the purpose of obtaining high performance MCE materials, heavy rare earth compounds become the most promising candidates. Because, as a potential maximum magnetic entropy is defined as $S_M = R \ln (2J + 1)$, where R is the gas constant and J is total angular momentum quantum number. However, in most of the cases, such potentially large S_M does not exist at several tens degrees of Kelvin temperature range that could be useful for hydrogen liquefaction, due to the crystal electric field reducing the large entropy even in zero magnetic field condition. Such temperature range of several tens degrees of Kelvin is generally comparable to the crystal electric field (CEF) energy levels for heavy rare earth ions (schematic illustration is presented in Fig. 1). Magnetic entropy change (ΔS_M) strongly depends on the degeneracy of the CEF ground state, which is lifted by external magnetic field through Zeemann splitting, leading to MCE. In this context, understanding the CEF level scheme for heavy rare earth compounds is important for designing the MR materials for hydrogen liquefaction.

2. Inelastic neutron scattering of HoB_2

In inelastic neutron scattering (INS) experiments, the energy levels of the CEF can be determined by measuring the energy spectrum of the purely paramagnetic phase, because there is no internal magnetic field induced by ferromagnetic long-range order. As an example, we selected the MR material HoB_2 with a huge MCE to evaluate the CEF energy level scheme. HoB_2 was recently discovered to exhibit a very large $|\Delta S_M|$ value near the hydrogen liquefaction temperature [2]. INS experiments were performed using the High-Resolution Chopper Spectrometer (HRC) beamline. The experimentally determined CEF level scheme shown in Fig. 2(a) was illustrated, which reproduces the experimental INS spectrum. (Fig. 2(b)). In order to calculate magnetic entropy change with the determined CEF parameters, we conducted the mean-field calculation, which successfully reproduced the ΔS_M, observed in previous magnetization measurement [2] (Fig. 2(c)).

Here, we discuss how the CEF states of the obtained HoB_2 affect the magnetic entropy change ΔS_M when a magnetic field is applied. When the temperature of the system is assumed to be 20 K, the energy gap between the ground state (Γ_1^B) and the excited states Γ_6^C and Γ_6^B can be considered pseudo-degenerated with respect to the system temperature. When applying magnetic fields along a principal axis, the pseudo-degeneracy is lifted, leading to such a large $|\Delta S_M|$ (Fig. 2(d)).

3. Mean-field calculation with CEF and exchange parameters

We also calculated the ideal CEF level scheme for general heavy rare earth ions with site symmetries, cubic O_h and hexagonal D_{6h} by using mean-field calculations. Figure 3(a) shows one example, crystal field parameter dependence of $|\Delta S_M|$ (5 T, 20 K) for cubic O_h.

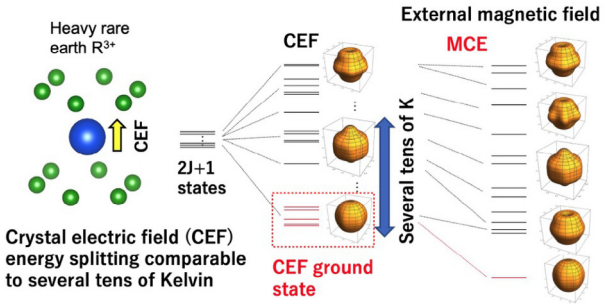

Figure 1. Schematic illustration of complicated crystal electric field (CEF) energy level splitting in heavy rare earth ions (with schematic drawings of electrons wave functions in each energy level), and Zeemann splitting of the CEF levels resulting in a large magnetocaloric effect. For several tens degrees of Kelvins energy scale, CEF splittings are generally comparable to the system temperature in heavy rare earth system.

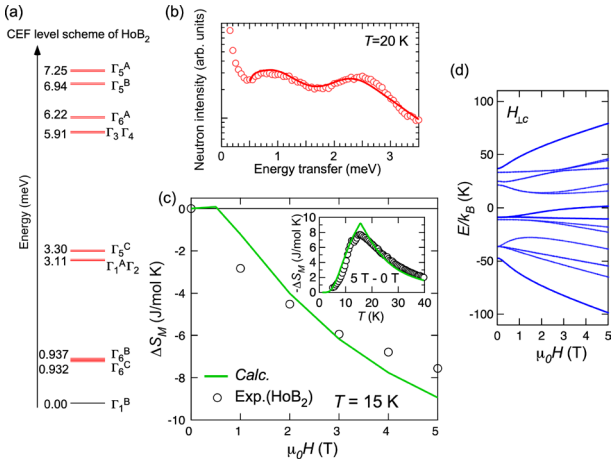

Figure 2. (a) Crystal electric field (CEF) level scheme in HoB_2 was determined by the present neutron scattering experiment. (b) The neutron intensity (open circle) was successfully explained by theoretical calculation curve (solid line) with the CEF parameters. (c) Magnetic field and temperature dependence of magnetic entropy change (open circle) is roughly consistent with those calculated with the mean-field calculation with the determined CEF parameters. (solid line) The data were taken from Ref. [3]. (d) Calculated Zeemann splitting for HoB_2 in magnetic field perpendicular to the c-axis.

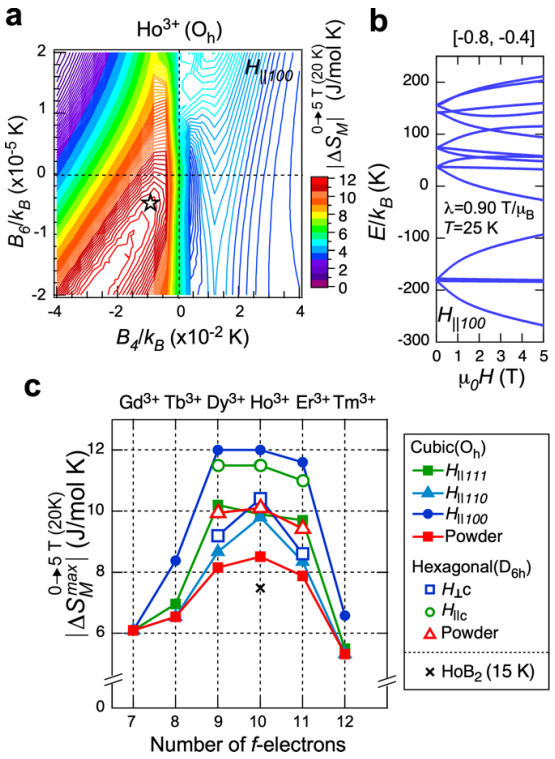

Figure 3. Contour map of magnetic entropy change of Ho3+ in the cubic Oh symmetry at $T = 20$ K in magnetic field change from 0 to 5 T along [100] direction. (b) Zeemann splitting in magnetic field along [100] direction at T = 25 K for the set of CEF parameters indicated by the star symbol in (a). (c) Heavy rare earth ion dependence of the maximum magnetic entropy change, predicted by the present mean-field calculations for the cubic Oh and hexagonal D_{6h} symmetries. The experimental value of HoB_2 at 15 K is also plotted [3].

The $|\Delta S_M|$ influences significantly the crystal field parameters. It is important to note that this does not necessarily show that $|\Delta S_M|$ is largest when the crystal field is zero. In this way, in addition to the degree of degeneracy of the pseudo ground state of the crystal field, the degree of how much the ground state is isolated when a magnetic field is also an important factor in producing a large $|\Delta S_M|$.

The calculation results are summarized in Fig. 3(c). The maximum $|\Delta S_M|$ for Ho^{3+} with the hexagonal symmetry for powder case, corresponding to HoB_2 case, is 10.1 J mol^{-1} K^{-1}, which is 30% larger than that of HoB_2. We, therefore, found that there is still room to improve $|\Delta S_M|$ even in one of the largest MCE materials, HoB_2.

4. Concluding remarks

The relationship between ΔS_M and crystal field parameters derived in this study provides new guidelines for searching for compounds with larger magnetocaloric effects near the hydrogen liquefaction temperature. Recent advancements in density functional theory calculations have unlocked the possibility of predicting CEF parameters for rare-earth systems based on the crystal information. A combination of DFT calculations and the relationships between $|\Delta S_M|$ and the CEF parameters derived in this study would accelerate the search for compounds with a large MCE and help to design more magnetic refrigeration materials.

References

[1] T. Numazawa, et. al., Cryogenics **62,**185 (2014).
[2] P. Baptista de Castro, et. al., NPG Asia Mater. **12**, 35 (2020).
[3] N. Terada, et. al., Communications Materials **4** 13 (2023).

N. Terada[1], H. Mamiya[1], H. Saito[2], T. Nakajima[2,3], T. D. Yamamoto[1], K. Terashima[1], H. Takeya[1], O. Sakai[4], S. Itoh[5,6], Y. Takano[1], M. Hase[1], and H. Kitazawa[1]

[1]National Institute for Materials Science; [2]Institute for Solid State Physics, The University of Tokyo; [3]RIKEN Center for Emergent Matter Science (CEMS); [4]Neutron Science and Technology Center, CROSS; [5] Institute of Materials Structure Science, KEK; [6]Materials and Life Science Division, J-PARC Center

Relief of Spin Frustration through Magnetic Anisotropy in the Quasi-one-dimensional $S = 1/2$ Antiferromagnet $Na_2CuSO_4Cl_2$

1. Introduction

Exotic spin states are expected to be observed in low-dimensional magnets. In most low-dimensional magnets, however, there is relatively strong three-dimensional (3D) magnetic coupling, which induces magnetic ordering at finite temperatures. More to the point, the coexistence of such coupling and magnetic anisotropy stabilizes the 3D spin structure in low-dimensional magnets. Therefore, to identify quantum phases, it is usually important to explore a model compound with negligibly small interchain or interlayer couplings. Although it is rare, a moderately strong interchain interaction can play an important role in quasi-one-dimensional (quasi-1D) spin systems with a uniform Dzyaloshinskii-Moriya (DM) interaction in realizing an exotic spin state.

The $S = 1/2$ quasi-1D antiferromagnet $Na_2CuSO_4Cl_2$ exhibits peculiar DM interactions that are uniform along its spin chains and antiparallel with respect to neighboring chains [1, 2]. Linear spin chains along the *a* axis are formed by the exchange interaction $J = 14.2$ K through the Cu-Cl-Cl-Cu path, which is much larger than the interchain interaction $J' = 0.18$ K estimated from the Néel temperature $T_N = 0.54$ K. Based on the crystal structure, $Na_2CuSO_4Cl_2$ exhibits substantial DM interactions that are aligned parallel to the *b* axis [Fig. 1]. However, the DM vector is aligned antiparallel between the adjacent chains. In this case, helical correlations with opposing helicity are present when interacting spin chains feature peculiar DM interactions that are uniform along the chain and antiparallel with respect to neighboring chains, thus resulting in unique spin frustration. However, the magnitude of DM vector (***D***) and the magnetic structure, which is required to understand the DM-induced frustration effect, were not determined.

2. Experiments

Large single crystals of $Na_2CuSO_4Cl_2$ were successfully grown by using a low-temperature molten-salt reaction process [1]. High-purity $CuCl_2$ and Na_2SO_4 powders were mixed with the molar ratio of 1 : 1 and vacuum sealed into a quartz tube. The mixture was heated at 470°C for two days and then slowly cooled. High-field multifrequency ESR measurements were performed using pulsed magnetic fields up to 13 T in the frequency range from 70 to 260 GHz at several temperatures. A standard of 2,2-diphenyl-1-picrylhydrazyl (known as DPPH) was employed as a $g = 2.0036$ marker for the magnetic field. Neutron-diffraction measurements in a wide reciprocal space were performed using a time-of-flight (TOF) neutron diffractometer (BL18 SENJU) installed at the MLF of the J-PARC [3]. The collected data were processed with the software STARGAZER [4].

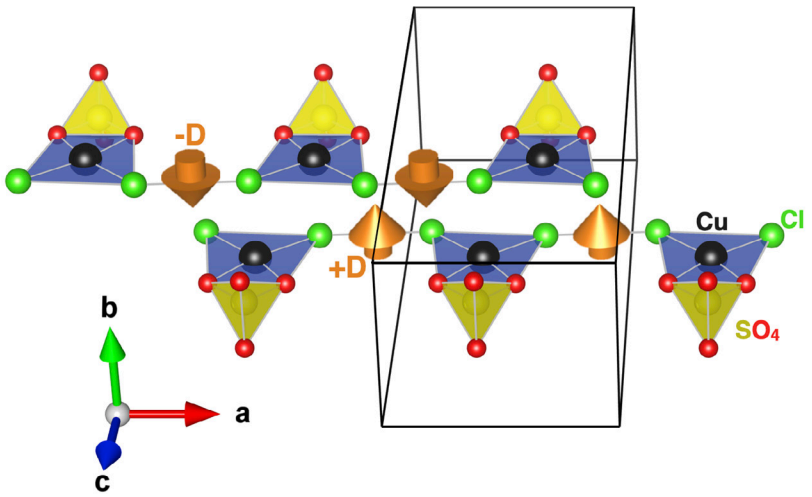

Figure 1. The crystal structure of $Na_2CuSO_4Cl_2$. The Cu^{2+} ions (black) displayed with nearby oxygen (red), SO_4 ions (yellow tetrahedra), and chlorine ions (green). The direction of the Dzyaloshinskii-Moriya vector D, as determined by ESR measurements, is indicated by the orange arrow.

3. Results and discussion

The direction and magnitude of ***D*** in $Na_2CuSO_4Cl_2$ was determined using ESR. Considering a single Heisenberg chain with a uniform DM interaction, in the case of $H \parallel \boldsymbol{D}$, the ESR doublet M_+ and M_- appear equidistant to the left and right of the paramagnetic resonance line P^* in the temperature range of $T << |\boldsymbol{D}|$ [5]. As shown in Fig. 2(a), two lines (P^* and M_+) are clearly observed for a field along the b axis. The reason why the M_- line is not seen is because it becomes difficult to separate the P^* and M_- lines in the temperature region of $T > |\boldsymbol{D}|$ [6]. The temperature evolution of the 240 GHz ESR line at $H \parallel b$ is shown in Fig. 2(c), indicating that M_+ develops when the temperature decreases. These results indicate an antisymmetric exchange with a uniform ***D*** pointing along the b axis, as shown in Fig. 1. The values of the g factors and $|\boldsymbol{D}|$ are estimated to be $g_a = 2.07(1)$, $g_b = 2.23(2)$, $g_c = 1.99(1)$, and $|\boldsymbol{D}| = 1.01(3)$ K by fitting the frequency dependencies of the resonance fields of mode P^* and M_+. The estimated value is larger than the Néel temperature $T_N = 0.54$ K of $Na_2CuSO_4Cl_2$.

Below T_N, about 100 magnetic reflection peaks were observed on the (n/2 k l) where n is an odd integer. The presence of the (n/2 k l) magnetic peaks indicates that nearest-neighbor Cu atoms within a chain have exactly antiparallel magnetic moments and the magnetic unit cell is twice as large as a chemical unit cell along the a axis. Four magnetic Cu^{2+} ions are located on the Wyckoff positions 4c: $\mathbf{r}_1 = (0.636, 0.25, 0.966)$, $\mathbf{r}_2 = (0.136, 0.25, 0.534)$, $\mathbf{r}_3 = (0.364, 0.75, 0.034)$, and $\mathbf{r}_4 = (0.864, 0.75, 0.466)$ in the orthorhombic unit cell with space group *Pnma*. In this case, the possible magnetic structure can be represented by only four irreducible spin arrangements (↑, ↑, ↑, ↑), (↓, ↑, ↑, ↑), (↑, ↓, ↑, ↑), and (↓, ↓, ↑, ↑), where the parentheses show the relative phase factors of the spins on the sites ($\mathbf{r}_1$, $\mathbf{r}_2$, $\mathbf{r}_3$, $\mathbf{r}_4$). Therefore, in the case that the spins are pointing along one of the crystal axes, there are only 12 possible magnetic structures. Figure 3(a) shows the observed intensities I_{obs}^{Nuc} and I_{obs}^{Mag} plotted against calculated intensities I_{calc}^{Nuc} and I_{calc}^{Mag} for the nuclear and magnetic peaks. The I_{calc}^{Mag} presented in Fig. 3(a) are calculated for the magnetic structure shown in Fig. 3(b). Based on how good a fit is, a candidate magnetic structure is obtained, as shown in Fig. 3(b). There is no large deviation between the calculated magnetic intensities with full Cu^{2+} moment of 1 μB and the line fitted to the observed nuclear intensity in the almost extinction-free region [Fig. 3(a)]. The spin direction is parallel to the ***D*** expected from the crystal structure, indicating that the DM interaction is not the driving force for the magnetic phase transition.

Most low-dimensional copper salts exhibit long-range magnetic ordering at low temperature, with the spins pointing in a specific direction in the crystal, suggesting that there is a finite magnetic anisotropy in these salts. In copper salts, there is no anisotropy

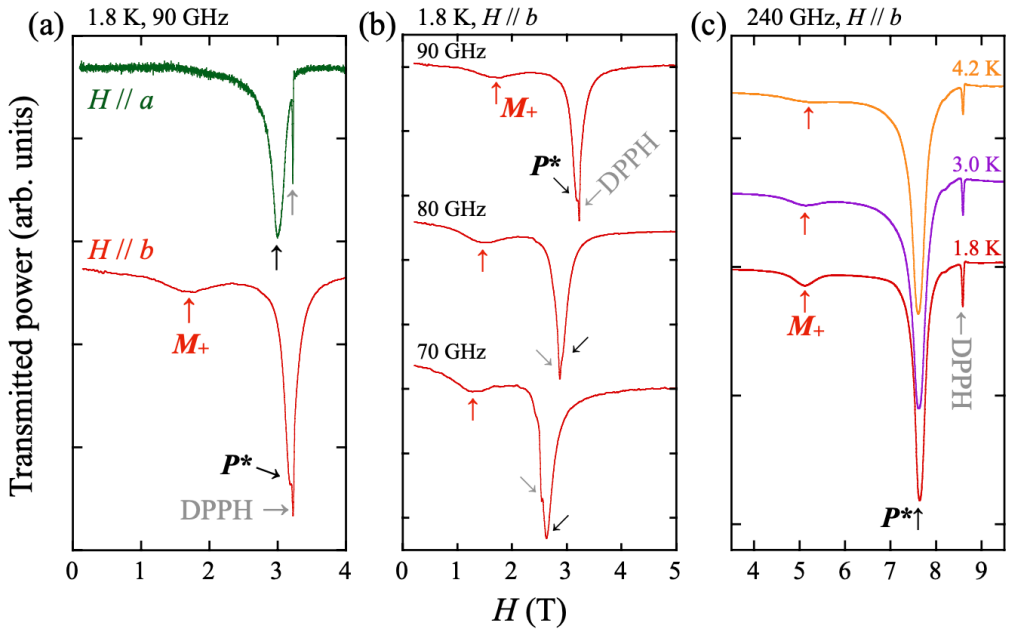

Figure 2. ESR spectra of $Na_2CuSO_4Cl_2$ at 1.8 K with a magnetic field applied along the a axis and b axis. The red arrows mark mode M_+. The black arrows mark the paramagnetic mode P^*. The narrow peaks marked by gray arrows are the mode DPPH. (b) ESR spectra for a magnetic field parallel to the DM vector ($H \parallel b$) for various frequencies. (c) Temperature evolution of the 240 GHz ESR spectra at $H \parallel b$.

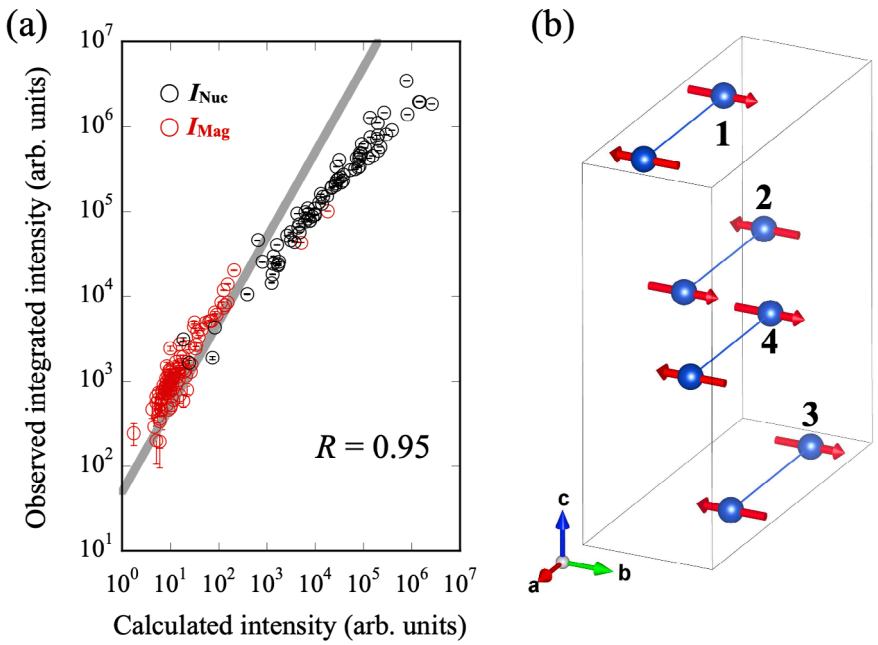

Figure 3. (a) Observed intensities of the nuclear and magnetic scattering plotted against the calculated values for the nuclear and magnetic peaks. The intensities of the magnetic scattering are calculated for the magnetic structure shown in (b). The solid gray line is a linear fit to the observed nuclear intensities below 1000 intensity units. The values in the plot show the obtained ordered moment and Pearson's correlation coefficient R. (b) Possible magnetic structure of $Na_2CuSO_4Cl_2$. The thick black lines show the magnetic unit cell. The Cu^{2+} positions are labeled 1 – 4 according to their positions $\mathbf{r}_1$ – $\mathbf{r}_4$.

energy arising from the crystal field because Cu^{2+} ions have a spin of 1/2, therefore, the specific spin structure in the magnetic ordered state is a result of the co-influence of the magnetic dipole interaction, symmetric anisotropic exchange interaction, and DM interaction (antisymmetric anisotropic exchange). Unfortunately, it is not possible to estimate the magnitude of these anisotropies from the present experimental results. The DM interaction mediates a spin-spin coupling of the form $\boldsymbol{D} \cdot (\boldsymbol{S}_1 \times \boldsymbol{S}_2)$, which is usually responsible for the helimagnetic spin arrangement in 1D spin chains. In contrast, a magnetic dipole interaction and symmetric anisotropic exchange interaction require the spins to point along a specific direction in the crystal, either parallel or antiparallel. The estimated *g* factors and magnetic structure of $Na_2CuSO_4Cl_2$ strongly suggest the presence of a magnetic dipole interaction and/or symmetric anisotropic exchange interaction. We consider that other terms in the anisotropic spin Hamiltonian counteract the effects of the DM interaction and stabilize the Néel-type structure in this system. In addition to $Na_2CuSO_4Cl_2$, $K_2CuSO_4X_2$ (X = Cl, Br) are candidates for DM-induced frustrated S = 1/2 quasi-1D antiferromagnets [6, 7]. The other anisotropy terms contribute to relieving the DM-induced frustration, which should also occur in $K_2CuSO_4X_2$. Both the DM and intrachain interactions depend on the orbital overlap in the chains and are proportional to each other. In addition, the other anisotropies depend on the crystal structure. The structural similarity between the chains in $Na_2CuSO_4Cl_2$ and $K_2CuSO_4X_2$ suggests that the ratio of these effects may be similar. We believe it is important to find a different model compound to study the intrinsic magnetism on the unique frustration induced by the DM interactions.

References

[1] M. Fujihala et al., Phys. Rev. B **101**, 024410 (2020).
[2] M. Fujihala et al., Phys. Rev. B **105**, 144410 (2022).
[3] T. Ohhara et al., J. Appl. Crystallogr. 49**,** 120 (2016).
[4] T. Ohhara et al., Nucl. Instrum. Methods Phys. Res., Sect. A **600**, 195 (2009).
[5] K. Y. Povarov et al., Phys. Rev. Lett. **107**, 037204 (2011).
[6] A. I. Smirnov, et al., Phys. Rev. B **92**, 134417 (2015).
[7] M. Hälgi et al., Phys. Rev. B **90**, 174413 (2014).

M. Fujihala[1,2], Y. Sakuma[1], S. Mitsuda[1], A. Nakao[3], K. Munakata[3], R. A. Mole[4], S. Yano[5], D. H. Yu[4], K. Takehana[6], Y. Imanaka[6], M. Akaki[7], S. Okubo[7], and H. Ohta[7]

[1]*Department of Physics, Tokyo University of Science;* [2]*Advanced Science Research Center, Japan Atomic Energy Agency;* [3]*Neutron Science and Technology Center, CROSS;* [4]*Australian Nuclear Science and Technology Organisation;* [5]*National Synchrotron Radiation Research Center;* [6]*National Institute for Materials Science;* [7]*Molecular Photoscience Research Center, Kobe University*

Zigzag Antiferromagnetic Order in the Kitaev Spin-liquid Candidate $RuBr_3$ with a Honeycomb Lattice

1. Introduction

A search for elementary excitations with the fractional quantum number has been one of the most intriguing topics in condensed matter physics. Recently, compounds with a honeycomb lattice have attracted attention due to a theoretical breakthrough [1, 2]. Kitaev has found that a spin liquid state is realized in a spin 1/2 honeycomb lattice magnet with bond-dependent ferromagnetic Ising interactions as an exactly solvable ground state [1].

To reveal the nature of the fractional excitations, the magnetic properties of candidate compounds have been investigated. Intensive studies have been made on α-$RuCl_3$. α-$RuCl_3$ exhibits a zigzag antiferromagnetic order at 8-14 K [3-5]. Earlier works, including inelastic neutron scattering experiments, have revealed that most of the spin excitations are left even above the transition temperature [6, 7], indicating that ferromagnetic Kitaev interactions dominate the magnetism in this compound.

On the other hand, the presence of the zigzag antiferromagnetic order also suggests the sizable contributions of non-Kitaev interactions [8, 9]. Thus, it has been desired to suppress these magnetic interactions to tune the system closer to the Kitaev limit. One of the promising ways is to replace ligands of candidate compounds. We have discovered new polymorphs of RuX_3 (X = Br [10], I [11]) by high pressure synthesis, and found that Ru^{3+} forms the honeycomb structure in these compounds. To reveal the substitution effect in the Ru^{3+} based honeycomb compounds, we have investigated the crystal and magnetic structures of $RuBr_3$ with the honeycomb structure [10].

2. Experiments

The polycrystalline sample was prepared by high pressure synthesis starting from $RuBr_3$ with the chain structure ($P6_3/mcm$). Powder neutron diffraction experiments were performed using the high-resolution time-of flight (TOF) neutron powder diffractometer SuperHRPD installed at the beam line BL08 of J-PARC [12]. The total amount of 1.4 g of the polycrystalline sample was sealed in a vanadium-nickel cylindrical can and then set to the ^{4}He closed-cycle refrigerator. SuperHRPD has three sets of detector banks: backscattering (BS), quarter-angle (QA) and low-angle (LA) detector banks. All the three diffraction patterns were simultaneously used with the same weighting in the crystal-structure refinement, while the diffraction patterns from QA and LA detector banks with the *d*-range larger than 2.9 Å were used for the magnetic-structure refinement.

3. Crystal and magnetic structures

The neutron diffraction pattern revealed that the polymorph of $RuBr_3$ is the same as that of the BiI_3 structure, which crystallizes in space group of *R*-3. The neutron powder diffraction pattern at room temperature is shown in Fig. 1. All the peak positions and intensities are well fitted by the BiI_3 structure. The BiI_3 structure is also referred to as one of the low-temperature structures of α-$RuCl_3$ [5]. The crystal structure refined from the neutron diffraction pattern is shown in Fig. 2(e). The Br atoms form the hexagonal closed-packed structure. Ru atoms occupy two-thirds of the vacancies for every two Br layers, resulting in the regular honeycomb lattice. The powder diffraction patterns collected at low

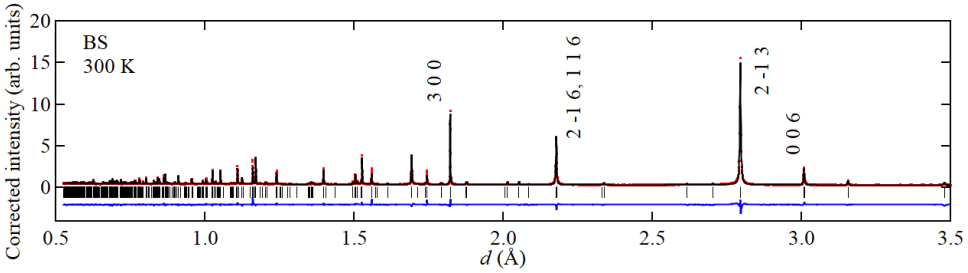

Figure 1. Neutron diffraction pattern collected at 300 K by the backscattering (BS) bank. The red dots, black curve, and blue curve represent the observed intensities, calculated intensities, and the difference between them. The difference is shifted for clarity. The vertical black bars indicate the peak position expected from the space group *R*-3.

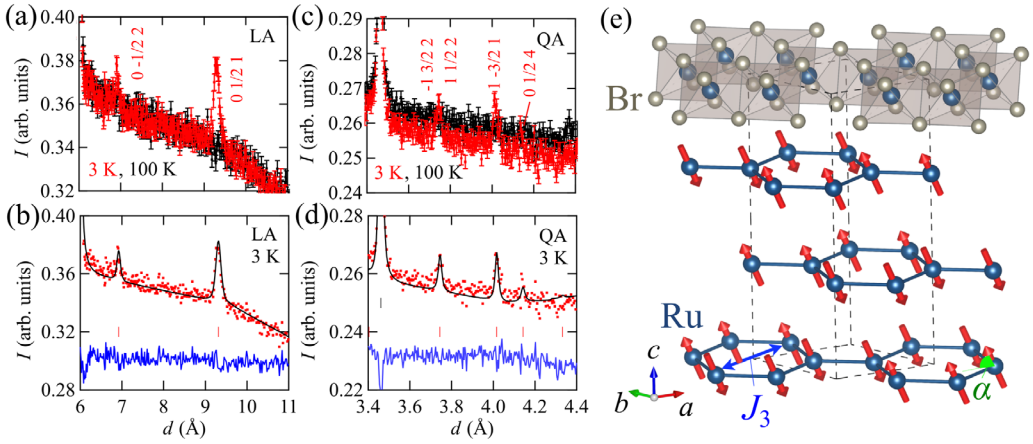

Figure 2. (a-d) Neutron diffraction patterns focused on the magnetic reflections. Intensities at 3 (red dots) and 100 K (black dots) are compared in (a, c), while the observed intensities (red dots) are plotted with calculated intensities (black curves) and the difference between them (blue curves, shifted for clarity) in (b, d). The vertical red bars indicate the peak position expected from zigzag antiferromagnetic order. Corresponding indexes of magnetic reflections are shown in (a, c). (e) Schematic view of crystal and magnetic structures refined from the neutron diffraction pattern.

temperatures indicate that the BiI_3 structure is preserved down to low temperatures.

The magnetic structure is solved from five peaks observed below T_N = 34 K. The neutron diffraction patterns collected at the LA and QA detector banks are shown in Fig. 2(a) and 2(c), respectively. Candidates for initial magnetic structures were obtained using the magnetic representation theory [13]. The magnetic representations for the Ru moments are decomposed into two one-dimensional representations of the *k*-group with the magnetic modulation vector of (0, 1/2, 1). The one representation corresponding to a zigzag antiferromagnetic structure well reproduces the intensities, as shown in Fig. 2(b) and 2(d). The magnetic structure determined from the refinement is given in Fig. 2(e). The magnetic moment is canted from the *ab*-plane for 64(12) degrees. The magnitude of the magnetic moment is estimated as 0.74(12) μ_B, which is comparable to or larger than that for α-$RuCl_3$ [3-5].

4. Discussions

The magnetic structure is characterized by the canting angle of 64 degrees, which is much larger than 32-48 degrees in $RuCl_3$ [4, 5, 14]. From theoretical viewpoints, this suggests that the non-Kitaev interactions are much weaker than the Kitaev interactions for the nearest neighbors [8, 9]. In addition, the Weiss temperature of -58 K and the T_N higher than $RuCl_3$ suggests that the third nearest neighbor interactions J_3 (see Fig. 2(e)) are enhanced. These results indicate that tuning of the Kitaev and non-Kitaev interactions can be accomplished by replacing the ligand sites, providing another route for exploring Kitaev spin liquids.

References

[1] A. Kitaev, Ann. Phys. **321**, 2 (2006).
[2] G. Jackeli and G. Khaliullin, Phys. Rev. Lett. **102**, 017205 (2009).
[3] R. D. Johnson et al., Phys. Rev. B **92**, 235119 (2015).
[4] H. B. Cao et al., Phys. Rev. B **93**, 134423 (2016).
[5] S.-Y. Park et al., cond-mat arXiv 1609.05690v1. (2016).
[6] A. Banerjee et al., Nat. Mater. **15**, 733, (2016).
[7] S. -H. Do et al., Nat. Phys. **13**, 1079 (2017).
[8] J. G. Rau et al., Phys. Rev. Lett. **112**, 077204 (2014).
[9] J. Chaloupka and G. Khaliullin, Phys. Rev. B **92**, 024413 (2015).
[10] Y. Imai et al., Phys. Rev. B **105**, L041112 (2022).
[11] K. Nawa et al., J. Phys. Soc. Jpn. **90**, 123703 (2021).
[12] S. Torii et al., J. Phys. Soc. Jpn. **80**, SB020 (2011).
[13] Y. Izyumov and V. Naish, J. Magn. Magn. Mater. **12**, 239 (1979).
[14] J. A. Sears et al., Nat. Phys. **16**, 837 (2020).

Y. Imai[1], K. Nawa[2], Y. Shimizu[3], W. Yamada[1], H. Fujihara[1], T. Aoyama[1], R. Takahashi[2], D. Okuyama[2], T. Ohashi[3], M. Hagihala[4], S. Torii[4], D. Morikawa[2], M. Terauchi[2], T. Kawamata[5], M. Kato[5], H. Gotou[6], M. Itoh[3], T. J Sato[2], and K. Ohgushi[1]

[1]*Department of Physics, Graduate School of Science, Tohoku University;* [2]*Institute of Multidisciplinary Research for Advanced Materials, Tohoku University;* [3]*Department of Physics, Nagoya University;* [4]*Institute of Materials Structure Science, KEK;* [5]*Department of Applied Physics, Graduate School of Engineering, Tohoku University;* [6]*Institute for Solid State Physics, University of Tokyo*

Square and Rhombic Lattice States of Magnetic Skyrmions in a Centrosymmetric Magnet $EuAl_4$

1. Introduction

Recently, topological objects in condensed matters have attracted significant attention as the source of rich emergent phenomena and functions. One typical example is the magnetic skyrmion with swirling spin texture, which is characterized by topologically-stable particle-like nature and now intensively studied as the potential candidate for high-density information carrier.

Magnetic skyrmions were originally observed in a series of noncentrosymmetric magnets, where a competition between the Dzyaloshinskii-Moriya and ferromagnetic exchange interactions stabilizes a triangular skyrmion lattice (SkL). On the other hand, the SkL states were also recently discovered in centrosymmetric compounds, in which extremely small diameter (less than 5 nm) of skyrmions are commonly realized [1–3]. For such systems, a distinct skyrmion formation mechanism mediated by itinerant electrons has been proposed. So far, only few centrosymmetric magnets hosting skyrmions are known, and further search of skyrmion-hosting materials is highly desired.

As an ideal candidate material, we focus on a centrosymmetric tetragonal magnet $EuAl_4$, in which the magnetism is governed by the Eu^{2+} ions. This compound undergoes multiple-step magnetic transitions before reaching the forced ferromagnetic (FM) state for the external magnetic field H || [001]. As seen in the H-T (temperature) magnetic phase diagram (Fig. 1(a)), four distinctive magnetic phases (I, II, III, and IV) are identified at lower temperatures. Although a preceding neutron scattering study revealed incommensurate magnetic orders at zero field [4], the magnetic structure for each phase in the magnetic fields has not been experimentally identified. Here, we successfully observed square and rhombic lattice states of nanometric skyrmions in $EuAl_4$ by performing small-angle neutron scattering (SANS) experiments [5].

2. Experiments

SANS measurements were carried out at BL15 (TAIKAN) in Materials and Life Science Experimental Facility of J-PARC. A thin crystal with a thickness of 0.2 mm having the widest surface of 5 mm by 2.5 mm parallel to the (001) plane was installed in a cryostat equipped with a horizontal-field superconducting magnet. An incident neutron beam with a wavelength band of 0.7-7.7 Å was exposed on the sample. The incident beam was always directed along the [001] axis within the accuracy of 2 degrees. The SANS patterns were obtained with rotating and tilting the sample up to 2 degrees. Background data were obtained above T_c in a magnetic field of 0.05 T and subtracted from the data obtained at low temperature to leave only the magnetic signal.

In polarized SANS experiments, a polarized incident neutron beam was obtained by a supermirror polarizer. The neutron spin polarization at the sample position was controlled to be parallel to the [001] axis of the sample by guide fields and the horizontal-field superconducting magnet. A supermirror spin analyzer was set between the sample and the detectors and was used to separate the spin-flip (SF) and non-spin-flip (NSF) scattering signals. The total beam polarization measured using a direct beam was 0.85 for the neutrons with wavelengths longer than 3.5 Å. The mixing of the SF and NSF signals was corrected considering the total beam polarization.

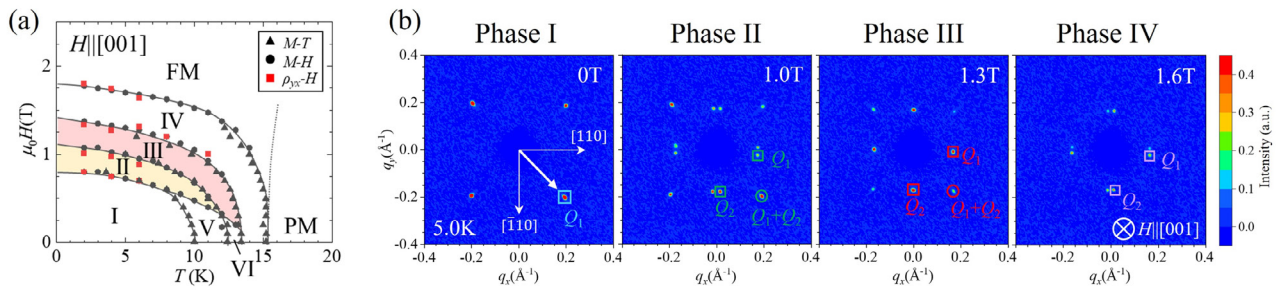

Figure 1. (a) H(magnetic field)-T(temperature) magnetic phase diagram of $EuAl_4$ for H || [001]. (b) Typical SANS patterns for phases I-IV taken at 5 K for H || [001].

3. Results and discussion

First, to identify the magnetic modulation vector in each phase, we performed SANS experiments for the (001) plane at 5.0 K in $H \parallel [001]$. Figure 1(b) exhibits the typical SANS patterns for phases I-IV, revealing multiple-step reorientations of the fundamental magnetic modulation vector $\boldsymbol{Q}_1$ as a function of H. Here, the observed $\boldsymbol{Q}_1$ is always incommensurate in phases I-IV, and the modulation period is 2.2 nm for phase I and 3.5 nm for phases II-IV. Notably, we also identified the clear $\boldsymbol{Q}_1+\boldsymbol{Q}_2$ reflections in phases II, III, and IV, proving that these phases are double-Q states.

Next, to investigate the detailed spin orientations in each phase, we carried out polarized SANS experiment for $H \parallel [001]$ and measured the intensities of SF and NSF scattering (I_{SF} and I_{NSF}, respectively) separately for various temperatures at 1 T. In phases II and III, magnetic reflections are observed for both I_{SF} and I_{NSF} channels, proving that the modulated spin component possesses both in-plane and out-of-plane components normal to $\boldsymbol{Q}$. This suggests that phases II and III are characterized by the screw-type spin modulation. In phase IV, however, the magnetic scattering appears only in the I_{SF} channel, indicating that only the in-plane component normal to $\boldsymbol{Q}$ exists. Thus, phase IV can be characterized by the in-plane sinusoidal spin modulation. By considering the double-Q nature of phases II-IV, the resultant spin textures for each phase are illustrated as shown in Fig. 2, indicating the rhombic and square lattices of magnetic skyrmions with a diameter of 3.5 nm for phases II and III, respectively, and the rhombic vortex lattice for phase IV.

4. Summary

In this work, the centrosymmetric tetragonal magnet $EuAl_4$ turns out to host square and rhombic lattice states of nanometric skyrmions by means of SANS experiments. Unlike previously reported skyrmion-hosting materials, $EuAl_4$ shows two distinctive topological magnetic phases with multiple-step reorientation of fundamental magnetic modulation vector Q as a function of the magnetic field, which probably reflects the delicate balance of itinerant-electron-mediated interactions. The present results demonstrate that rare-earth intermetallics with delicate balance of magnetic interactions can be a promising platform to realize the competition of multiple topological magnetic phases in a single compound, which would be a good guideline for further search of exotic materials with emergent functional responses.

References

[1] T. Kurumaji et al., Science **365**, 914 (2019).
[2] M. Hirschberger et al., Nature Commun. **10**, 5831 (2019).
[3] N.D. Khanh et al., Nat. Nanotech. **15**, 444 (2020).
[4] K. Kaneko et al., J. Phys. Soc. Jpn. **90**, 064704 (2021).
[5] R. Takagi et al., Nature Commun., **13** 1472 (2022).

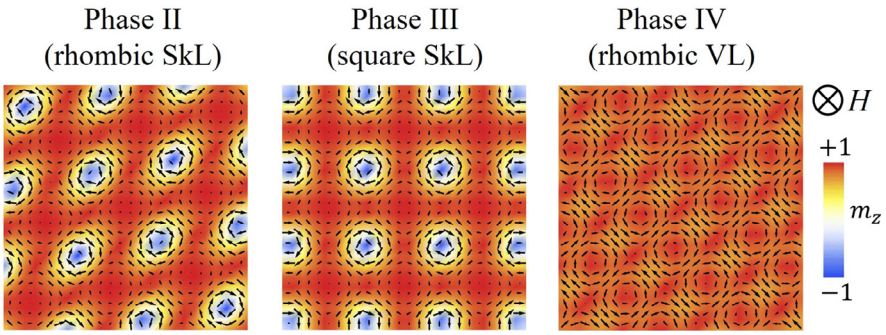

Figure 2. Schematic illustrations of spin textures for phases II, III, and IV, corresponding to the rhombic skyrmion lattice (SkL), square SkL, and rhombic vortex lattice (VL).

R. Takagi[1,2,3,4], N. Matsuyama[1], V. Ukleev[5], L. Yu[5,6,7], J.S. White[5], S. Francoual[8], J.R.L. Mardegan[8], S. Hayami[1,3], H. Saito[9], K. Kaneko[10,11], K. Ohishi[12], Y. Ōnuki[4], T. Arima[4,13], Y. Tokura[1,4,14], T. Nakajima[4,9], and S. Seki[1,2,3,4]

[1]Department of Applied Physics, University of Tokyo; [2]Institute of Engineering Innovation, University of Tokyo; [3]PRESTO, JST; [4]RIKEN Center for Emergent Matter Science (CEMS); [5]Laboratory for Neutron Scattering and Imaging (LNS), Paul Scherrer Institute (PSI); [6]Institute of Physics, École Polytechnique Fédérale de Lausanne (EPFL); [7]Institute of Materials, EPFL; [8]Deutsches Elektronen-Synchrotron DESY; [9]Institute for Solid State Physics, University of Tokyo; [10]Materials Sciences Research Center, JAEA; [11]J-PARC Center, JAEA; [12]Neutron Science and Technology Center, CROSS; [13]Department of Advanced Materials Science, University of Tokyo; [14]Tokyo College, University of Tokyo

Evolution of Magnetism and Superconductivity Toward the Quantum Critical Point in the Heavy Fermion System

1. Introduction

Quantum critical phenomena are one of the central issues in condensed matter physics. In the vicinity of the quantum critical point (QCP) where two different interactions compete at $T = 0$, the quantum fluctuation plays a major role to realize unconventional superconductivity as well as other exotic ground states [1-3]. This could be observed when the phase transition occurs at $T = 0$ by tuning parameters rather than temperature, such as magnetic field, pressure, and chemical substitutions. For instance, in a heavy fermion system, magnetic Ruderman-Kittel-Kasuya-Yosida (RKKY) interaction conflicts with the non-magnetic Kondo effect and the Fermi liquid, which is a basic concept of interacting fermions, often fails. Such a "non-Fermi liquid" (NFL) state is observed in thermodynamic and transport quantities. For thermodynamic properties, $-\ln T$ or T^{-n} ($n < 1$) increase toward $T = 0$ is a hallmark of the NFL and is often observed in strongly correlated electron systems.

Furthermore, unconventional superconductivity often appears in a region of the phase diagram enclosed by a dome-shaped boundary near QCP. The properties of the system in the superconducting (SC) dome are dominated by quantum criticality, and the mechanism of the superconductivity is strongly related to the quantum critical spin fluctuations in many cases. However, it is challenging to reveal the spin state in the SC dome in which the strong impact of quantum critical fluctuations must be turned up. Moreover, in most cases, the quantum phase transitions are identified experimentally as first-order phase transition.

As an example of the quantum critical compounds showing superconductivity, tetragonal $CeCoIn_5$ is one of the extensively investigated heavy fermion compounds which is believed to show dx^2-y^2 superconductivity at ambient pressure ($T_c = 2.3$ K at $B = 0$) [5, 6]. $CeCoIn_5$ shows the NFL behaviors in various quantities just above the SC upper critical field H_{c2}(= 5 T//c), such as $-\ln T$ divergence in the specific heat divided by the temperature and T-linear dependence in electrical resistivity[7], suggesting that the magnetic field could induce quantum critical fluctuation[8].

It is known that chemical substitution could induce a magnetic phase transition. Recently, the coexistence of superconductivity and magnetic ordering was also suggested in Zn substitution system $CeCo(In_{1-x}Zn_x)_5$ [9-11]. By substitution of In with a tiny amount of Zn, a small modification in the system, corresponding to an energy scale in the order of a few Kelvin, occurs without any structural phase transition, and it is possible to tune only magnetism and superconductivity. In this regard, $CeCo(In_{1-x}Zn_x)_5$ is one of the ideal systems to investigate the role of magnetic quantum criticality in the evolution of the superconductivity. In $CeCo(In_{1-x}Zn_x)_5$, the SC transition temperature T_c is continuously reduced from 2.3 K (x = 0) to ~1.4 K (x = 0.07) by doping Zn, and then the AFM order, with a transition temperature of $T_N \sim 2.2$ K, is found for x larger than 0.05 at $B = 0$. However, in the doping range where $x < 0.05$, T_N becomes smaller than T_C, yielding that a significant response due to superconductivity masks weak signal of AFM state and its quantum critical fluctuation in the SC dome. This situation has also been observed in many quantum critical superconductors; it is unclear whether the quantum phase transition and its fluctuations exist even deeper inside the SC phase.

To reveal the possible weak magnetism and quantum criticality both inside and outside the SC dome in $CeCo(In_{1-x}Zn_x)_5$, we employed the muon spin rotation/relaxation technique [12].

2. Experimental

All muon experiments were performed at the D1 spectrometer, Materials and Life Science Facility, J-PARC, Tokai, Japan. We used 4 MeV positively charged muons. Conventional μSR in the dilution refrigerator was carried out. Plate-shaped single crystals of $CeCo(In_{1-x}Zn_x)_5$, whose basal planes are perpendicular to the tetragonal c-axis, were grown by the indium-flux method [9].

3. Results and Discussions

Figure 1(a, b) shows the temperature dependence of the muon spin relaxation spectra under zero-magnetic field (ZF-μSR) in $CeCo(In_{1-x}Zn_x)_5$(x = 0.0, 0.03). At $x \leq 0.025$, muon spins depolarize only because of the nuclear magnetic fields. This result strongly suggests non-magnetic ground states for $x \leq 0.025$. In contrast, at x = 0.03, a tiny change was observed in the spectra at low temperatures and $B = 0$ as shown in Fig. 1(b), demonstrating the presence of a very weak magnetically ordered state in the SC dome. This slow muon spin relaxation is easily quenched by applying weak magnetic

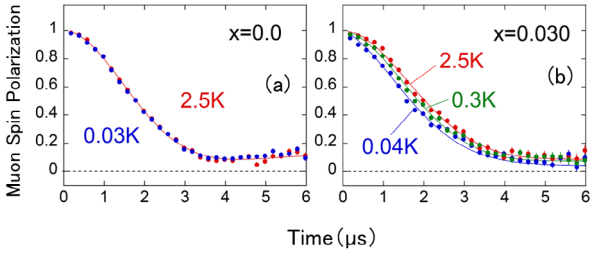

Figure 1. ZF-μSR spectra in $CeCo(In_{1-x}Zn_x)_5$ (a) x = 0.0, (b) x = 0.03.

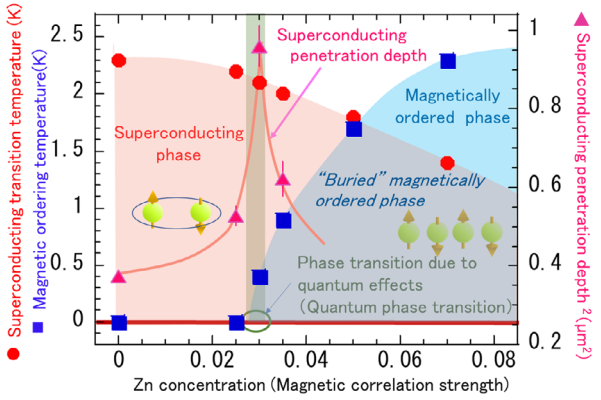

Figure 2. x-*T* phase diagram of magnetically ordered temperature (■) and superconducting transition temperature (●) and superconducting penetration depth (▲) [12].

field along initial muon spin polarization direction, indicating that the internal magnetic field at the muon site is static or quasistatic.

A more pronounced signature of the coupling between the QCP and the SC state appears in the magnetic penetration depth. The magnetic penetration depth characterizes the superconducting properties, because it is related to the superfluid weight. The superfluid weight may be an indicator of QCP, since it is determined by microscopic aspects of electronic states. To measure the penetration depth using μSR, a magnetic field was applied along the *c*-axis or *ab*-plane.

In Fig. 2, we summarize the x-*T* phase diagram of magnetism and superconductivity from the present μSR experiments, along with the AFM and SC transition temperatures for x = 0.07 estimated by the experiments of the neutron scattering and the specific heat [10]. Since magnetic ordering also appears in the SC phase of x ≥ 0.03, we plotted the x dependence of the penetration depth at 1.0 K (pure SC phase). It was found that a magnetically ordered state develops at x ≥ 0.03, coexisting with the superconductivity. The magnitude of the ordered magnetic moment is continuously reduced with decreasing x, and it disappears below x ~ 0.03, indicating a second-order phase transition and the presence of the QCP at this critical Zn concentration. Furthermore, the magnetic penetration depth diverges toward the QCP. These facts provide evidence for the intimate coupling between quantum criticality and Cooper pairing [12].

References

[1] J. A. Hertz, Phys. Rev. B **14**, 1165-1184 (1976).
[2] H. Löhneysen *et al.*, Rev. Mod. Phys. **79**, 1015-1075 (2007).
[3] P. Gegenwart, Q. Si, F. Steglich, Nat. Phys.**4**, 186 (2008).
[4] G.R. Stewart, Rev. Mod. Phys. **73**, 797 (2001).
[5] C. Petrovic *et al.*, J. Phys.: Cond. Mat. **13**, L337 (2001).
[6] K. An *et al.*, Phys. Rev. Lett. **104** 037002 (2010).
[7] J. Paglione *et al.*,Phys. Rev. Lett. **91**, 246405 (2003).
[8] A. Bianchi *et al.*, Phys. Rev. Lett. *91*, 257001 (2003).
[9] M. Yokoyama *et al.*,J. Phys. Soc. Jpn. **83**, 033706 (2014).
[10] M. Yokoyama *et al.*, Phys. Rev. B **92**, 184509 (2015).
[11] M. Yokoyama *et al.*,Phys. Rev. B **105**, 054515 (2022).
[12] W. Higemoto, M.Yokoyama *et al.*, PNAS **119**, e2209549119 (2022).

W. Higemoto[1,2,3], M. Yokoyama[4], T. U. Ito[1,2], T. Suzuki[1,3], S. Raymond[5], and Y. Yanase[6,7]
[1]*Advanced Science Research Center, Japan Atomic Energy Agency;* [2]*Muon Science Section, Materials and Life Science Division, J-PARC Center;* [3]*Department of Physics, Tokyo Institute of Technology;* [4]*Department of Physics, Ibaraki University;* [5]*Universite Grenoble Alpes;* [6]*Department of Physics, Kyoto University;* [7]*Institute for Molecular Science*

Ambipolarity of Dilute Hydrogen in Power Semiconductor β-Ga_2O_3 Revealed by μSR

1. Introduction

Power semiconductors are used in a variety of electronic devices as key components for voltage conversion and AC to DC conversion. Gallium oxide is now being studied as a candidate material for next-generation power semi-conductors. Because of its characteristics, gallium oxide is expected to have higher breakdown voltage and lower power consumption than silicon, which is currently the main material used. In order to precisely control electrical properties such as carrier density, it is necessary to understand the main factors affecting electrical properties (impurities, oxygen and gallium defects, etc.) and to investigate in detail their relationship with synthesis and device fabrication methods.

Hydrogen (H) is a ubiquitous impurity in materials. Since the discovery that H in silicon has a significant effect on its electrical properties, H has attracted considerable attention in the field of functional materials, including various semiconductor and solar cell materials. Theoretical studies on gallium oxide also indicate that H can contribute to *n*-type conduction. However, experimental knowledge has been very limited due to the lack of methods to study trace amounts of H.

To clarify the electronic structure of muons as pseudo-H, muon spin rotation / relaxation (μSR) experiments were performed on β-Ga_2O_3, the most stable structure among gallium oxides [2]. Hereafter, we introduce the elemental symbol Mu to denote muon as pseudo-H. Conventional μSR measurements were performed using the ARTEMIS spectrometer installed in the S1 area at the MLF, J-PARC. The high-intensity muon beam enabled us to observe the time evolution of the muon spin polarization $G_z(t)$ up to ~25 μs.

2. Results and discussion

The normalized and background-subtracted μSR time spectra at 300 K are shown in Fig. 1(a). The zero field (ZF) spectrum clearly consists of two components, one exhibiting slow Gaussian relaxation with partially recovered at $t \gtrsim 12$ μs (Mu_1) and the other exhibiting no relaxation at all (Mu_2). The recovery of $G_z(t)$ at a later time is a characteristic behavior of the Kubo-Toyabe function at ZF:

$$G_z^{\mathrm{KT}}(t;\Delta,B_{\mathrm{LF}}=0) \equiv \frac{1}{3}+\frac{2}{3}(1-\Delta^2t^2)\exp(-\Delta^2t^2),$$

where Δ is the linewidth determined by random local fields from nuclear magnetic moments of Ga, B_{LF} is the magnitude of longitudinal field (LF).

ZF and LF spectra at 300 K were analyzed by global curve fit using the following function:

$$G_z(t) = f_1 G_z^{\mathrm{KT}}(t;\Delta,B_{\mathrm{LF}}) + f_2\,,$$

where f_i (i = 1, 2 and $f_1 + f_2 = 1$) are the relative yields of the Mu_i components. As shown by solid lines in Fig. 1(a), $\Delta = 0.140(1)$ μs^{-1} and $f_1 = 0.433(3)$ well reproduce the experimental data. Comparison of Δ with the predicted Δ at several candidate Mu as pseudo-H sites, as evaluated

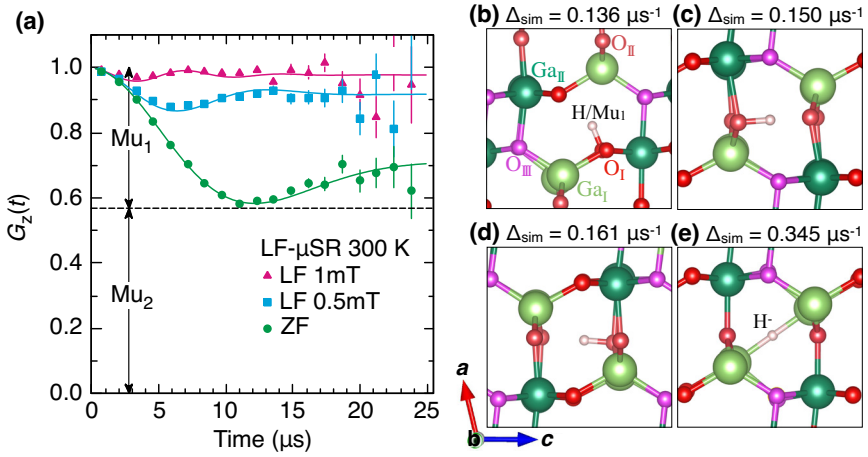

Figure 1. (a) μSR time spectra for single crystalline β-Ga_2O_3 at 300 K. 4×10^8 positron events were collected for ZF and 2×10^8 for LF spectra. (b–e) Local structures H-related defects and predictions of the linewidth Δ corresponding to (b) H_I, (b) H_{II}, (c) H_{III}, and (d) H^- state. $H_{I–III}$ are bonded to O as H^+, while H^- forms bonding with two Ga^{3+} ions.

by first-principles density-functional theory (DFT) calculations, shows good agreement with the structure shown in Fig. 1(b). As described earlier, this interstitial H has been reported to act as a donor [1], indicating that it also corresponds electronically to Mu_1 in the dilute limit (~10^5 cm^{-3}).

Meanwhile, the rapid motion of Mu_2 is inferred from the fact the absence of interstitial sites free of local magnetic fields from Ga nuclear magnetic moments (with 100% natural abundance), which is only compatible with the situation where the relaxation due to the local field is suppressed by the motional averaging.

Various instances of experimental evidence indicate that muons injected as ion beams are in a metastable state. The recently established ambipolar model assumes ambipolarity in the sense that muons can be in the donor and acceptor states simultaneously as such metastable states (relaxed-excited states) [3]. Specifically, we assume that the two relaxed-excited states correspond to the donor level ($E^{+/0}$), and the acceptor level ($E^{0/-}$) in Fig. 2(a). We further assume that which charged state each takes is determined by the band structure and the relationship between $E^{+/0}$ and $E^{0/-}$ in the material. The present experimental results are in good agreement with this model, since $E^{+/0}$ is in the conduction band (CB), the corresponding H (or Mu) is always ionized [H → H^+ + e^-, see Fig. 2(b)] to provide electrons, causing unintended *n*-type conduction. Furthermore, $E^{0/-}$ is located close to the CB but on the lower energy side [left side of the Fig. 2(a)] than the charge neutral level E_F^{int}, suggesting that the state corresponding to $E^{0/-}$ can actually act as an acceptor and exchange electrons with the CB. Considering this and the fact that the acceptor-like neutral state Mu^0 in various materials has been reported to exhibit fast diffusion, the Mu_2 state exhibits fast diffusion motion through the neutral state due to the charge exchange reaction with conduction electron (Mu^- ⇆ Mu^0 + e^-), as shown in Fig. 2(b). This Mu_2 state has been overlooked in previous studies because of its indistinguishability from background components [4] and was revealed for the first time using the high-intensity muon beam at the J-PARC MLF.

The findings revealed in this study are expected to provide new guidelines for the development for downsizing and performance enhancement of devices.

References

[1] H. Li and J. Rovertson, J. Appl. Phys., **115**, 203708 (2014).
[2] M. Hiraishi, et al., Phys. Rev. B, **107**, L041201 (2023).
[3] M. Hiraishi, et al., J. Appl. Phys., **132**, 105701 (2022).
[4] P. D. C. King, et al., Appl. Phys. Lett., **96**, 062110 (2010).

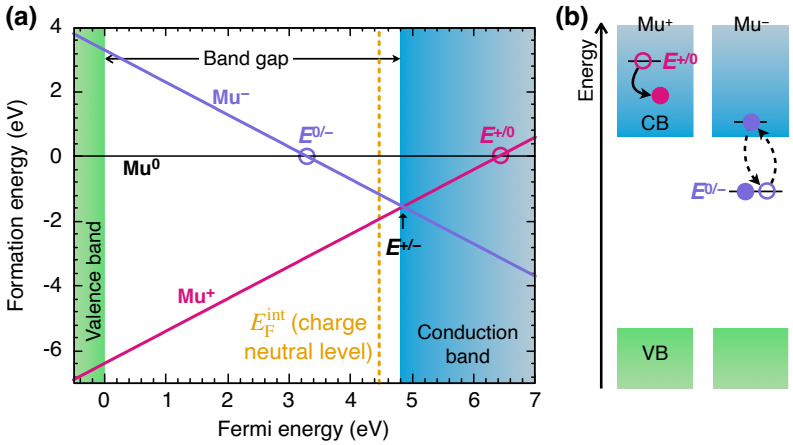

Figure 2. (a) The relationship between the formation energy of Mu^q ($q = 0, \pm1$) and the Fermi energy in β-Ga_2O_3 [1], where the symbols $E^{+/0}$, $E^{0/-}$, and $E^{+/-}$ correspond to mutual intersection points among each formation energy of the charged states. (b) Schematic diagram of the band structure corre-sponding to the donor ($Mu^+ = Mu_1$) and acceptor ($Mu^- = Mu_2$) levels.

M. Hiraishi[1,2], H. Okabe[1,3], A. Koda[1,4], R. Kadono[1,4], T. Ohsawa[5], N. Ohashi[5], K. Ide[6], and T. Kamiya[6,7]

[1]Muon Science Section, Materials and Life Science Division, J-PARC Center; [2]Graduate School of Science and Engineering, Ibaraki University; [3]Institute for Materials Research, Tohoku University (IMR); [4]Department of Materials Structure Science, The Graduate University for Advanced Studies (Sokendai); [5]National Institute for Materials Science (NIMS); [6]Materials and Structures Laboratory, Tokyo Institute of Technology; [7]Materials Research Center for Element Strategy, Tokyo Institute of Technology (MCES)

Determination of Light Element Composition for Asteroid Ryugu Using Muon Beam

1. Introduction

What was the early solar system like, and why did life emerge on Earth? The composition of the solid material in the solar system is one element of the fundamental and essential data to solve these big mysteries. Many pieces of information related to this issue have previously been obtained from meteorites: meteorites classified as CI have been thought as the most primordial materials we have been able to obtain so far. However, it was not known whether these meteorites were truly primordial and free from terrestrial contamination.

The Hayabusa2 project aimed to bring solid material from C-type asteroid Ryugu directly back to Earth that is expected to have kept information about the early state of the solar system. In 2014, the Hayabusa2 spacecraft was launched from Earth and after its arrival at asteroid Ryugu in 2018, two sample collection operations were successfully completed. In 2020, the Hayabusa2 provided 5.4 g of Ryugu material to Earth. As an initial analysis, various studies of Ryugu samples have been conducted [1-8].

The returned samples from Ryugu are precious. Therefore, although the sample heterogeneity is expected, it is impractical to use large amount samples for destructive analysis that is commonly applied for quantification of light elements, such as C, N and O. To solve this problem, we applied a non-destructive elemental analysis method to the Ryugu samples using muon beams [1, 9].

Our research group has been developing the muon elemental analysis method at J-PARC for the last 15 years and applying this method for various sample analyses [10-14]. This method is based on the measurement of characteristic muonic X-rays emitted after muon stop in the sample having 200 times larger energies compared to fluorescent X-ray energies. High energy muonic X-rays enable us to quantify the light elements even if these exist inside the material.

2. Experimental

The muon experiment was conducted at the D2 experimental area in the MUon Science Establishment (MUSE) of J-PARC MLF [15]. To analyze Ryugu samples, a dedicated experimental setup was developed, as shown in Fig. 1 [16] that can handle the sample and conduct muon irradiation under the helium atmosphere conditions. That is, the sample is completely free from the contamination by terrestrial materials during muon irradiation, and the analyzed samples can be applied to other analyzes involving destructive methods. This setup allowed us to use large amount of samples (123 mg in total) for muon analysis that allowed us to reduce the effects of sample heterogeneity. During the muon experiment, the momentum of the muon was tuned at 29.2 MeV/c and the duration of muon irradiation was 116 hours. To obtain calibration data for quantitative analysis, we also performed muon irradiation for 4 carbonaceous meteorites (Orgueil, Murray, Yamato980115 and Tagish Lake).

3. Results and discussion

Figure. 2 shows a muonic X-ray spectrum for the Ryugu sample. X-rays originated muon captures on C, N, O, Na, Mg, Si, S, Fe, and Ni atoms were clearly observed, that is, the main components of the Ryugu sample were identified as these elements. X-rays from muonic Be and Cu were derived from the muon stop by measuring system. The quantitative analysis was conducted using calibration data obtained from three meteorite samples of Murray, Yamato980115 and Tagish Lake. The elemental compositions of these meteorites were determined by energy dispersive X-ray spectroscopy equipped in scanning electron microscope, prompt gamma-ray analysis by neutron activation and elemental analysis by combustion. A linear relationship between the elemental composition and intensity of muonic X-ray for each element, and using the calibration data, the elemental composition of the Ryugu sample was determined from muonic X-ray intensity.

The elemental composition of Ryugu was similar to

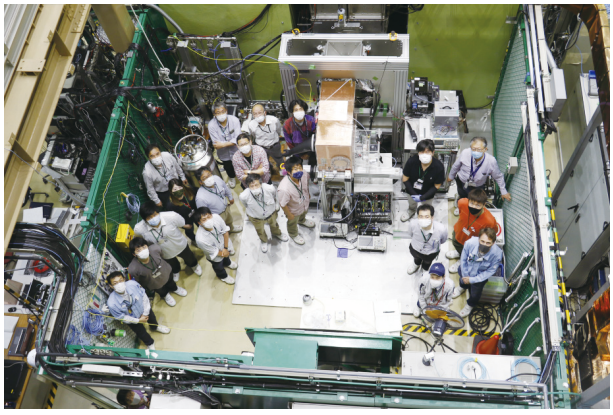

Figure 1. Photo of the experimental group's members and the muon analysis system for the Ryugu sample.

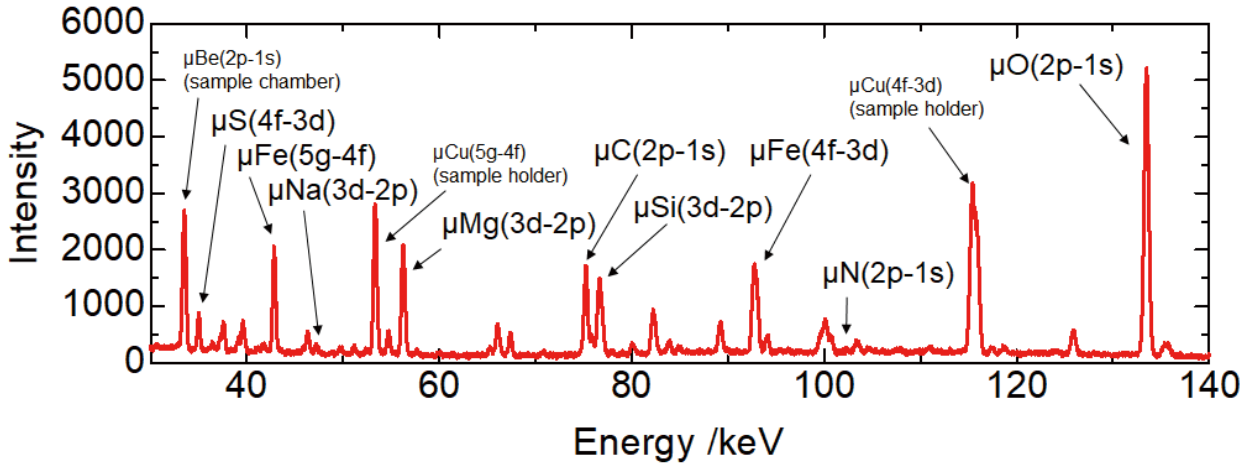

Figure 2. Muonic X-ray spectrum obtained from the Ryugu sample with major peak assignments.

that of CI (carbonaceous meteorite of Orgueil), which was thought to be the most primordial material in the solar system. This shows that Ryugu is one of the representative materials of solid matter in the solar system. On the other hand, a clear difference in oxygen concentration between Ryugu and Orgueil was found; the oxygen concentration of Ryugu was 25% lower than that of Orgueil. One possible reason of such difference is derived from the alteration of Orgueil by water and oxygen in the atmosphere. In fact, it has been reported that the abundance of Fe^{2+} is higher in Ryugu than in Orgueil, which indicates that Fe^{2+} in Orgueil was oxidized to Fe^{3+} immediately after it fell to Earth [1]. The elemental composition determined by muon analysis method was in good agreement with these determined by other destructive analysis methods [2, 7, 8].

We concluded that the most predominant and completely unaltered solid material in the solar system was obtained by the Hayabusa2 project. In the future, the results of the analysis of the Ryugu sample, including muon analysis method, may replace the result of CI as the canonical elemental composition for solid materials in the solar system.

References

[1] T. Nakamura et al., Science, **379**, eabn8671 (2022).
[2] H. Naraoka et al., Science, **379**, eabn9033 (2022).
[3] T. Noguchi et al., Nature Astronomy, **7**, 170 (2022).
[4] R. Okazaki et al., Science, **379**, eabo043 (2022).
[5] R. Okazaki et al., Earth Planets Space, **74**, 190 (2022).
[6] H. Yabuta et al., Science, **379**, eabn9057 (2022).
[7] T. Yokoyama et al., Science, **379**, eabn7850 (2022).
[8] E. Nakamura et al., Proc. Jpn. Acad., Ser. B, Phys., **98**, 227 (2022)
[9] K. Ninomiya et al., submitted to Meteoritics & Planetary Science.
[10] K. Ninomiya et al., J. Phys. Conf. Ser., **225**, 012040 (2010).
[11] K. Ninomiya et al., Bull. Chem. Soc. Jpn. **85**, 228 (2012).
[12] K. Terada et al., Sci. Rep., **4**, 5072 (2014).
[13] K. Ninomiya et al., Anal. Chem., **87**, 4597 (2015).
[14] K. Shimada-Takaura et al., J. Nat. Med. **75**, 532 (2021).
[15] K. Shimomura et al., Nucl. Instrum. Methods Phys. Res. Sect. A, **600**, 192 (2008).
[16] T. Osawa et al., ACS Earth Space Chem., **7**, 699 (2023).

K. Ninomiya[1], I. Chiu[1], K. Terada[1], T. Osawa[2], T. Wada[3], T. Nakamura[3], S. Nagasawa[4], T. Minami[4], M. Katsuragawa[4], S. Takeda[4], T. Takahashi[4], M. K. Kubo[5], A. Taniguchi[6], S. Watanabe[7], T. Azuma[8], K. Mizumoto[9], S. Takeshita[10,11], I. Umegaki[10,11], K. Shimomura[10,11], and Y. Miyake[10,11]

[1]Osaka University; [2]Japan Atomic Energy Agency; [3]Tohoku University; [4]The University of Tokyo; [5]International Christian University; [6]Kyoto University; [7]JAXA; [8]RIKEN; [9]Tokyo University of the Arts; [10]Muon Science Section, Materials and Life Science Division, J-PARC Center; [11]Institute of Materials Structure Science, KEK

Energy-resolved Neutron-induced Soft-error Cross Section from 10 meV to 800 MeV Measured by Time-of-flight Method

1. Overview

We measured successfully a semiconductor neutron-induced soft-error cross section from 10 meV to 1 MeV by time-of-flight measurement at MLF. The findings reveal, for the first time, a complete picture of the energy dependence of soft-errors (J-PARC Proposal No. 2022A0249) [1]. As a result, we were able to clearly observe the effect of the cross section of the $^{10}B(n,\alpha)^{7}Li$ reaction below 0.1 MeV.

2. Background

Today, sophisticated electronic devices support our lives in numerous ways, but they increasingly fall victim to soft-errors caused by cosmic rays. When cosmic rays, which pour down from space, collide with oxygen or nitrogen atoms in the atmosphere, neutrons are emitted. When neutrons collide with a semiconductor in an electronic device, they can cause "soft-errors", a phenomenon whereby the data stored in a semiconductor are changed. Soft-errors have the potential to impact social infrastructures causing communication failures, and other adverse effects (Fig. 1).

In considering measures against soft-errors in electronic devices, it is important that the system design considers the frequency of the soft-error-induced failures of each device. Meanwhile, the frequency of soft-error-induced failures varies greatly depending on the energy of neutrons reaching the device. Therefore, detailed data on the energy dependence of soft-error cross section is crucial. The soft-error cross section $\sigma(E)$ is defined as

$$\sigma(E) = N(E)/\Phi(E) \qquad (1)$$

which identifies a neutron fluence $\Phi(E)$ as the total number of neutrons per unit area impinging on the semiconductor device, and the total number of soft-errors, $N(E)$, generated by these neutrons. In addition, neutrons in the natural environment and neutrons generated by accelerators have different energy distributions. Therefore, the soft-error rate (SER), which is the number of soft-errors occurring per unit time in a specific neutron irradiation environment can be indicated as

$$SER = \int_0^\infty \sigma(E)\phi(E)dE \qquad (2)$$

using the neutron flux $\phi(E)$ at each neutron energy E and the soft-error cross section $\sigma(E)$. Thus, the soft-error cross section is the most important basic data that is necessary for calculating the failure rate of semiconductor devices due to soft-errors.

For this purpose, we measured the soft-error cross section in the high-energy neutron region (1 MeV to 800 MeV) at Los Alamos Neutron Science Center (LANSCE) in 2020 [2]. However, it is impossible to measure the neutron energy range below 1 MeV at the LANSCE radiation effects facilities, because the interval repetition of the proton beam, which is produced as a

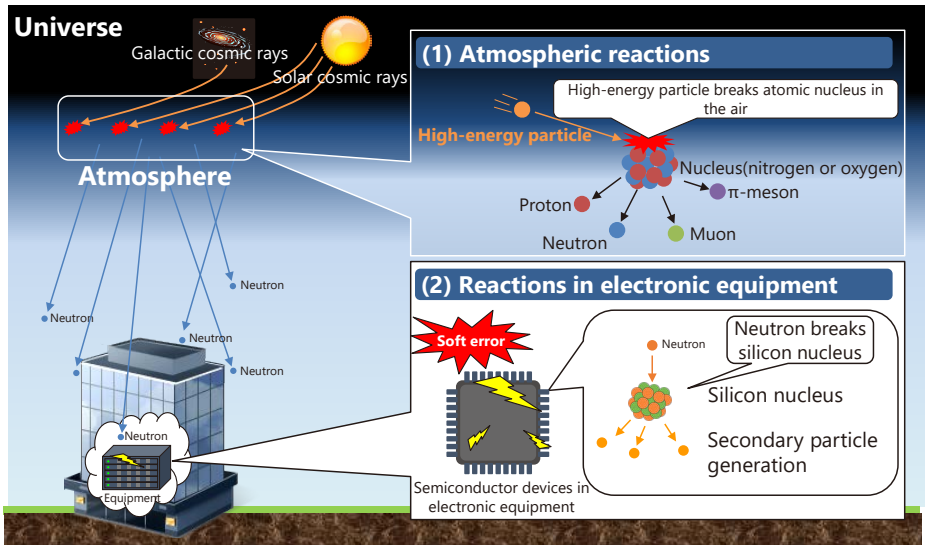

Figure 1. Mechanism of soft-error.

pulsed neutron beam, is 1.8 μs (1.8 μs corresponds to the neutron flight time of 0.6 MeV neutrons over a neutron flight path length of 20 m) and the neutron intensity below 1 MeV is very low. Therefore, we decided to use the facility at the MLF to perform a measurement of a continuous energy-dependent neutron-induced soft-error cross section for an energy range extending below 1 MeV.

3. Measurement method and experiment

In this study, we measured soft-errors caused by low-energy neutrons below 1 MeV using the time-of-flight method with a high-speed soft-error detector reported in 2020. The experiment was conducted by a high-speed soft-error detector at the instrument for neutron source characterization (NOBORU) installed at MLF BL10. The intensity of neutrons used for irradiation at this facility was evaluated using the gold foil activation method. The soft-error cross section in an FPGA 40 nm was measured for continuously varying energies with high energy resolution. Figure 2 shows the fitted curve of the measured time structure of the proton pulse at an accelerator power of 200 kW [3]. As can be seen, the energy resolution of measurements in the high energy region above about 0.1 MeV is not very high since the proton pulse of this facility is double-bunch with a peak to peak distance of 600 ns.

4. Results and discussions

The results of time-of-flight spectrum of the soft-error counts for the FPGA is shown in Fig. 3 ((a) shows a time resolution of 20 ns and (b) shows a time resolution

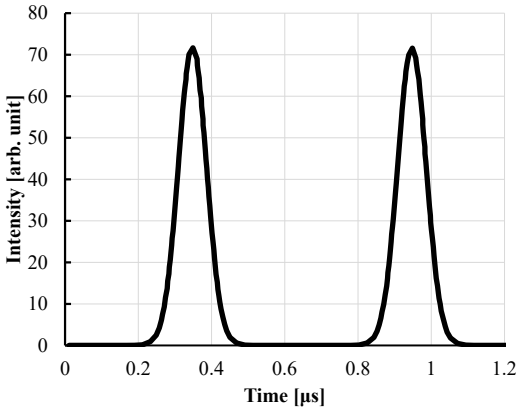

Figure 2. Time structure of proton pulse at J-PARC (200 KW).

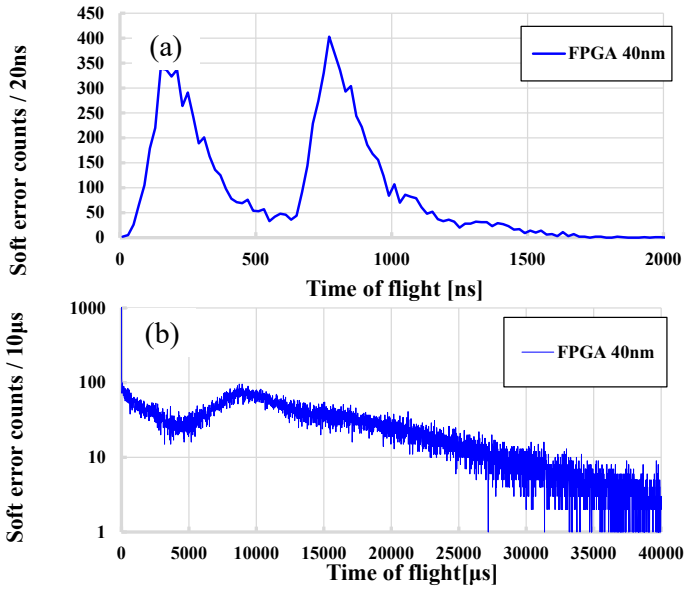

Figure 3. Time-of-flight spectrum of the soft-error counts.

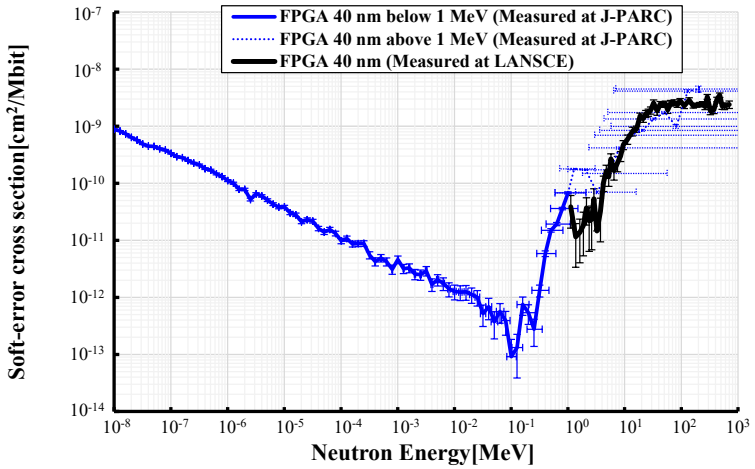

Figure 4. soft-error cross section of the FPGA 40 nm.

of 10 μs). Figure 3 (a) depicts clearly the double pulse structure. However, we were not able to deduce the cross section from this since the pulse width of each proton pulse was about 100 ns and because of that the energy resolution was very poor. Figure 3 (b) indicates that soft-errors occurred even at large flight time values and low energy. Figure 4 shows the soft-error cross section derived from soft-error counts and neutron energy spectrum. The data show that the soft-error cross section tends to be lowest around 0.1 MeV but increases as the energy decreases further. We consider that this is due to the influence of Boron, which is present in trace amounts in semiconductors.

5. Conclusion

We measured a neutron-induced soft-error cross section for FPGAs using the time-of-flight technique for an energy range from 10 meV to 800 MeV at J-PARC and LANSCE. The effect on the cross section of the ^{10}B(n,α)^{7}Li reaction was clearly observed below 0.1 MeV neutrons. The findings allow us to calculate more accurately the failure rate due to soft-errors, a rate which is the key to evaluating soft-errors and planning countermeasures.

References

[1] H. Iwashita et al., IEEE Trans. Nucl. Sci.,**70**, 216 (2023).
[2] H. Iwashita et al., IEEE Trans. Nucl. Sci., **67**, 11 (2020).
[3] H. Hasemi et al., Nucl. Instrum. Methods Phys. Res. A **773**, 137 (2015).

H. Iwashita[1,2], R. Kiuchi[1], Y. Hiroshima[1], Y. Okugawa[1], T. Sebe[2], M. Takeda[2], H. Sato[2], T. Kamiyama[2], M. Furusaka[2], and Y. Kiyanagi[2]
[1]Environment and Energy Laboratories, NTT; [2]Faculty of Engineering, Hokkaido University

Breakthrough of Neutron Interferometer

1. Introduction

Neutron interferometer is an apparatus for the ultra-high precision measurement of neutron-related interactions. Numerous experiments for various fields have been performed since the first successful test of a single-crystal neutron interferometer. These include measurements of neutron-nuclear scattering length, demonstrations of classical physics with elementary particles, validations of quantum mechanics, and investigations of exotic interactions as predicted by new physics beyond the standard model of elementary particles [1].

The interferometer uses mirrors to split the neutron wave into two paths and then superpose them again. The potential difference between the two paths is observed as a phase shift in the interference fringes. The sensitivity is proportional to the neutron wavelength and the interaction length, however, the conventional interferometers that use silicon crystal are limited by the lattice constant in terms of the available neutron wavelengths and are also size constrained by the dimensions of the ingot [2]. To overcome those limitations, neutron interferometers using multilayer mirrors were developed [3, 4]. The neutron wavelength to be used can be freely selected by controlling the structure of the neutron multilayer mirrors.

2. Multilayer interferometer with pulsed neutrons

A novel neutron interferometer integrating unpolarized neutron multilayer mirrors was introduced at J-PARC. The interferometer concurrently measures phase shifts at diverse wavelengths by identifying the wavelength from the time of flight (TOF). This is not only statistically advantageous, but also allows for tracking temporal disturbances of the apparatus. This overcomes the weakness of conventional interferometers.

The experiment was conducted at the low-divergence branch of BL05 (NOP) within the Materials and Life Science Experimental Facility [5]. The beam power sustained during the experiments was 620 kW. Pulsed neutron beam was transported through the neutron bender at BL05 to the interferometer. The interferometer comprised two beam-splitting etalons (BSEs) that split neutron waves into two parallel paths and later recombine them (Fig. 1). The BSEs were designed with half and total reflection mirrors separated by an air gap of 189 μm. The mirrors, deposited on a flat SiO_2 substrate, were bonded by optical contact to maintain parallelism. The parallelism was preserved at approximately 30 nm. The flat SiO_2 substrates with the mirrors were bonded by optical contact to maintain parallelism. The parallelism between the mirrors was preserved at approximately 30 nm. The mirrors can reflect momentum transfers in the range of $0.232 < Q < 0.292$ nm^{-1}. The BSEs were positioned with the incident angle of 1.05° and distance of 140 mm. The interference fringes as a function of TOF were observed by using two-dimensional position sensitive detector. A precision stage was developed to insert the device and/or sample to be measured into the path in the interferometer. To minimize external disturbances, the interferometer and the sample insertion assembly were placed on an active vibration isolator and maintained at a stable temperature of 23°C inside a thermostatic chamber.

Figure 2(a) shows the raw data containing interference fringes. The peak of neutron counts was in the wavelength range from 0.8 nm to 1.1 nm, which can be reflected by the mirrors. It also shows that the interference fringes disappear when one of the two paths is blocked by cadmium plate. This proved that the observed intensity oscillation was an interference between the two paths. Figure 2(b) and (c) show the interference fringe with and without inserting a 0.3-mm-thick Si

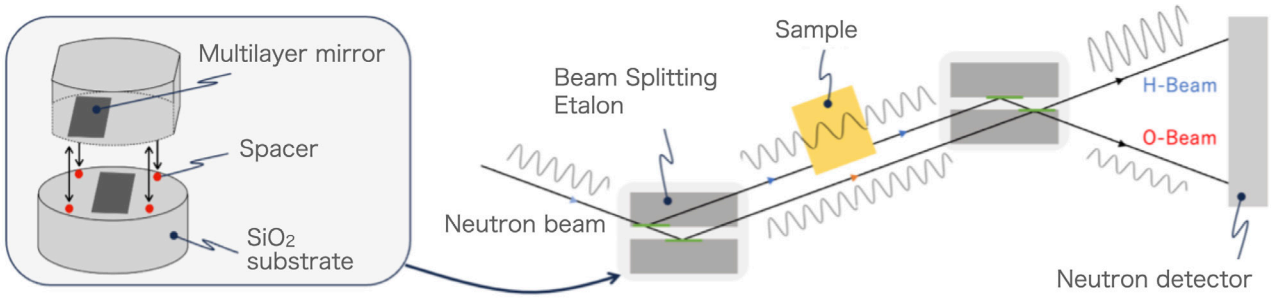

Figure 1. Experimental setup for the multilayer interferometer with pulsed neutrons at BL05 NOP.

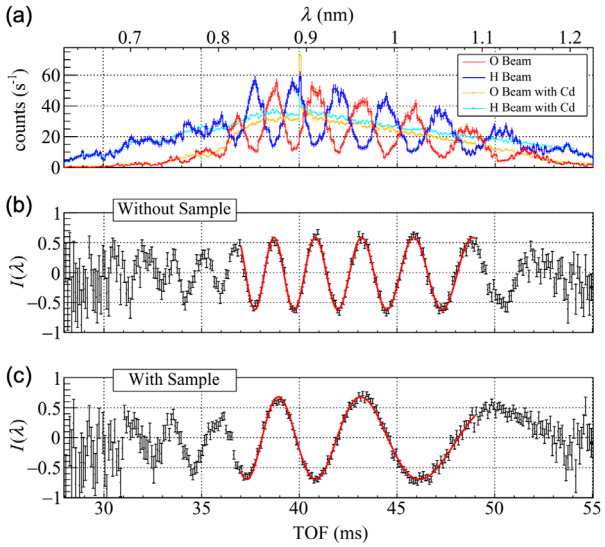

Figure 2. (a) TOF spectra of neutron intensity in the O and H beams. The interference fringes disappear when one of the two paths was blocked by cadmium plate. (b) Normalized interference fringes without sample. $I(\lambda) = (I_O / I_{OCd} - I_H / I_{HCd}) / (I_O / I_{OCd} + I_H / I_{HCd})$, where I_O and I_H are the intensity of O and H beam respectively, I_{OCd} and I_{HCd} are the intensity of O and H beam with blocking one path respectively. (c) Normalized interference fringes with silicon sample inserted into one of the two paths.

sample into one of the paths, respectively. A distinct phase change was observed with and without the sample. The obtained uncertainty in the measured phase shift was 0.02 rad per 20 min. This sensitivity exceeded that measured by NIST (0.31 rad per min) [6] by a factor of 3 and was comparable to that measured by ILL [7] (0.08 rad per min).

The refractive index of the sample can be determined using the phase shift. From the refractive index, the neutron-nuclear scattering length of the nuclei in the sample can be calculated. To demonstrate our interferometer's capabilities, we conducted experiments to determine the neutron-nucleus scattering lengths of various nuclei. Scattering lengths for silicon, aluminum, and titanium were measured and found to be consistent with literature values. Deviations from literature values were found for the neutron-vanadium scattering length. A precise analysis of our sample did not reveal any impurities. This suggests the uncertainty of previous studies. These results show that our new interferometer is robust and highly reliable [8].

3. Future plans

The number of neutrons available for measurements can be increased by optimizing the configuration of the multilayer mirrors in the interferometer for the spectrum of the incident beam by two orders of magnitude. Systematic uncertainties originating from the sample shape can be suppressed by ultra-high precision machining technology. By expanding the air gaps in the BSEs, the interferometer can be utilized for various physics experiments, such as the scattering length of gas samples requiring containers of sufficient size [9]. The utilization of a high-sensitivity neutron interferometer opens possibilities for a wide range of new physics search experiments.

References

[1] H. Rauch and S. A. Werner, "*Neutron Interferometry*", 2nd ed. (Oxford, New York, 2015)
[2] H. Rauch, W. Treimer, and U. Bonse, Phys. Lett. **47A**, 369 (1974).
[3] M. Kitaguchi, et al., Phys. Rev. A **67**, 033609 (2003).
[4] Y. Seki, et al., J. Phys. Soc. Jpn. **79**, 124201 (2010).
[5] K. Mishima, et al., Nucl. Instrum. Methods A **600**, 342 (2009).
[6] P. Saggu, et al., Rev. Sci. Instrum. **87**, 123507 (2016).
[7] Y. Hasegawa, et al., Nature (London) **425**, 45 (2003).
[8] T. Fujiie, et al., Phys. Rev. Lett. **132**, 023402 (2024).
[9] K. Li, et al., Phys. Rev. D **93**, 062001 (2016).

T. Fujiie[1,2], M. Hino[3], T. Hosobata[2], G. Ichikawa[4,5], M. Kitaguchi[1,4,6], K. Mishima[4,5], Y. Seki[7], H. M. Shimizu[1,4], and Y. Yamagata[2]
[1]Department of Physics, Nagoya University; [2]Center for Advanced Photonics, RIKEN; [3]Institute for Integrated Radiation and Nuclear Science, Kyoto University; [4]Institute of Materials Structure Science, KEK; [5]Neutron Science Section, Materials and Life Science Division, J-PARC Center; [6]Kobayashi-Maskawa Institute, Nagoya University; [7]Institute of Multidisciplinary Research for Advanced Materials, Tohoku University

Measurement of the ^{241}Am Neutron Capture Cross Section with Fe and Si-filtered Neutron Beam Using the NaI(Tl) Spectrometer of the ANNRI Beamline

1. Introduction

Partitioning and transmutation have been the approaches taken by Japan in order to solve the long-term accumulation of High-Level nuclear Waste (HLW). At the Japan Atomic Energy Agency (JAEA), the transmutation of minor actinides (MA) is currently targeted by means of Accelerator Driven-Systems (ADS), a sub-critical facility that employs a proton accelerator to generate keV neutrons within the core, via spallation reactions. The reaction core is meant to be constituted of mainly MAs, with a high concentration of ^{241}Am amongst all MAs. Hence, accurate data of all neutron induced reaction for all MAs that will constitute the ADS core is paramount for the design and safety assessments. In particular, the neutron capture cross section has been found to be one of the main sources of criticality uncertainty of ADS. The reason for this is that, while transmutation of MAs is meant to be carried out by fission reactions, the neutron capture reaction is the main reaction channel open for most MAs in the core in the keV region. Hence, an accurate characterization of not only the fission channel but the competing neutron capture channel is of utmost importance for the design of ADS facilities [1] .

Regarding ^{241}Am, the uncertainty in evaluated nuclear data libraries such as JENDL-5 [2] stems from the fact that experimental data in the keV for the neutron capture cross section presents high uncertainty. The reason for this is that ^{241}Am is highly radioactive, a fact that limits the amount of mass that can be measured. This combined with the low overall value of the neutron capture cross in the keV range, means that continuous experimental efforts are required using highly intense pulsed-neutron beams. The past experimental data with high uncertainty for ^{241}Am in the keV-neutron region, which can reach up to 45%, are shown in Fig 1.

2. Experimental setup

The experiments were performed at the Accurate Nucleon-Nucleus measurement Reaction Instrument (ANNRI) using the newly developed neutron filtering technique. This technique hinges on molding the incident neutron flux, which is in double-bunch mode, into quasi-monoenergetic neutron beams by using materials that present the characteristic of sharp minima in the neutron total cross section, since only neutrons with the energy of the sharp minima can stream through the filters and reach the sample position while the rest are stopped. A schematic of the neutron filtering technique can be seen in Fig. 2

With the neutron filtering technique, the effects of the double-bunch can be severely diminished. At the same time, since most of the high-energy neutrons are not allowed to reach the sample position, the background events caused by such neutrons after interacting with the sample, which carry a delay in time and, hence, are seen throughout long time-of-flight regions, are mostly removed, allowing for accurate experiments to be performed. This is of particular importance for measurements with radioisotopes, such as ^{241}Am, as they have to be sealed, with the casing becoming one

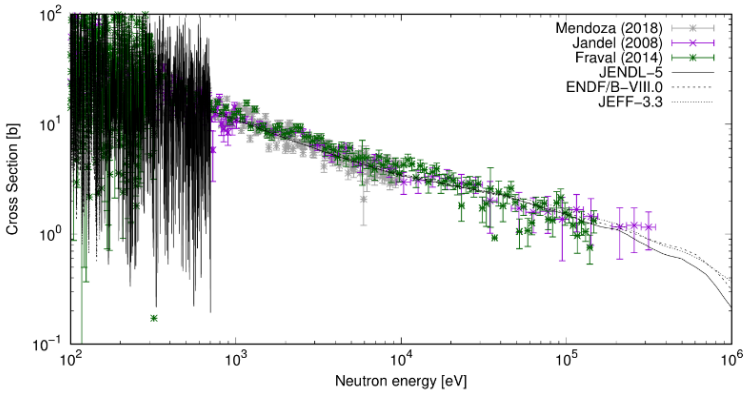

Figure 1. Present status of the experimental and evaluated data for the neutron total cross-section of ^{241}Am

of the main sources of background. Nonetheless, with the use of the neutron filtering technique the influence of the casing is massively reduced due to minimal high-energy neutrons reaching the sample. Further information about the neutron filtering technique is provided here [3].

In the present experiment, ^{nat}Fe and ^{nat}Si were employed as filters in order to tailor the incident double-bunch neutron flux into quasi-monoenergetic neutron beams with averaged neutron energies of 23.5 keV (Fe); and 51.5 and 127.7 keV (Si). A ^{241}Am sample with a mass of 7.47 ± 10 mg and an activity of 957 MBq, was measured in the present experiment together with dummy case and a carbon sample to derive the sample-dependent background. The pulse-height weighting technique [4] was employed to derive the ^{241}Am neutron capture yield and the neutron cross section of ^{241}Am was determined relative to the ^{197}Au neutron capture yield measured with a Au sample and using the reference cross section value of JENDL-5. This process can be expressed as:

$$\sigma_{Am}(E_n) = \frac{Y_{Am}(E_n)C_{Am}(E_n)C_{fis}(E_n)}{Y_{Au}(E_n)C_{Au}} \frac{S_{Au}P_{Au}}{S_{Am}P_{Am}} \frac{\sigma_{Au}(E_n)}{C_{tresh}}$$

where $\sigma_{Am}(E_n)$ is the neutron capture cross section of ^{241}Am. $Y_x(E_n)$, $C_x(E_n)$, $S_x(E_n)$, $P_x(E_n)$, are the neutron capture yield, the correction for self-shielding and multiple scattering effects, the sample area density and the number of proton shots for ^{241}Am and ^{197}Au, respectively. $C_{fis}(E_n)$ is the fission correction for 241Am, while C_{tresh} is the correction for undetected events below the detection threshold of 600 keV. Finally, $\sigma_{Am}(E_n)$ is the neutron capture cross section of ^{197}Au from JENDL-5.

3. Cross section results

The present results for the neutron capture cross section of ^{241}Am obtained with the neutron filtering technique at the neutron averaged energies of 23.5, 51.5 and 127.7 keV are shown in Fig. 3. As can be clearly seen, the present results signify a massive improvement

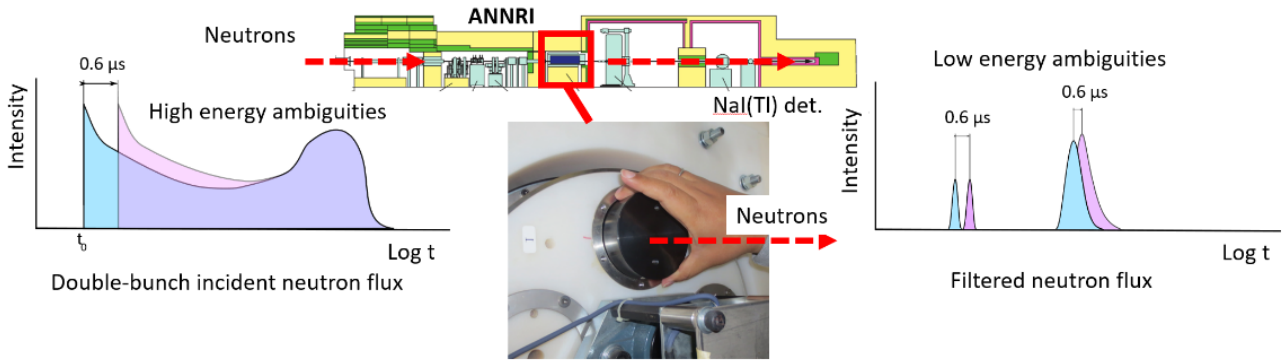

Figure 2. Schematic of the BL04 of the MLF. The neutron filter material, namely ^{nat}Fe and ^{nat}Si, was introduced in the rotary collimator.

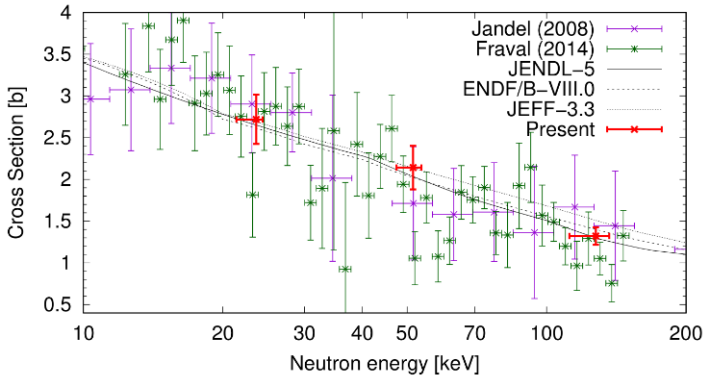

Figure 3. ^{241}Am neutron capture cross section results using the Si (51.5 and 127.7 keV) and Fe (23.5 keV) neutron filters with experimental and evaluated data.

in cross section accuracy, since they display with much lower uncertainty (8–12%) than that of the past experimental data (15–45%). This is important in order to reduce the nuclear data uncertainty influence in the design of ADS facilities.

4. Conclusions

The neutron capture cross section of ^{241}Am was determined in the ANNRI beamline at the averaged neutron energies of 23.5, 51.5 and 127.7 keV by means of the newly developed neutron filtering technique, that allows for the neutron induced cross section to be measured with high accuracy. The present cross section results for ^{241}Am were determined relative to the neutron capture yield of ^{197}Au and display uncertainties of 8–12%, much lower than those present in past experimental data of 15–45%, signifying a major cross section uncertainty improvement for the design of ADS facilities. Further information about the present experiment can be found here [5].

References

[1] Iwamoto H, Nishihara K, Sugawara T, et al. J Nucl Sci Technol. 2013;50:856–862.
[2] Iwamoto O, Iwamoto N, Kunieda S, et al.. J Nucl Sci Technol. 2023;60:1–60.
[3] Rovira G, Kimura A, Nakamura S, et al. Nucl Inst Methods Phys Res A. 2021 ;1003:165318.
[4] MacKlin RL, Gibbons JH. Phys Rev. 1967;159: 1007–1012.
[5] Rovira G, Kimura A, Nakamura S, et al. J Nucl Sci Technol . 2023;60:489–499.

G. Rovira[1], A. Kimura[1,2], S. Nakamura[1,2], S. Endo[1,2], O. Iwamoto[1], N. Iwamoto[1], T. Katabuchi[3], Y. Kodama[3], and H. Nakano[3]
[1]Nuclear Science and Engineering Center, JAEA; [2]Neutron Science Section, Materials and Life Science Division, J-PARC Center; [3]Laboratory for Zero-Carbon Energy, Tokyo Institute of Technology

Development of Pulsed Magnet System for Sample Environment equipment

1. Introduction

With the development of various measurement techniques, such as magnetization, electric resistance, specific heat, ESR and NMR, high magnetic field environment has become indispensable in material science. Neutron scattering experiments under high magnetic fields have unique features, they allow us to trace the origin of the induced phase in the high magnetic field.

These technologies have been mainly developed in the so-called high magnetic field facilities in the world. On the other hand, neutron scattering experiments using a high magnetic field can directly determine the magnetic structure, so it is possible to obtain information on the origin of the phase induced by a high magnetic field.

To meet the growing demand for high magnetic field applications for neutron diffractions, several high magnetic field environments have been developed in neutron facilities globally. Superconducting magnets have been used with magnetic fields of up to 17 T [1]. A 4 MW hybrid magnet comprised of superconducting and normal resistive magnets with magnetic fields of up to 26 T had been operated at the Extreme Magnet Field Facility (HFM) of the Helmholtz Center Berlin Institute (HZB) in Germany [2].

High-intensity pulsed neutron beam at the MLF has already become available, and we have received requests from users to introduce pulsed-type high-magnetic-field equipment to the MLF. Pulsed magnetic equipment does not only require large power, but can also be made compact and movable. Therefore, we have developed a pulsed high magnetic field device that can generate more than 30 T.

2. Development of pulsed magnet system

Figure 1 shows the cross-section of the developed pulsed magnet equipment. It comprises a vacuum chamber, a closed-cycle refrigerator for sample cooling down to 4 K, and a nitrogen bath made of a rectangular cross-section stainless-steel (SUS) tube. The coil is inserted in the nitrogen bath. It is immersed in liquid nitrogen to reduce the resistance and quickly remove the Joule heat generated by the pulsed current of the coil. Automatic liquid nitrogen supply equipment (LNAS, Value-impact Co., Ltd.) is introduced to achieve a fully automatic repetitive operation.

Figure 2 depicts a photograph of the coil. A high-tensile strength Cu–Ag alloy with 1 mmϕ (CA10-0PIWC-7, SWCC Showa Cable System Co., Ltd.) for the wire is used. The sum of the turns is approximately 200. The coil inductance and resistance at 100 Hz are 670 μH and 100 mΩ at 77 K, respectively. The current to the coil is applied by a capacitor bank pulsed power supply made by pulsed magnet Gr. in the MLF [3].

The sample is attached to a 7 mmϕ single-crystalline sapphire rod that is connected to the GM refrigerator and cooled down to 4 K through heat conduction. The sample is placed in the center of the coil. The scattering angle, 2θ, is 42°. Thermometers (Cernox, Lake Shore Cryotronics Inc.) are attached near the end of the sapphire rod and the second stage of the GM refrigerator. The sample and the sapphire rod are enclosed by an aluminum radiation shield of 1 mm thickness to prevent a temperature rise. Figure 1 shows only the aluminum

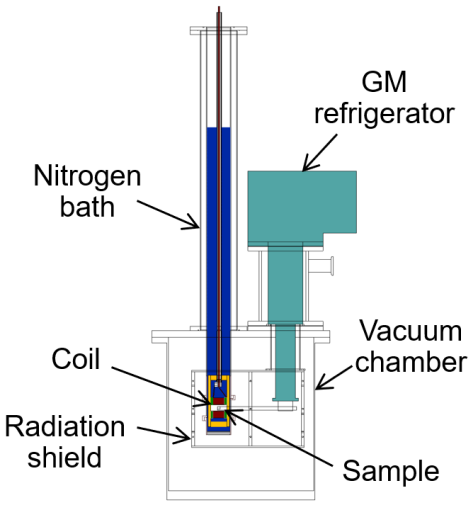

Figure 1. Cross-section of the pulsed magnet equipment.

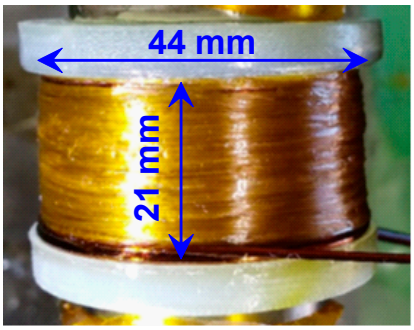

Figure 2. Photograph of the coil.

frame to which the shield is connected to show the inside. For the temperature control of the sample, a polyimide film insulation heater is wound around the second stage of the GM refrigerator. The temperature can be adjusted by a temperature controller (Model 336 Cryogenic Temperature Controller, Lake Shore Cryotronics, Inc.) which can be controlled approximately from 4 K to room temperature. We have confirmed that the temperature gradient between the sample and the refrigerator cold head is as small as 1.2 K.

3. Experiment and results

The pulsed magnet system was commissioned on NOBORU (BL10) [4]. A single-crystalline multiferroic $TbMnO_3$ [5] was used as a test sample. Its size was approximately $4.5 \times 4 \times 3.5$ mm^3. It was placed in a position that would facilitate the application of the magnetic field along the a-axis. It is a multiferroic material that coexists in magnetic and ferroelectric orders. For example, it is expected to be a multifunctional and high-performance next-generation electric/magnetic device. At zero magnetic fields, the magnetic moments of Mn in $TbMnO_3$ are incommensurate, and the propagation wave vector (0, k_{Mn}, 1) in the Pbnm orthorhombic unit is (0, 0.28, 1) below 28 K. In a magnetic field of 30 T, they become commensurate and show a propagation wave vector of (0, 0.25, 1).

As a demonstration of the pulsed magnet system, the change in the TOF spectrum of the Mn moments with and without a magnetic field is experimentally validated. The TOF spectra are shown in Fig. 3. The TOF spectra of the red and blue points are 0 and 30 T, respectively. Because the neutron counts are integrated for approximately 10,000 incident beam pulses (approximately 7 min) at 0 T, the count number displayed in Figure 3 is reduced to 1/100 to match the count number of 40 shots at 30 T. Figure 3 is also depicted as an example of a pulsed magnetic field waveform applied to a sample.

There are Bragg peak signals in Fig. 3 that correspond to the propagation wave vector (0, 0.28, 1) of the Mn moments at 0 T and (0, 0.25, 1) of it at 30 T. The TOF of the Bragg peaks are estimated to be approximately 10.25 ms and 10.4 ms using the Gaussian function, respectively. The magnetic field dependence of the diffraction peaks with and without a magnetic field was

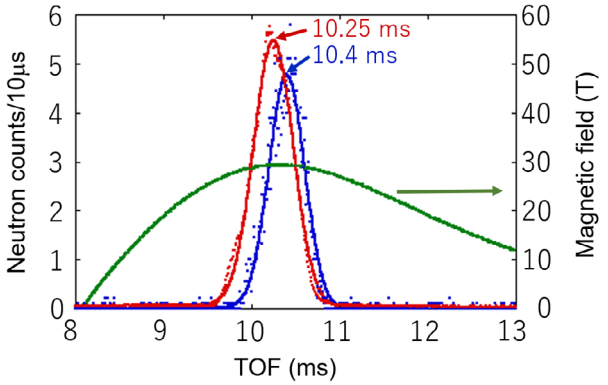

Figure 3. TOF spectra applied to the sample.

clearly observed using the pulsed magnet system.

N. Qureshi et al. also performed a pulsed magnetic field experiment using TbB_4 as a sample [6]. However, this was a single-wavelength experiment using a nuclear reactor at ILL (thermal neutron three-axis spectrometer, IN22), so it is not possible to see a wide range of wave number space such as at the MLF.

4. Future plans

We have successfully developed 30 T pulsed magnet equipment, so next we will proceed with the development of higher pulsed magnet equipment. So far, we have succeeded in increasing the maximum magnetic field up to 35 T and performing a neutron experiment.

We are developing pulsed magnet equipment up to 40 T, which is the largest class of sample environment devices for neutron facilities.

References

[1] Meissner, M.; Smeibidl, P., *Neutron News* **2001**, *12*, 12–18.
[2] Steiner, M.; Tennant, D.A.; Smeibidl, P., *J. Phys. Conf. Ser.* **2006**, *51*, 470–474.
[3] Watanabe, M.; Nojiri, H., *J. Neutron Res.* **2019**, *21*, 39–45.
[4] M. Watanabe, T. Kihara, H. Nojiri, Quantum Beam Sci. **2022**, 7, 1.
[5] Quezel, S.; Tcheou, F.; Rossat-Mignod, J.; Quezel, G.; Roudaut, E., *Phys. B* **1977**, *86–88*, 916–918.
[6] N. Qureshi.; F. Bourdarot, E. Ressouche, W. Knafo, F. Iga, S. Michimura, L.-P. Regnault, and F. Duc, *PHYSICAL REVIEW B 106,* 094427, **2022**.

M. Watanabe[1], T. Kihara[2], and H. Nojiri[3]
[1]Technology Development Section, Materials and Life Science Division, J-PARC Center; [2]Research Institute for Interdisciplinary Sci-ence, Okayama University; [3]Institute for Materials Research, Tohoku University

New Material Exploration to Enhance Neutron Intensity Below Cold Neutrons

1. Introduction

Slow neutrons, such as cold neutrons, are important nondestructive probes not only for basic physics but also for the structural genomics advancements in the life sciences and the battery technology advancements needed for the transition to a hydrogen society. Neutron-based science, also known as high-intensity-dependent science, demands that we increase the source's intensity as high as possible.

A new unique method focusing on nanosized particle aggregation has been proposed to increase neutron intensity below the cold neutron energy region [1–3]. The aggregation of nanosized particles matches the wavelength of below cold neutrons, resulting in a similar effect to coherent scattering, or so-called Bragg scattering, leading to higher neutron intensities. Nanodiamonds [4–6] (Fig. 1) and magnesium hydride (MgH_2) [7] have recently been determined numerically and experimentally to have the potential to increase neutron intensity by several orders of magnitude. The major challenge with nanodiamonds in practical applications is the molding method.

In order to find a solution to this problem, we focused on another carbon structure, graphene. Graphene [8] is expected to be the lightest and strongest material in the world due to its geometric structure. It is being scaled up for practical applications, such as aerospace and space, etc [9].

Conversely, large amounts of nanosized end materials are also being produced in this development progress.

We conceived that nanosized graphene could cause coherent neutron scattering under particle size conditions similar to nanodiamonds. Moreover, it might be possible to use it in high neutron radiation conditions due to graphene's strong sp2 bonds. We performed neutron scattering measurement experiments, such as total neutron cross-section and small-angle neutron scattering on nanosized graphene using the RIKEN Accelerator-driven compact Neutron Source (RANS) [10] and iMATERIA at J-PARC [11].

The potential of nanosized graphene aggregation is reported as a reflector material below cold neutrons, together with experimental results.

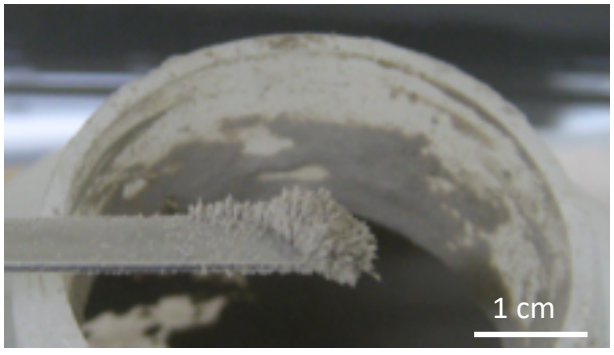

Figure 1. Photograph of nanodiamond powder [4].

2. Nanosized graphene flower aggregation

A distinctive graphene called a "graphene flower" with a "sunflower" shape [12, 13] is produced by combination of phenolic formaldehyde resin carbonization and the hot isostatic pressing (HIP) process. Note that this graphene flower is far from how we imagine graphene as a two-dimensional structure material. The produced graphene flower, as shown in Fig. 2, was composed of multiple petal-like graphene layers of less than 20 nm thick growing from the carbonized sphere surface. Seed-like graphene was composed of many 1–100 nm sized graphenes inside the sphere, forming a concave–convex structure. Finally, graphene flowers were combined to form a nanosized graphene aggregate.

For this study, two graphene sample types, namely, graphene 1 and 2, were prepared under different HIP conditions. As shown in Fig. 3(a), graphene 1 produced petal-like graphene on the surface and granular seed-like graphene inside the sphere. Graphene 2 formed petal-like graphene but almost no seed-like graphene, as shown in Fig. 3(b). The samples were shaped to 20 mm in diameter × 2 mm in thickness.

3. Experiment

In order to evaluate the total neutron cross-section, the neutron transmission experiment was carried out using the RANS neutron source [10], which was generated by the p-Be reaction of a 7 MeV proton bombardment. In a slab-type mesitylene moderator arrangement neutron beamline, a slit-type collimator was installed to increase the available neutron intensity at the sample position.

Small-Angle Neutron Scattering (SANS) Experiments were performed at the J-PARC iMATERIA [11].

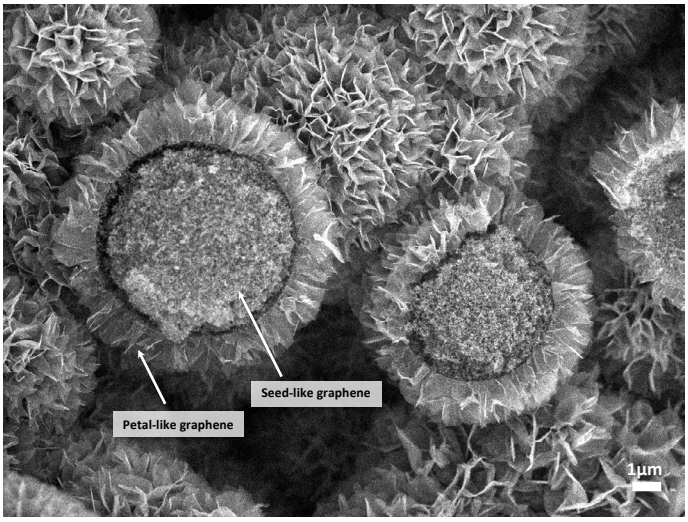

Figure 2. The SEM image of a graphene flower produced by the HIP treatment [13]. As indicated by the arrows in the figure, the graphene flower is composed of multiple petal-like graphene and seed-like graphene. Petal-like graphene forms multiple layers of petals less than 20 nm thick growing from the carbonized sphere surface. The seed-like graphene is composed of many 1–100 nm sized graphenes inside the sphere, forming a concave–convex structure [13].

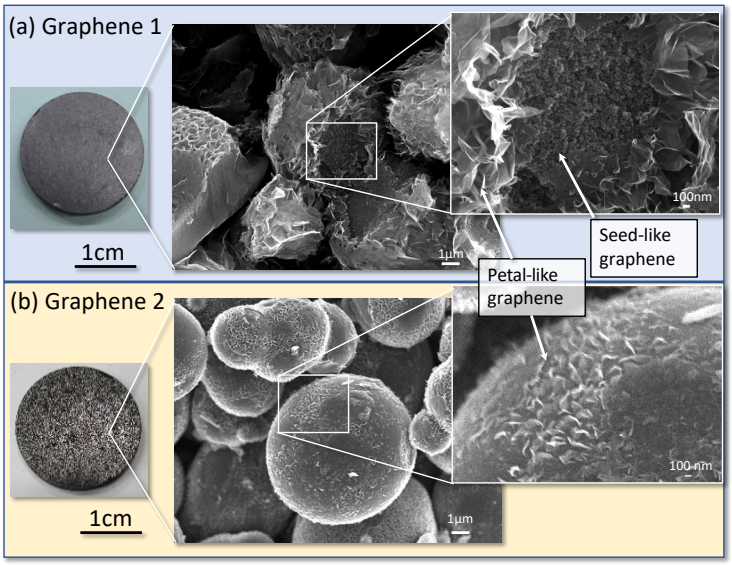

Figure 3. Photographs of graphene materials prepared under various HIP conditions [13]. (a) Graphene 1, which formed petal-like graphene and nm-sized granular seeds, called "seed-like graphene", was fabricated under HIP conditions with a maximum temperature of 1390°C at a rate of 900°C/h, 1 h holding time, then cooled naturally; (b) Graphene 2, which formed petal-like graphene, but no seed-like graphene, was fabricated under HIP conditions with a maximum temperature of 1300°C at a rate of 200°C/h and then cooled immediately without any retention time.

4. Results and discussion

Total neutron cross-sections were calculated using the transmission data, as shown in Fig. 4, where coherent scattering predominated for the 0.5–2 meV region, concerning the nanodiamond literature [4]. Compared to graphite, nanodiamond had several hundred higher total neutron cross-sections below the meV region. Graphene 1 was approximately one-third of the total neutron cross-section data of nanodiamonds. Conversely, it was several tens of times higher than

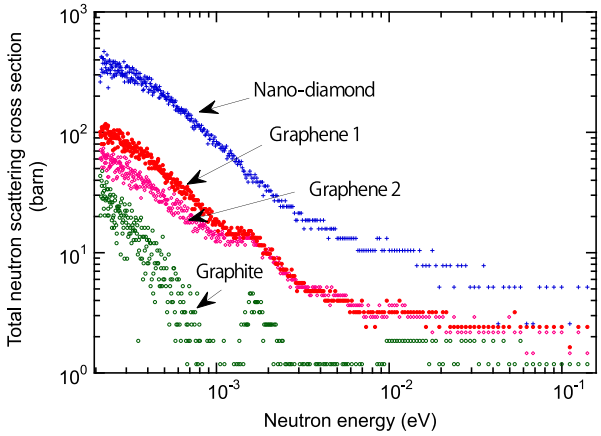

Figure 4. Total neutron scattering cross-section [13].

Table 1. Calculated invariant Q [13, 14].

Sample	Graphene1	Graphene2	Graphite	Nanodiamond
Invariant Q	0.0213	0.0114	0.0081	0.0164

graphite. Graphene 1 had somewhat higher total cross-section than graphene 2, showing seed like graphene rather than petal like graphene are more effective for coherent scattering.

Table 1 shows the velues of invariant, Q [13, 14] for measured SANS data, representing the scattering cross-section due to small-angle scattering. In particular, nanodiamond and graphene 1 showed a larger Q. These findings agree with the scattering cross-section values determined by transmission experiments.

Note that the nanosized graphene, which is still in the early development stages, has the potential to rival or even surpass nanodiamonds with further fabrication process optimization, including nanosized graphene aggregation.

5. Conclusions

We concentrated on nanosized graphene aggregation to intensify below cold neutrons, which are similar to those of nanodiamonds. For the first time, the measured data revealed that nanosized graphene aggregation increased total neutron cross-sections and small-angle scattering in the cold neutron energy region, most likely due to coherent scattering, implying the possibility of below cold neutron applications.

References

[1] V.V. Nesvizhevsky et al., Physics of Atomic Nuclei, ***65*** 400 (2002).
[2] V.V. Nesvizhevsky et al., NIM A, ***595*** 632 (2008).
[3] E.V. Lychagin et al.,NIM A, ***611*** 302 (2009).
[4] M. Teshigawara et al., NIM A, ***929*** 113 (2019).
[5] T. Ersez et al., Physica B Condens. Matter, ***551*** 278 (2018).
[6] M. Jamalipour et al., NIM A, ***1033*** 166719 (2022).
[7] J. R. Granada et al., EPJ Web of Conferences, ***231*** 04002 (2020).
[8] K. S. Novoselov et al., Science, ***306*** *(5696)* 666 (2004).
[9] L. Zou1 et al., J. Data Inf. Sci., 3 82 (2018).
[10] Y. Ikeda et al., J. Neutron Res., ***1*** 1 (2022).
[11] S. Koizumi et al., Quantum Beam Sci., ***4*** 42 (2020).
[12] US8951451B2
[13] M. Teshigawara et al., Nanomaterials, ***13*** (1) 76 (2023).
[14] G. Porod, Kolloid-Z, ***124*** 83 (1951).

M. Teshigawara[1], Y. Ikeda[2], M. Yan[2], K. Muramatsu[3], K. Sutani[3], M. Fukuzumi[4], Y. Noda[5], S. Koizumi[5], K. Saruta[1], and Y. Otake[2]
[1]Neutron Source Section, Materials and Life Science Division, J-PARC Center; [2]Center for Advanced Photonics, RIKEN; [3]INCUBATION ALLIANCE INC; [4]Department of Materials and Analysis, Hyogo Prefectural Institute of Technology; [5]Institute of Quantum Beam Science, Ibaraki University

Neutron Source

Neutron Source Section

1. Organizational change

The 3NBT group, which belonged to the neutron source section, was reassigned as the 4th accelerator section from fiscal year 2022 to promote rational organizational management. The tasks and responsibilities of the 3NBT group, which were the operation, maintenance, and R&D for the beam transportation line from the 3 GeV synchrotron to the neutron source, and related devices, including the cooling water system, were transferred to the 4th accelerator section.

2. Operational overview

In the beginning of fiscal year 2022, on April 7, the beam power at the MLF was raised from 730 kW to 830 kW, which was the highest level of beam power on record for the long-term user program. Since the proton beam pulses at the 3 GeV rapid cycle synchrotron (RCS) outlet are shared between the MLF and the 30 GeV main ring (MR), the beam power at the MLF becomes lower than that at the RCS outlet and is changed in accordance with the operation mode of the MR. The share of the MR is 3.1% in slow extraction mode and 11.8% in fast extraction mode. 830 kW at the MLF was attained when the power at the RCS outlet was raised from 760 kW to 860 kW with a slow extraction mode of the MR, but due to the mode change to fast extraction, the power at the MLF was reduced to 770 kW from June 4, even though the power at the RCS outlet was raised to the highest value on record of 870 kW. The stable operation continued, and the beam operation of the MLF ended on June 26 after a two-day operation for beam study and the maintenance works during the long outage started.

After almost 5 months of maintenance works, the beam operation of the user program started on November 21 with a beam power of 780 kW at the MLF, which was a little bit less than that before the long outage due to the trouble with the accelerator component. The beam power at the MLF was changed several times between 730 kW and 810 kW due to the change of the beam operation mode of the MR for beam study. The beam operation of the MLF had continued very well with the excellent availability of more than 95% and ended on March 15 as scheduled.

3. Remote-handling operations of the proton beam window and the moderator and reflector assembly

Here, some important remote-handling operations in the hot cell are highlighted. One was the replacement of the used proton beam window and volume reduction. The proton beam window is mounted on the shielding plug and integrated into one unit, as shown in Fig. 1 left photo. When the operation of the proton beam window reaches the material lifetime, which is ca.10000 MWh, the unit is replaced with a new one with a new proton beam window mounted on it, and the used unit is temporally moved to the storage space. Then, usually in later years, the used proton beam window is dismounted from the unit and replaced in the hot cell by remote handling to reuse the shielding plug. In 2022, the used proton beam window, which ended its operation in 2020, was replaced and the utility pipes were cut into pieces by the cutting machine shown in Fig. 1 right photo for volume reduction by remote handling operation. The operations were successful, and the new unit was ready to be used as a spare proton beam window.

Another notable operation was the remote handling test of the moderator and reflector assembly carried out using a spare assembly, as shown in Fig. 2. An assembly consists of a shielding plug, a reflector, and three different types of moderators with utility pipes for liquid hydrogen and water fixed to them, and only the used moderators with utility pipes and reflector are replaced while the shielding plug is reused just like the proton beam window. Because the operating lifetime of a moderator and reflector assembly is comparatively long, 30000 MWh corresponding to 8 years at 1 MW, the last remote handling operation was done during the

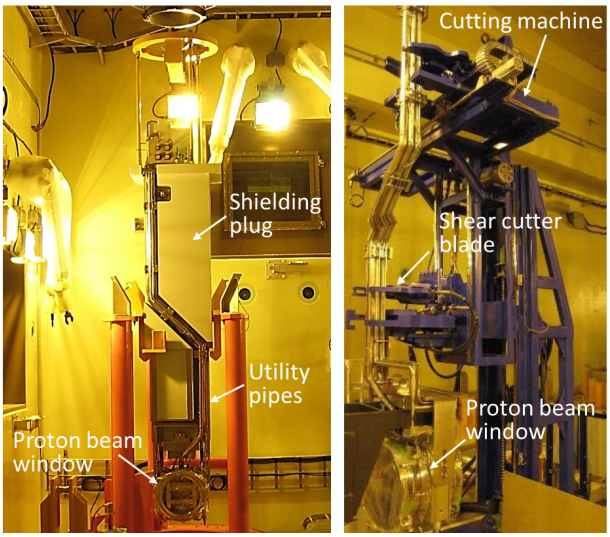

Figure 1. Unit of a proton beam window (left) and the cutting machine (right).

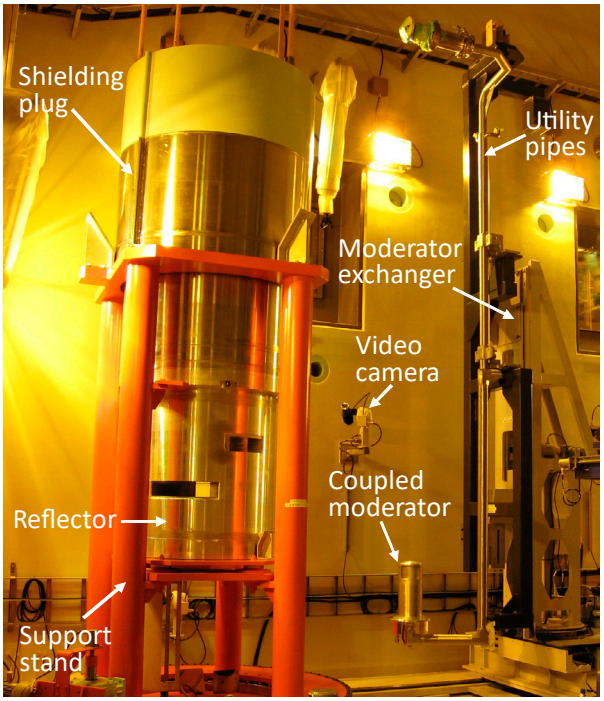

Figure 2. Moderator and reflector assembly and a coupled moderator held by the moderator exchanger.

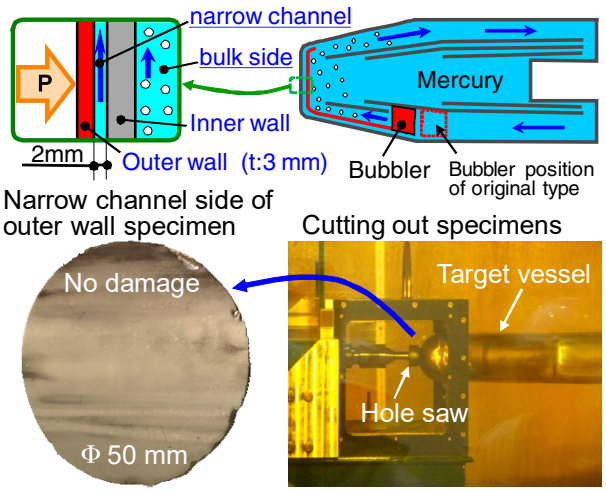

Figure 3. Structure of the target vessel (top) and the surface of the outer wall specimen (bottom left) and the cutting machine (bottom right).

commissioning period before the beam operation of the MLF started more than 10 years ago, so the inheritance of skills and experiences is very important. The remote handling procedures were checked carefully to handle the actual radioactive assembly in the near future.

4. Investigation of pitting damage mitigation effect and target vessel replacement

All the handling works of the used target vessel are conducted fully remotely by the remote-handling devices such as the master-slave manipulator, the power manipulator, the crane, and video cameras, because the dose rate at the outer surface of the used target vessel is more than 1000 Sv/h.

On September 26, specimens were cut out from the forefront wall of the used target vessel, as shown in Fig. 3 bottom right photo, which was operated with 836 kW at maximum. This time, the specimen of the inner wall of the mercury vessel, which was protected against the pitting damage by micro-bubble injection into mercury flow as shown in Fig. 3 top, could not be obtained, because the specimen fell into the mercury vessel. But the damage on the specimen of the outer wall of the mercury vessel, the mercury boundary wall, was negligibly small as shown in Fig. 3 bottom left photo, which was a promising result for the stable beam operation with greater beam power.

On October 11, the used mercury target vessel was replaced with a new one which had the same structure as the former one. This type of target had an improved structure of the mercury flow channel. That is, the bubbler was installed at a position 92 mm closer to the beam window than the original type, as shown in Fig. 3 top, to increase the bubble number density near the beam window for promoting the pressure wave mitigation effect.

5. International collaborations

Three international collaboration workshops were held during the reporting period. One took place from October 10 to 11 with the European Spallation Source (ESS) on-site at Lund in Sweden with online capability. The main topics were commissioning works in every aspect of the project. The others were organized on-site at J-PARC. One was held from February 27 to March 1 with ISIS of Rutherford Appleton Laboratory. Information exchange in the field of the accelerator system and neutron/muon target system was its primal scope. Another workshop was held from March 22 to 24 with the Spallation Neutron Source (SNS) of Oak Ridge National Laboratory to discuss the neutron source system issues. Many fruitful discussions were held at all workshops.

K. Haga, M. Ohi, M. Teshigawara, T. Naoe, T. Wakui, H. Kinoshita, H. Kogawa, Y. Yamaguchi, and M. Harada
Neutron Source Section, Materials and Life Science Division, J-PARC Center

Transportation of Used Mercury Target Vessel #3

1. Introduction

Mercury target vessels for the pulsed spallation neutron source suffer cavitation and irradiation damages, which depend on the beam power and operating time. To assess the current situation of the cavitation damage, as a preventive maintenance, the usage period of the mercury target vessel has been set at one year and after that, it is replaced. The used mercury target vessel covered with an airtight storage container without shielding functions and other used radio-active components are temporarily stored in the storage room in the MLF (B1F). Due to the limited storage capacity of the storage room, the transportation of the used mercury target vessel to the RAM (Radio Active Material) building in the J-PARC site began in 2019 and has been conducted during the summer shutdown period every year. The transportation of the used mercury target vessel #3 was conducted from the end of June 2022, and this was the fifth transport work.

2. Mercury target vessel #3

The used mercury target #3 with a size of ca. 1.2 m × 1.2 m × 2.4 m was put in a storage container with a size of ca. 1.8 m × 1.8 m × 2.9 m. The total weight was ca. 5 ton. The beam operating condition during the use of the mercury target vessel #3 and its state after use are shown in Table 1.

Table 1. Beam operating condition during the use of mercury target vessel #3 and state after use.

Period of beam operation	2011.12–2014.6
Beam operating time	7537 h
Averaged beam power	272 kW
Accumulated beam power	2050 MWh
Total irradiation damage	2.3 dpa
Maximum surface dose rate after beam operation (86 days cooling)	382 Sv/h
Maximum surface dose rate of storage container before transportation	796 mSv/h

3. Storage space of used radioactive components

MLF has a storage room connected to the hot cell with a space of ca. 18 m × 8 m as shown in Fig. 1. 5 used mercury target vessels and 3 used proton beam windows covered with storage container have been stored there. The RAM building has three large storage pits with a space of ca. 10 m × 7 m and two small storage pits with a space of ca. 5 m × 7 m as shown in Fig. 2.

4. Components and trailer required for storage and transportation

4.1 Shielding cask

Since the surface dose rate of the storage container, including the mercury target vessel used in the design beam operation conditions is very high, it was put into a shielding cask with a maximum thickness of 235 mm in the MLF with the purpose to secure a surface dose rate of less than 2 mSv/h at contact and stored in the RAM building for a prolonged period of time, still in its shielding cask. The size and weight of the shielding cask are ca. 2.2 m × 2.4 m ×3.3 m and 47 ton, respectively.

4.2 Shipping cask

Specialized type II shipping cask that can withstand a fall from a height of 1.6 m was used repeatedly to transport the shielding cask, including the used mercury target vessel. The size and weight of the shipping cask are ca. 3.2 m × 3.4 m × 4.0 m and 29 ton, respectively.

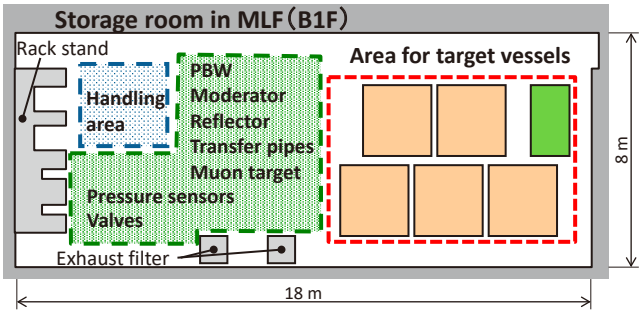

Figure 1. Storage room in MLF.

Figure 2. Storage pits in RAM building.

4.3 Trailer

A trailer was used to transport the vessel from the MLF to the RAM building. There are very few trailers that can accommodate the width (ca. 3.4 m) of the shipping cask, the total weight (ca. 81 ton) and the height of the building entrance (ca. 4.7 m) in MLF, so the lowboy trailer with a maximum capacity of 100 ton was selected.

5. Transportation from the MLF to the RAM building

The procedure for transporting the used mercury target vessel from the MLF to the RAM building is shown in Fig. 3. The used mercury target vessel covered with the storage container was moved from the storage room to the hot cell (1F) and placed in the shielding cask with a maximum thickness of 235 mm by remote handling. The shielding cask, including the used mercury target vessel, was moved to the large components handling room (3F), and then the airtightness, surface dose rate and surface contamination were inspected. The maximum surface dose rate of the shielding cask, including the used mercury target vessel #3, was 87 μSv/h. The shielding cask was moved to the components gateway (1F) and placed in the shipping cask on the trailer. The airtightness, surface dose rate and surface contamination of the shipping cask were inspected. The measurement results are shown in Table 2. Under traffic restrictions, the shipping cask, including the used mercury target vessel #3, was transported by the trailer within ca. 10 minutes to the RAM building which is ca. 300 m away from the MLF. The shielding cask, including the used mercury target vessel #3, was taken out from the shipping cask and then stored in the large storage pit in the RAM building. The transportation work, including the preparation, took 10 working days. After this transportation work, 5 used mercury target vessels were stored in the large storage pit and other radioactive components were stored in small storage pits. The shielding casks were removed from the large storage pit and visual and airtight inspections were conducted every year.

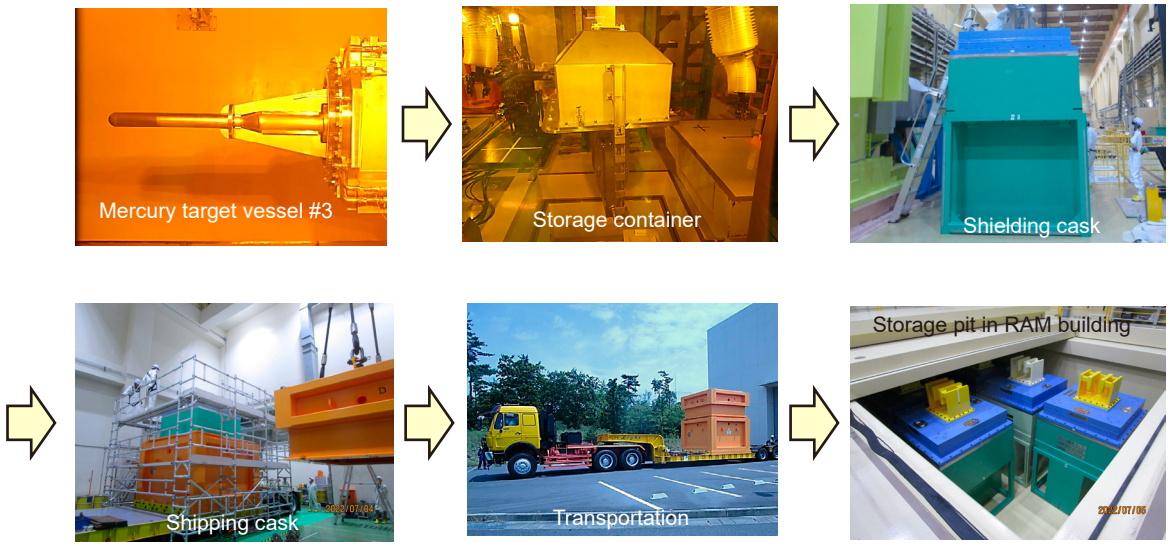

Figure 3. Transportation of used mercury target vessel from MLF to RAM building.

Table 2. Measurement results of dose rate and surface contamination density.

	Regulation	Results
Surface dose rate	< 2 mSv/h	7.5 μSv/h (Shipping cask) 0.5 μSv/h (Trailer)
Dose rate at 1 m	< 100 μSv/h	2.5 μSv/h (Shipping cask) 0.3 μSv/h (Trailer)
Dose rate at driver's seat	< 20 μSv/h	0.2 μSv/h (B.G.)
Surface contamination density	$\beta(\gamma) < 0.4$ Bq/cm^2 H-3 < 4 Bq/cm^2	$\beta(\gamma) < 0.4$ Bq/cm^2 H-3 < 4 Bq/cm^2

T. Wakui, A. Futakawa, T. Naoe, H. Kogawa, H. Kinoshita, M. Harada, T. Ito, M. Sekijima, and K. Haga
Neutron Source Section, Materials and Life Science Division, J-PARC Center

Preparation of the Proton Beam Window in 2022

1. Introduction

The proton beam window (PBW) is a boundary of the proton beam line and the neutron target in the Materials and Life Science Experimental Facility (MLF) (Fig. 1). The proton beam line is evacuated to a pressure of around 10^{-5} Pa. The neutron target is inserted into the helium vessel, which is filled with helium gas with ambient pressure. The PBW is irradiated with a 3 GeV proton beam, with current of 333 μA at maximum. Because of the radiation damage of the PBW material, the lifetime of the PBW is estimated to be 10 GWh and we replace the PBW every 3 years [1]. In 2020, PBW No.3 was replaced with PBW No.4, and the used PBW No.3 was stored in the drying room in the MLF to cool down the radioactive materials. Because the PBW was irradiated by a 3 GeV proton beam, it is highly radioactive. Even after 2 years cooling time, the PBW itself has high radioactivity. During this summer maintenance period, we replaced the used PBW mounted on the shielding plug with the new one using remote handling work.

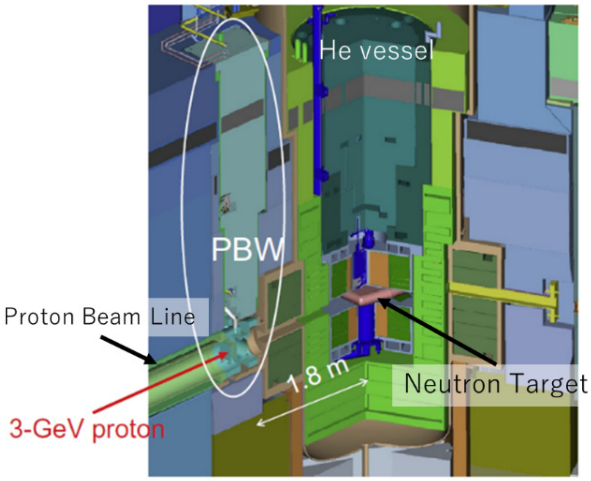

Figure 1. Bird's-eye view of the proton beam window.

2. Proton beam window (PBW)

Figure 2 shows the structure of the PBW. The PBW is made with two layers of aluminum plate (thickness 2.5 mm) and is cooled by water. The water channel is 3.0 mm thick, and the water velocity is 1.2 m/s at the beam window. The proton beam passes this aluminum wall. A pillow seal is used for the proton beam duct and remotely set and released for maintenance. The PBW's height is 4 m, including a shielding plug, and its weight is 10 tons. The PBW itself is replaced with a new one but the shielding plug is reused for the next PBW. Because the used PBW is highly radioactive, we have to do remote handling work to replace the PBW with a new one in the hot cell.

3. Handling of the PBW in the hot cell

The PBW handling work was done from July 25 to August 5, 2022. At first, the water pipes of the PBW were dried up in the drying room. Pipes above the shielding plug were cut by handy saw to improve the workability of the remote handling (Fig. 3). Then, the PBW was moved to the hot cell by shielding cask. The shielding cask has a 30 cm thick iron shield and remote handling gripper for the PBW shielding plug and reflector plug (Fig. 4).

The PBW was held by the remote handling device and its bolts were removed by a power manipulator. Then, the PBW was detached from the plug and passed to the cutting device for size reduction for storage.

The photo on the left side of Fig. 5 shows the PBW on the cutting device and the one on the right shows the process of cutting the pipes. The window itself was placed in a storage box and the pipes were cut by the cutting device (left of Fig. 5). Then, the PBW was stored in a storage room under the hot cell. The pipes, cut into three pieces, were put into another container (right of Fig. 5).

After the cutting process was completed, the new

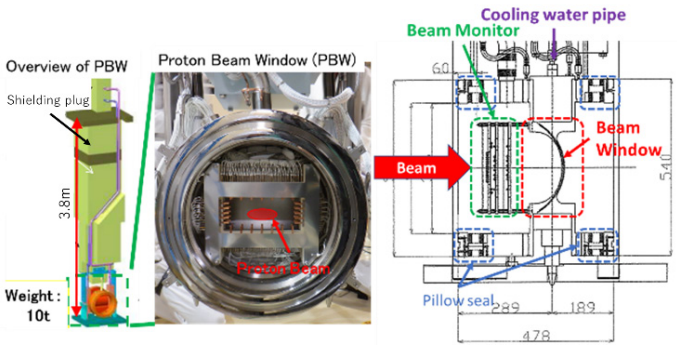

Figure 2. Structure of the proton beam window.

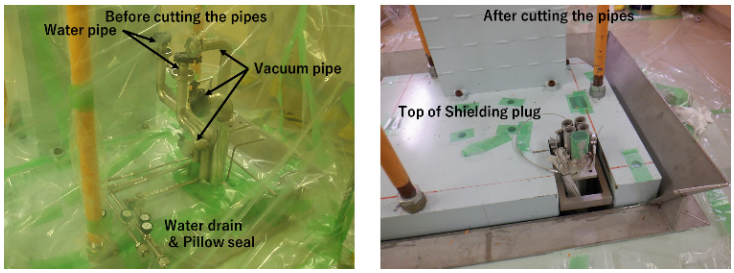

Figure 3. Pipe cutting above the shielding plug (Left: before cutting. Right: after cutting.)

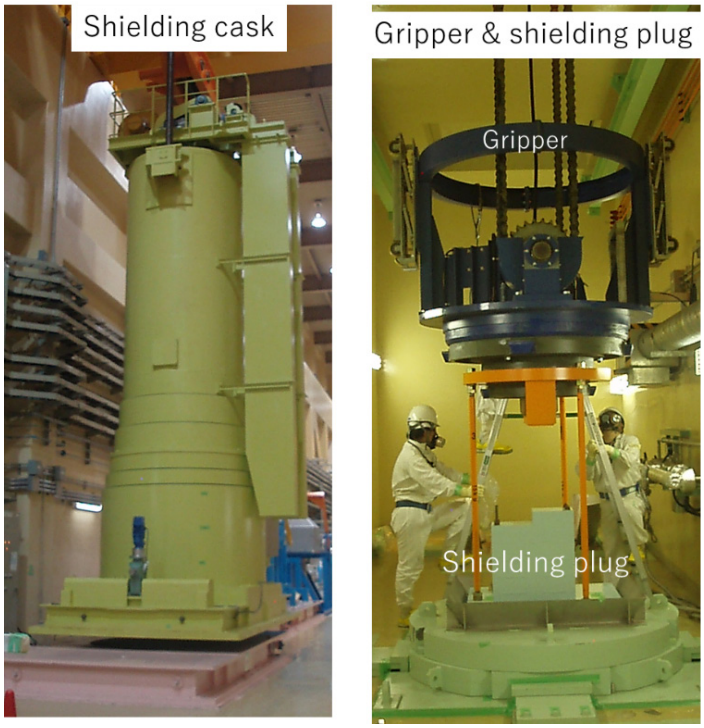

Figure 4. Shielding cask (left) and gripper of the cask (right).

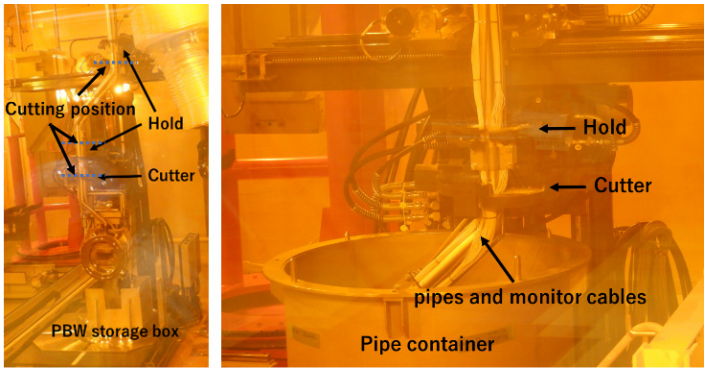

Figure 5. PBW on the cutting device (left). Cutting of the pipe (right).

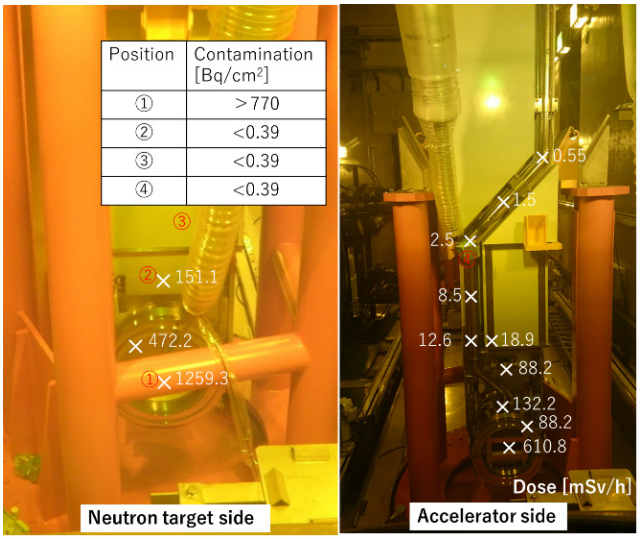

Figure 6. Results of the dose rate and surface contamination measurement of the PBW. The left figure shows the neutron target side and the right figure shows the accelerator side.

PBW was installed to the shielding plug by remote handling; then, it was stored in the drying room until the next replacement work.

4. Dose rate measurement of the PBW

Before removing the PBW from the shielding plug, the dose rate and surface contamination were measured. Figure 6 shows the dose distribution and surface contamination of the PBW and the shielding plug. The dose rate at the center of the window was the highest, it measured 1.26 Sv/h at 10 cm from the surface. The surface contamination of the PBW of the neutron target side was the highest and it was larger than 770 Bq/cm^2.

PBW No.3 was used from October 2017 to June 2020 and its accumulated beam power was 5.63 GWh. The dose measurement was conducted in August 2020.

5. Summary

The used PBW #3 was removed from the shielding plug and the new PBW #5 was installed, completing the preparations for the next PBW replacement in 2023.

6. Future plans

The lifetime of the PBW was estimated referring to the result of the post irradiation experiment (PIE) test of the PBW in PSI [2, 3]. Now we are preparing for the PIE test in the MLF.

References

[1] S. Meigo et al., J. Nucl. Mat. **450** 141–146 (2014).
[2] Y. Dai, Y. Foucher, M.R. James, B.M. Oliver, J. Nucl. Mater. **318** (2003) 167.
[3] Y. Dai, D. Hamaguchi, J. Nucl. Mater. **343** (2005) 184.

M. Ooi
Neutron Source Section, Materials and Life Science Division, J-PARC Center

Neutron Science

Neutron Science Section

1. Introduction

Even though we still suffer the consequences of the COVID-19 pandemic in Japan, the MLF has already been opened to foreign users in addition to Japanese users. The strict safety measures against the spread of new strains of the CORONA virus have already been lifted, although some restrictions for immigration still remain.

The user operation in the Materials and Life Science Experimental Facility (MLF) was also back to normal. The operation of the accelerator was quite stable, achieving 830 kW of operational power and over 95% operating rate, which have been the best performances ever in the MLF. Also, the numbers of MLF users are obviously recovering after COVID-19 as shown in Fig. 1.

2. User program

303 and 291 in general proposals (involving one-year proposals and new-user proposals) were submitted for the operation periods of 2022A and 2022B, respectively. The number of applied proposals has remained almost stable in recent years, and 266 of them were carried out in 2022. In addition, out of five long-term proposals, four have been approved. The trend of the total number of proposals is shown in Fig. 2. The number seems to be again similar to the number before COVID, in the range between 300 to 400 in each proposal round. The proposal competition rate is also quite constant.

3. Instruments up to date

Initially, 23 beamlines (BL) for neutron experiments were designed for future instruments in the MLF and 21 of them are under operation at the moment. Experiments performed in the MLF require variety of so-called sample environments (SE), which can tune physical conditions on sample, such as temperature, magnetic field, pressure, ambient gas, electrical field,

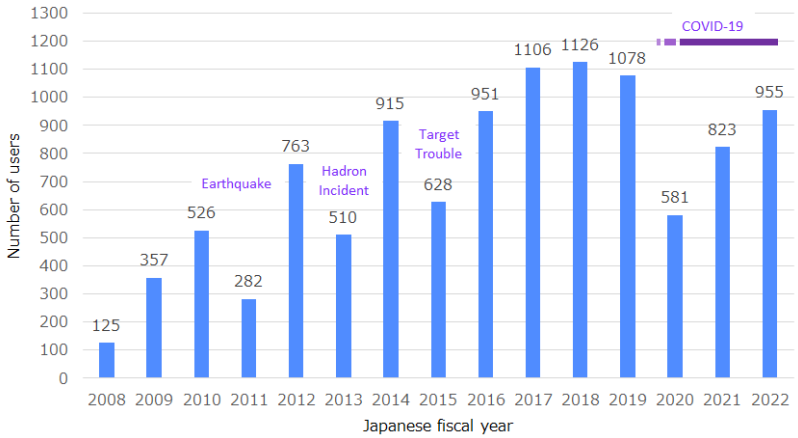

Figure 1. The number of unique users* in J-PARC MLF (*Number of issued personal dosimeters).

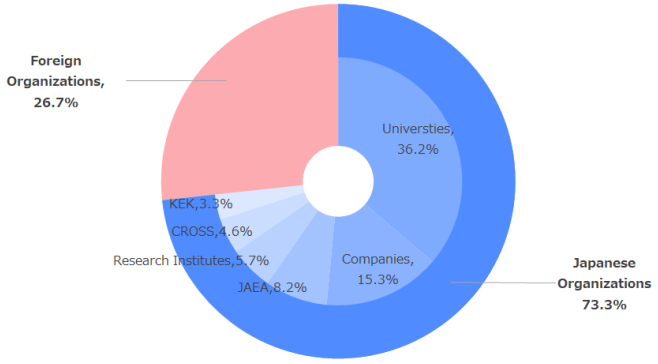

Figure 2. The breakdown for PI's affiliation of approved short term proposals in JFY2022.

and so on. The SE devices are the key to the success not only of the experiments themselves but also activating the facility. The versatile SE devices can attract many users from all over the world. All BL in the MLF keep making effort to install and develop new or characteristic SE devices for advanced experiments.

The newly designed Paris-Edinburgh high-pressure apparatus has been developed for investigating properties of quantum harmonic oscillators under pressure of hydrogen material. Hydrogen vibration excitations of fluorite-type $ZrH_{1.8}$ and $TiH_{1.84}$ were investigated at pressures up to 21 GPa by incoherent inelastic neutron scattering experiments. From the pressure dependence of lattice parameters determined by diffraction experiments, the relations between metal-hydrogen distance and the first excitation energy E_1 of $ZrH_{1.8}$ and $TiH_{1.84}$ at high-pressures were found [1]. The developed high-pressure system for this experiment is depicted in Fig. 3.

Most of the neutron experiments are facing the background (BG) issues, in particular the BG from the sample container/cavity, which sometimes causes seriously distorted interpretation of the obtained data. A team of BL02 (DNA) developed a low-background sample container (sample-cell) specifically for aqueous protein solution samples, to be used with a neutron back-scattering spectrometer (Fig. 4). It was found that the scattering intensity of an aluminum sample-cell coated with boehmite using D_2O was lower than that of a sample cell coated with regular water (H_2O). Meticulous attention to cells with small individual weight differences and the positional reproducibility of the sample cell relative to the spectrometer neutron beam position enabled the accurate subtraction of the scattering profiles of the D_2O buffer and the sample container. Consequently, high-quality information on protein dynamics could be extracted from diluted protein solutions [2].

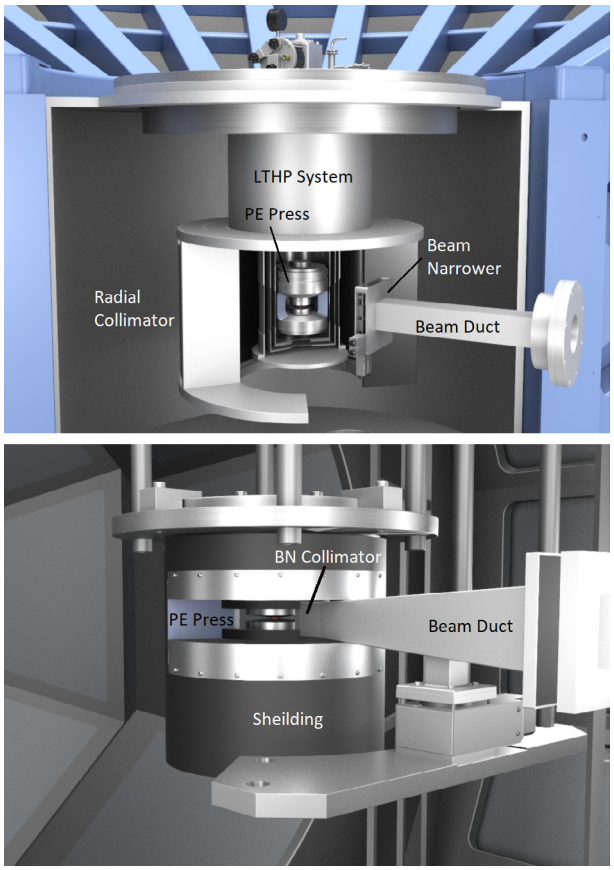

Figure 3. The Paris-Edinburgh cell for inelastic scattering experiments at high pressure installed at (top) BL01 and (bottom) BL21 [1].

4. Other activities

The 11th International Workshop on Sample Environment at Scattering Facilities (ISSE-WS) was held in Nasu, Japan from August 28 to September 1. This workshop series takes place every 2 years under the patronage of the International Society for Sample Environment (ISSE). Engineers, technicians and scientists working on sample environment at the neutron/synchrotron facilities in the world and industrial partners participate in this workshop to present various topics related to sample environment and to discuss new techniques, collaboration among facilities and so on. There were 87 participants, including five online participants, gathered in Japan from 11 countries [3]. Also, some of the other activities were as follows: The Commissioning Workshop of ESS & J-PARC collaboration (October 10, 2022); The 6th Neutron Muon School (December 12 to

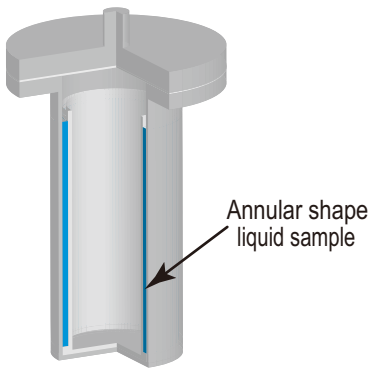

Figure 4. Cross section of a cylindrical aluminum container commonly used for neutron quasi-elastic scattering [2].

16, 2022); Quantum Beam Science Festa 2022 in Tsukuba (March 13 to 15, 2023).

5. Scientific achievements

Important scientific outcomes are frequently produced from the MLF neutron activities. In 2022, the number of published papers was 208, also, 11 press releases were done. One of the achievements was introduced in the article "Development of Metal Exhibiting Gigantic Elastic Strain Exceeding 4.3% ~ Expectations for Application to High Performance Spring Materials by Realization of Large Elastic Deformation ~" [4].

The compatibility of low Young's modulus and high strength has been a challenge for artificial bones, dental materials, springs, other mechanical element parts, etc. Bulk single crystals in a copper-aluminum-manganese alloy system with large crystal elastic anisotropy were successfully synthesized. Structural analysis by in situ neutron diffraction during tensile tests at the MLF TAKUMI revealed that the crystal lattice expands and contracts while maintaining its structure. The alloy has unparalleled properties in terms of elastic strain and Young's modulus compared to conventional materials, and is expected to be applied to high-performance springs, connectors, sealing materials, precision machinery, medical equipment, etc.

6. Award

MLF won two awards this year. The JSNS (Japanese Society for Neutron Science) Encouragement Award: Dr. Wu Gong for "Studies on Microstructure Evolution and Mechanical Properties in Structural Metallic Materials by in-situ Neutron Diffraction", and the JSNS Poster Award: Dr. Wenqi Mao for "Effect of Grain Refinement on Deformation-induced Martensitic Transformation".

References

[1] T. Hattori et al., Phys. Rev. B, **106** 134309 (2022).
[2] T. Tominaga et al., Life, **12** 675 (2022).
[3] S. Ohira-Kawamura, Neutron News, **34** 2 (2023).
[4] S. Xu et al., Nature Communications, **13** 5307 (2022).

M. Nakamura[1], T. Yokoo[1,2], and A. Sano-Furukawa[1]
[1]Neutron Science Section, Materials and Life Science Division, J-PARC Center; [2]Institute of Materials Structure Science, KEK

BL01: 4D-Space Access Neutron Spectrometer 4SEASONS

1. Introduction and use trends

4SEASONS is a direct-geometry time-of-flight neutron spectrometer for thermal neutrons, and one of the Public Beamlines in the MLF [1]. In 2022, 16 General Use (short-term) proposals, 1 Long-Term proposal, 1 Fast-Track proposal, and 1 Instrument Group Use proposal were approved for 4SEASONS. 10 reserved proposals were given beamtime to compensate for the vacancy. Conversely, one General Use proposal was postponed to 2023 because of an instrument trouble. 72% of the General Use proposals were submitted by international users. 61% of the submitted proposals were in the field of magnetism, while the rest of them targeted phonons and other atomic vibrations. 14 peer-reviewed papers were published.

2. Instrument upgrade

Detectors: 4SEASONS utilizes 2.5-m-long position sensitive ^{3}He detectors (PSDs) to cover a wide solid angle. However, this kind of detector tends to cause pile-up when it detects strong neutron counts [2], which results in spurious signals in the processed data. To mitigate the problem, we are introducing the pulse-width-and-height (PWH) limitation function of a new detector electronic module (new NEUNET [3]). Following the preliminary work in 2021, we performed a test measurement in 2022 to evaluate the effectiveness of the function for eliminating the spurious signals. We applied one new NEUNET board to 8 PSD tubes, and observed two strong Bragg peaks of a single crystal of $SrTiO_3$ and spurious streak signal caused by them [Fig. 1(a)]. Figure 1(b) shows position dependence of the intensity along the tube in which the strong spurious signal was observed. There is a broad spurious signal over the tube in addition to the strong Bragg peaks at both ends. By applying the PWH limitation, the spurious signal was reduced by a factor of five. Although this reduction is outstanding, finite spurious signal still remained [Fig. 1(b)-B]. Then, we further applied rejection of high-count-rate signals. By rejecting the signals over 80 kcps, the spurious signal was reduced to the background level [Fig. 1(b)-C]. This work was published in Ref. [4]. We are considering applying the new NEUNET boards and the function to all the PSDs.

Disk chopper: 4SEASONS had been utilizing two disk choppers rotating at 25 Hz at maximum to define the wavelength band of the incident beam. In 2022, the disk chopper placed on the downstream side was replaced with a new one [Fig. 2(a)]. The new disk chopper was developed by the Technology Development Section of the MLF and has a maximum rotation speed of 50 Hz. The high rotation speed is expected to cut the unnecessary neutron wavelength band more sharply without interfering with the usable band. We measured the transmission of the new disk chopper with a vanadium standard and white beam with several phase delays. Figure 2(b) compares the observed and calculated transmission curves for one of the phase delays. Both curves show good agreement proving the chopper was manufactured as designed.

Sample environment: 4SEASONS had recently prepared several new sample environment devices. One is a new sample stick for the top-loading GM refrigerator; it can heat a sample up to 500 K. Another one is a bottom-loading GM refrigerator, which can cool a sample down to 4 K, and is expected to provide lower background environment compared with the top-loading refrigerator. In 2022 we performed test operations of these devices, and confirmed the designed performances. We also introduced a remote-control system for the bottom

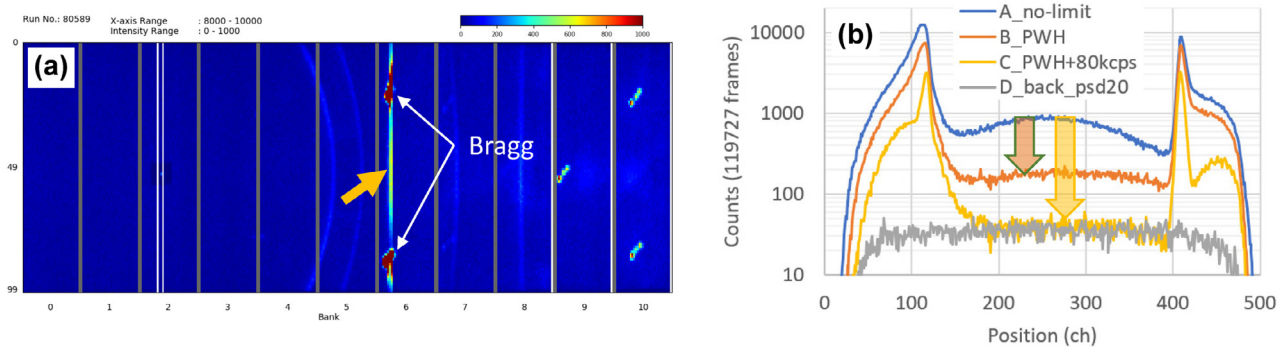

Figure 1. (a) Bragg peaks (white arrows) and spurious streak (orange arrow) detected on the PSDs. The incident energy (E_i) was 26.3 meV. (b) Position dependence of the intensity of the Bragg peaks and the spurious signal [4].

loader, which can monitor and control the compressor of the refrigerator remotely through the software IROHA2 [5]. In addition, we purchased a new cryofurnace, which is designed to heat the sample up to 750 K. The cryofurnace will be open to users next year after commissioning work is completed.

Vacuum system: The vacuum system to evacuate or vent the scattering chamber of 4SEASONS consists of a roughing pump, a turbo-molecular pump, and a cryopump. It was significantly upgraded in 2022. First, the roughing pump was replaced with a pair of new roughing pumps, which provide higher pumping power near the atmospheric pressure compared with the previous pump [Fig. 3(a)]. Second, a set of air dryers was incorporated into the system [Fig. 3(b)]. This set of air dryer introduces dry air into the chamber during venting to minimize moisture absorption by the chamber walls. Lastly, the controller of the vacuum system was renewed to operate the pumps and relevant valves automatically. These upgrades enable a faster and safer operation of the system.

Acknowledgements

We thank R. Komine, H. Hasemi, H. Tanaka, K. Inoue, and W. Kambara for their support and advice. The on-beam test of NEUNET was performed with the help of S. Sato. The instrumentation works described here were supported by the engineers of the Neutron Science Section and the Technology Development Section of the MLF.

References

[1] R. Kajimoto et al., J. Phys. Soc. Jpn. **80**, SB025 (2011).
[2] D. Raspino et al., 2015 IEEE Nuclear Science Symposium and Medical Imaging Conference, doi: 10.1109/NSSMIC.2015.7581915.
[3] S. Sato et al., EPJ Web of Conferences **231**, 05004 (2020).
[4] S. Sato et al., J. Neutron Res. **24**, 427 (2022).
[5] T. Nakatani et al., JPS Conf. Proc. **8**, 036013 (2015).

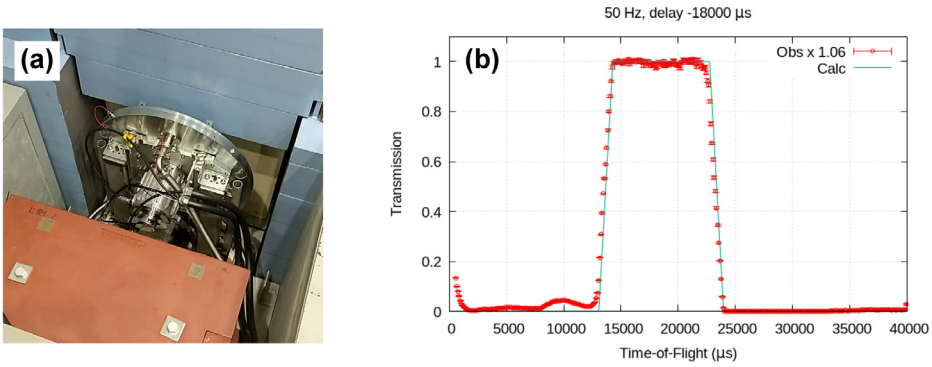

Figure 2. (a) Renewed disk chopper. (b) Transmission curve of the disk chopper operated at 50 Hz as a function of time. The phase delay is −18000 μs. Symbols and lines denote the observed and calculated curves, respectively.

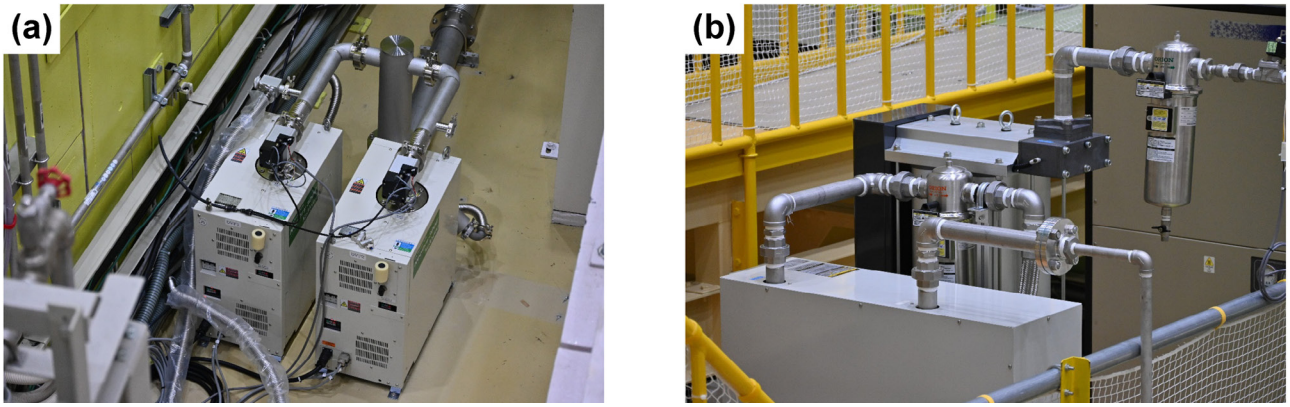

Figure 3. (a) New roughing pumps (Kashiyama NeoDry300E). (b) The set of air-dryers (Orion Q700B-EDCT and RAX55F).

R. Kajimoto[1], M. Nakamura[1], K. Kamazawa[2], Y. Inamura[1], K. Iida[2], K. Ikeuchi[2], and M. Ishikado[2]
[1]Neutron Science Section, Materials and Life Science Division, J-PARC Center; [2]Neutron Science and Technology Center, CROSS

Current Status of BL02 DNA in 2022

1. Introduction

DNA is a TOF type Si crystal analyzer backscattering spectrometer installed at the neutron spallation source of the Japan Proton Accelerator Research Complex (J-PARC) [1, 2]. DNA uses a pulse-shaping chopper to extract pulsed neutrons with sharp time-structure from strong but broad ones of the coupled moderator, which achieves μeV-order energy resolution in wide energy transfers of the meV-order. Furthermore, the signal-to-noise ratio at DNA achieves ~10^5, which makes it possible to cover a variety of research fields with small scattering amplitudes or with small quantities of samples (of the order of milligrams).

The number of peer-reviewed papers from DNA in 2022 was 14, including 1 proceedings paper, and it has continued to increase since 2017. Five press releases of high-impact results were issued in 2022. In addition, Mr. Yuki Hirota, who is third-year doctoral student at Setsunan University, stayed as a "JAEA Fellow of advanced science" for three months to conduct research on the dynamics of water within chitin and chitosan for the application of polysaccharides to fuel cell membranes. The outcomes were compiled in two original papers [3, 4], and he successfully completed his degree in September 2023.

2. User Program in the periods 2021B and 2022A

In 2022, 26 (2021B) and 17 (2022A) General Proposals (GP) were submitted to BL02. 7 GPs, including 2 New User Promotion (NUP), and 11 GPs including 2 NUP's were approved for 2021B and 2022A, respectively. The ratio of the approved beamtimes to total proposed beamtimes was 18% for 2021B and 63% for 2022A. The competition rate was high: 3.7 and 1.5 for 2021B and 2022A, respectively. Additionally, 3 and 1 reserved proposals were also conducted in 2021B and 2022A, respectively.

After the recovery from the pandemic situation, almost all experiments were conducted with the users present. In addition, 2 General Proposals (Long Term Program) (hereafter LTP) ran at BL02 in 2021B and 2022A.

3. Beamline activities

In DNA, a focusing mirror is placed just before the sample to increase the neutron flux. The focusing mirror installed at the time of construction had low neutron reflectivity, so we replaced it with highly reflective mirrors in 2021. It was confirmed that the neutron flux measured by gold foil irradiation doubled compared to the amount before the replacement. The $I(\lambda)$ at the sample position also doubled in all energy regions up to 20 meV. Additionally, the beam became more focused after the replacement, as shown in the lower pictures of Fig. 1. Together with the replacement of the focusing mirror, the steel guide jackets of the focusing mirror were also replaced with new nonmagnetic ones. This replacement enabled us to use safely the magnet developed for BL02 without the interference from the magnetic steel materials.

Although DNA has already achieved a very high signal-to-noise ratio of ~10^5, the split elastic line from the sample environmental instruments interferes with the QENS signal. In 2021, we introduced an oscillating radial collimator that successfully reduced the background from the sample environment equipment. In particular, the background for the Si311 analyzer, which contains the Bragg reflection of Al, was greatly reduced, as shown in Fig. 2 for the Vanadium standard sample before and after introducing the oscillating radial collimator. Now, the Si311 analyzer data have become clean and ready for practical use.

In recent years, we have continued to work on the automation of our equipment. We used to operate

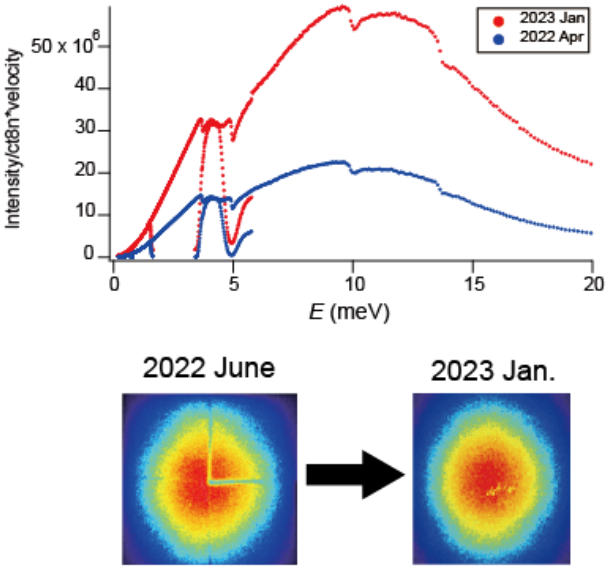

Figure 1. (Upper) $I(\lambda)$ measured at sample position before (April 2022) and after (January 2023) the replacement of the focusing mirror. (Lower) Beam intensity distribution before and after the replacement.

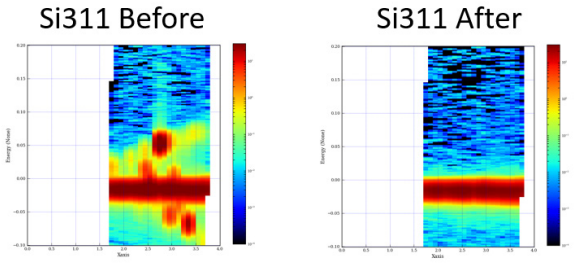

Figure 2. Intensity map of Vanadium standard in *Q*(horizontal)-*E*(vertical) map obtained with Si311 analyzer before and after introducing the oscillating radial collimator.

manually the high voltage power supply for the ^{3}He inelastic detectors and had to wait until the prescribed vacuum level has been reached after replacing the sample environment equipment. To resolve this situation, we replaced the high voltage power supply with a new system, which can be remotely controlled. The commissioning for the automatic operation has been proceeding this year.

As for the software development, we are developing a kernel density estimation (KDE) method. In 2021, we estimated the error bars for the fitting parameter using actual QENS data and found that the KDE method improved the fitting error, especially for data with low statistics.

In parallel with the development of new equipment and software, we are also working on the problems of aging. Followed by the replacement of two banks with damaged Si111 analyzer mirrors in 2021, two more of the Si111 analyzer mirrors at scattering angles (2θ) of $7.5° < 2\theta < 16.5°$ and $43.5° < 2\theta < 52.5°$ were successfully replaced in 2022, which improved the homogeneity of the QENS signal.

Unfortunately, breakage of the timing cable of the inelastic detector located in the vacuum chamber was discovered at the end of the long maintenance period, which excluded DNA from the user program in December. After the replacement of the cable with a new one during the year-end shutdown, the DNA data acquisition system safely restarted. User beamtimes cancelled due to the trouble at the timing cable were all reallocated in the supplemental MLF operation for over one month that the government decided for compensation against the rapid raise of electricity rate. During the replacement of the cable, we found that some of the other cables have hardened and may break in near future. We plan to replace all these cables in the vacuum chamber in the summer long shutdown of 2023. Since the hardening of the cable sheath materials occurred 10 years after the construction was completed, we decided to renew all the cables in the vacuum chamber every 10 years.

4. Other activities

The 'Basis for supporting innovative drug discovery and life science research (BINDS)' is a national project aimed at accelerating Japanese life science by providing a range of technologies to life and pharmacy scientists. Neutron probe is regarded as one of the promising technologies since 2022 (Phase 2 of BINDS) and BL02 at the MLF supports utilization by the BINDS program for innovative studies on protein dynamics within our instrument group beamtime. We aim at contributing to outstanding life science research through successful measurements of dilute protein solution samples.

5. Future plans

We will proceed further with the replacement of the damaged Si111 analyzer mirrors. At the same time, we plan to make a new N_2 monitor and ^{3}He detectors, which will be safe from the aging caused by the strong pulsed neutrons of the MLF.

References

[1] Kaoru SHIBATA et. al., JPS Conference Proceedings, **8** (2015), 036022.
[2] Y. Kawakita et al., EPJ Web of Conferences **272** (2022) 02002.
[3] Y. Hirota et al., Bioengineering **9** (2022) 599.
[4] Y. Hirota et al., Bioengineering **10** (2023) 62.

M. Matsuura[1], Y. Kawakita[2], T. Yamada[1], T. Tominaga[1], H. Tamatsukuri[2], H. Nakagawa[2,3], and K. Tatsumi[4]
[1]Neutron Science and Technology Center,CROSS, [2]Neutron Science Section, Materials and Life Science Division, J-PARC Center [3]Materials Sciences Research Center, JAEA, [4]Technology Development Section, Materials and Life Science Division, J-PARC Center

IBARAKI Biological Crystal Diffractometer iBIX

1. Introduction

The complementary use of both neutron diffraction data and X-ray diffraction data is one of the powerful methods to obtain the structure information of all atoms in the protein samples because neutron diffraction data include more information about hydrogen (deuterium) atoms, and X-ray diffraction data include more information about non-hydrogen atoms. Understanding the enzyme chemistry of proteins at the atomic level requires the visualization of hydrogen atoms at active sites and remote residues, co-factors, substrates, and water molecules. IBARAKI biological crystal diffractometer, iBIX is a TOF neutron single crystal diffractometer to elucidate the hydrogen, protonation, and hydration structure of mainly biological macro-molecules [1, 2]. In 2019, the iBIX diffractometer, equipped with 34 detectors, was available for user experiments on mainly biological macromolecules, organic compounds, and polymer samples. The specifications of iBIX are shown in Table 1.

2. Current status

In 2022, J-PARC was operated regularly at an accelerator power of 800 kW. We were able to collect a full data set of biological macromolecules for neutron structure analysis with around 2.0 Å resolution in less than one week by using the iBIX at the accelerator power of 700 kW. The maximum unit cell size was 135 × 135 × 135 $Å^3$. The typical crystal volume of the sample measured by the iBIX was around 1.0 mm^3. In 2022, neutron protein structure analysis with iBIX is supported by BINDS (Basis for supporting innovation drug discovery and life science research). Using the iBIX, the following tests were performed: 1 test measurement for industrial use proposal (applied from BINDS), 2 test measurements for a J-PARC proposal, 6 test measurements for a proposal of an innovative research project of the Ibaraki Neutron Beamline and 6 test measurements for a proposal of a leading research project of the Ibaraki Neutron Beamline. Subsequently, 9 proposals were moved on to the full data collection for neutron structure analysis.

3. Maintenance and development

It has been over 10 years since the iBIX instrument was installed on the beamline, so some of the beamline instruments have been already replaced in the last few years due to age deterioration. One of the remaining instruments due for replacement is the disk-chopper. The cumulative time of servomotor rotation has exceeded the service life. We replaced the servomotor and the servo amplifier of the disk chopper (Fig. 1).

Table1. Specifications of iBIX.

Moderator	Coupled
Range of wavelength of incident neutron (Å)	0.7 ~ 4.0 (1^{st} frame) 4.0 ~ 8.0 (2^{nd} frame)
Neutron intensity ($n/s/cm^2$) (@1 MW)	0.7×10^8
L_1 (m)	40
L_2 (mm)	491
Solid angle of detectors (% for 4π str)	22.0
Detector covered region (deg.)	15.5 ~168.5
Detector size (mm^2)	133 × 133
Detectors pixel size (mm^2)	0.52 × 0.52
No. of detectors	34
Sample environment	Gas flow type cooling system by N_2 gas (~100 K)
	Heating system for polymer sample (~600 K)
	Tensile loading system for polymer sample (~200 N, ~90 mm, 1~1000 mm/sec)

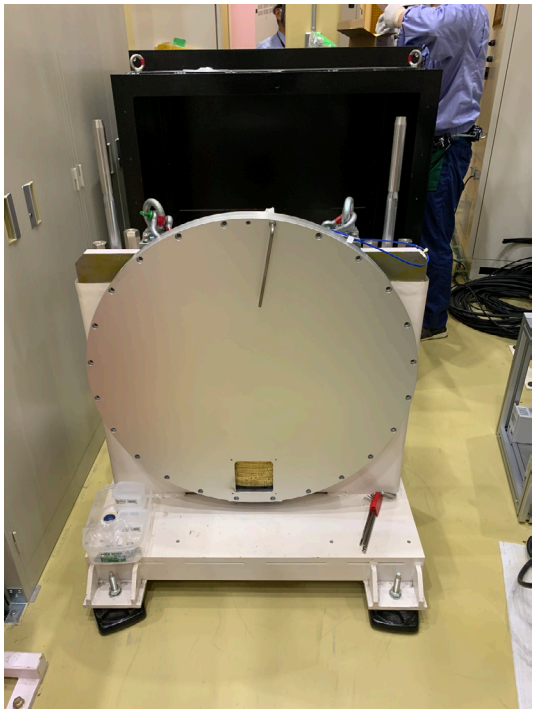

Figure 1. Neutron disk-chopper for iBIX.

The disk-chopper system is already available for user experiments.

The measurement software of iBIX is renewed based on the standard instrument control software framework of the MLF (IROHA2). We can carry out the operation and monitor the devices (detector, goniometer, and chopper) under the remote access environment. We are able to use all its functions under a multi-platform environment (Windows, Mac, Linux etc.) via a web browser (e.g. at AQBRC with J-LAN network).

4. Future plans

In the near future, the accelerator power of J-PARC will increase to about 1 MW. iBIX should be available regularly for full data-set measurement of samples with a volume of less than 1 mm^3. However, the sample size is still large, and the measurement time is still long, especially for the users. We would like to reduce the difficulties of preparation of a large crystal as much as possible. In other words, it is necessary to further improve the measurement efficiency of iBIX by developing the beamline instrument. Currently, we are considering the possibilities for improvement of the measurement efficiency. Furthermore, to automatize the measurement process, firstly we will develop a new goniometer with an automatic sample centering system and control software. As the next step, we will develop a simple automatic sample changer. And then, we will realize the test measurement under the remote access environment (without entering and leaving the experimental hatch).

To promote the industrial use of iBIX, we will enhance the support system and exploration of materials field research. That will include, for example, development of a new sample environment and a new measurement method and so on.

References

[1] I. Tanaka, K. Kusaka, T. Hosoya, N. Niimura, T. Ohhara, K. Kurihara, T. Yamada, Y. Ohni-shi, K. Tomoyori and T. Yokoyama, Acta Cryst., **D66** 1194 (2010).

[2] K. Kusaka, T. Hosoya, T. Yamada, K. Tomoyori, T. Ohhara, M. Katagiri, K. Kurihara, I. Tanaka and N. Niimura, J. Synchrotron Rad., **20** 994 (2013).

K. Kusaka, T. Yamada, N. Yano, T. Hosoya, and I. Tanaka
Frontier Research Center for Applied Atomic Sciences, Ibaraki University

Resonance Parameter Analysis in Double-bunch mode at MLF (BL04 ANNRI)

1. Introduction

Neutron cross sections, particularly in the epithermal neutron energy range, can be reproduced by resonance formalisms with parameters. The resonance parameters can be determined by the cross-section measurements and the resonance shape fitting. The evaluated resonance parameters are listed in nuclear data libraries: JENDL [1], ENDF/B [2], and JEFF [3], which are used for studies of nuclear technology, radiation, and physics. The Accurate Neutron-Nucleus Reaction measurement Instrument (ANNRI) in the Material and Life science experimental Facility (MLF) was constructed to measure the neutron cross sections [4, 5]. In the MLF, proton beam incident is injected into the spallation target of the MLF in a double-bunch mode to increase neutron beam intensity. In this mode, one pulsed proton beam consists of two groups of protons 600 ns apart from each other. This double-bunch mode turns one resonance into two peaks at a high neutron energy region, especially more than several tens eV. This is why it is necessary to take into account the double-bunch structure in the shape fitting to derive the correct resonance parameters. In this study, we incorporated the effect of double-bunch structure into a resonance analysis code, REFIT [6], and adapted it to determine the resonance parameters.

2. Implementation of the double-bunch effect

Figure 1 shows the time distribution of the proton current measured by the current transfer monitor in the MLF [7]. The width of the proton beam is approximately 100 ns, and the shape (red) is slightly distorted compared to the Gaussian distribution. The black line represents two Gaussian distributions with FWHM of 100 ns for reference.

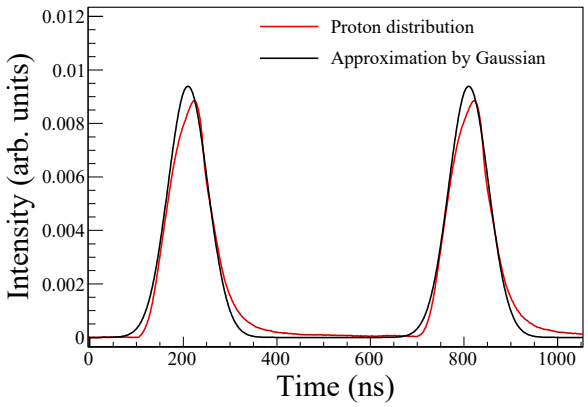

Figure 1. Time distribution of proton current measured by the current transfer monitor in the MLF and two gaussian distributions.

In addition to the time distribution of the proton beam, there is a resolution function, $\psi(E_n, t)$, which comes from the time distribution of neutrons caused by the deceleration of the neutron velocity in a moderator. The resolution function in ANNRI was reported by Kino et al. [8]. The double-bunch effect was taken into account by convolving the time distribution of protons, $h(t)$, with this resolution function as follows:

$$\psi'(E_n, t) = \int \psi(E_n, \tau) h(t - \tau) d\tau$$

where $\psi'(E_n, t)$ is the modified resolution function which denotes the time distribution of neutrons on the moderator surface.

3. Resonance analysis and results

The neutron capture and total cross sections of ^{181}Ta were measured in ANNRI. The details of the experiment and analysis are described in Ref [9]. Here, we just report on the effects of proton distributions on resonance analysis using these data.

The resonance parameters were obtained by fitting the experimental data with resonance formula using REFIT. For comparison, the fittings were performed using the proton distributions of single- and double-bunches in Figs. 2 and 3. The proton distribution of the single-bunch was assumed to be a single Gaussian distribution with FWHM of 100 ns. Table 1 lists the obtained resonance parameters, together with the values of JENDL-4.0 [10].

In the low energy region (Fig. 2), the effect of the double-bunch is small, and it appears that the fitting results for two proton distributions do not show significant differences. However, the gamma widths in the single-bunch tend to be a little larger than those of the double-bunch because the resonance broadening due to the double-bunch affects the resonance parameters. On the other hand, in the high energy region (Fig. 3), the figure indicates that the fitting is no longer possible with the distribution of single-bunch. The experimental data, especially the capture cross section, clearly shows that the double-bunch makes one resonance two peaks.

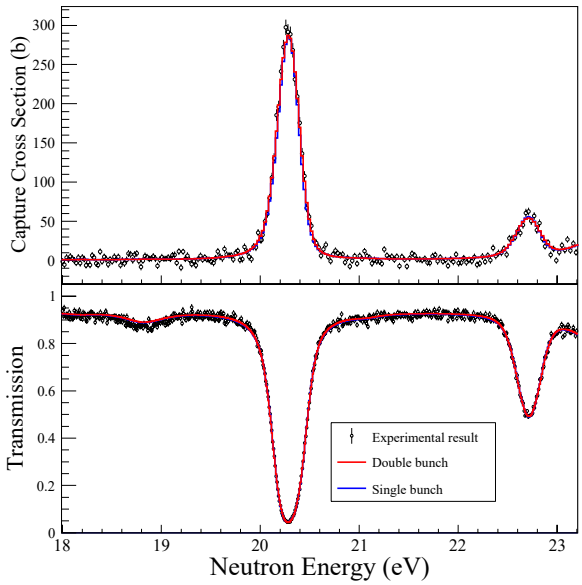

Figure 2. Fitting results and experimental results in the low neutron energy region.

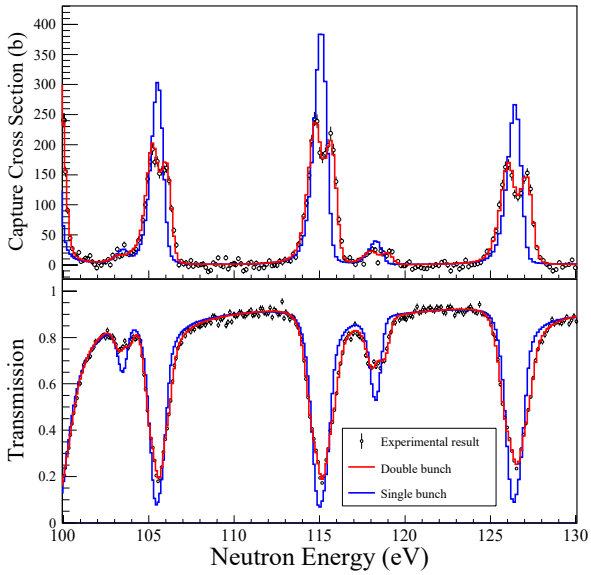

Figure 3. Fitting results and experimental results in the high neutron energy region.

Table 1. Obtained resonance parameters.

	Resonance Energy (eV)	Gamma width (meV)	Neutron width (meV)
Double-bunch	20.293 ± 0.001	55.5 ± 0.6	1.042 ± 0.003
Single-bunch	20.298 ± 0.001	61.2 ± 0.7	1.003 ± 0.003
JENDL-4.0 [10]	20.29	52.0	1.097
Double-bunch	115.03 ± 0.01	44.9 ± 1.4	39.9 ± 0.5
Single-bunch	115.09 ± 0.01	64.6 ± 2.0	29.7 ± 0.4
JENDL-4.0 [10]	115.08	57.0	39.6

Therefore, taking into account the double-bunch structure is essential for deriving resonance parameters.

4. Conclusion

In order to derive the resonance parameters from the capture and total cross sections of ^{181}Ta measured in ANNRI of MLF, the fitting was employed with REFIT in which the double-bunch structure of the MLF is considered. The comparison is made with the result for which a single-bunch proton distribution was adopted. From this research, it was found that the application of a double-bunch structure to the fitting has an essential role to perform resonance analysis of experimental data.

References

[1] O. Iwamoto et al., Jour. Nucl. Sci. Technol., **60**, 1 (2023).
[2] D. Brown et al., Nucl. Data Sheets, **148**, 1 (2018).
[3] A. J. M. Plompen et al., Eur. Phys. Jour. A, **56**, 181 (2020).
[4] M. Igashira et al., Nucl. Inst. Meth. A, **600**, 332-334 (2009).
[5] A. Kimura et al., Jour. Nucl. Sci. Technol., **49**, 708-724 (2012).
[6] M. C. Moxon et al., NEA-0914/08, Organization for Economic Co-operation and Development, Nuclear Energy Agency (2011).
[7] S. Endo et al., Jour. Nucl. Sci. Technol., **59**, 318 (2021).
[8] K. Kino et al., Nucl. Instr. Meth. A, **736**, 66 (2014).
[9] S. Endo et al., Nucl. Sci. Eng., (2023) published online.
[10] K. Shibata et al., Jour. Nucl. Sci. Technol., **48**, 1 (2011).

S. Endo[1,2], A. Kimura[1,2], S. Nakamura[1,2], G. Rovira[1], O. Iwamoto[1], and N. Iwamoto[1]
[1]*Nuclear Data Center, Nuclear Science and Engineering Center, JAEA;* [2]*Neutron Science Section, Materials and Life Science Division, J-PARC Center*

Status of Fundamental Physics Beamline BL05 (NOP) in 2022

1. Introduction

Neutron Optics and Physics (NOP/ BL05) at the MLF in J-PARC is a beamline for studies in the field of fundamental physics. The beamline is divided at the upstream into three branches, the so-called Polarized, Unpolarized, and Low-Divergence branches, used in different experiments in a parallel way [1-2].

A neutron lifetime measurement is conducted at the Polarized beam branch with a spin flip chopper. Pulsed ultra-cold neutrons (UCNs) by a Doppler shifter are available at the Unpolarized beam branch. At the Low-Divergence beam branch, the search for an unknown intermediate force is performed by measuring neutron scattering with nano particles. The beamline is used also for R&D of optical elements and detectors.

2. Measurement of the neutron lifetime

The decay of neutrons is closely related to the mechanism of the synthesis of elements in the universe and to particle physics. The neutron lifetime has been measured in two ways: 1) by counting the incident neutrons and the protons from neutron beta decay (beam method) and 2) by storing UCNs in a container and determining the neutron lifetime according to the disappearing time (storage method). Currently, the lifetime determined via the former method is 888.0 ± 2.0 s, and that for the latter is 878.4 ± 0.5 s, with a difference of 9.5 s (4.6 σ) [3]. This discrepancy is called "neutron lifetime puzzle" and has remained unsolved for nearly 20 years. The smaller decays compared with the disappearance suggest that neutrons are lost owing to decay into dark matter or collisions with dark matter. In general, different methods are needed to validate the experimental results, as utilizing the same experimental methods may lead to the same mistakes. Using the polarization beam branch at NOP/BL05, an experiment was conducted via a different method, in which instead of protons, electrons were measured from the neutron beta decays. The first lifetime result was published in 2020 as $898 \pm 10(stat.)^{+15}_{-18}$ (*syst.*)s, which is consistent with both the beam and bottle methods [4]. A spin-flip chopper (SFC), which shapes the neutron beam into bunches, was replaced with a larger one in 2020, and the intensity was increased by 3 times [5]. Commissioning began in 2021, and physics run for the neutron lifetime began after the SFC was tuned. So far, a statistical uncertainty achieved at 1.5 s, and another 100 days of beamtime brings it to 1 s. The largest source of systematic uncertainty is undefined background. Research is underway to resolve this background event.

3. Measurement of diffuse scattering of ultracold neutrons

UCNs are transported through guide tubes like a dilute gas, with losses due to absorption and inelastic scattering by the nuclei in the tube walls. Diffuse reflections at the guide surfaces increase the losses because they make the UCN residence times longer. Therefore, for a correct estimation of the UCN transport, it is necessary to accurately estimate the effect of diffuse reflection. For this purpose, a setup for diffuse scattering of UCN was constructed with the Doppler shifter-type pulsed UCN source of BL05 (Fig. 1) [6].

When diffuse scattering occurs in the guide tube, the spectrum of time-of-flight (TOF) distribution changes due to the large orbit dispersion. In this experiment,

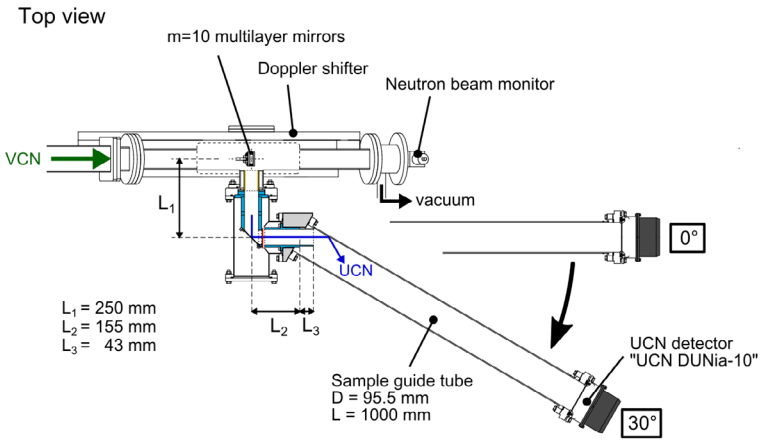

Figure 1. Schematic diagram of the experimental setup.

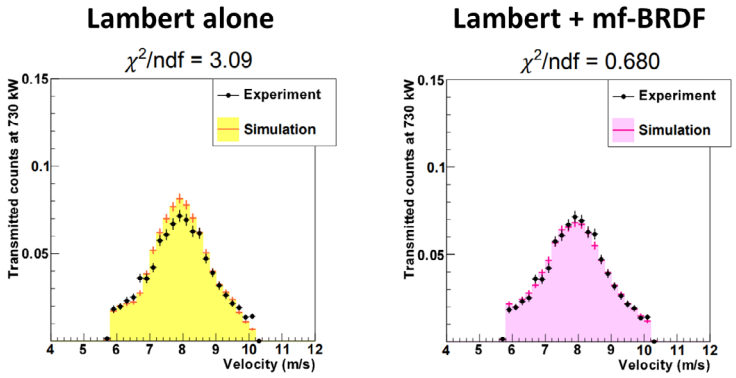

Figure 2. Comparison between the velocity distribution of pulsed UCNs injected and transported at an angle of 30° and a transport simulation calculated with different reflection models (Left) Lambert only (Right) Lambert and mf-BRDF.

a pulsed UCN source was injected into a cylindrical guide tube (1000-mm-long, 95.50-mm-diameter, made of aluminum with electroless nickel-phosphorus plated surface) inclined at 0°, 10°, 15°, and 30° to the injection direction, and the transport efficiency and deformation of the TOF peak were observed. The simultaneous use of Lambert's cosine law and the mf-BRDF model could explain the post-transport velocity distribution better than Lambert's cosine law alone (Fig. 2) [6]. This setup can be applied to the measurement of various guide tubes, and we plan to use these measurements to fabricate better UCN guide tubes in the future.

4. Multilayer-type neutron interferometer

A neutron interferometer is a device that splits the wavefunction of a single neutron into two paths, superimposes them, and detects the potential difference between the two paths as a phase difference. It was put into practical use in the 1970s and it has contributed significantly to the development of quantum mechanics, e.g., the verification of spinors and the phase shift of matter waves due to gravity. Thus far, neutron interferometers have been cut out of silicon ingots, which could only use mono-energetic neutrons and were limited in size.

A multilayer-type neutron interferometer is expected to be a new device to overcome these limitations and improve the sensitivity by using neutrons with longer wavelength and/or making the flight path longer. Especially with TOF method, the time-dependent systematic uncertainty can be suppressed, since the interference fringes are observed on the TOF spectrum.

The Jamin-type neutron interferometer using beam splitting etalons [5, 6], which is a high-precision assembly of multilayer neutron mirrors on a quartz substrate, was demonstrated at the low-divergence beam branch at BL05. The beam width is 100 μm while the beam paths are 300 μm apart, so they are completely separated. When a certain material is inserted into a path, the phase changes depending on the refractive index of the material. This can be applied to measure neutron scattering length of nuclei. Fujiie et al. have successfully demonstrated the measurements of the scattering lengths of some nuclei [11]. We will advance the sophistication of this interferometer and its application research in the future.

References

[1] K. Mishima et al., Nucl. Instruments Methods Phys. Res. Sect. A, vol. 600, no. 1 (2009)342–345.
[2] K. Mishima, Hamon Neutron Netw. news,vol. 25, no. 2 (2015) 156–160.
[3] R.L. Workman et al., (Particle Data Group 2022), Prog. Theor. Exp. Phys. 2022, 083C01 (2022).
[4] K. Hirota et al., Prog. Theor. Exp. Phys. (2020) 123C02.
[5] G. Ichikawa et al., Proceedings of science, PoS (PANIC2021) 457.
[6] S. Imajo *et al.*, Phys. Rev. C **108**, 034605 (2023).
[6] N. Naganawa et al., Eur. Phys. J. C 78, 11 (2018) 959.
[7] N. Muto et al., J. Instrum, 17 (2022) P07014.
[8] K. Hirota et al., J. Imaging 7 (2021) 4.
[9] M. Kitaguchi, et al., Phys, Rev. A 67, 033609 (2003).
[10] Y. Seki, et al., J. Phys. Soc. Jpn. 79, 124201 (2010).
[11] T. Fujiie et al., Phys. Rev. Lett. 132, 023402 (2024).

K. Mishima[1,2] on behalf of NOP collaboration
[1]*Neutron Science Section, Materials and Life Science Division, J-PARC Center;* [2]*Institute of Materials Structure Science, KEK*

BL06: Commissioning Status of Village of Neutron Resonance Spin Echo Spectrometers (VIN ROSE)

1. Introduction

Neutron spin echo (NSE) is a variety of inelastic and quasi-elastic neutron scattering techniques realizing the finest energy resolution in the field of neutron scattering [1]. Because the energy resolution of the energy transfer measurement is not limited by the energy spectrum of the incoming neutrons in the NSE technique, a moderately (10–15% FWHM) monochromatic neutron beam can be acceptable. In addition, the intermediate scattering function can be directly derived by NSE, so that the method is suitable for investigating slow relaxation dynamics in condensed matter, and high-intensity and high-energy-resolution NSE spectrometers have been developed [2].

Kyoto University and The High Energy Accelerator Research Organization (KEK) have been working jointly on the beam line BL06 construction since 2011. BL06 consists of two types of resonance NSE spectrometers, which are a modulated intensity by zero effort (MIEZE) instrument and a neutron resonance spin echo (NRSE) instrument by branching the beam with two curved supermirror guide tubes [3]. The spectrometers are equipped with neutron resonance spin flippers (RSFs), which enable us to downsize the instruments, so that the two spectrometers have been able to be located very closely [4].

In this report, the status of the MIEZE and NRSE spectrometers at BL06 in FY2022 is summarized.

2. Commissioning status at BL06 in FY2022

At BL06, the user program has started partially with the MIEZE spectrometer since the 2017B proposal round, while the NRSE spectrometer for fine-energy resolution is still under commissioning.

In FY2022, the achieved scientific highlight of BL06 is the spin dynamics in $MnSi_{1-x}Ge_x$ with the MIEZE spectrometer [5], which is described in section 3 in detail.

To upgrade the detectors at BL06, a flat-panel PMT (FRP) system [6] with a ^{6}Li-glass scintillator was tested. It is described in section 4.

3. Spin dynamics in $MnSi_{1-x}Ge_x$

In this study, the spin dynamics in $MnSi_{1-x}Ge_x$ was investigated. Polycrystalline samples were used, and the temperature was controlled by a 4 K GM cryostat, which is available as sample environment at BL06. BL12 HRC, which gives $S(Q, \omega)$, was also complementary used, and the observed quasi-elastic scattering data were compared with the obtained intermediate scattering function $S(Q, t)$ at BL06. Since the Q resolution of the MIEZE spectrometer is better than that of BL12 and $S(Q, t)$ can be directly observed from the MIEZE experiments, the relaxation time of the spin dynamics can be clearly deduced, which shows good agreements with the values derived from the obtained intrinsic energy width from the HRC experiments. The results have been summarized and published (see ref. [5]).

4. FRP system

A Flat-panel and Resistor type PMT (FRP) system developed for a two-dimensional position-sensitive neutron detector was tested at the MIEZE spectrometer. Since the FRP system consists of a multi-anode PMT (MA-PMT), a resistor network board and an FRP amplifier, and provides similar signals to those of the RPMT detector [7], it can easily substitute the RPMT system.

In this study, the FRP system with a ^{6}Li glass scintillator was tested at the MIEZE spectrometer. A flat-panel-type MA-PMT assembly H12700A-10 (Hamamatsu Photonics K.K.) and an enriched lithium 6 glass scintillator GS20 (Scintacor) with 0.8 mm thickness were used as an FRP system, which was compared with a current RPMT system with a 0.2-mm-thick ^{6}Li glass scintillator.

In Fig. 1, the measured direct-beam intensities with the FRP system and the RPMT system are compared. At long wavelengths (> 12Å), the ratio is almost in agreement, and increases gradually to around 1.6 as the wavelength gets shorter. Because the quantum efficiencies given by the catalogues are similar (~0.3) for the FRP and the RPMT, this result suggests that the long-wavelength neutrons are fully captured with the 0.2-mm-thick scintillator, while the short-wavelength neutrons transmit partially the 0.2-mm-thick scintillator. The 0.8-mm-thick scintillator captures more short-wavelength neutrons, then the FRP system could count more neutrons than that of the current RPMT system. In Fig. 2, the specular reflectivities measured by the FRP system and the RPMT system from the same sample are compared. The results show very good agreements. Because the RPMT system has been discontinued, this result confirms that the FRP system can substitute the RPMT system.

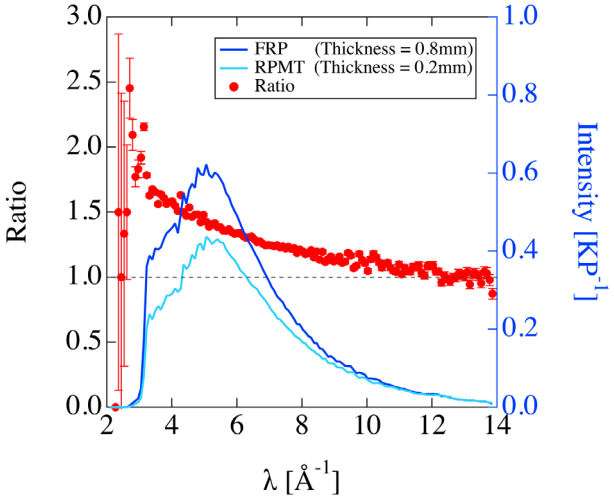

Figure 1. Comparison of the measured direct-beam intensities normalized by the kicker pulse between the FRP system (blue line) and the RPMT system (light blue line), in which the thicknesses of scintillators are different (0.2 mm for the RPMT system and 0.8 mm for the FRP system). The corresponding intensity ratio is shown by red circles.

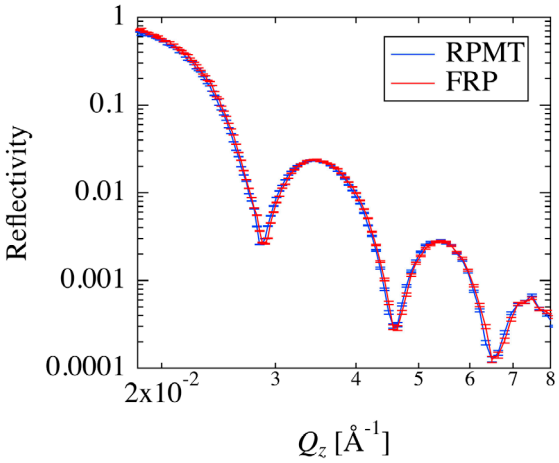

Figure 2. Comparison of the reflectivity measurements between the FRP system (red line) and the RPMT system (blue line).

5. Summary

In this report, the activities of BL06 VIN ROSE in FY2022 were summarized. The main achievements were introduced, i.e., the spin dynamics in $MnSi_{1-x}Ge_x$ investigated by MIEZE and the attempt to substitute the current RPMT detector system with the FRP system. In the case of the spin dynamics of $MnSi_{1-x}Ge_x$, very fast diffusion in rather low-Q region is observed, which is very suitable for the MIEZE spectrometer. To upgrade the detector system of the MIEZXE spectrometer, the FRP system can substitute the current RPMT system.

References

[1] F. Mezei ed., Neutron Spin Echo, Lecture Notes in Physics, (Springer, Berlin) **128**, (1982).
[2] B. Farago et al., *Neutron News* **26**, (2015) 15.
[3] M. Hino et al., *J. Nucl. Sci. Tech*, **54**, (2017) 1223.
[4] M. Hino et al., *Physics Procedia* **136-141**, (2013) 136.
[5] S. Aji et al., *Phys. Rev. B*. **108**, (2023) 054445.
[6] S. Sato, *Hamon* **27**, (2017) 8.
[7] K. Hirota et al., *Physica B* **385-386** (2006) 1297.

H. Endo[1,2], M. Hino[3], T. Oda[4], and H. Seto[1,2]
[1]Neutron Science Division, Institute of Materials Structure Science, KEK; [2]Neutron Science Section, Materials and Life Science Division, J-PARC Center; [3]Institute for Integrated Radiation and Nuclear Science, Kyoto University; [4]The Institute for Solid State Physics, The University of Tokyo

BL08: Maintaining the Aluminum Window of the SuperHRPD Sample Vacuum Chamber

1. Introduction

The BL08 Super High Resolution Powder Diffractometer [1, 2] scattering chamber currently in use was installed at the MLF in the summer of 2009. The sample vacuum chamber has five large vacuum windows, each made of a 1.5 mm thick aluminum plate. The largest window is 790 mm high and 740 mm wide. The sample vacuum chamber, which has been in operation for more than ten years, requires a vacuum break when the sample or the sample environment is changed, and has been repeatedly vacuumed and broken more than 1300 times as of the beginning of FY2022. The aluminum vacuum windows have reached the originally scheduled maintenance period, then the windows were replaced during the summer maintenance.

2. The sample chamber of SuperHRPD

The SuperHRPD diffractometer consists of a vacuum sample chamber and each detector bank surrounding it, as shown in Fig. 1. The sample chamber and detector banks are divided into separate sections and are located at several positions 10 mm from the vacuum window. The main body of the SuperHRPD diffractometer is housed in a 300 mm thick concrete instrument shield. Replacing the vacuum window requires extensive work to dismantle the shield and each detector bank and remove only the vacuum chamber, but this could not be done during the summer maintenance period due to cost, schedule, and temporary storage space issues. Therefore, a method to remove only the vacuum chamber was considered to minimize the number of parts to be removed.

3. For safe and secure construction

A method of lifting only the sample chamber by crane was proposed, but since the sample chamber was not a simple cylindrical shape and the center of gravity position was inaccurate, it was lifted by crane using a combination of a lifting jack and a guided frame (Fig. 2). The jack used was a model JWM025URL10D manufactured by Tsubakimoto Chain Co. The sample chamber, weighing nearly 400 kg, was raised at a slow rate of 100 cm in 30 minutes by a jack installed at the bottom and carefully lifted so as not to damage the vacuum window. The vacuum window and O-ring for the removed vacuum sample chamber were replaced, and after an off-line vacuum test with the new vacuum windows, it was returned to its original position in a reverse process. After the installation, alignment work was carried out and a vacuum test was performed with the existing vacuum system, and this work was successfully completed. Verification by actual measurements confirmed that there were no differences in the data before and after the vacuum sample chamber maintenance.

Prior to the replacement, a 1.5 mm thick aluminum window was used, but considering future maintenance cycles, it was decided to use a 3.0 mm thick aluminum window for this replacement. There was concern that

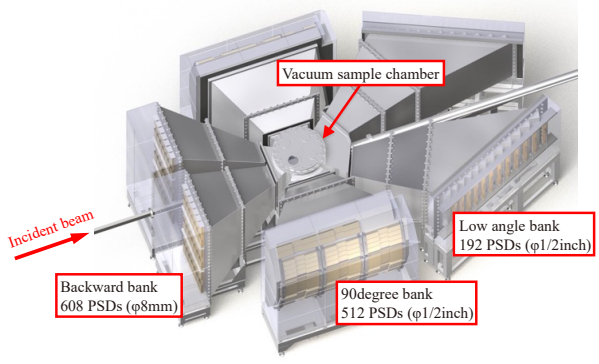

Figure 1. 3D image of the SuperHRPD diffractometer. The vacuum sample chamber and each detector bank have independent structures.

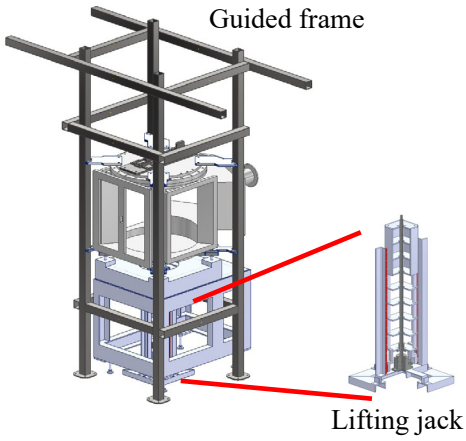

Figure 2. Structural diagram of the guide frame and lifting jack that are assembled to safely lift the vacuum sample chamber.

the increased window thickness would affect the scattering intensity and background, but as shown in Fig. 3, verification experiments confirmed that the effect of the window thickness was negligible.

4. Summary

The vacuum window of the SuperHRPD sample chamber has been replaced. The thickness of the aluminum window was changed to 3.0 mm, which is expected to have a service life longer than the previous replacement cycle.

References

[1] S. Torii, M. Yonemura, T. Y. S. Panca Putra, *et al.*, J. Phys. Soc. Jpn., SB020 SB020-1-4 (2011).

[2] S. Torii, M. Yonemura, Y. Ishikawa, *et al.*, J. Phys.: Conf. Ser., 502 012052 (2014).

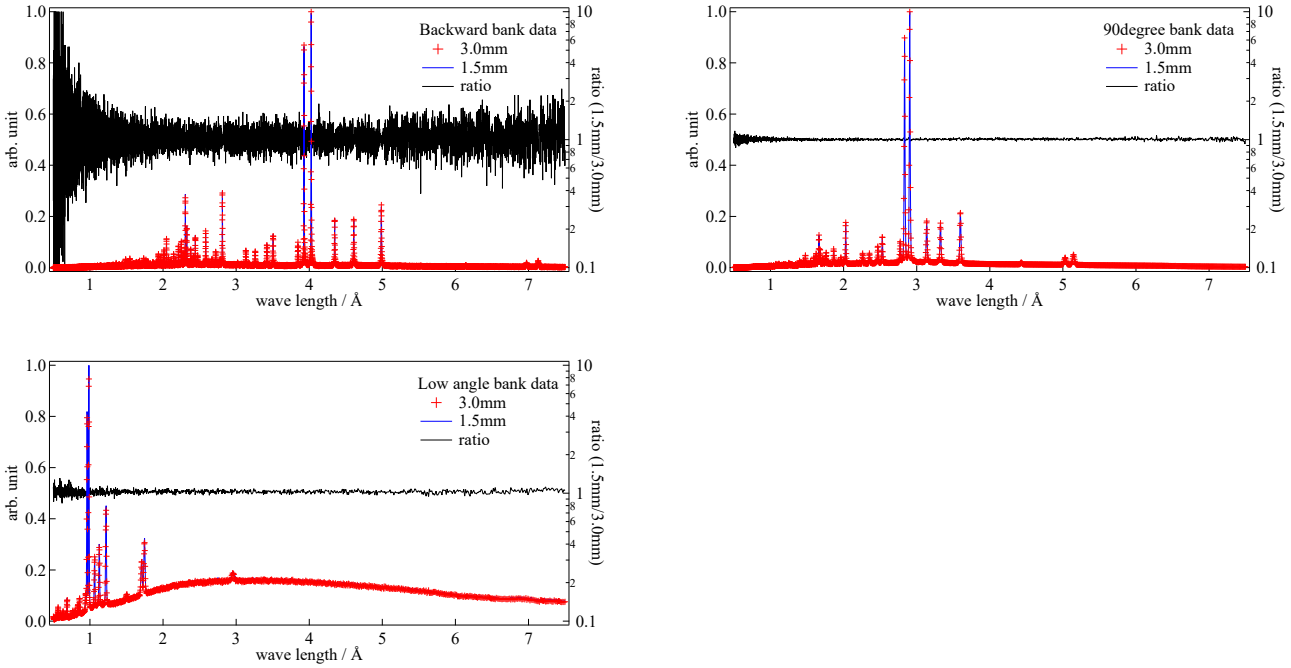

Figure 3. Verification of the change in diffraction peaks due to different thicknesses of the vacuum window. No effect of thickness was observed for each detector bank. The reason why the backward bank detector has a large ratio swing is because the binning width is very fine.

S. Torii[1,2], S. Yamauchi[1,2], and K. Mori[1,2]

[1]*Neutron Science Section, Materials and Life Science Division, J-PARC Center;* [2]*Institute of Materials Structure Science, KEK*

Current Situation of BL09 in FY2022

1. Introduction

The special environment powder diffractometer (SPICA) located at BL09 of J-PARC MLF was founded by the New Energy and Industrial Technology Development Organization (NEDO), together with the High Energy Accelerator Research Organization (KEK) and Kyoto University. In the NEDO projects (i.e., RISIN (FY2009 – 2015), RISING2 (FY2016 – 2020) [1], and RISING3 (in progress; FY2021 – 2025) [2]), SPICA is dedicated to structural investigations for the next-generation rechargeable batteries, as well as commercial lithium-ion batteries. SPICA was designed and developed to achieve a high resolution ($\Delta d/d$) of 0.08% with high intensity [3]. To realize the high $\Delta d/d$, SPICA has been situated at approximately 50 m from the neutron source system. SPICA focuses on neutron diffraction experiments under special environments, especially in charge-discharge operations (i.e., *operando* measurements). In addition, an annex building for SPICA (next to the 1st experimental hall of J-PARC MLF) was built to prepare samples for neutron diffraction experiments, assemble rechargeable batteries and conduct their charge-discharge evaluations before and/or after *operando* measurements. Currently, SPICA is widely used in various experiments, particularly in the field of battery science [4–10].

2. Specifications of SPICA

SPICA was installed at BL09, which has the thin side of a decoupled poisoned moderator with the shortest time resolution (or the shortest pulse at full width in half maximum (FWHM) region) of all MLF moderators. The neutron intensity on the thin side is weaker than that on the thick side (i.e., BL18, 19, and 20 on the 2nd experimental hall); however, the thin side has the advantage of a symmetrical peak profile, which can be used to extract strain information from the samples. The primary flight path from the moderator to the sample position (L_1) is 52 m, and the secondary flight path from the sample position to the detectors (L_2) is approximately 2 m, as shown in Fig. 1. An elliptical supermirror guide gradually changes the mirror coating from m = 3 to 6 toward the sample position, making it efficient to increase the number of neutrons at the sample position. SPICA utilizes 1568 ^{3}He gas-filled one-dimensional position-sensitive detectors (PSDs) with a diameter of 1/2 inch and an active length 0.60 m from a total of 0.67 m. The detector banks are formally grouped according to the scattering angle (2θ): backscattering bank ($150 \leq 2\theta \leq 175°$), high-angle multi-purpose bank ($120 \leq 2\theta \leq 150°$), 90-degree multi-purpose bank ($60 \leq 2\theta \leq 120°$), low-angle multi-purpose bank ($10 \leq 2\theta \leq 60°$), and small-angle bank ($5 \leq 2\theta \leq 15°$). In particular, the detectors in the multi-purpose bank ($10 \leq 2\theta \leq 150°$) have been placed continually on a cylindrical locus approximately 2 m from the sample position. The $\Delta d/d$ value was evaluated for each bank: $\Delta d/d$ = 0.12% for the backscattering bank, $\Delta d/d$ = 0.47% for the 90-degree multi-purpose bank, and $\Delta d/d$ = 1.27% for the low-angle multipurpose bank. The chopper rotated at a frequency of 25 Hz, which was the same as the repetition rate of the proton beam injection. The natural bandwidth of the SPICA is 2.9 Å. Three single-disc choppers were used for bandwidth selection to prevent frame overlapping and operated with 25/4 to 25/1 Hz repetition to select bandwidths.

3. Organized "charging station" for experimental rechargeable batteries in the BL09 annex building

The BL09 group has been organizing the "charging station" for experimental rechargeable batteries in a radiation-controlled area of the BL09 annex building. As

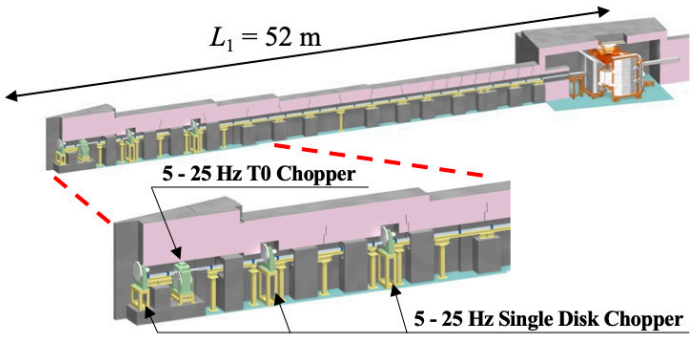

Figure 1. Layout of BL09 SPICA.

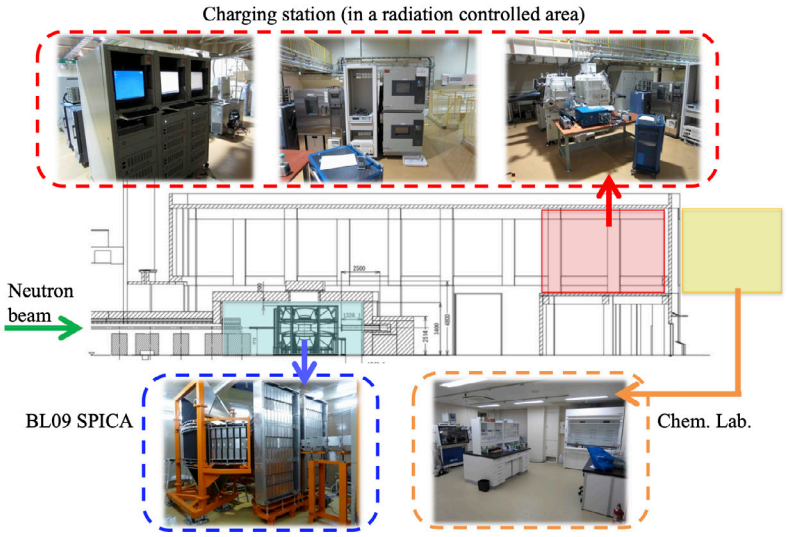

Figure 2. BL09 SPICA and the "charging station" in the BL09 annex building.

shown in Fig. 2, there are some apparatuses, like potentiostats, thermostatic chambers, glove boxes, etc., at the charging station by SPICA. After the *operando* neutron diffraction experiments on SPICA, the rechargeable batteries can directly move to the charging station in order to charge/discharge again for a long time. As a matter of course, the rechargeable batteries can be assembled at the charging station as well as at the chemical laboratory (Chem. Lab.). The charging station is critical to monitor the battery reaction from structural point of view, using neutron diffraction.

References

[1] https://www.rising.saci.kyoto-u.ac.jp/rising2/
[2] https://www.rising.saci.kyoto-u.ac.jp/en/
[3] M. Yonemura et al., J. Phys. Conf. Ser., **502** 012053 (2014).
[4] Y. Kato et al., Nat. Energy, **1** 16030 (2016).
[5] S. Taminato et al., Sci. Rep., **6** 28843 (2016).
[6] K. Mori et al., ACS Appl. Energy Mater., **3** 2873 (2020).
[7] K. Mori et al., J. Phys. Chem. C, **125** 12568 (2021).
[8] F. Takeiri et al., Nat. Mater., **21** 325 (2022).
[9] K. Kino et al., Appl. Phys. Express, **15** 027005 (2022).
[10] Y. Izumi et al., Adv. Energy Mater., **13** 2301993 (2023).

K. Mori[1,2], T. Saito[1,2], S. Song[1,2], and S. Torii[1,2]
[1]*Institute of Materials Structure Science, KEK;* [2]*Neutron Science Section, Materials and Life Science Division, J-PARC Center*

BL10: NOBORU

1. Introduction

In FY 2022, fifteen general-use proposals, one long-term proposal and two project-use proposals were carried out at NOBORU. One long-term proposal was postponed due to the entry restriction for foreigners because of the COVID-19 pandemic. This year, in addition to the fixed-point observations that have been conducted every year, we tested a fast-response gamma-ray detector using a plastic scintillator (BC-404) and a photomultiplier tube (Hamamatsu R329-02). Recently, requests to use high-energy neutrons above eV have gradually begun to increase. In order to respond to such requests, a test to measure the pulse shape functions at high energy neutrons was performed at NOBORU.

2. Experimental setup

The pulse shape of the neutrons in the time-of-flight (TOF) region of milliseconds or less was measured by detecting prompt gamma-rays generated by neutron resonances. In this measurement, it was necessary to sufficiently suppress contamination by flash gamma-rays coming from upstream. Therefore, the gamma-ray detector was enclosed in a shield of lead blocks (for gamma-ray suppression) and lithium fluoride plates (for neutron-absorption). Various samples of gold, silver, copper, tantalum, hafnium, and zinc with 0.1, 0.2, 2, 0.030, 0.025, and 5 mm thicknesses, respectively, were irradiated by neutrons. The distance between the surface of the plastic scintillator and the samples was 20 cm. A 5 cm thick lead collimator with a ϕ 37 mm aperture was located in front of the scintillator. An aluminum plate with the samples was mounted on an XY stage with a movable range of 15 cm $\times$ 10 cm. The stage movement and data acquisition were controlled by IROHA2 and automatic measurements were performed while changing samples. Figure 1 shows the experimental setup.

3. Results

A TOF spectrum measured with the tantalum sample is shown in Fig. 2. Resonance peaks with a good signal-to-noise ratio were obtained at TOF greater than 50 μs for tantalum and 10 μs for copper. The sample was placed at about 14 m from the moderator, indicating that resonances up to several hundred eV were measured. In the early TOF region, the double-bunch structure of the proton beam is reflected in the resonance spectrum. Figures 3a and 3b show resonance spectra measured with a gold target. It is seen that each resonance forms as a pair of peak structures 600 ns apart. The peak shapes tailing to low energy side also reflect the time structure of the incident neutrons.

A previous study using PHITS simulation data concluded that a time structure based on the Cole-Windsor (CW) function is the most suitable pulse shape function for NOBORU viewing the decoupled moderator [1, 2]. Figure 3a also shows that the spectrum acquired without sample (only with an aluminum plate) well reproduce the background distribution in the spectrum taken with the gold target. Such clean data allow for real data analysis in the higher energy region. The measured data

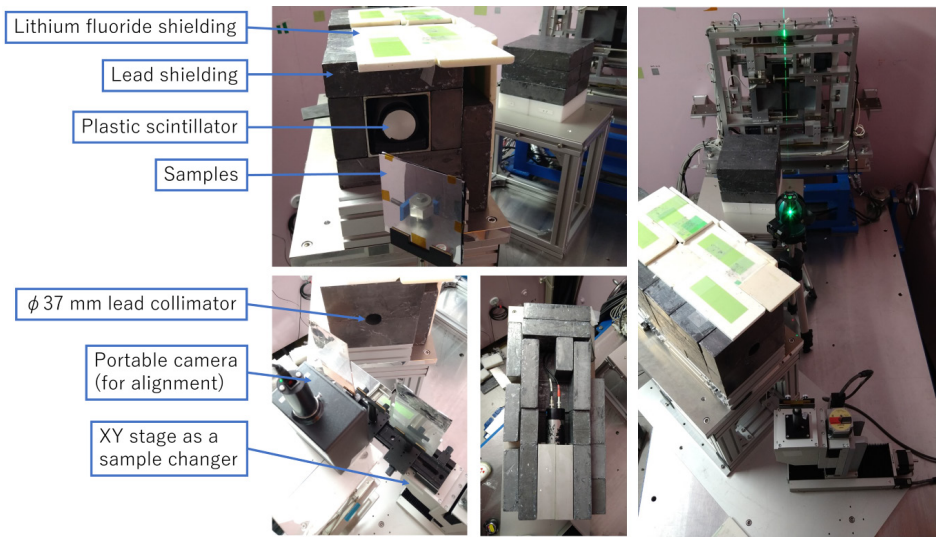

Figure 1. Experimental setup for the low background gamma-ray measurement at NOBORU.

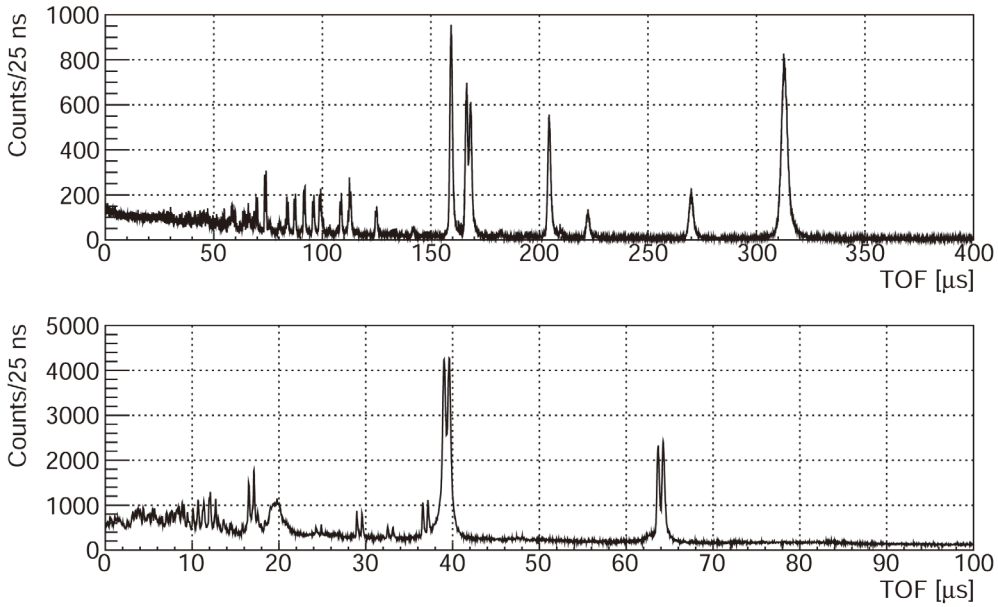

Figure 2. TOF spectra measured with tantalum (upper) and copper (lower) target.

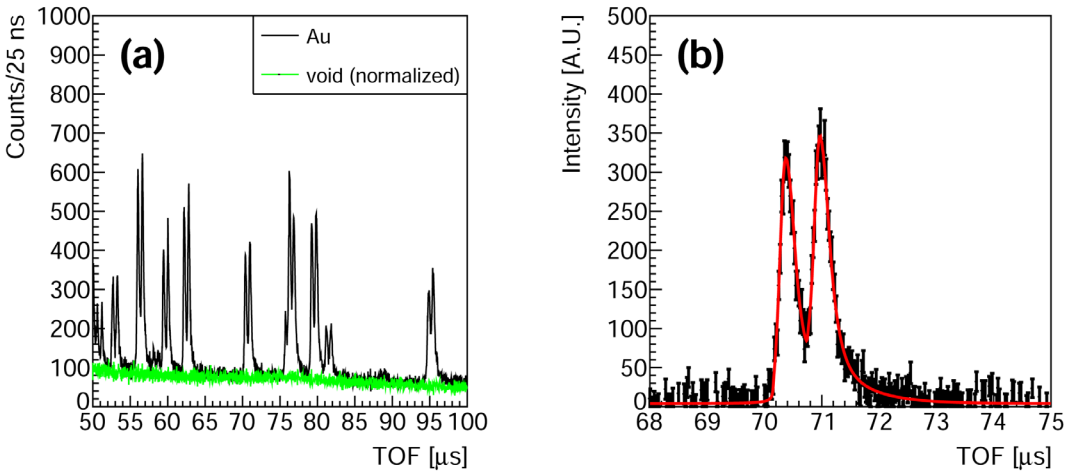

Figure 3. (a) TOF spectra measured with (black) and without (green) Au target. (b) TOF spectrum derived with background subtraction (black points) and fitted using CW function (red curve).

obtained in this study will re-evaluate the validity of the previous study (Fig. 3b) and is expected to provide a more realistic pulse shape function for future measurements with high-energy neutrons.

References

[1] H. Hasemi et al., Nucl. Instr. and Meth. A, **773**, 137-149 (2015).
[2] https://www.j-parc.jp/researcher/MatLife/ja/instrumentation/

K. Oikawa and Y. Tsuchikawa
Neutron Science Section, Materials and Life Science Division, J-PARC Center

Developments at BL11 PLANET

1. Introduction

This year, we have tackled the following challenges:

i) Extension of the available pressure range with Paris-Edinburgh (PE) press equipped with 1-mm-cup diameter non-toroidal anvils
ii) Performance evaluation of radial collimators (RCs) with a gauge size (GS) of 0.75 mm
iii) Background reduction by Cd screens in front of the detector shielding panels
iv) Diffraction experiments using a DAC with vertical geometry to improve data reliability

The details are shown below.

2. Extension of the available pressure range with Paris-Edinburgh (PE) press equipped with 1-mm-cup diameter non-toroidal anvils

In 2018, we tried to extend the available pressure range by reducing the cup diameter of the double toroidal anvils for a PE press. The world record reaching 40 GPa has been achieved by using 1.5-mm cup diameter anvils [1]. However, the further extension using 1.0-mm cup diameter anvils failed, although a higher-pressure generation was expected. This would be due to consumption of the applied load by a toroidal part, leading to less efficient compression of the sample. To further extend the maximum available pressure range, non-toroidal anvils with 1.0-mm cup diameter are tested.

Figure 1 shows the new anvil design and the comparison of the pressure generation curve with those for previous designs. No saturation of pressure generation has been observed and a pressure of 45 GPa was achieved. However, the signal to anvil peak ratio is very small; thus, further improvement of the beam optics will be necessary.

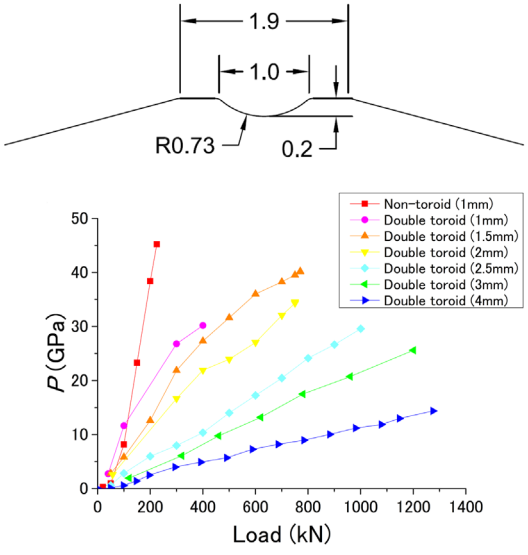

Figure 1. (Top) Enlarged view of the new design. (Bottom) Comparison of the pressure generation curve with those for previous designs.

3. Performance evaluation of RCs with a GS of 0.75 mm [2]

As the beam power increases, the use of a smaller sample that enables experiments at higher pressures has become possible. Last year, radial collimators with a nominal GS of 0.75 mm were developed for experiments above 30 GPa using PE presses or diamond anvil cells (DAC). This year, the performance is quantitatively evaluated in terms of GS, transmission, and efficacy in the experiments using the above high-pressure devices.

Figure 2 (upper) shows the scan profile of the 0.996-mm diameter iron ball mounted on a vanadium needle, along with the fit by convolution of radial collimator function, $T(z)$ and the cross-section profile of the iron ball. Figure 2 (lower) compares the $T(z)$ obtained by fitting with those simulated based on the design parameters. The true GSs of three RCs with nominal GS of 3.0, 1.5, and 0.75 mm are 2.78(2), 1.07(2), and 0.50(3) mm, respectively. The detailed results of other tests will be shown in Ref. [2]. These results indicate that the 0.5 mm GS radial collimators have been fabricated as intended and display the smallest GS among those ever manufactured for neutron scattering experiments in the world.

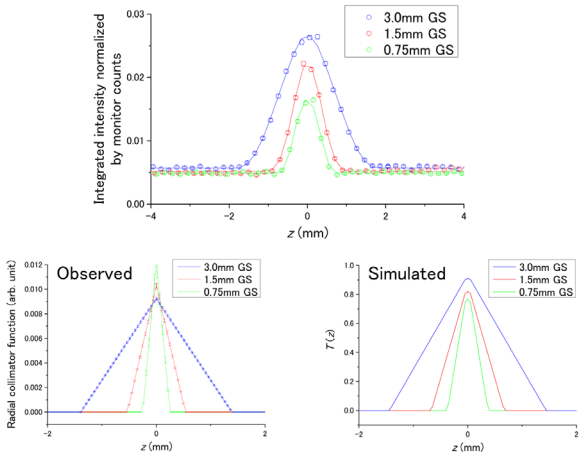

Figure 2. (Top) Scan profile of 1-mm diameter iron ball with 3.0 mm, 1.5 mm, and 0.75 mm GS radial collimators and the fit by convolution of the radial collimator function and the cross-section profile of the iron ball. (Bottom) Radial collimator functions obtained by the fit (left) and those simulated using design parameters (right).

4. Background reduction by Cd screens in front of the detector shielding panels

The detector banks of PLANET are equipped with shielding panels to block neutrons coming around from the side of RCs. The panels are designed to fold down to make room for replacing the huge 6-axis press with smaller presses. However, the folding mechanism left gaps in the panels, resulting in incomplete shielding [see Fig. 3 (upper right)]. As the signal intensity decreased with a decreasing sample volume, background coming from the gaps became non-negligible. Last year, the 1-mm-thick Cd screens were installed in front of the shields to eliminate it. This year, the efficacy was evaluated.

Figure 3 compares detector maps before and after installation of Cd screens. Many horizontal lines in the upper right figure are mostly eliminated and the integrated intensity is reduced into approximately one-third in the energy range below Cd cut-off (0.5 eV) (Fig. 3 lower).

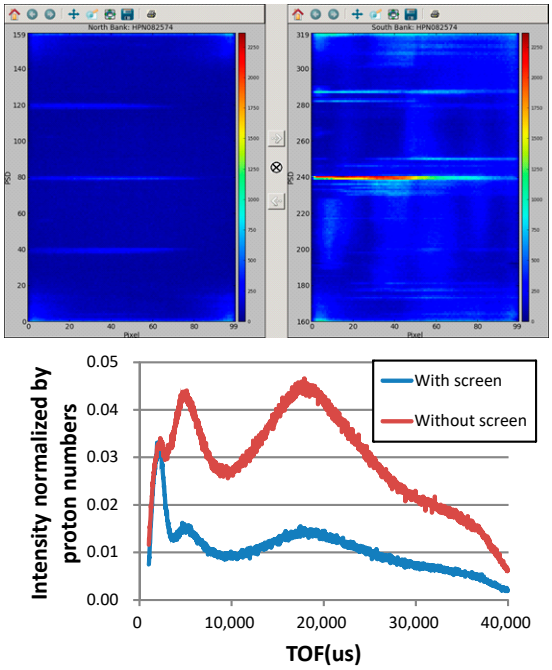

Figure 3. Detector maps before (upper right) and after installation of Cd screens (upper left) and integrated intensity over the whole detector area (lower).

5. Diffraction experiments using a DAC with vertical geometry to improve data reliability

In recent years, we have developed an experimental technique using a DAC. In the previous data measurements, with the compression axis of the DAC horizontal, the incident beam was injected into the sample through one of the diamond anvils (horizontal geometry). This setup has caused problems, such as contamination of diffraction patterns by diamond Bragg spots and loss of neutron beam in certain wavelength range due to Bragg scattering by the single-crystal diamond (the so called "Diamond Dips"). Last year, we introduced software that helped to eliminate these effects but failed to eliminate them completely.

This year, we have tried vertical geometry in which the compression axis of DAC is aligned vertically. It is because with this geometry, incident beam introduced into the sample does not hit the diamond anvils in its path, which would fix the aforementioned problems. To achieve this setup, we developed beamline optics, including the motorized X-Z stage to precisely align the beam collimator with an exit size of 0.5 mm wide and 0.1 mm high (Fig. 4), and software to control it. Next year, the performance will be evaluated in on-beam experiments.

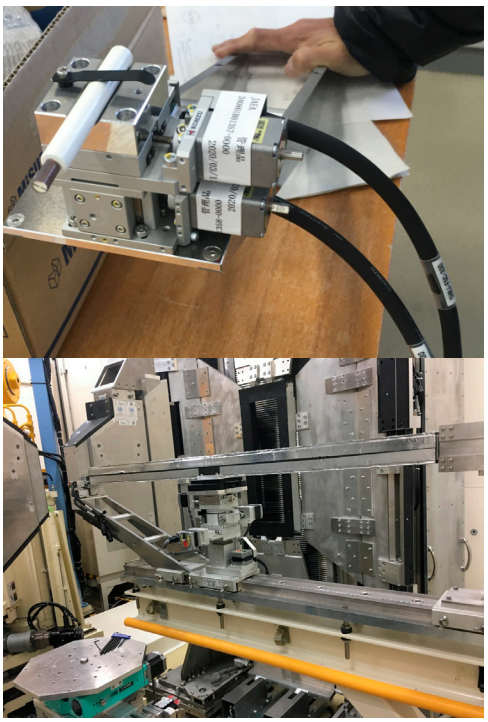

Figure 4. (Upper) Newly devised collimator and motorized stage (Lower) Stage with them installed.

References

[1] T. Hattori, et al., High Press. Res. 39 417 (2019).
[2] T. Hattori, et al., Nucl. Instrum. Methods. Phys. Res. A 1059 168956 (2024).

T. Hattori[1], A. Sano-Furukawa[1], S. Machida[2], J. Abe[2], K. Funakoshi[2], and N. Okazaki[2]
[1]Neutron Science Section, Materials and Life Science Division, J-PARC Center; [2]Neutron Science and Technology Center, CROSS

High Resolution Chopper Spectrometer HRC

1. Introduction

The High Resolution Chopper Spectrometer (HRC) is being operated at BL12 in the MLF under the S-type project of IMSS, KEK, and the IRT project of ISSP, the University of Tokyo, in order to study dynamics in condensed matter, especially in a wide range of correlated electron systems. The activities of the HRC in FY2022 are summarized in this report.

2. Instrumentations

A cryofurnace (T = 4 – 700 K) was manufactured and delivered in the last fiscal year, and the experiment control program YUI was modified to accommodate it. We performed the commissioning and confirmed that the highest temperature was 760 K at the heater control position and 700 K at the sample can bottom with a standard sample can.

For low temperature experiments down to 0.3 K, a ^{3}He gas sorption type refrigerator, Heliox, was used for collaborative experiments on the S-type project. Heliox maintains the lowest temperature, 0.3 K, for 40 hours. The performance of ^{3}He gas sorption type refrigerators, which are commercially available, was surveyed and reviewed by cryogenic engineers and instrument staffs of HRC and POLANO, and specifications were developed for a refrigerator with a higher performance than Heliox. We manufactured a ^{3}He gas sorption type refrigerator, where the lowest temperature, 0.3 K, is maintained for 100 hours, and it was delivered in March 2023, as shown in Fig. 1.

The phase control algorithm of the Fermi choppers was improved by introducing the algorithm developed for the correlation chopper on POLANO, and its performance will be investigated. The wave shape of the 25 Hz timing signal input to the Fermi chopper was disturbed by noise from the T0 chopper control system, causing disruption of the Fermi chopper's control. The 25 Hz timing signals were wired from the signal distributor to the choppers individually, and as a result, the problem was settled. The touch panel of the T0 chopper was repaired. Backups of the stabilizer of the T0 chopper were purchased, because production will be discontinued soon.

A scheduled maintenance was performed for the roughing pumps and the air dryer in the vacuum system of the scattering chamber, and for the vacuum pumps of the T0 chopper and the guide tube. During the regeneration process of the cryopump, the ultimate pressure was increased. A small broken piece, probably from the B_4C liner of the vacuum chamber or from the vane of the cryopump, was stuck in the pressure relief valve of the cryopump, where the vacuum was leaked. The ultimate pressure was recovered by removing the piece. Since the autumn of 2022, there has been a small leak in the vacuum scattering chamber and a loss of neutron intensities. It was discovered that the holding mechanism of the incident collimators was broken and the neutron intensities decreased due to changing the position of the collimators. By repairing the holding mechanism of the incident collimators, the neutron intensities were recovered. However, the vacuum leak was not resolved. We have not yet found the cause of the vacuum leak.

In the computational environment, scheduled export process of spe files from HANA, detector diagnostic program, and import of a beam monitor detector were implemented. The FLnet server that monitors the vacuum system has been malfunctioning due to aging, and we attempted to update it, and we purchased as many parts as we could in FY2022. The remaining parts will be purchased in FY2023 to complete the renewal.

On the HRC, high angle detectors and low angle detectors are mounted at L_2 = 4 m and ϕ = 3 – 62° and

Figure 1. ^{3}He gas sorption type refrigerator delivered to the HRC in March 2023.

−13 − −31° and at L_2 = 5.2 m and ϕ = −0.6 − −5.1°, respectively, where L_2 is the distance between the sample and the detector, ϕ is the scattering angle. Due to difference in the resolution and the background, it was hard to connect the data on high angle detectors and the data on low angle detectors. We tried again to connect both data and found out that these data might be compared by removing noise reasonably and correcting the detector efficiency with calculated values. We also found noise signals related to the detector electronics and noise signals when the beam shutter was closed. Some improvements are required. The low angle detectors are aligned in a double-layered configuration to increase the counting rate: the detectors in the front layer face the sample and the detectors in the rear layer are placed just at the lower stream of the front layer [1]. However, the rate of increasing intensities depends on the neutron energy. This configuration should be also reconsidered.

3. Scientific results

The magnetic anisotropy in the van der Waals compounds $CeTe_3$ and $CeTe_2Se$ was investigated. In $CeTe_2Se$, the magnetic moments in the ordered state point along the magnetic hard axis, whereas they point along the magnetic easy axis in $CeTe_3$. Using the HRC, the crystalline electric field (CEF) excitations were observed, and the magnetic anisotropy was discussed [2]. Figure 2 shows CEF excitations at E = 22.9 meV and 26.3 meV in $CeTe_2Se$. In a previous study, it was suggested that the magnetic moments in $CeTe_2Se$ point along the magnetic hard axis due to the quantum order-by-disorder. In an order-by-disorder, an unexpected order emerges due to some large fluctuations (disorder). The antisymmetric spin-orbit interaction (ASOI) due to a lack of inversion symmetry has been reported to give anisotropy to magnetic fluctuations. An enhancement of the magnetic quantum fluctuations is possibly controlled by the competition between the magnetic anisotropy determined by CEF and the influence of the ASOI in these systems.

Magnetic excitations were investigated on the metallic magnet FeSn with a Kagome spin-lattice using the HRC, 4SEASONS (BL01) at the MLF, and SEQUOIA at the Spallation Neutron Source (SNS) [3]. Well-defined spin waves were observed at low energies and the Hamiltonian parameters were determined. Broad Dirac magnons were observed at high energies, reflecting interactions with the Stoner continuum.

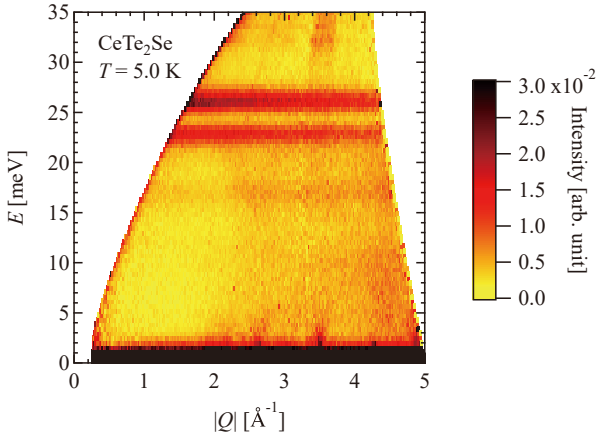

Figure 2. Background-subtracted inelastic neutron scattering intensity in the momentum(Q)-energy(E) space measured at T = 5 K for $CeTe_2Se$ (Reproduction from Ref. [2]).

HoB_2, which shows giant magnetocaloric effect, is expected to be a target material for magnetic refrigeration in the liquid hydrogen temperature range. Using the HRC, CEF excitations were observed and five CEF levels were found to be densely located in the low energy region: pseudo-degeneration [4]. This indicates that the pseudo-degeneracy of the CEF ground state in a zero magnetic field plays a major role in producing the giant magnetocaloric effect. The relationship between magnetocaloric effect and CEF parameters derived in this study can provide a guideline in the search for magnetocaloric materials. Details are described in Research and Development Highlights in this report.

References

[1] S. Itoh et al., MLF Annual Report 2016,101 (2017).
[2] D. Ueta et al., J. Phys. Soc. Jpn., **91** 094706 (2022).
[3] S.-H. Do et al., Phys. Rev. B, **105** L180403 (2022).
[4] N. Terada et al., Commun. Mater., **4** 13 (2023).

S. Itoh[1,2], T. Masuda[3,2], D. Ueta[1,2], T. Nakajima[3], T. Yokoo[1,2], S. Asai[3], H. Saito[3], D. Kawana[3], R. Sugiura[3], T. Asami[3], S. Yamauchi[1,2], S. Torii[1,2], T. Seya[1,2], H. Ohshita[1,2], N. Kaneko[1,2], Y. Ihata[4], and H. Tanino[1,2]

[1]Neutron Science Section, Materials and Life Science Division, J-PARC Center; [2]Institute of Materials Structure Science, KEK; [3]The Institute for Solid State Physics, The University of Tokyo; [4]Technology Development Section, Materials and Life Science Division, J-PARC Center

BL14 AMATERAS

1. Introduction

AMATERAS is a cold-neutron disk-chopper spectrometer designed for studying dynamical properties in atomic, molecular, and magnetic systems from cold to sub-thermal energy range with high efficiency and flexible resolution [1, 2]. It has been 14 years since AMATERAS was opened for the user program. During this time, we have continuously upgraded various components of the instrument while facilitating the users' experiments. In FY2022, Dr. Masami Nirei, a postdoctoral researcher, joined the instrument group. Furthermore, this fiscal year, we obtained funding granted by the JAEA President for upgrades to the neutron detectors and the vacuum control system, aiming to enhance the user program.

2. User program, outcomes, and outreach activities

35 and 34 general proposals (short-term) were submitted to AMATERAS in the 2022A and 2022B rounds, respectively. Consequently, 16 experiments for the short-term general proposals, including some "reserved" proposals, one experiment for the long-term proposal and one experiment for the project proposal were carried out this year. 13 of the performed general proposals were submitted by foreign users. Most users were still unable to visit the facility for their experiments due to travel restrictions, so the instrument group carried them out in their absence. The first user group that visited after the Covid-19 pandemic restrictions were lifted was from Europe. As usual, the majority of the proposals submitted to AMATERAS were in the research field of magnetism and strongly correlated electron systems. On the other hand, the humidity control system, a shared sample environment in the facility, was used for the first time for an experiment for industrial application.

In FY2022, 14 refereed papers related to scientific research by using AMATERAS and one proceedings paper were published, and two students received their degrees. As of our outreach activities, we hosted for three months a doctoral student, Ms. Kotomi Nakamura, from Ochanomizu University, as a Fellow of Advanced Science. In addition, AMATERAS accepted four students during the 6th Neutron and Muon School held in December 2022. They learned the techniques of the inelastic neutron scattering measurement on a low-dimensional magnetic system in a hands-on experiment at AMATERAS (Fig. 1).

3. Instrument-related upgrades

We have proceeded off-line and on-beam commissioning on the top-loading cryofurnace that we purchased last year. This is a cryogen-free system incorporating a pulse-tube cryocooler and a one-shot ^{3}He cooling system (Fig. 2). This cryofurnace enables measurements at temperatures ranging from 0.3 to ~700 K, utilizing low-T, mid-T, and high-T probes. After

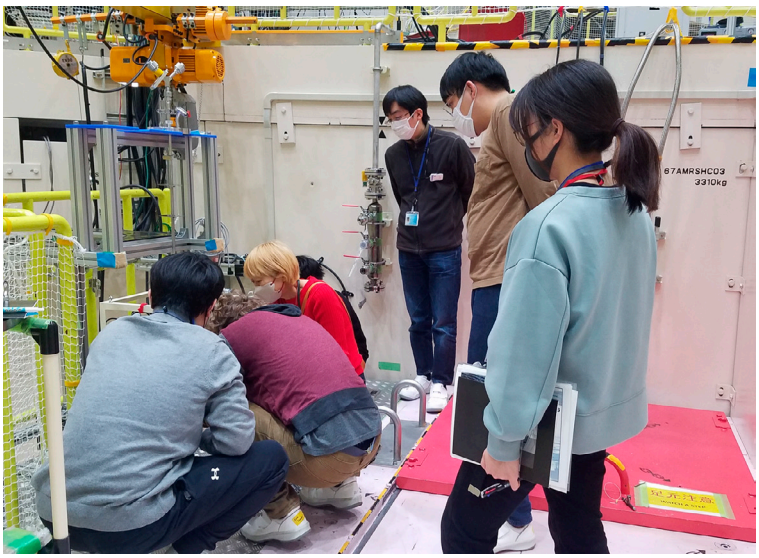

Figure 1. Students and staff members of AMATERAS mounting the sample onto the sample rod of the cryostat.

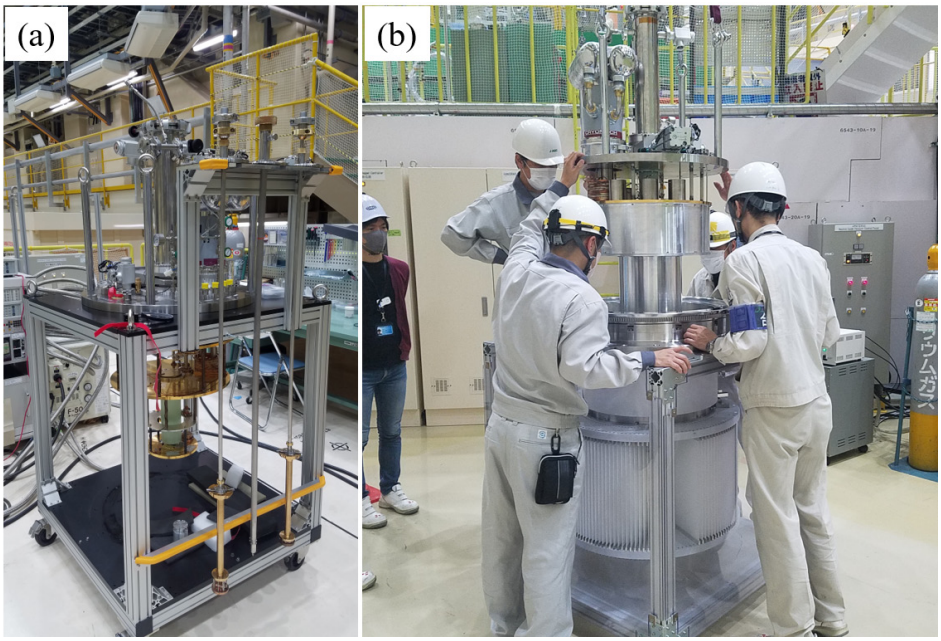

Figure 2. Photos of the cryogen-free top-loading cryofurnace. (a) Inside the cryofurnace and sample probes and (b) the cryofurnace being set onto the dedicated radial collimator.

conducting offline cooling tests, we carried out on-beam commissioning to investigate the background, sample position and cooling performance in the vacuum scattering chamber. Based on the results of this commissioning, we are improving the design of the cryostat to ensure safer and easier sample installation and to reduce the cooling time in the initial cooling process. Additionally, we have integrated a new chiller to circulate the cooling water on the helium compressor for the pulse-tube cryocooler included in this cryofurnace, allowing its operation independently of the facility's cooling water. In the coming year, we will be introducing more improvements to the system for the user program.

We have also developed an automatic vacuum control system for the vacuum scattering chamber over the last few years. Our vacuum control system comprises two sets of a screw pump, a mechanical booster pump, a gate valve, and a butterfly valve for rough evacuation and a cryopump with a main gate valve to achieve high vacuum. In FY2022, we completed the full automation of the evacuation process. Our next step is to upgrade the control system to fully automate the venting process to improve safety and work efficiency and to reduce our workload.

There are 286 one-dimensional position sensitive neutron detectors inside the vacuum chamber with a length of 3 m and diameter of 1 inch each. When we start evacuation/vent of the vacuum chamber, high voltage applied to the detectors should be turned off to prevent their damage due to vibrations caused by air currents. In near future, we are planning to prepare an interlock system for the high voltage that automatically turns off the high voltage of the detectors monitoring status of the vacuum control system.

References

[1] K. Nakajima *et al.*, J. Phys. Soc. Jpn. **80**, SB028 (2011).
[2] K. Nakajima, RADIOISOTOPES **66**, 101 (2017).

S. Ohira-Kawamura[1], M. Kofu[1], N. Murai[1], Y. Inamura[1], M. Nirei[1], D. Wakai[1,2], and K. Nakajima[3,1]
[1]*Neutron Science Section, Materials and Life Science Division, J-PARC Center;* [2]*NAT Corporation;* [3]*Materials Sciences Research Center, JAEA*

Upgrading TAIKAN

1. Introduction

The small- and wide-angle neutron scattering instrument TAIKAN (BL15) has been developed and upgraded to analyze the microstructure and hierarchical structure of materials in various scientific fields with high precision and efficiency using a 1 MW spallation neutron source at J-PARC [1]. In FY2022, the software for the instrument control and the sample exchanger for 1 Tesla (T) magnet filed measurement were developed to promote efficient and remote measurements.

2. Development of the software for instrument control for BL15

Since the beginning of the TAIKAN operation in 2011, as shown in Fig. 1, the application-type GUI software called "Utusemi-1" [2] using Python scripts has been used to control the sample environment (SE) devices and the measurement with He^3 detectors. It was a simple GUI with a user-friendly operation. However, it did not allow an easy set up of complicated measurement conditions and prevented the integration of new software for the control of devices.

As shown in Fig. 2, many SE devices, such as temperature and humidity control systems [3], viscosity measurement, tensile tester, UV/VIS [4], and magnetics, have been developed at BL15 for user experiments in various research fields (polymers, proteins, steel materials, magnetic materials, etc.)

To overcome the limitations of Utusemi-1 which caused difficulties in the operation of complex measurements, the scalability of SE devices, and the display of measurement information, "Utusemi-2", a browser-based GUI software (see its screenshot in Fig. 2) has been developed by the MLF computational environment team.

In FY2022, the Utusemi-2 was installed and customized for the BL15 measurement system, including the development of control software for SE devices.

3. Development of the sample changer for 1 T magnet

In SANS measurements at BL15 under magnetic fields below 1 T up until last year, it was necessary to exchange the samples after each measurement. Therefore, to perform automatic sample exchange in the magnetic fields, a new sample changer with 7 sample positions was developed as shown in Fig. 3.

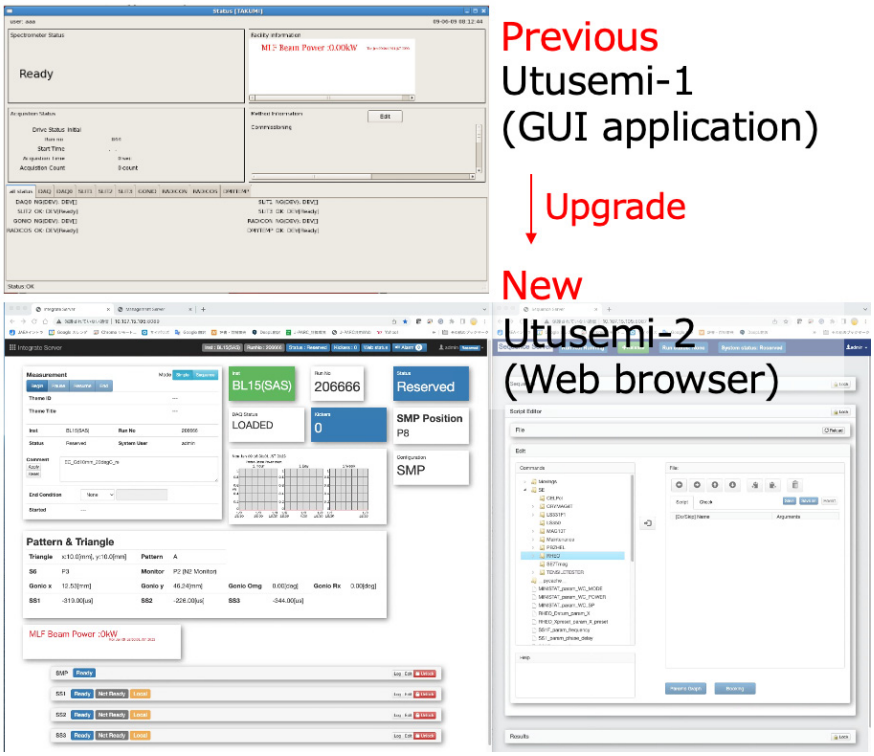

Figure 1. Screenshots of the GUI of Utusemi-1 (previous) and Utusemi-2 (new) for the measurement control system in BL15.

Figure 2. Sample environment devices devel-oped at BL15 TAIKAN.

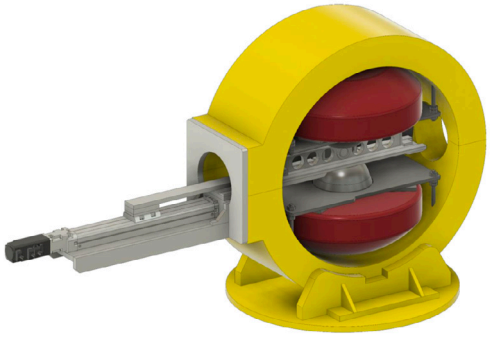

Figure 3. Drawing of 1 T magnet with sample changer.

4. Future plans

In the BL15 user experiments, the installation of Utusemi-2 software for instrumental control in BL15 will lead to simplifying the execution of complex sequencing measurements and the addition of user-developed SE devices. In addition, the development of the sample changer for 1 T magnet filed measurement is expected to further promote the usage of the analysis of magnetic structure for magnetic and steel materials.

References

[1] S. Takata, et al., JPS Conf. Proc., **8** 036020 (2015).
[2] Y. Inamura, T. Nakatani, J. Suzuki, and J. Otomo, J. Phys. Soc. Jpn., **82** (2013) SA031.
[3] H. Arima-Osonoi, et al., J. Appl. Cryst. **56** 1802-1812 (2023).
[4] Hiroki Iwase, Masaaki Akamatsu, Yasuhiro Inamura, Yoshifumi Sakaguchi, Kazuki Kobayashi, and Hideki Sakai, Langmuir **39** 12357-12364 (2023).

S. Takata[1], K. Hiroi[1], K. Ohishi[2], H. Iwase[2], Y. Kawamura[2], T. Morikawa[2], and M. Ueda[2]
[1]Neutron Science Section, Materials and Life Science Division, J-PARC Center; [2]Neutron Science and Technology Center, CROSS

Developments of Multi Incident-angle Neutron Reflectometry

1. Introduction

Neutron reflectometry (NR) is very useful for investigations of structures of surfaces and buried interfaces. SOFIA is a horizontal-type neutron reflectometer constructed at BL16 of the MLF, J-PARC [1, 2]. Due to the high-flux beam of J-PARC, less than one hour is needed for taking full *Q*-range data and only a few seconds for limited *Q*-range data in the case of a sample with 3 inches (76 mm) in diameter. However, several hours are still needed for a small sample, such as 10 mm × 10 mm, which is a typical size of a sample for X-ray reflectometry.

So far, the SOFIA employed double frame mode with chopper rotation speed of 12.5 Hz (half of the neutron pulses generated at the source) to extend the *Q*-range by using wider wavelength band. This enables us to perform time-slicing measurements within a wider *Q*-region without any incident-angle scan. However, the *Q*-region is still limited, even with the double frame mode, due to the limitation of the wavelength band, and the neutron flux is reduced by a half because every other neutron pulse is cut by the chopper. With taking the merit and demerit of the double frame mode mentioned above, a multi-incident neutron reflectometry (MI-NR) [6] at the SOFIA reflectometer is going to be realized by the combination of the higher flux beam at 25 Hz for higher incident-angle and wider wavelength band beam at 12.5 Hz for lower incident-angle. It should be noted here that the longer exposure time is required for the measurement at higher incident-angle because of the reduced reflectivity. Therefore, the reduction of the flux due to the double frame mode at the lower incident-angle has no effect on the total measurement time because it is limited by the statistic at the higher incident-angle.

To realize the combination of the two beams above, two disk choppers were installed at the exit of the guide tube last year. The choppers were made of circular aluminum plates with thickness of 4 mm, and Gd_2O_3 was painted on them to stop neutrons by the choppers. As two beams with different tilt angles, 2.22° and 5.71°, are acceptable at the SOFIA, the choppers have two windows: one is at the edge to realize the MI-NR at the 2.22° beam, and the other at the middle of the disk to cut the beam with the tilt angle of 5.71° to illuminate free-liquid surface with high incident-angle.

In order to transport the two beams at the chopper position to the virtual sources 4500 mm from the choppers, a focusing guide was installed at the middle of the choppers and virtual sources. The guide is 1300 mm in length and equipped with 3 Qc supermirrors inside, in

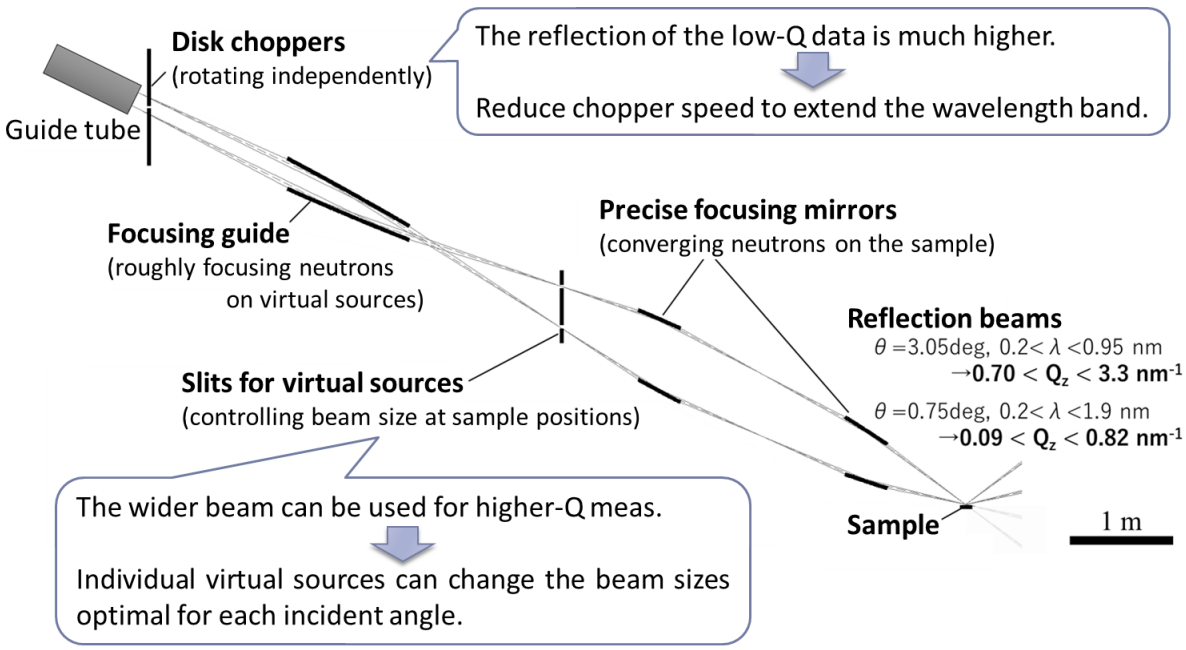

Figure 1. Design of optics for realizing MI-NR at the SOFIA.

which the shapes of the top and bottom sizes are ellipses with foci at the upper and lower half of the beam at the chopper position and lower and upper exit at the virtual sources, respectively. Note here that a separator was placed to avoid the cross talk of the two beams after the chopper, in which an iron plate was placed at the center to cut fast neutrons and two 2.5 Qc supermirrors on glasses were placed on the top and bottom sides of the iron plate to guide neutrons.

This year, a slit system with two apertures to make virtual sources with the optimized gaps depending on the incident angle and sample size was installed. In addition, a set of precise focusing mirrors to transport neutrons from the virtual sources to a sample position with different incident angles was also installed. A set of FRP detectors was used to count the neutrons reflected on the sample separately. Because the peeling of the Gd_2O_3 painting on the chopper blades due to the centrifugal force occurred, the test measurements of the MI-NR could not be performed.

2. Beam transport optics

A blueprint of the beam transport optics and photos of the instruments installed are shown in Fig. 2. The incident beams from the chopper exits are separated to upper and lower beams with the separator and irradiate the focusing guide tubes as explained above.

Figure 3 shows the beam profiles at the virtual neutron source. The distance between the upper and lower beams was 34 mm, which was almost equal to the designed value. Therefore, we could say that the accuracy of the construction of the guide tubes was precise enough.

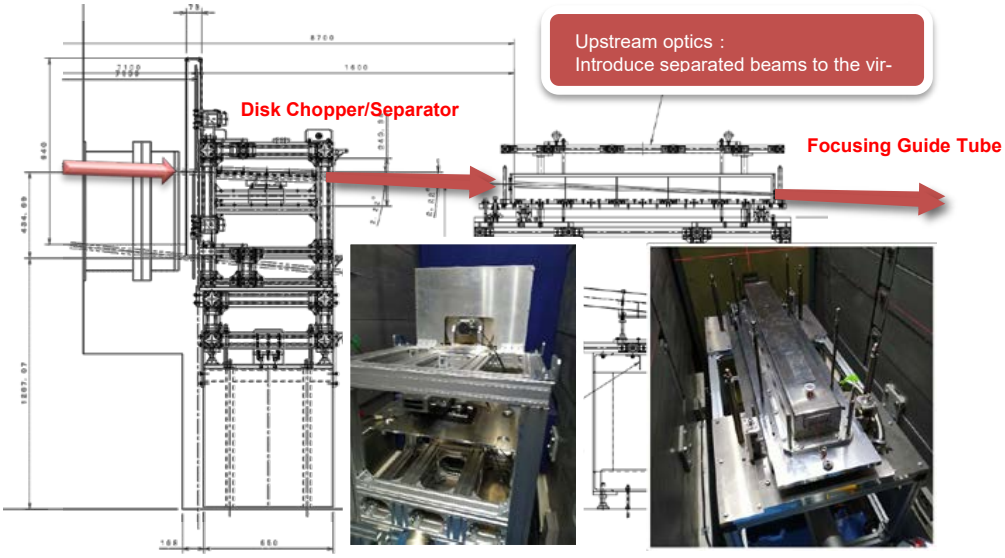

Figure 2. The beam transport optics after the upgrade.

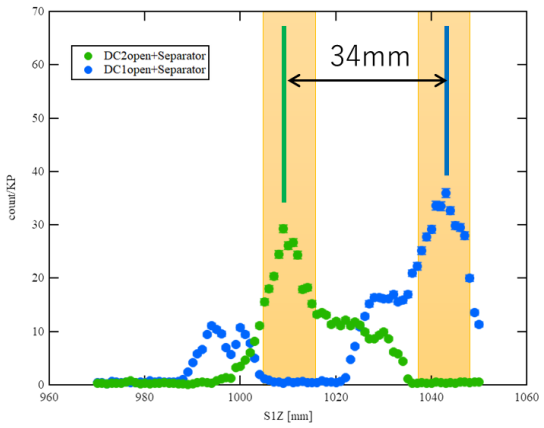

Figure 3. The observed beam profiles of the separated incident beams at the virtual neutron source.

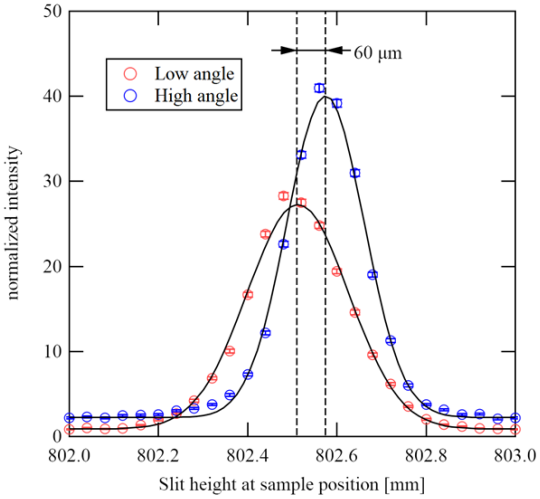

Figure 4. The observed beam profiles of the separated incident beams at the sample position.

3. Precise focusing mirrors

The slits for the virtual neutron source were made of borosilicated glass with Gd_2O_3 painting and set parallel at the precision better than 25 μrad. All the parts of the precise focusing mirrors were manufactured with ultra-precision cutting machines. Two sets of opposing mirrors were installed at the beam line at upstream and at downstream. The tilt errors of the mirrors were estimated to be between 30 and 50 μrad in FWHM by using a laser interferometer.

Figure 4 shows the beam profiles at the sample position. A misalignment of 60 μm is observed, but the beam centers could be adjusted by tuning the virtual neutron source.

4. Detectors

A set of FRP detectors was installed, and the efficiency and the resolution were improved 2 times and 1.5 times, respectively.

5. Conclusion and prospects

The necessary items for realizing MR-NR have been installed and the rough adjustments were performed. All the instruments worked well but the performance of some items was not up to the expectations. The refinements of the instruments will be done in FY2023, and the first MI-NR measurement will be demonstrated.

References

[1] N. L. Yamada *et. al.*, *Euro. Phys. J. Plus*, **44** (2011) 9424.
[2] K. Mitamura *et. al.*, *Polymer J.*, **45** (2013) 100.
[3] S. Takeda *et. al.*, *Opt. Express*, **24** (2016) 12478-12488.
[4] T. Hosobata *et. al.*, *Opt. Express*, **25** (2017) 20012-20024.
[5] T. Hosobata *et. al.*, *Opt. Express*, **27** (2019) 26807-26820.
[6] N. L. Yamada *et. al.*, *J. Appl. Crystallogr.*, **53** (2020) 1462-1470.
[7] S. Satoh, *Plasma Fusion Res.* **13** (2018) 3-6.
[8] F. Nemoto *et. al.*, *Nucl. Instrum. Methods Phys. Res. Sect. A*, **1040** (2022) 166988.

N. L. Yamada[1,2], M. Yamada[1,2], F. Nemoto[3], S. Satoh[1,2], and H. Seto[1,2]
[1]Neutron Science Section, Materials and Life Science Division, J-PARC Center; [2]Institute of Materials Structure Science, KEK; [3]National Defense Academy

Online Data Processing Application Suite for Polarized Neutron Reflectometer SHARAKU

1. Introduction

The neutron reflectometer SHARAKU installed at BL17 in the MLF has been used for the structure analysis of the surface and interfaces in a sample. Because it can perform the spin-polarization analysis of the reflected neutron using polarizing mirrors and spin flippers, it can be used for the analysis of the magnetic structure. Various kinds of sample environments are available: magnets up to 7T, a 4K-refrigerator, a temperature/humidity-controlled chamber, and so on. Therefore, SHARAKU has been used for structure analysis in a wide variety of research fields, such as polymer [1–3] and magnetic thin films [4, 5]. In recent years, we have been developing a versatile application suite to handle the measurement data obtained at SHARAKU to maximize the efficiency of the experiment.

2. Data reduction in neutron reflectometry

The event recording system at the MLF stores the time-of-flight (TOF), detected time, and position on the detectors for each neutron. To obtain the NR profile, the momentum transfer, q, for each neutron is calculated from the TOF and the reflection angle. The histogram of q for the reflected neutron is normalized by that for the incident neutrons. The data processing to convert the raw experimental data to the NR profile has been carried out using the software *Refcal* or *Utsusemi*, which are designed for SHARAKU and the common package for the instruments in the MLF, respectively [6]. The users usually transfer the converted NR data to their storage medium after the experiment before leaving the J-PARC site because the experimental data cannot be accessed from the outside of J-PARC. If they copy not only the converted NR data but also the raw experimental data files, they can perform the data analysis on their own PC by installing the above software packages. However, they sometimes find it difficult to install the software, including the libraries dependent on the computer environment at the user side. Thus, the data analysis and visualization at the users' laboratories are limited outside J-PARC; therefore, there has been a potential demand to enable the data processing without an effort to build the software environment and to handle the massive raw experimental data after the experiment.

3. Web application suite for NR

To carry out the data processing of the NR data without installing any software, we developed a web-based application environment on the intra-network of J-PARC (JLAN). The users can operate the application suite to deal with the reflectivity data via internet browser software. The web application was coded by the application framework Flask with Python. The applications are accessible in JLAN and can be used for monitoring the experiment and processing the data during the beamtime. This web application can be used on web browser software such as Firefox and Chrome.

Figure 1 shows the screenshots of the web applications for SHARAKU. The data information viewer shown in Fig. 1(a) displays a table of the acquisition time, measurement conditions and comment for each run. The user can refer to each raw data by clicking the run number at the left column in the table. In order to obtain the NR data, the observed spectrum of the reflected neutron intensity is normalized by that of the incident beam. Such data conversion can be carried out only by clicking the "Reflectivity Converter" button below the table after selecting the run numbers of the direct and reflection data in the "I_0" and "Ref" columns, respectively. Figure 1(b) shows the application for the data conversion to obtain the NR profile. A conventional NR profile is constructed by concatenating the reflection data that have been acquired at several different incident angles to cover a wide q range. The conversion application automatically estimates the run numbers for the series of the reflection data for each sample and concatenates them. Thus, for conventional samples, the NR profiles are available only by mouse operation. The converted data can be downloaded with the log file of the sample environment during the measurement.

4. Internet access

The web application suite described above cannot be used outside of the J-PARC because of the strict limitation of the network access to the intra-network of J-PARC. Therefore, the same web application environment is also available on the internet using Amazon Web Services (AWS) [7]. The experiment data is stored to a cloud storage and the users can view the experiment data and carry out the data analysis anywhere outside J-PARC by web browser software without installing any

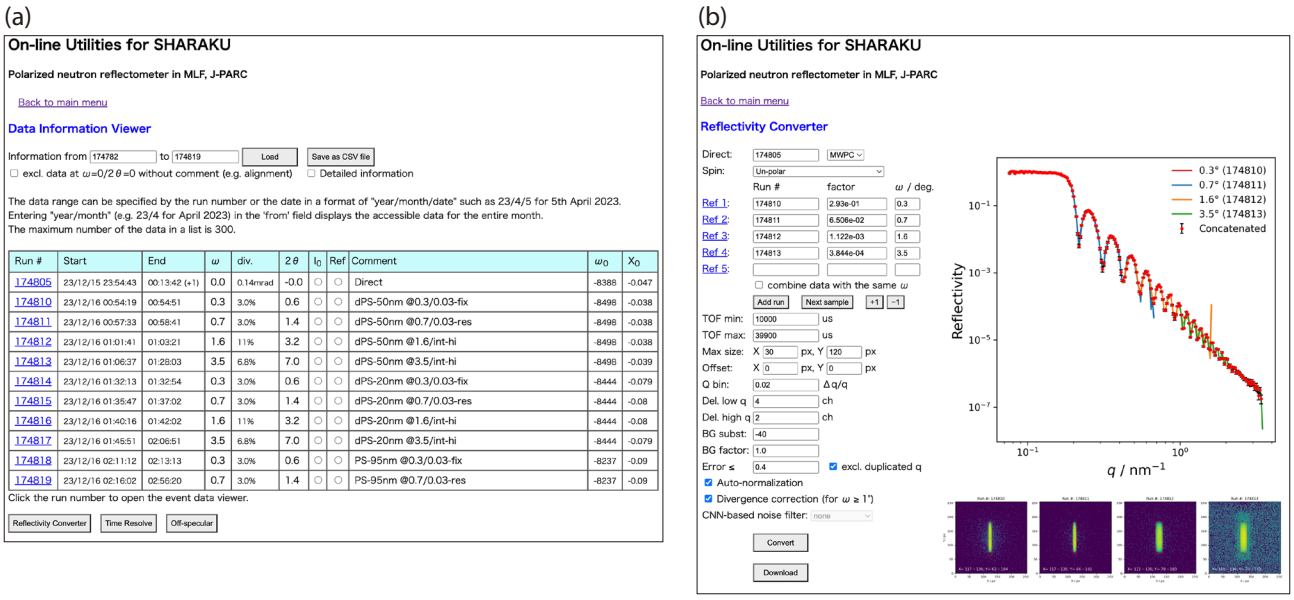

Figure 1. Screenshots of the web applications for SHARAKU: (a) list of the experiment data with the sample information and (b) data conversion application from the raw data to the NR profile.

additional plug-in or network setting on their computer. The access to the experiment data is protected by user authorization. Each user can handle only the data taken by themselves. The experiment data are automatically uploaded within 30 min after each measurement. Therefore, the user can discuss the experiment with the off-site collaborators during the beamtime.

The application suite also includes utility software to support the experiment and analysis. The sequence builder generates the script file for the automatic measurement. The NR profile simulator predicts the experimental data obtained at SHARAKU for a given sample structure and measurement condition [8]. The users can evaluate the observable q range and the statistical error in the experiment data. The above utilities are available on the internet without authorization.

5. Summary

The web application suite was developed for SHARAKU, and is used to perform the experiment and analyze the data with an easy-to-use GUI. It can also be used on the internet. Therefore, the users can handle their data after the experiment in the same manner as they do during the beamtime at the J-PARC site. Currently, novel functions based on data science, such as deep learning [9], are being developed. State-of-the-art analysis methods will be available in near future.

References

[1] K. Yamaguchi et al., Phys. Chem. Chem. Phys., **24**, 21578 (2022).
[2] K. Shimokita et al., Langmuir, **38**, 12457 (2022).
[3] W. Yoshimune et al., ACS Appl. Mater. Interfaces, **14**, 53744 (2022).
[4] R. Akiyama et al., J. Phys. Chem. Lett, **13** 8228 (2022).
[5] S. M. Suturin et al., Mater. Today Commun., **33**, 104412 (2022).
[6] https://mlfinfo.jp/groups/comp/en/
[7] https://nr.bl17-sharaku.mlf.plus/
[8] https://nr.bl17-sharaku.mlf.plus/simulate
[9] H. Aoki et al., Sci. Rep., **11**, 22711 (2021).

H. Aoki[1,2], K. Kasai[3], T. Hanashima[3], D. Yamazaki[4], K. Soyama[4], K. Akutsu[3], and N. Miyata[3]
[1]Neutron Science Section, Materials and Life Science Division, J-PARC Center; [2]Institute of Materials Structure Science, KEK; [3]Neutron Science and Technology Center, CROSS; [4]Neutron Instrumentation Section, Materials and Life Science Division, J-PARC Center

Status of SENJU 2022

1. Introduction

SENJU is a TOF single-crystal neutron diffractometer designed for precise crystal and magnetic structure analyses under multiple extreme environments, such as low-temperature, high-pressure, and magnetic-field, as well as for taking diffraction intensities of small single crystals with a volume of less than 1.0 mm^3 down to 0.1 mm^3 [1]. Since the operation of SENJU started in 2012, our instrument group has carried out continuous commissioning and upgrades.

In 2022, we installed a newly developed wide area detector at the bottom of the sample position, and updated the data-processing software, STARGazer-Online. In addition, we also report on the purposes of the instrument beam-time for SENJU.

2. Installing a wide area detector

The detector is one of the essential components for a single-crystal neutron diffractometer, and we have used a wavelength-shift fiber (WLSF) type scintillation area detector system for SENJU. The original detector size is 256 mm × 256 mm square (64 × 64 pixels). Recently, Nakamura and collaborators successfully developed a WLSF-type scintillation area detector with a larger detectable area, 512 mm × 512 mm square (128 × 128 pixels), and we installed the wider detector at the bottom of the sample position of SENJU. Figure 1 shows the latest detector arrangement of SENJU, and No. 37 is the newly installed area detector. Figure 2 shows a diffraction image of a molecular single crystal observed by the new detector.

Generally, diffraction data observed at the edge region of an area detector is not used for data processing because most Bragg peaks observed at the edge region are partially recorded peaks, and estimations of integrated intensities are difficult. Consequently, the ratio of the available region becomes larger when the detectable area becomes larger. In the case of the WLSF detector for SENJU, the ratio of the available area is 66% for the original detector and 82% for the newly installed detector.

Figure 1 shows the detector arrangement of SENJU, including the newly installed detector (Detector No. 37), and Fig. 2 shows diffraction images observed by both the original detector and the new detector. Structure analysis of a standard sample crystal with the new detector showed that the new detector works well for the intensity integrations of Bragg peaks and the structure refinement. The new detector has been available for the user program since the 2022B period.

3. Upgrading of STARGazer-Online

STARGazer-Online (SGO) is a remote data-processing and data-visualization application for SENJU that works on web browsers such as Firefox, Chrome, and Safari. We

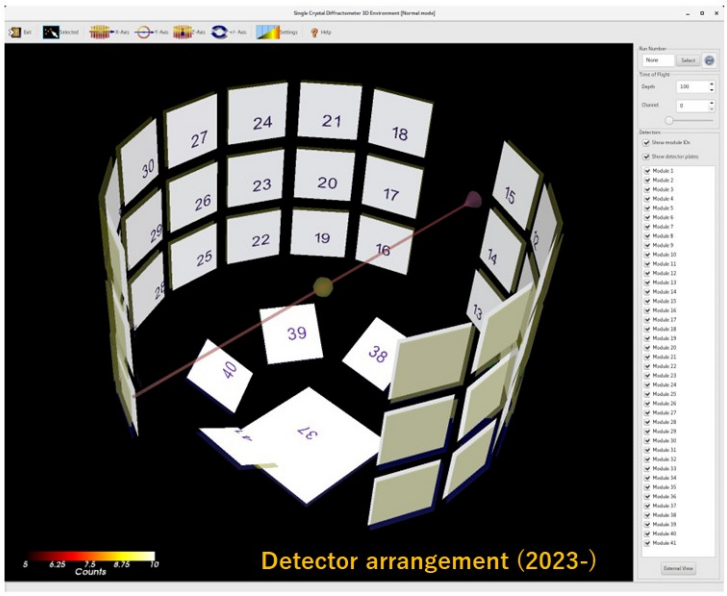

Figure 1. Detector arrangement of SENJU including the new area detector (No. 37).

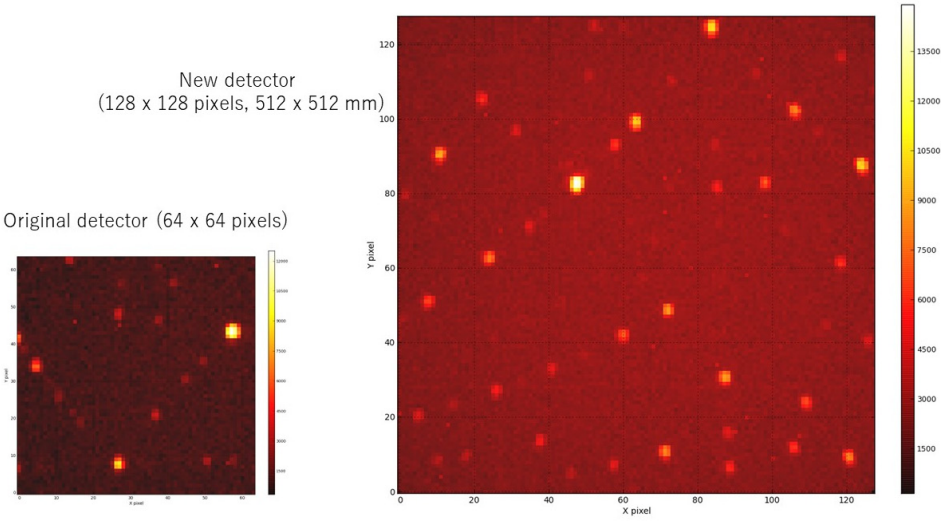

Figure 2. Diffraction image of a standard sample crystal observed by the original area detector (left) and the new area detector (right).

have been continuously upgrading SGO to keep up with the latest scientific research.

In recent years, multi-condition diffraction measurements, in which one sample is measured under multiple conditions to investigate the sample-environment-dependent structural changes, have been increasing at SENJU. In addition, structural analysis of materials containing large neutron absorption coefficient elements, such as europium and samarium, has also been growing. The data processing for those experiments required some special processing techniques that were not implemented in SGO, and the data had to be processed by instrument group member's custom-made scripts. Consequently, instrument group members had to spend a long time on such kind of an experiment.

Here, we integrated some custom-made scripts into SGO to enable users to process the multi-condition data and the highly absorbing materials data by themselves. One of the significant upgrades was adding a function to extract peak profiles and peak intensities from multiple diffraction data, which was initially developed by Kiyanagi et al. In this function, the profile and intensity of a specified region are obtained from diffraction data with multi-conditions at once. The diffraction data number and the region are set from the SGO GUI.

Another major update is a function for the absorption correction. In this function, the absorption effect of each Bragg peak is estimated from the shape, cell parameters, and formula of the sample crystal and the neutron wavelength-dependent absorption coefficients of each element. All parameters are also set from the SGO GUI.

4. Use of the instrument beam time

In 2022, the instrument beam time was used mainly for measurements of standard samples, and a vanadium-nickel alloy for calibration of the detector efficiency.

Reference

[1] T. Ohhara et al., J. Appl. Cryst., **49** 120 (2016).

T.Ohhara[1], R. Kiyanagi[1], A. Nakao[2], K. Munakata[2], Y. Ishikawa[2], K. Moriyama[2], I. Tamura[3], and K. Kaneko[1]
[1]Neutron Science Section, Materials and Life Science Division, J-PARC Center; [2]Neutron Science and Technology Center, CROSS; [3]New Research Reactor Promotion Office, JAEA

Recent Research and Advancements in BL19 TAKUMI

1. Introduction

BL19 TAKUMI, the engineering material diffractometer in the MLF of J-PARC, is mainly used for *in situ* studies of the microstructure evolution, mechanical properties, as well as residual stress mapping in engineering materials. TAKUMI can track various types of crystallographic information, including phase fraction, lattice strain (stress), texture, dislocation density, stacking fault probability, etc., through carefully analyzing neutron diffraction patterns. Additionally, a variety of specific sample environments at TAKUMI enable the *in situ* studies under various extreme conditions, such as cryogenic deformation (10 K~), thermomechanical controlled processes (~1473 K), fatigue, etc.

2. User program and publications

In FY2022, 31 general-use programs, 1 long-term program and 1 project-use program were successfully conducted on TAKUMI. Thanks to the improvement in the COVID-19 situation, users have essentially conducted their experiments on-site, and beamline staffs have carried out four proposals on behalf of the users. The statistics about the experimental types and the materials of the experiments conducted during FY2022 are summarized in Fig. 1. The *in situ* studies during loading test increased from 60% to 80% compared to FY2021, mainly due to the increase in the low temperature loading test. On the other hand, the beamtime percentage for residual stress mapping was 11%, which was mainly occupied by additive manufacturing samples. High-entropy alloy, which has attracted significant attention in recent years, dominated the metal and alloy part to occupy 37% of the beamtime, the same percentage as iron and steel. The rest of the beamtime was used for light metals (Ti- and Mg- based alloys, 22%) and composites (4%).

Thanks to the efforts of the users and the collaborators, 30 papers using the data measured at TAKUMI have been published in 2022. The statistics on experimental types and materials used in the papers are summarized in Fig. 2. Additionally, two poster awards and a young researcher prize were received in relation to the experiments at TAKUMI. Some highlights of the papers are introduced as follows:

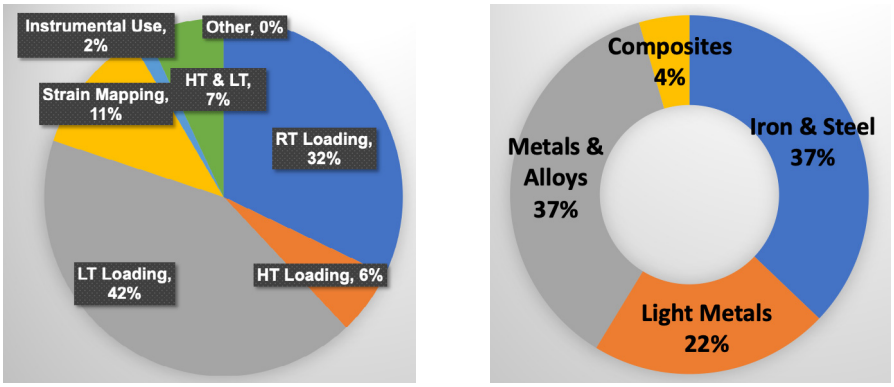

Figure 1. The statistics of beamtime of TAKUMI in FY2022. (a) The types of experiments conducted at TAKUMI and (b) the types of materials used in those experiments. The percentages represent the beamtime (in days).

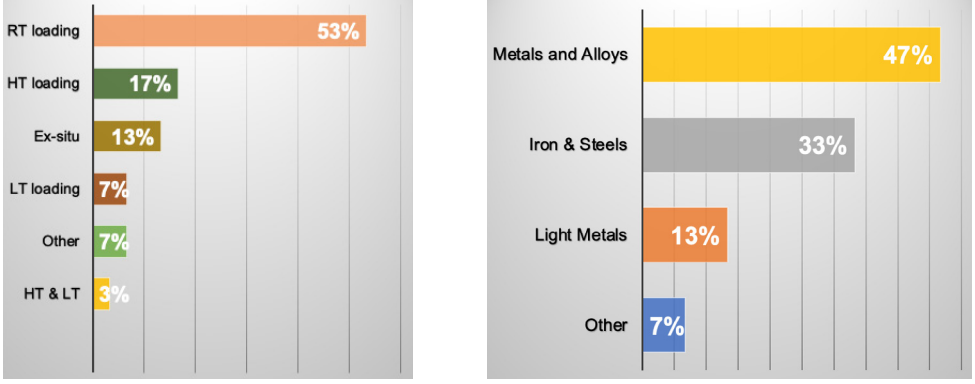

Figure 2. The statistics of papers using TAKUMI published in 2022. (a) The types of experiments conducted at TAKUMI and (b) the types of materials used in those experiments. The percentages represent the number of papers.

(a) **"Metalloid substitution elevates simultaneously the strength and ductility of face-centered-cubic high-entropy alloys"**, by Daixiu Wei, *et al.* [1]. The quantitative evaluation of dislocation density, volume fraction of martensite, and stacking fault probability, through *in situ* neutron diffraction, revealed that the unusual synergy of high strength and extraordinary ductility in high-entropy alloys with Si addition is attributed to the activity of multiple deformation modes.

(b) "**Flexible and tough superelastic Co-Cr alloys for biomedical applications**", by Takumi Odaira, *et al.* [2]. Neutron diffraction has verified that a novel Co-Cr-based alloy exhibits a significant elastic strain of 2.82%, followed by a huge superelastic recovery strain of 15.8%. The latter is attributed to martensitic transformation.

(c) "**Evidence supporting reversible martensitic transformation under cyclic loading on Fe–Mn–Si–Al alloys using *in situ* neutron diffraction**" by Takahiro Sawaguchi, *et al.* [3]. The behavior of martensitic and reversion transformations during cyclic tension–compression loading at RT in three Fe–30Mn–(6–x)Si–xAl (x = 0–2, mass%) steels was studied by *in situ* neutron diffraction. The Fe–30Mn–4Si–2Al alloy is confirmed to provide a higher plastic fatigue life compared to the others due to its reversible martensitic transformation.

(d) "**Effect of hydrogen on evolution of deformation microstructure in low-carbon steel with ferrite microstructure**", by Kazuho Okada, *et al.* [4]. Neutron diffraction revealed that hydrogen-charge changed the dislocation structure in a ferritic-pearlitic 2Mn-0.1C steel. It was found that hydrogen increased the relative velocity of screw dislocations to edge dislocations, leading to a tangled dislocation morphology at the initial stage of deformation, and increased the density of screw dislocations at the later stage of deformation.

(e) "**Rediscovery of Hall-Petch strengthening in bulk ultrafine grained pure Mg at cryogenic temperature: a combined *in-situ* neutron diffraction and electron microscopy study**", by Ruixiao Zheng, *et al.* [5]. *In situ* neutron diffraction clarified the dominated deformation mode of ultrafine grained pure Mg at 77 K. Grain boundary sliding, which led to the softening of bulk ultrafine grained pure Mg specimen at room temperature, was suppressed at 77 K, indicating the regain of Hall-Petch strengthening at cryogenic temperatures.

3. Upgrades and maintenances

The following upgrades and maintenance were performed to make TAKUMI more user-friendly and more stable in FY2022:

(1) The chamber for cryogenic loading test was modified for DIC strain measurement. Macro strain as well as the localized strain can be accurately measured combined with *in situ* neutron diffraction during cryogenic deformation.

(2) A new compressive jig was developed for the cryogenic system and has been used for users' experiments. *In situ* neutron diffraction experiments during a compression test can be performed down to 20 K at TAKUMI.

(3) A set of grips for the high-temperature tensile test using the induction heating system was fabricated and tested. *In situ* neutron diffraction experiments during the tension test using the induction heating system is now available.

(4) An option for exporting the averaged loading data (e.g., strain and stress) corresponding to each slice was added in Emaki GUI, the software for neutron data reduction at TAKUMI.

References

[1] D.X. Wei, L.Q. Wang, Y.J. Zhang, W. Gong, T. Tsuru, I. Lobzenko, J. Jiang, S. Harjo, T. Kawasaki, J.W. Bae, W.J. Lu, Z. Lu, Y. Hayasaka, T. Kiguchi, N. L. Okamoto, T. Ichitsubo, H.S. Kim, T. Furuhara, E. Ma, H. Kato, *Acta Materialia* **225** 117571 (2022).

[2] T. Odaira, S. Xu, K. Hirata, X. Xu, T. Omori, K. Ueki, K. Ueda, T. Narushima, M. Nagasako, S. Harjo, T. Kawasaki, L. Bodnárová, P. Sedlák, H. Seiner, R. Kainuma, *Advanced Materials* **34** 2202305 (2022).

[3] T. Sawaguchi, Y. Tomota, F. Yoshinaka, S. Harjo, *Acta Materialia* **242** 118494 (2022).

[4] K. Okada, A. Shibata, W. Gong, N. Tsuji, *Acta Materialia* **225** 117549 (2022).

[5] R. Zheng, W. Gong, J. Du, S. Gao, M. Liu, G. Li, T. Kawasaki, S. Harjo, C. Ma, S. Ogata, N. Tsuji, *Acta Materialia* **238** 118243 (2022).

W. Gong[1], T. Kawasaki[1], W. Mao[1], K. Aizawa[2], and S. Harjo[1]

[1]Neutron Science Section, Materials and Life Science Division, J-PARC Center; [2]Materials and Life Science Division, J-PARC Center

The Current Status of the Versatile Neutron Diffractometer, iMATERIA

1. Introduction

The local government of Japan's Ibaraki Prefecture, where the J-PARC sites are located, has decided to build a versatile neutron diffractometer (IBARAKI Materials Design Diffractometer, iMATERIA [1]) (fig. 1) to promote industrial applications for the neutron beam in J-PARC. iMATERIA is planned to be a high-throughput diffractometer that could be used by materials engineers and scientists in their materials development work, including in chemical analytical instruments.

The applications of neutron diffraction in materials science are (1) to analyse the structure of newly developed materials, (2) to clarify the correlation between structures and properties (functions), and (3) to clarify the relation between structural changes and improvements of functions, especially for practical materials. A diffractometer with super high resolution is not required to achieve those goals. The match of features, like intermediate resolution around $\Delta d/d = 0.15\%$, high intensity and wide d coverage is more important.

This diffractometer is designed to face a decoupled-poisoned liquid hydrogen moderator (36 mm, off-centered) (BL20), and it has an incident flight path (L1) of 26.5 m, with three wavelength selection disk-choppers and straight neutron guides with a total length of 14.0 m. The instrumental parameters are listed in Table 1. There are four detector banks, including a low-angle and small-angle scattering detector bank. The angular coverage of each detector bank is also shown in Table 1. The rotation speeds for the disk-choppers are the same, with a pulse repetition rate of 25 Hz for the most applications (SF mode). In this case, the diffractometer covers $0.18 < d$ (Å) < 2.5 with $\Delta d/d = 0.16\%$ and covers $2.5 < d$ (Å) < 800 at three detector banks of 90-degree, low-angle and small-angle with gradually changing resolution. When the speed of the wavelength selection disk-choppers is reduced to 12.5 Hz (DF mode), we can access a wider d-range, $0.18 < d$ (Å) < 5 with $\Delta d/d = 0.16\%$, and $5 < d$ (Å) < 800 with gradually changing resolution with doubled measurement time compared to the SF mode.

2. Current status

All of the four banks, high-resolution bank (BS bank), special environment bank (90-degree bank), low-angle bank and small-angle bank, are operational. It takes about 5 minutes (in DF mode) to obtain 'Rietveld-quality' data in the BS bank at 700 kW beam power for about 1 g of standard oxide samples.

Figure 2 shows a typical Rietveld refinement pattern for a $LiCoO_2$ sample, cathode material for a lithium-ion battery (LIB), at the BS bank by the multi-bank analysis function of Z-Rietveld software [2]. It takes 20 min in

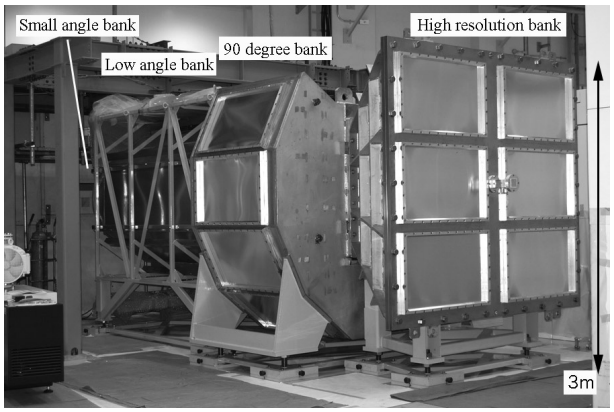

Figure 1. IBARAKI Materials Design Diffractometer, iMATERIA without detector for each bank and instrument shielding. The BS bank, 90-degree bank and low-angle bank can be seen from right to left. The small-angle detector bank, which is not shown in the picture, is situated in the low-angle vacuum chamber (left-hand side of the picture).

Table 1. Instrumental parameters of iMATERIA. L2 is the scattered flight path. The d-range (q-range) for each bank is the maximum value for 2-measurement mode.

L1	26.5 m	
Guide length		Total 14 m (3 section)
Position of Disk choppers		7.5 m (double) 11.25 m (single) 18.75 m (single)
High Resolution Bank	2θ L2 d-range	$150^\circ \le 2\theta \le 175$ 2.0 – 2.3 m $0.09 \le d\ (A^\circ) \le 5.0^\circ$
Special Environment Bank	2θ L2 d-range	$80^\circ \le 2\theta \le 100^\circ$ 1.5 m $0.127 \le d\ (A^\circ) \le 7.2$
Low Angle Bank	2θ L2 d-range	$10^\circ \le 2\theta \le 40^\circ$ 1.2 – 4.5 m $0.37 \le d\ (A^\circ) \le 58$
Small Angle Bank	2θ L2 q-range	$0.7^\circ \le 2\theta \le 5^\circ$ 4.5 m $0.007 \le q\ (A^{\circ -1}) \le 0.6$

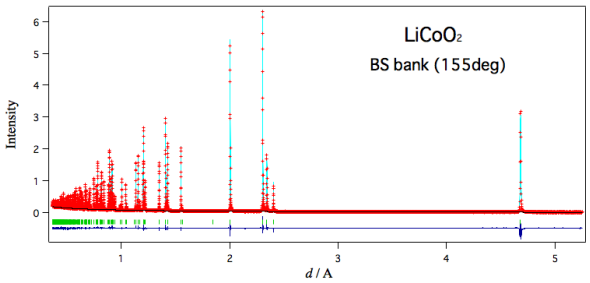

Figure 2. Rietveld refinement pattern for $LiCoO_2$ at the BS bank of iMATERIA.

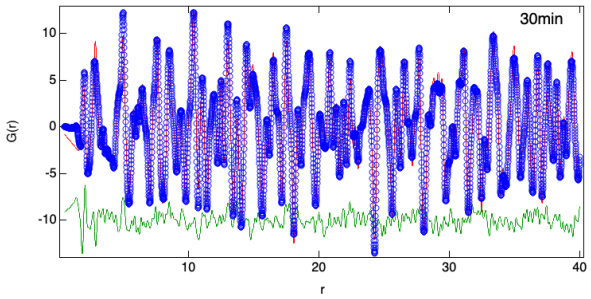

Figure 3. PDF refinement pattern for $Li(Ni_{0.5}Co_{0.2}Mn_{0.3})O_2$ at the BS bank of iMATERIA.

DF mode to collect the available Rietveld data, due to the high neutron absorption cross section for natural Li ($\sigma_s^{Nat} = 70$ barn).

3. Sample environments

The automatic sample changer is the most important sample environment for high-throughput experiments. Our automatic sample changer [3] consists of a sample storage, elevating system of two lines, two sets of pre-vacuum chambers and a sample sorting system. We can handle more than 600 samples continuously at room temperature (RT) without breaking the vacuum of the sample chamber.

The vanadium-furnace (~900 °C), the gas flow furnace (~1000 °C), and the 4 K and 1 K cryostats are ready for experiments.

The rapid heating/quenching furnace with automatic sample changer (RT – 1273 K with heating speed 10 K/s and cooling speed > 20 K/s) [4] and the universal deformation testing machine (max loading 50 kN with RT – 1273 K) [5] are available for texture measurements.

The in-operando charge and discharge measurement system for LIB with a sample changer is available in cylindrical, coin and laminated types of batteries.

4. Application for local structure analysis in iMATERIA data.

In materials science research, information on local structure (PDF; Pair Distribution Function) is as important as the average structure of crystals. The iMATERIA data have been prepared for local structure analysis. With the cooperation of the NOVA group, the iMATERIA data were loaded into a program managed by the NOVA group, allowing a reduced pair distribution function, $G(r)$, to be derived. Figure 3 shows the results of the PDF refinement of $Li(Ni_{0.5}Co_{0.2}Mn_{0.3})O_2$, the cathode material of Li batteries, using PDFgui software [6]. We found that acquiring the BS bank data for PDF refinement took about 30 minutes in DF mode at 800 kW beam power, 3-5 times longer than the measurement time required for Rietveld analysis.

References

[1] T. Ishigaki, *et. al.*, Nucl. Instr. Meth. Phys. Res. A 600 (2009) 189-191.
[2] R. Oishi, *et. al.*, Nucl. Instr. Meth. Phys. Res. A 600 (2009) 94-96.
[3] A. Hoshikawa, *et. al.*, J. Phys.: Conf. Ser. 251 (2010) 012083.
[4] Y. Onuki, *et. al.*, Metall. Mat. Trans. A. 50 (2019) 4977-4986.
[5] Y. Onuki, *et. al.*, Quantum Beam Sci., 4 (2020) 31.
[6] C. L. Farrow, *et. al.*, J. Phys.: Condens. Matter 19 (2007) 335219.

T. Ishigaki
Neutron Industrial Application Promotion Center, CROSS

Status of the High Intensity Total Diffractometer (BL21, NOVA)

1. Introduction

Total scattering is a powerful technique to analyze non-crystalline structure in materials with atomic Pair Distribution Function (PDF). NOVA was designed to perform total scattering and is the most intense powder diffractometer with reasonable resolution ($\Delta d/d \sim 0.35$ %) in J-PARC MLF. It is easy to adapt NOVA to a wide range of fields: liquids, glass, local disordered crystalline, magnetic structure of long lattice constant and so on.

2. Polarized neutron scattering experiment

A neutron polarizer with polarized ^{3}He gas, referred to as a ^{3}He spin filter, based on the Spin Exchange Optical Pumping (SEOP) was equipped to perform polarized neutron scattering experiments at NOVA [1]. The polarizer was installed at the upstream of the beamline, and the neutron polarization was held by the magnetic field produced with a guide field coil to the sample. The scattered neutrons by the sample were analyzed with a ^{3}He cell located at 20 mm from the sample position in the vacuum chamber. Figure 1 shows a schematic view of the polarized neutron system. In 2022, in addition to the installation of NOVA-specific polarizer, the beam duct (downstream of the polarizer in the vacuum chamber) was upgraded to a non-magnetic material (SUS304 → aluminum material). Figure 2 shows the transmittance of the polarized neutron beam before and after the duct renewal. The blue lines show the transmittance of the polarized beam in which the spins of polarizer and analyzer are antiparallel (spin-flip (−+)). The oscillation in Fig. 2(a) is due to the magnetic field on the beam axis. After the upgrade, it was removed, and we confirmed that there was no problem with the polarized neutron beam.

We present examples of polarized neutron experiments. Figure 3 shows the polarized neutron scattering profiles of NaH and NiO. Since this was a test analysis, we used the results of 10-minute measurements. We performed trial separations of the incoherent component from light hydrogen in NaH, and of the magnetic scattering component in NiO. We can conclude that the results are at a sufficiently practical level.

3. Future plans

Currently, we are developing a reduction program for polarized neutron experiments and a remote-control system for cell positions.

In the future, we plan to approach the analysis of polarized PDFs, such as water.

Acknowledgement

The polarized neutron scattering experiment system was developed with Dr. Okudaira, Dr. Takada, Mr. Takahashi, Mr. Kobayashi, and Dr. Oku. We would like to thank Mr. H. Maya for his technical support in operating NOVA. The operation and developments of NOVA was performed under the S1-type program (2019S06) approved by the Neutron Scattering Program Advisory

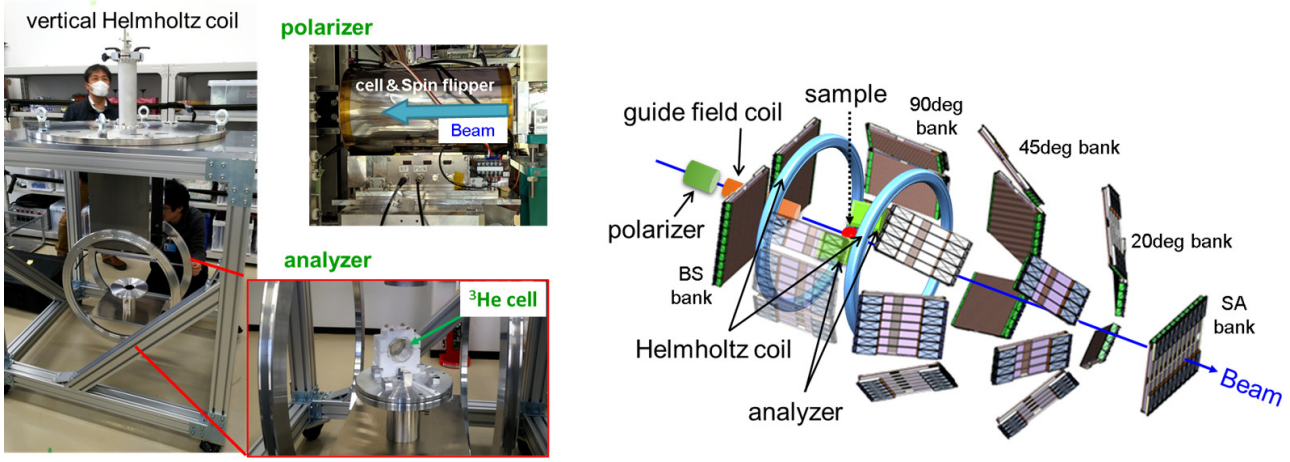

Figure 1. The schematic view of the polarized neutron system installed in NOVA.

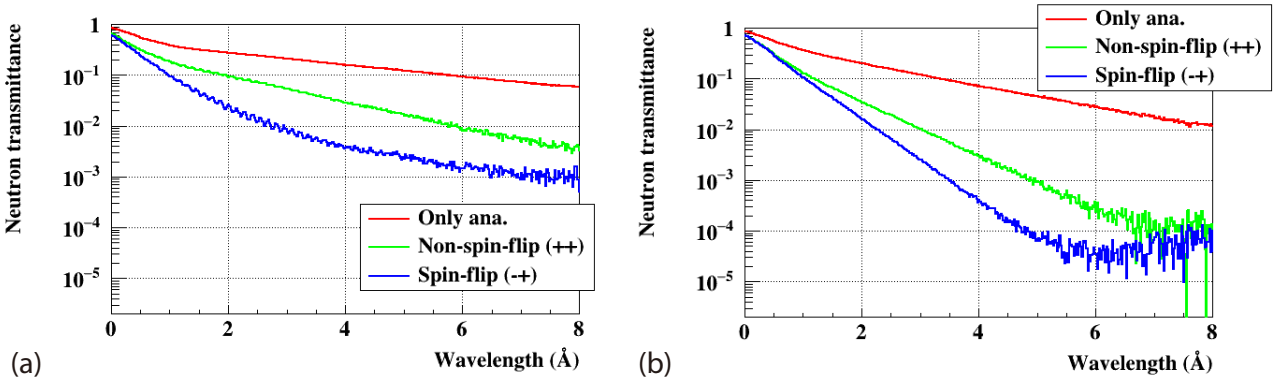

Figure 2. The transmittance of the polarized neutron beam (a) before and (b) after upgrading the beam duct.

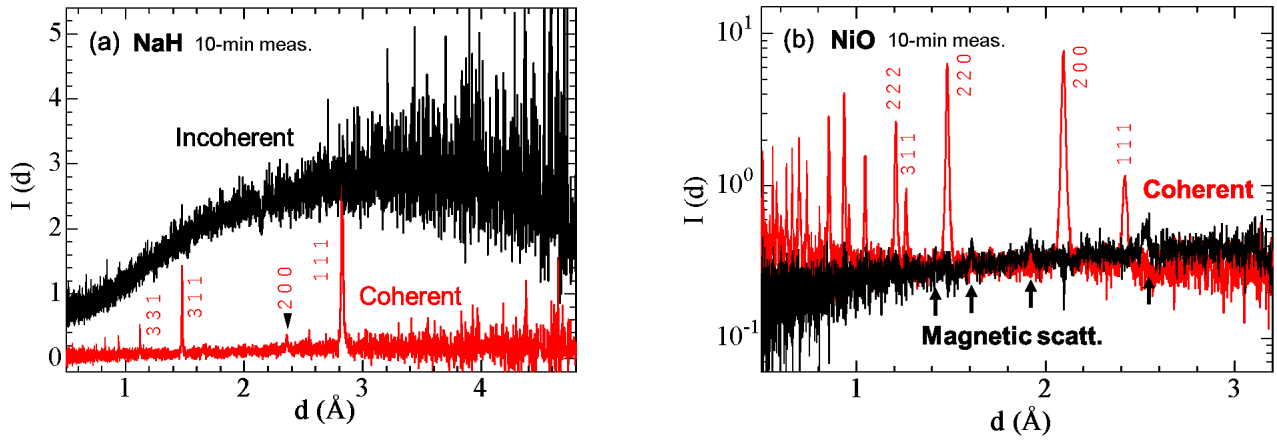

Figure 3. The polarized neutron scattering profiles of (a) NaH and (b) NiO. The data were obtained from short scans (10-minute measurements).

Committee of IMSS, KEK.

This work was supported by JSPS KAKENHI [grant numbers JP18H05518 (“Hydrogenomics”)], Research Grants in the Natural Sciences, the Mitsubishi foundation.

Reference

[1] T. Okudaira et al., Nucl. Instrum. Methods Phys. Res. A, **977** 164301 (2020).

T. Honda[1, 2, 3], H. Ohshita[1, 4], K. Ikeda[5], and T. Otomo[1, 2, 3]

[1]Institute of Materials Structure Science, KEK; [2]Neutron Science Section, Materials and Life Science Division, J-PARC Center; [3]Department Materials Structure Science, The Graduate University for Advanced Studies, SOKENDAI; [4]Technology Development Section, Materials and Life Science Division, J-PARC Center; [5]Neutron Industrial Application Promotion Center, CROSS

Current Status of the Energy-Resolved Neutron Imaging System RADEN

1. Introduction

The energy-resolved neutron imaging system "RADEN", installed at beamline BL22 in the MLF of J-PARC, is a dedicated instrument for wavelength/energy-dependent neutron imaging experiments, which utilizes fully the short-pulsed neutron's nature [1]. A variety of imaging experiments have been conducted at RADEN, such as Bragg edge imaging, neutron resonance absorption imaging, and polarized pulsed neutron imaging, in addition to the conventional neutron imaging. In this report, the recent results of the technical development and remarkable application studies conducted at RADEN are described.

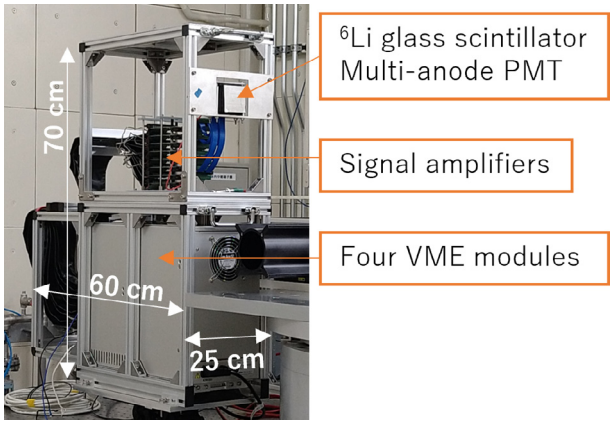

Figure 1. Photo of the modularized LiTA.

2. Upgrade of the resonance imaging detector

A two-dimensional neutron detector called lithium time-analyzer neutron detector (LiTA) has been developed for energy resolved neutron imaging [1,2]. LiTA consists of a lithium-6 glass scintillator (Scintacor, GS20), a 16 × 16 multi-anode photomultiplier tube assembly (Hamamatsu, H9500) and DAQ modules. The detector has its advantages in measurements in the high neutron energy range and high counting rate by utilizing its fast time response and optical transparency of the lithium glass scintillator. This characteristic has been used for neutron resonance absorption imaging and transmission measurement of high energy neutrons.

The hardware and software of the LiTA detector remained in its development stage for a while, and that caused inconveniences when it was used in many applications. Hence, the hardware has been redesigned to make it a compact and portable detector for wide and general use (see Fig. 1). With regard to the software upgrade, the LabVIEW-based dedicated data acquisition software was converted to the DAQ-MW, which is the MLF standard data acquisition system. The greatest advantage of the migration to DAQ-MW is the realization of sequence measurements controlled by the IROHA2 server. For example, it is possible to exchange many samples remotely or to perform CT measurement while rotating samples. Thus, the LiTA detector is now operated easily similar to the RADEN's regular detectors, such as μNID and nGEM. In addition, online analysis software was also introduced to confirm two-dimensional images, TOF, and pulse height distribution in real time from the data acquired by the LiTA. It is also possible to display two-dimensional images gated by a selected TOF range or pulse height and vice versa.

Next, we describe an upgrade affecting the TOF measurements. The 3NBT-CT signal, which is mostly used as the start signal of TOF measurements, is delayed several microseconds from the actual "T0 timing". Hence, the accessible upper energy limit of the measurement is about 100 keV. Due to this limitation, the identification of light elements, such as lithium, which has a resonance peak at several hundred keV, was not possible by the resonance absorption technique. In addition, a wide energy range of up to 1 MeV was demanded by several users. In order to break this upper energy limit, TOF recording and kicker pulse counting have been conducted independently with different trigger signals. That means, the RCS-XT signal, which arrives 100 microseconds before the actual T0, was used for the TOF start signal and the 3NBT-CT signal, which gives the neutron generation information, was used for the kicker pulse counting. This option allows the user to measure from the 0th second. For further upgrades, gamma-ray sensitivity and background of the LiTA will be studied, and the precise pulse function will be measured for quantitative imaging of elemental distribution.

3. Application study: Residual stress relaxation in induction-hardened gears using neutron Bragg edge imaging

Fatigue damage is a significant concern in large-scale engineering components. Understanding the distribution of nonlinear strain/stress around fatigue cracks is crucial for comprehending the behavior of fatigue and

crack growth in engineering materials. For example, induction-hardened gears produced by Neturen Co., Ltd had compressive residual stress from a unique double induction quenching (DIQ) process, which improved their fatigue life.

In our previous work, the Bragg edge imaging technique has been employed to map strain and microstructure in these gears [3]. This time, we studied the relaxation or redistribution of residual stress caused by fatigue loading at the tooth root of the gears by using Bragg edge imaging. After Bragg edge imaging, destructive X-ray diffraction (XRD) was also used to characterize the residual stress on the same sample's tooth root surface. However, the measurement volumes of Bragg edge imaging and XRD are distinct from each other and, hence, their results are complementary. Moreover, our study focused on non-destructively investigating the residual stress relaxation behaviors at Hofer's critical section of the teeth with the different loading conditions during fatigue tests [4]. The spatial distributions of the lattice spacing and the Bragg edge broadening in the DIQ gear product were obtained via single-edge fitting so as to evaluate residual strain/stress distribution. Then, the results were assessed together with XRD results. Our findings indicate that residual stress relaxation with fatigue damage primarily occurs in the compressive side of the DIQ gear tooth root (see Fig. 2), suggesting a connection between residual stress relaxation and fatigue damage. These valuable insights have the potential to enhance our understanding of fatigue damage mechanisms under various loading conditions and allow to make accurate estimates of the product service life, which will lead to an improvement of the gear production processes.

Currently, the Bragg edge imaging method is actively used at RADEN for application studies, involving a wide range of engineering materials and products, including high-Mn steels, welded components, railway axles, and more.

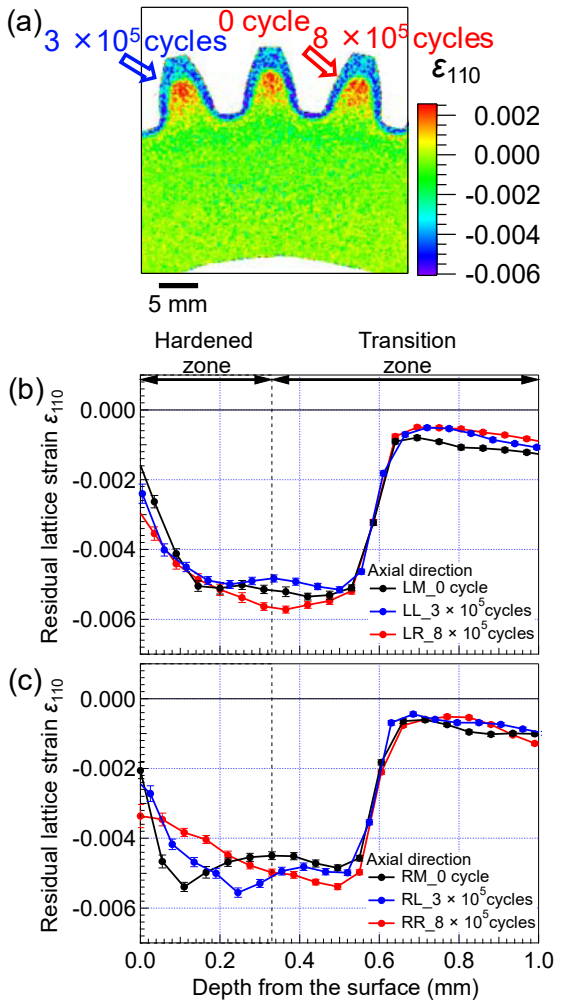

Figure 2. Residual lattice strain obtained via Bragg edge imaging: (a) a 2D map, (b) distributions for different load cycles on the tensile side of the teeth root, and (c) distributions on the compressive side of the teeth root in the axial direction.

4. Summary and future plans

RADEN is used in various fields, not only scientific, but also industrial, and the application spreads widely now. The RADEN group continues the development work on devices, data analysis software and on imaging techniques and demonstration studies, so as to promote user programs from a broad field.

References

[1] T. Shinohara et al., Rev. Sci. Instrum., **91** 043302 (2020).
[2] T. Kai et al., Physica B: Cond. Matt., **551** 496 (2017).
[3] Y.H. Su et al., Sci. Rep., **11** 4155 (2021).
[4] Y.H. Su et al., Int. J. Fatigue, **174** 107729 (2023).

Y. Tsuchikawa[1], Y. H. Su[2], T. Shinohara[1], T. Kai[1], K. Oikawa[1], H. Hayashida[3], J. D. Parker[3], Y. Matsumoto[3], Y. Nagai[3], and Y. Kiyanagi[4]
[1]Neutron Science Section, Materials and Life Science Division, J-PARC Center; [2]Technology Development Section, Materials and Life Science Division, J-PARC Center; [3]Neutron Science and Technology Center, CROSS; [4]Hokkaido University

Polarized Neutron Spectrometer POLANO

1. Introduction

POLANO is a direct geometry chopper spectrometer with medium energy and spatial resolution. For the purpose of conducting high-efficient polarization experiments in inelastic scattering technique, the POLANO has been optimized for high transfer energy (HTE) polarization analysis [1-3]. Since 2019, the POLANO has opened to a part of the user program that deals only with unpolarized neutron experiments. Some of the unique techniques and ideas of the time-of-flight (tof) method with a so-called event recording data acquisition processes came up. The omega-rotation measurement is one of the excellent ways, which enable us to measure the entire four-dimensional momentum Q (q_x, q_y, q_z) and energy E spaces. POLANO can also be available to measure the inelastic signals with the multi-Ei technique, though this is not a new technique but a resulting event recording system of the tof method. Utilizing the above-mentioned technique, a reasonable quality of data is being obtained, and scientific results (articles) will be generated using the POLANO spectrometer.

We also made significant efforts to develop and install polarization devices, including magnetic and related devices, in order to realize the HTE polarization. The HTE polarization can be realized by combining SEOP (spin exchange optical pumping) ^{3}He gas spin filter with a 5.5 Qc bending mirror analyzer.

2. On-beam activities

As in the past years, proposals for unpolarized neutron experiments are open for general use of the POLANO spectrometer. We constantly receive proposals and their total request beam time is around 30 days a half round. Most of the users require the same level of advanced experimental environment as other instruments (beam lines), such as high-magnetic field experiments, scattering angle rotation measurements, special sample environment experiments, and so on. The POLANO has been making an effort to meet these experimental requirements, in particular, with regard to its computational environment.

Along with the general user experiments, we are promoting polarized neutron commissioning. In order to accomplish effective on-beam commissioning, we consulted experts from other facilities. Professor L.J. Chang of NSRRC in Taiwan and Dr. G. Nilsen of RAL in the UK were invited as a KEK visiting researchers to contribute to the scientific use of polarized neutrons and provide technical advice.

3. Polarization commissioning

An in-situ polarized ^{3}He neutron spin filter (NSF) is installed in the POLANO for incoming neutron beam polarization [4]. The commissioning of the ^{3}He NSF was started using the neutron beam, and the ^{3}He polarization was confirmed to have achieved 80% by measuring the neutron transmission for a cell with ^{3}He gas of 21 atm-cm. The corresponding neutron polarization and neutron transmission are plotted in Fig. 1. The ^{3}He NSF was operated successfully over 10 days with no trouble or interruption. During the continuous operation, ^{3}He polarization was periodically monitored by adiabatic fast passage NMR [5], as shown in Fig. 2.

4. Newly aligned detectors

New position sensitive detectors (PSD), which are essential for the research of magnetism, have been added to the low-scattering PSD bank. For determining the

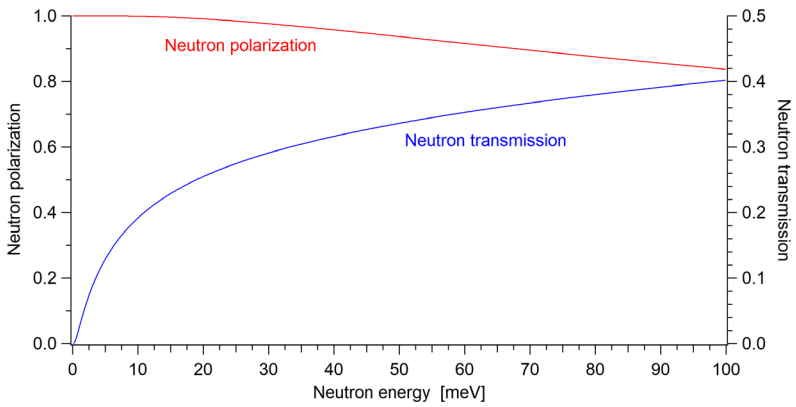

Figure 1. Neutron polarization and transmission for ^{3}He gas of 21 atm-cm and 80% polarization.

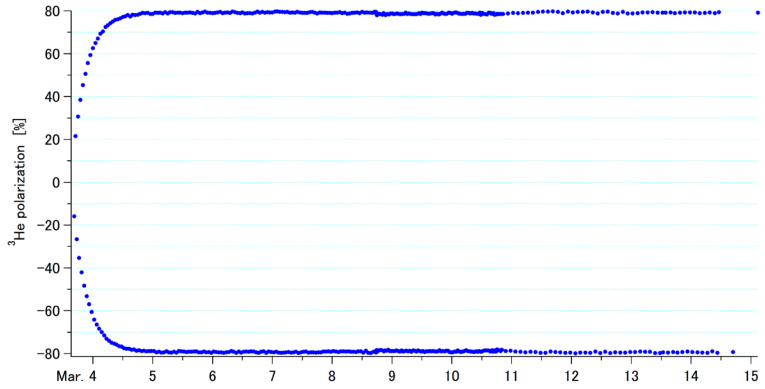

Figure 2. ^{3}He polarization measured during a continuous operation of the ^{3}He NSF in the POLANO.

precise neutron position in the detectors, the number of charges on both side of PSD tube (Q1 and Q2) has to be corrected by using the relation below.

$$\frac{x}{L} = \frac{AQ_2}{(Q_1 + BQ_2)} - C$$

Here L is the length of the detector, Q1 and Q2 are the pulse wave height values output from both ends of the detector and A, B and C are the coefficients to adjust the position. Then, the x corresponding to the neutron detected position can be determined.

In the calibration measurements, a polyethylene sample and 9 slits of cadmium plate were set up and three peaks due to incoherent scattering from the sample were observed on each detector. The spacing between these peaks was calculated according to the geometrical conditions and the ABC parameters were determined to match their lengths. The measured incoherent scattering peaks were fitted by a Gaussian function. A 2D detector map with slits pattern corrected by the fitted new ABC parameters is shown in Fig. 3. The algorithm for deriving the ABC parameters carried out in this study is useful and the development of software to automate its derivation has been planned.

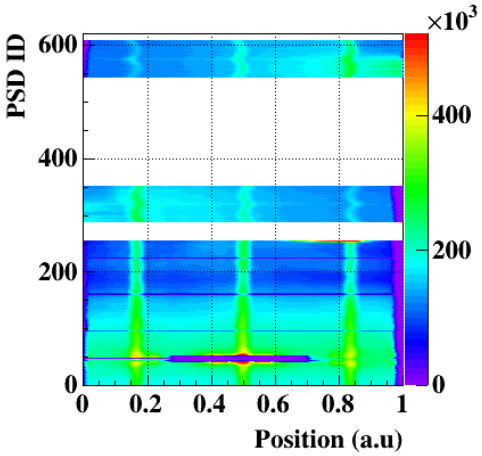

Figure 3. Calibrated position sensitive detector pattern.

5. Future prospects

In this year we have made significant efforts to refurbish and optimize the devices for the upcoming polarization experiments. Now, the POLANO is almost ready to launch a polarization experiment via an on-beam test at the MLF beamline BL23. In addition to beam commissioning, developments and updating devices and methods are indispensable to realize spherical polarimetry with a pulse neutron beam. In particular, the R&D of new devices, such as a spin flipper after the sample, high polarization ^{3}He filter, and large solid angle SEOP analyzer for the future HTE polarization will be conducted for better performance of the neutron polarization experiments.

References

[1] T. Yokoo, et. al., EPJ Web of Conferences, **83** 03018 (2015).
[2] T. Yokoo, et. al., AIP conference proceedings, **1969** 050001 (2018).
[3] MDPI Books, Quantum Beam Science 162 (2019).
[4] T. Ino et. al., J. Phys.: Conf. Ser. **862** 012011 (2017).
[5] T. Ino, JPS Conf. Proc. **22** 011016 (2018).

T. R. Yokoo[1,2], N. Kaneko[1,2], D. Ueta[1,2], S. Itoh[1,2], T. Ino[1,2], S. Yamauchi[1,2], K. Hayashi[1], and M. Fujita[3]
[1]Institute of Materials Structure Science, KEK; [2]Neutron Science Section, Materials and Life Science Division, J-PARC Center; [3]Institute for Materials Research, Tohoku University

Sample Environment at the MLF

1. Introduction

The MLF sample environment (SE) team provides the sample environment equipment that is shared for use among the MLF beamlines, the so-called BL-common equipment. The equipment is upgraded according to users' demands. The equipment that can produce extreme sample conditions is also developed. Additionally, we hosted the International Workshop on Sample Environment at Scattering Facilities (ISSE Workshop 2022) in this Japan fiscal year, and we would like to provide an overview of it.

2. Cryogenics and magnets

Six pieces of the BL-common cryogenic equipment are available for users' experiments. In JFY2022, (1) the superconducting magnet was operated for 15 experiments, (2) the ^{4}He cryostat for 10 experiments, (3) the ^{3}He cryostat for 6 experiments, (4) the ^{3}He-^{4}He dilution refrigerator (DR) insert for 11 experiments, (5) the Gifford-McMahon (GM) cryostat for 2 experiments, and (6) the GM cryofurnace for 1 experiment, including instrument proposals. These equipment pieces were used for 200.5 days of experimentation in total.

The BL-common cryogenic equipment was used on the two beamlines where it had not been operated previously; the superconducting magnet on POLANO (BL23), and a combination of the superconducting magnet and the DR insert on RADEN (BL22) (Fig. 1). In addition, an IROHA2 device module, which controls the temperature of the DR insert, was introduced to be available for users' experiments.

3. High temperatures

For the niobium furnace, there are two types of the sample stick with different thermocouples according to the temperature range; chromel-alumel thermocouples for the temperature range up to 1000°C and tungsten-rhenium thermocouples for the temperature range up to 1500°C. According to the regulations of the MLF, it is mandated that at least one user remain near the furnace and monitor its condition whenever the heater is in operation. In JFY2021, it was approved to operate the furnace with the chromel-alumel thermocouple stick monitoring remotely by installing the remote monitoring system with IROHA2. In JFY2022, the tungsten-rhenium stick was allowed to be used for the remote monitoring operation by the MLF equipment safety inspection. Using the stick, the high temperature user experiment above 1000°C has been performed on 4SEASONS (BL01) for the first time, in which the temperature reached 1227°C (1500 K).

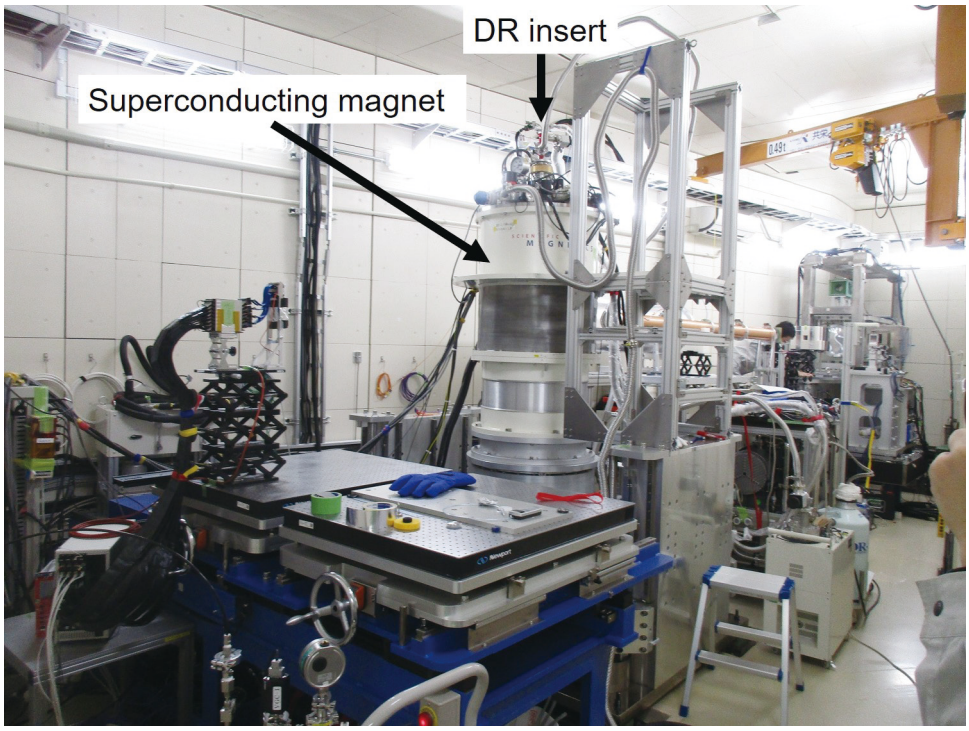

Figure 1. The superconducting magnet and the DR insert on RADEN.

4. Humidity

The H_2O/D_2O mixing vapor generator [1], introduced in 2021, was utilized for 27 experiments and operated for 82.5 days in JFY2022. For the first time, it was integrated into the inelastic scattering instrument BL14. Humidity control using this device is now available at BL02, 14, 15, and 17 beamlines, with seamless operation via IROHA2 control system.

5. ISSE Workshop 2022

The 11th International Workshop on Sample Environment at Scattering Facilities (ISSE Workshop 2022) took place at Resort Hotel Laforet Nasu, Japan, from August 28 to September 1. This workshop is held biennially and is organized by neutron/synchrotron facilities in the world that belong to the International Society for Sample Environment (ISSE) [2]. The 11th edition marked the first occasion when the workshop was held in an Asian country. Despite the effects of the COVID-19 pandemic, 87 engineers, technicians and scientists engaged in sample environment work participated in the event. 33 oral presentations, including online talks, and 36 poster presentations were given during the workshop (Fig. 2). Additionally, a round-table discussion on the international collaboration regarding sample environment in this pandemic time was also held. We exchanged information on new techniques related to sample environment and enjoyed interaction and fruitful discussion. The 12th edition will be held in Sweden in 2024.

References

[1] H. Arima-Osonoi et al., Journal of Applied Crystallography **56** (2023) 1802-1812.
[2] S. Ohira-Kawamura, Neutron News **34** (2023) 2.

Figure 2. Photos of the oral (left) and poster (right) sessions in the ISSE Workshop 2022.

M. Watanabe[1], Y. Sakaguchi[2], R. Takahashi[1], M. Ishikado[2], Y. Yamauchi[3], S. Ishimaru[3], S. Ohira-Kawamura[1,4], M. Nakamura[3], H. Arima[2], S. Takata[1,4], Y. Su[1], S. Zhang[2], T. Morikawa[2], K. Ohuchi[2], and T. Oku[1]
[1]Technology Development Section, Materials and Life Science Division, J-PARC Center; [2]Neutron Science and Technology Center, CROSS; [3]NAT Corporation; [4]Neutron Science Section, Materials and Life Science Division, J-PARC Center

Evaluation with Geant4 for Neutron Detector Performance

1. Introduction

Geant4 [1] is a toolkit for simulating the physical interactions of particles passing through matter; it is widely used in particle and nuclear physics, as well as astrophysics and medical applications. In Geant4, as shown in Fig. 1, the mean free path of a physical interaction is represented by the concept of a step, and the trajectory of a particle through a material is composed of multiple steps. In each step, the mean free paths of discrete physical interactions, such as scattering and absorption processes, are calculated sequentially and the physical interaction with the shortest distance is selected. Physical interactions that occur continuously, such as energy loss processes due to charged particles, are considered contributions to the step length, while physical interactions that occur at rest, such as decay and annihilation processes, are considered at the beginning of the step. Since the value of the mean free path depends on the material, the step is updated at the boundaries between materials. Generally, in Geant4, particles are tracked until their energy is zero in order to accurately determine where they stop, such as in an absorption process. On the other hand, to realize the effective simulation, a range cut is set as a threshold for particle production for secondary particles produced by physical interactions. Geant4 is written in C/C++, a general-purpose programming language. Because of advanced features such as event displays and multi-threaded processing, programs in Geant4 are often huge, and it is difficult for users to create programs from scratch. On the other hand, Geant4 provides many sample programs so that users can create their own applications based on them. This paper describes a simple application created to evaluate the performance of neutron detectors.

2. Geant4-based simulation

Figure 2 shows a N_2-Neutron Beam Monitor (N_2-NBM) as an example implementation of the simple neutron detector. The N_2-NBM detects neutrons via the $^{14}N(n, p)^{14}C$ reaction. The N_2-NBM is implemented as a multi-layer structure of the same size as the active area (65 mm × 65 mm). The detector housing material is 1-mm thick aluminum alloy. It is filled with a mixture of Ar and N_2 gases at 107.84 kPa with a mixing ratio of 94.02 : 5.98. The thickness of the gas layer is 12 mm. In the future, N_2-NBM with this detector parameter will be installed in several MLF neutron beamlines. Note that although the N_2-NBM is a gaseous radiation detector with some anode wires, its existence is negligible because of the minute size of the anode wires.

In Geant4, Neutron High Precision physics model (HP) is registered to reproduce neutron detection reactions such as the $^{14}N(n, p)^{14}C$ reaction. The evaluated nuclear data library, JEFF3.3 [2], is employed at HP to reproduce the physical processes of elastic scattering, inelastic scattering, absorption, and fission of neutrons with energies below 20 MeV. The QGSP_BIC_HP package [3] is applied in this study. The QGSP_BIC_HP package is a general-purpose physical process package used in radiation protection and shielding and medical applications and can also reproduce radioactive decay, including activation. In the simple application implemented, information on particles that have lost energy within the active area is collected, as shown in Table 1. The following information is collected during the simulation: particle name, track ID, parent ID, parent name, kinetic energy, original position, created process name and volume name of the original position. Track ID is a unique number assigned to each track, and parent ID is

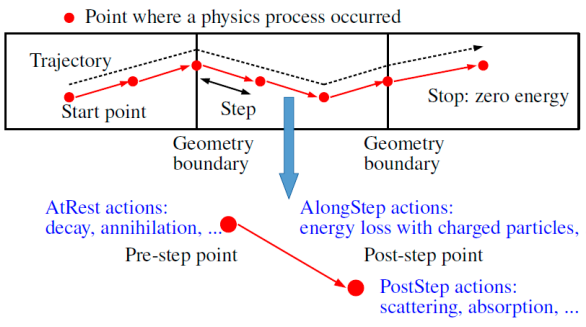

Figure 1. Concept of particle transportation in Geant4.

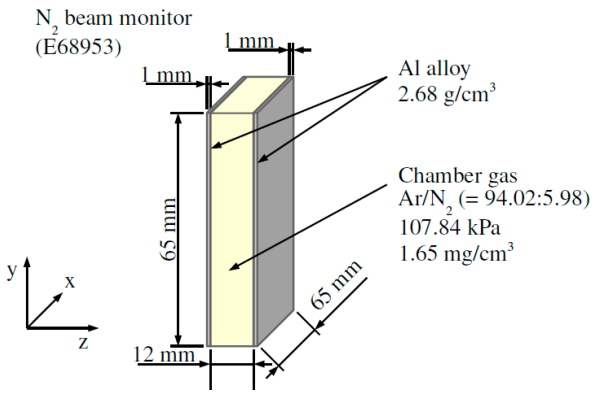

Figure 2. Implemented neutron detector (N_2-NBM).

Table 1. Information stored in the simulation.

Particle information	particle name, track ID, parent ID, parent name, kinetic energy, original position, created process name, volume name of original position
Behavior information in an active area	first position, last position, total energy deposit, total path length

the track ID of the parent particle. Volume name is the name given to the components of the simulation setup. In addition, the positions of incidence into and emission from active area, the amount of energy deposit within the active area, and the length of the track are collected as the behavior in the active area. These are derived by integrating the information obtained in each step.

3. Simulation results

Figure 3 shows the amount of energy deposit when 25 meV neutrons are vertically incident on the N_2-NBM. The detector size and material of the N_2-NBM follow Fig. 2. The number of simulation trials is 10^8. The initial energies of the proton and ^{14}C produced in the $^{14}N(n, p)^{14}C$ reaction, the neutron-detected reaction of N_2-NBM, are 0.58 MeV and 0.04 MeV, respectively,

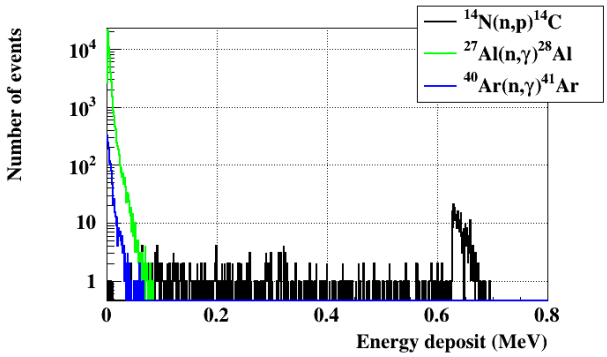

Figure 3. Energy deposit of 25 meV neutrons perpendicularly incident on the N_2-NBM.

indicating that the N_2-NBM analog signal is dominated by the proton contribution. On the other hand, ^{14}C is a radioactive isotope that emits β-rays, causing the energy deposit to exceed 0.62 MeV, the *Q* value for the $^{14}N(n, p)^{14}C$ reaction. The neutron efficiency of the $^{14}N(n, p)^{14}C$ reaction to 25 meV neutrons is expected to be $(6.730 \pm 0.259)\times10^{-6}$. Here, binominal distribution error is assigned as the error of neutron efficiency. The same treatment applies to the handling of neutron efficiency errors described below. The $^{27}Al(n, \gamma)^{28}Al$ reaction occurring in the detector housing and the $^{40}Ar(n, \gamma)^{41}Ar$ reaction occurring in the chamber gas are considered as competing reactions, as shown in Fig. 3. These competing reactions emit prompt γ-rays by absorbing neutrons and β-rays by β-decay of the radioactive isotopes ^{28}Al and ^{41}Ar. The half-lives of ^{28}Ar and ^{41}Ar are 2.3 minutes and 1.83 hours, respectively, and can be a background in actual measurements. On the other hand, the above-mentioned half-life of ^{14}C β-decay is 5730 years, so its contribution is negligible. Note that the simulations performed can be regarded as the amount of energy deposit obtained after an infinite amount of time. The neutron efficiencies of the $^{27}Al(n, \gamma)^{28}Al$ and $^{40}Ar(n, \gamma)^{41}Ar$ reactions are $(9.800 \pm 0.031)\times10^{-4}$ and $(1.974 \pm 0.044)\times10^{-5}$, respectively, which are much higher than those of the $^{14}N(n, p)^{14}C$ reaction. On the other hand, the distribution of the total absorption peak from the $^{14}N(n, p)^{14}C$ reaction and the energy deposit from the competing reactions can be separated clearly. Therefore, in actual operation, it can be expected that the threshold will be set to match the total absorption peak of the $^{14}N(n, p)^{14}C$ reaction to operate the N_2-NBM.

References

[1] S. Agostinelli, *et al.*, Nucl. Instr. and Meth. A **506** (2003) 250.
[2] A. J. M. Plompen, et al., Eur. Phys. J. A **56** (2020) 181.
[3] Geant4 Collaboration, "Physics List Guide rev. 7.0" (2022).

H. Ohshita[1,2], H. Endo[1,3], and T. Seya[1,2]
[1]*Institute of Materials Structure Science, KEK;* [2]*Neutron Instrumentation Section, Materials and Life Science Division, J-PARC Center;* [3]*Neutron Science Section, Materials and Life Science Division, J-PARC Center*

KENS Computing

1. Introduction

To create a stable experimental environment, the DAQ environment was virtualized using KVM. The number of physical machines was reduced from 88 to 5. Until now, the connection was made via the equipment local LAN, but by converting the physical switches to virtual switches, the physical switches and wiring in the rack were also greatly reduced. Fewer physical machines also means a lower incidence of hardware-related failures. The introduction cost was reduced by 92%, or more than 100 million yen. Power consumption was also reduced by 96%. The initial cost per unit has been significantly reduced, making it easier to secure budgets and plan replacements. Now 1~2 physical machines are systematically replaced every year, so that all the computers will be replaced in 5 years.

2. Migration to virtual machines

We have been monitoring resource usage with Zabbix since the physical machines, and based on CPU and memory utilization, we thought virtualization was feasible enough. First, after conducting virtualization for each application and confirming that it was working without problems, all functions of DAQ, storage, experiment control, and analysis were implemented in a virtual environment on a single physical machine, starting with the least-loaded experimental equipment. Today, the computational environment for all experimental equipment is deployed on a single physical machine.

3. Virtual machine configuration

Figure 1 is a diagram of the machine. The DAQ part uses DAQ-MW, and the parallel distributed environment that was also configured on physical machines is reproduced directly on KVM. In addition, control and analysis servers are also built as virtual environments. In addition, two network switches were used to construct two different intra-rack local LANs, which were also configured in the same network configuration as before virtualization using virtual switches. CPUs, and memory are allocated for 8 threads and 16 GB memory for DAQ, with the necessary resources reserved based on the Zabbix monitoring results. Although this capacity is more than sufficient, the increased availability of CPUs, such as AMD's EPYC series, which are available at a relatively low cost per Core, has made it possible to secure more resources. The total amount of memory allocated par VM and the number of VMs are used to calculate the total amount of memory, and a good cut-off capacity such as 256 GB, 512 GB, etc. is selected. The storage is currently available rack-mount servers, with the largest capacity being 12 3.5-inch HDDs. This is loaded with the estimated capacity needed for the next 5 years based on the Zabbix monitoring results. We try to select common

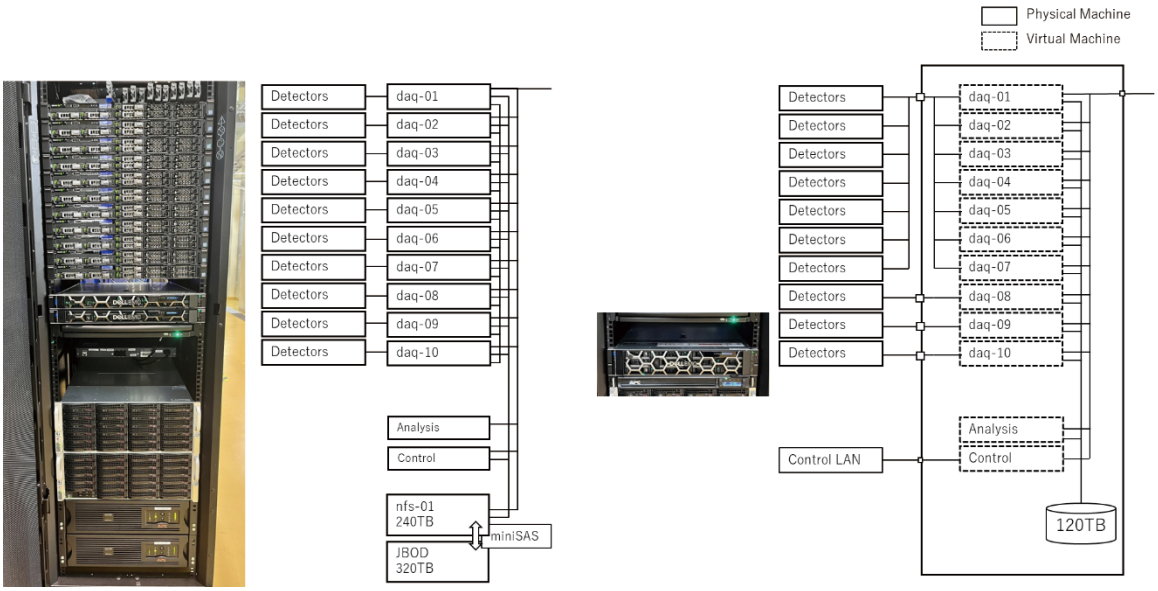

Figure 1. Diagram of the computer environment.

items as much as possible, such as capacity per piece of memory, power supplies, HDDs and SSDs, and RAID boards. This is done so that parts can be freely replaced when the machine is used as a testing machine after the end of the operation. Measured data from BL09, 21 exceed 500 TB in total. On the other hand, at the time of replacement, the most cost-effective capacity was 12 TB, and the capacity after RAID6 configuration was about 120 TB, which means that all the data on BL09, 21 cannot be contained on a single server. In this case, a separate storage server is prepared and stored there. Since the annual data volume for both BL09 and 21 is around 50 TB, the data is stored on the local server for about 2 years and then erased from the oldest data. Today, some products have capacities exceeding 20 TB per HDD. At the time of the next replacement, a stand-alone server for DAQ with a capacity of over 200 TB is likely to be the product of choice. If this happens, the operation to erase data as described above will be unnecessary. Data stored on a separate storage server is mounted on a machine in the same analysis environment, so it is configured in a way that the user does not have to worry about the physical location of the data at the user level.

4. Virtual machine management

The environment has been developed so that Zabbix can monitor not only the status of the servers, but also of iDRAC, UPS, and other devices that can be monitored by SNMP (Simple Network Management Protocol). This allows various parameters, such as the intake temperature of the server, the battery temperature of the UPS, and the quality of the input power supply to the UPS to be monitored all at once. In the event of a failure, the system is not only notified by Zabbix, but also by the properly configured alert email function in the hardware, such as APC and iDRAC, so that it receives double failure notifications. This is to ensure that failure notifications are not missed in the unlikely event that one or another element does not function properly. These measures enabled immediate detection of malfunctions. Since the maintenance contract is concluded directly with the manufacturer, not through a supplier, a system was established to centralize the process from manufacturer support requests to delivery of replacement parts and restoration work, enabling restoration within one to two days after a breakdown occurs. The system is designed to have hardware redundancy so that experiments can be continued even during restoration work, depending on the situation.

T. Seya[1,2] and H. Ohshita[1,2]

[1]*Institute of Materials Structure Science, KEK;* [2]*Neutron Instrumentation Section, Materials and Life Science Division, J-PARC Center*

Muon Science

Muon Section

1. Development of the D2 instrument

In recent years, elemental analysis with muonic X-rays is becoming popular in the D line. A lot of elemental analyses were conducted on archaeological objects, meteorites, and lithium-ion batteries. To obtain the data in a shorter time, the sample environment and the detectors were refurbished. The major change was in the sample chamber, the newly installed hemispherical chamber has 11 ports to mount the detectors (Fig. 1).

2. Progress of the laser system for ultra-slow muon generation

The ultra-slow muons are generated by ionizing the evaporated muonium from the muon-stopping target by irradiating coherent lights. To realize the efficient ionization of the muonium, vacuum ultraviolet (VUV) light (122.09 nm Lyman-α) and coherent light with wavelengths shorter than 360 nm are required. So far, over 10 μJ Lyman-α light has been successfully generated and applied to ultra-slow muon generation. To generate high-power VUV light, the power of the fundamental pulses of 1062.78 nm is required to be 100 mJ, and specially produced Nd:YGAG and Nd:YSAG ceramics rods (ø4 mm, 80 mm long) are used in the diode-pumped amplifiers as a gain medium. However, when using such a long rod, it was difficult to eliminate the optical wavefront distortion caused by the inhomogeneity in the medium. Thus, we decided to change the pumping configuration from a conventional side pump to an end pump geometry to reduce the optical path length in the gain medium (Fig. 2). The pump light from the laser diodes (LDs), which used to be injected from the side of the rod, will be injected coaxially. The new pumping geometry requires spatial profile shaping for the pump light beam from LDs, but the wavefront distortion can be dramatically reduced by shortening the crystal length. In the new method, sapphire substrates are bonded to the light input and output surfaces of Nd:YSAG for efficient cooling and end-face protection. The amplifier module is composed of 9.3 mm cubic Nd:YSAG ceramic, sapphire plates (ø25.4, t=2 mm) bonded on the ceramic, and a water-cooling holder (Fig. 3).

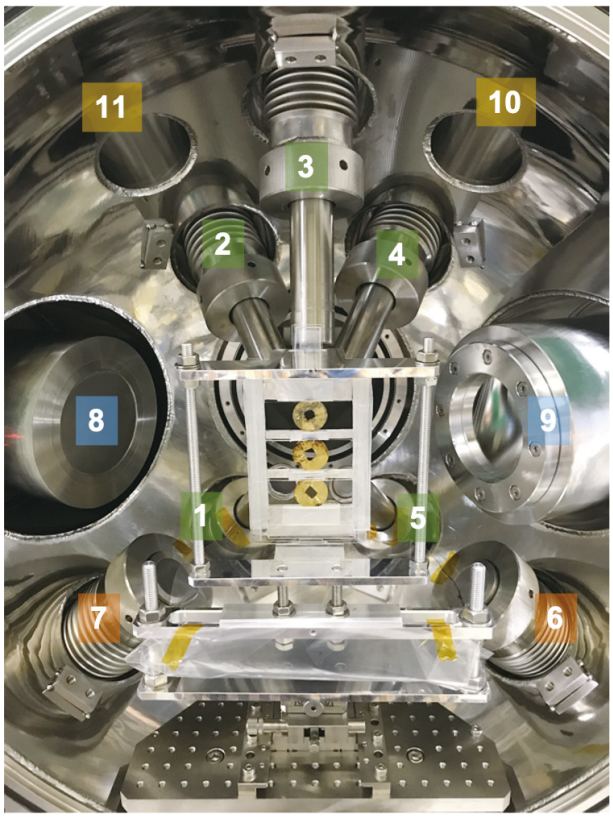

Figure 1. Picture of the Hemispheric chamber in the view from downstream of the beam. Gold coins are set at a sample position. The Ge detectors and multi-pixel detectors are equipped at Port 1 - 7, and Port 8 - 9, respectively. Ports 10 -11 can be used for decay counters and other detectors.

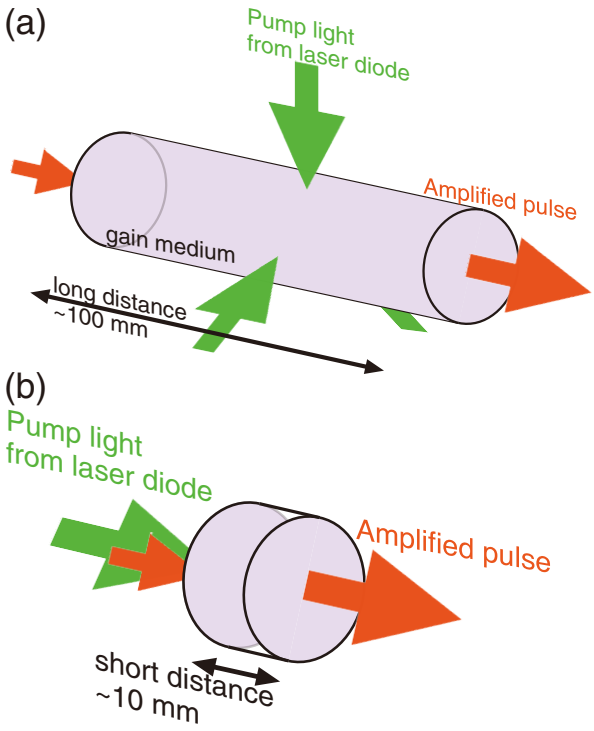

Figure 2. Schematic of pumping geometry. (a) conventional side pump for long laser rod and (b) end pump for short laser disk.

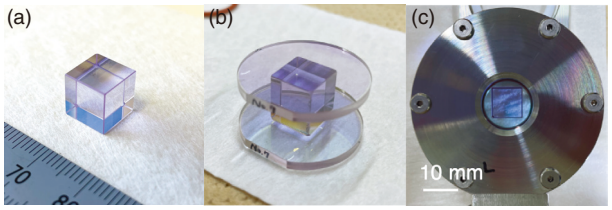

Figure 3. SNd:YSAG ceramic for power amplifier. (a) polished ceramic cube, (b) bonded ceramic cube with sapphire plates and (c) set in a water-cooling holder.

3. The kicker system of the S line

The kicker is essential for the simultaneous single-pulse operation of the S1 and S2 areas. However, as shown in Fig. 4, the number of failures has increased in the last few years. This could be due to MOS-FET degradation in the kicker power supply. Therefore, just before the start of the 2022B period, we replaced some MARX boards preventively by measuring the MOS-FET leakage current. However, many boards identified as healthy in the preventive diagnosis failed in the 2022B period. As a next countermeasure, we plan to replace the MOS-FET devices with modern SiC devices; we have already selected the SiC devices and verified the operation of the power supplies alone. The replacement work will be done after clearing the technical issue of mixing the use of the SiC device with the existing MOS-FET.

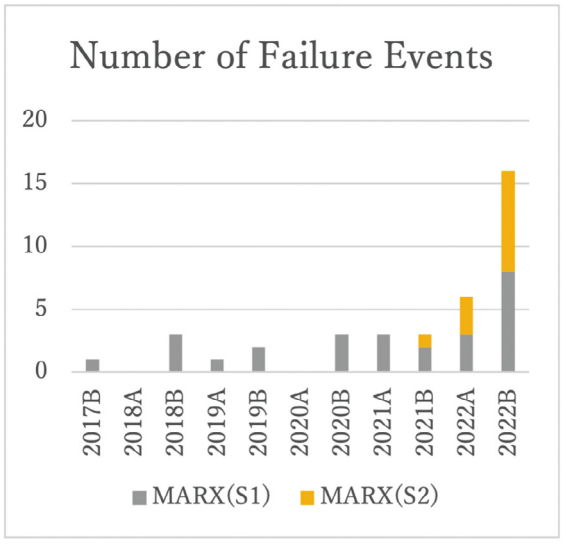

Figure 4. Number of MARX board failures that occurred in each operating period. Gray (yellow) bars represent the number of failures in the circuit that kicks the beam toward S1 (S2), respectively.

4. The H2 area construction

The first branch of the H-line named the H1 area was completed in January 2022, and then the commissioning was performed. The intensity of the surface muons was measured and was almost the same as its design value (10^8 muons/s), despite the absence of a DC separator (or Wien filter) and the failure of the power supplies of the capture solenoids. Currently, the H1 area is open for users. In the second branch of the H line, the H2 area, applying the technique developed in the U line, ultra-slow muons are produced and re-accelerated up to 4 MeV, and the world's first muon accelerator will be realized. The beamline is planned to be extended further to produce a novel low-emittance muon beam by accelerating up to 212 MeV. The beam will be used in the measurement of the muon g-2 and electric dipole moment and the transmission muon microscope (TμM). A new building on the east side of the MLF is necessary to extend the beamline. The engineering design of the extension building will be finalized in the next fiscal year. The H2 area construction was completed in March 2023 (Fig. 5) and the self-radiation inspection was done in April. The commissioning will be performed in the subsequent periods.

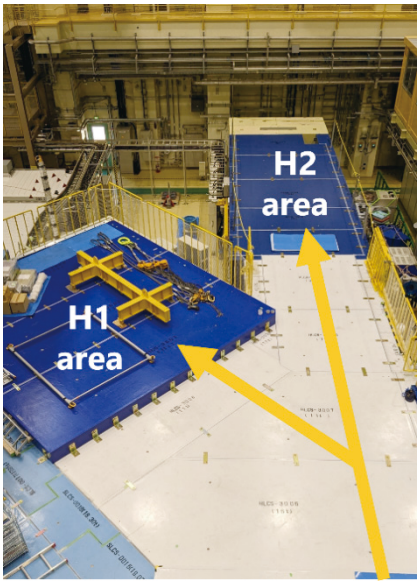

Figure 5. Picture of the H-line after the H2 area construction.

Muon Rotating Target

1. Present status of the rotating target

As part of the summer maintenance of the muon production target, the rotary feedthrough and rotary coupling were replaced. An anomalous increase in the rotational torque was observed after a replacement was done in the previous year, and this was also investigated. As a result of the investigation, it was found that the standard vacuum sealing gasket replaced last year, was 0.1 mm shorter in diameter than the regular one, which caused a misalignment of the rotary shaft and a load on the bearing of the rotary feedthrough. The vacuum sealing gasket was replaced with a regular one, and an Oldham type coupling with a larger allowable misalignment (from 0.25 mm to 0.6 mm) was adopted for the replacement work. After the work was completed, a rotation test was conducted, and the rotational torque was found to be normal. Beam operation was resumed and has continued stably without any increase in torque.

Although the above-mentioned work was performed in a high-dose and tritium atmosphere, the maximum individual exposure dose was successfully reduced by about 40% compared to the previous summer maintenance work by applying exposure dispersion and internal exposure prevention measures using an airline system (see Fig. 1).

Figure 1. Rotary feedthrough exchanging working with airline mask and anorak suit.

2. Modification of the MPS circuit

At J-PARC, interlocks are issued by the Machine Protection System (MPS) in the event of an anomaly. In the conventional MPS for rotating targets, the MPS is triggered when the torque of the rotating motor continuously exceeds the MPS alarm set value for a certain period of time, because a mechanical lock or the like was assumed. In this circuit, the MPS could not be triggered when the rotating motor torque fluctuated in a short period of time. Last year, the circuit was modified to immediately trigger the MPS when the motor torque momentarily exceeds the threshold value. In this case, however, the MPS threshold had to be set considerably larger to prevent false detection. Since the maximum torque output of a rotating motor is limited, a momentarily large rotating motor torque will not immediately cause the mechanism to fail. On the other hand, if a larger-than-normal torque is continuously generated, the target rotation mechanism continues to be subjected to a large load, and this situation directly leads to equipment failure.

We have changed the MPS circuit related to the muon target rotating motor torque from a circuit in which the MPS is triggered by an instantaneous increase in torque to one in which the MPS is triggered by using the average value of the rotating torque during a certain period as a threshold value. It detects whether or not the average torque value is above the threshold value every 30 seconds and counts up the number of times the value is above the threshold value. When the number of detections in the last 20 minutes exceeds 20 times, the MPS is triggered. The MPS alarm is detected every 30 seconds. The motor torque value during stable rotation is 5%, and the threshold is set at 12%.

3. Preparation of a spare target

The third rotating target was completed by incorporating the bearing box and cooling jacket fabricated using HIP in the previous year. Rotating target No. 3 has been tested at the factory for rotation and attachment to the plug shield, and it has been confirmed that there are no problems. The target will be commissioned for remote insertion into a new storage vessel and stored as a spare unit.

S. Matoba[1,2], Y. Kobayashi[1,2], and N. Kawamura[1,2]

[1]Muon Science Laboratory, Institute of Materials Structure Science, KEK; [2]Muon Science Section, Materials and Life Science Division, J-PARC Center

Beam Commissioning at D1/2 Areas

1. Introduction

The D line of MLF MUSE has a long superconducting solenoid, which can provide positive and negative decay muons from a few MeV/c to 120 MeV/c in addition to surface muons. The primary proton beam energy of the MLF is as high as 3 GeV, resulting in a high negative muon yield. In particular, thanks to the recent increase in beam power, the world's highest intensity negative muon beams are available. Using this high-intensity negative muon beam, various experimental applications have been developed, such as nondestructive elemental analysis using negative muon characteristic X-rays and negative muon spin rotation/relaxation. In this report, we cover the current status of the decay muon beam commissioning at the D line and other developments.

2. Radiation control for high energy decay muon beam

As seen in the examples of experiments, such as μSR under pressure and nondestructive elemental analysis, the demand for the use of high-energy (momentum) muons is increasing year by year. There are two main problems in the use of high-energy muons at the D line. One is the lack of output power of the quadrupole magnets (triplets) for the D1 area downstream of the branch. The other is the radiation dose when negative muon beams are used. The former problem was solved by replacing the magnets and the magnet power supply with a high-specification one (see the report by Yuasa et al.). On the other hand, the latter radiation problem is a trade-off between the allowable radiation dose and the muon energy required for the experiment and should be handled carefully. Here, we report on the latter.

When a negative muon is bound to a nucleus, it emits neutrons through the following reaction

$$ {}^{A}_{Z}X + \mu^{-} \rightarrow {}^{A-x}_{Z-x}X + \gamma + xn + \nu_{\mu}. \qquad (1) $$

In the MLF experimental hall, the radiation dose equivalent rate is controlled not to exceed 25 μSv/h to avoid radiation exposure. For this reason, the maximum momentum of the negative muon beam currently available is limited to 45 MeV/c.

On the other hand, in the nondestructive analysis of cultural heritage objects, for example, the demand for elemental analysis at deeper depths (i.e., higher momentum) has been increasing year by year. This is a natural demand, since elemental analysis using negative muons has advantages that other methods cannot imitate. Therefore, a simple interlock system is required to utilize higher momentum while suppressing the radiation dose. In order to realize this, an interlock system for the Q magnets in the pion transport section was studied and commissioned.

In this interlock system, some or all of the Q magnets in the pion transport section (Fig. 1) are not excited at momenta above 45 MeV/c. Even if the beam profile changes in the pion transport section due to a change in the state of the Q magnets, most of the phase space information is lost due to the decay of the pions in the solenoid section. Therefore, it can be assumed that the downstream beam profile is not significantly affected. Hence, a simple interlock can be configured to utilize a high momentum negative muon beam provided that one (or more) of the Q magnets is (are) not excited according to the momentum.

The following commissioning was performed in order to clarify the intensity reduction when the Q magnets in the pion transport section are not excited. Beam intensity and dose equivalent rate were measured when all Q magnets in the pion transport section were not excited. Three points (point C, E, and X in Fig. 1) were selected for dose equivalent rate measurements because these points have empirically high dose equivalent rates.

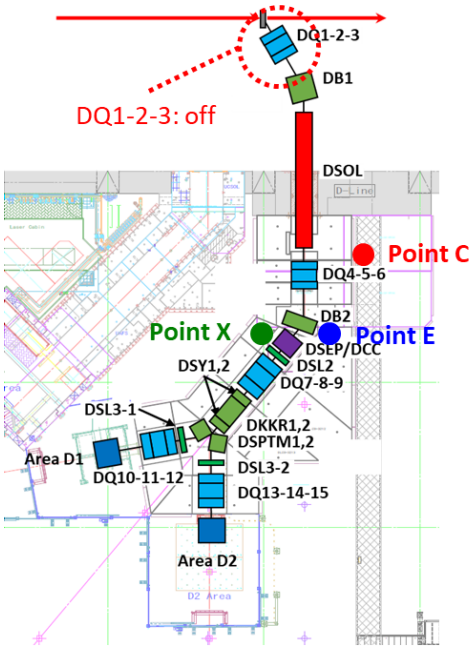

Figure 1. Schematic diagram of the D line showing the locations of radiation measurement (points C, E, and X).

Figure 2 shows the momentum dependence of the measured negative muon beam intensity and dose equivalent rate. Below 45 MeV/c, all Q magnets DQ1-2-3 in the pion transport section were excited, and above the momentum, all DQ1-2-3 were not excited. The momentum dependence of the dose equivalent rate was suppressed to approximately 5 μSv/h or less if the magnets DQ1-2-3 were not excited, which was not a problem at all. On the other hand, the intensity dropped by two orders of magnitude when DQ1-2-3 was not excited. Nevertheless, the intensity near 100 MeV/c was strong enough to be used in experiments (~10^5 muons/sec). Based on these results, we can expect to find the conditions to obtain sufficient beam intensity to perform experiments in the momentum region between 45 MeV/c and 100 MeV/c, while suppressing the radiation dose, by no excitation of only one or two Q magnets. We plan to further refine the conditions in the future.

3. Remote access/experiment

When a user conducts an experiment at the MLF, once the sample setting and other tasks are completed and the system is in a steady state, it is possible to automate the process to some extent by setting up a sequence in the IROHA2 system. However, if the user wants to change the sequence during the measurement, or if some trouble (sudden temperature change, etc.) occurs and requires immediate action, the user must go to the MLF from the dormitory, for example. In some cases, the user must walk about 28 minutes from the dormitory to the MLF, which is about 2.4 km away. In addition, with the recent trend toward remoteness, users are required to access the J-LAN intra network (the network in J-PARC where DAQ machines and other equipment are installed) from an external network.

To solve these problems and improve convenience, we set up a system for remote access and remote control (Figure 3). We set up a server for remote control, which can access the IROHA2 sequence server and other equipment for measurements, in KEK's Tokai 1 building. This enabled users to respond quickly to any urgent situation, such as a sudden change in temperature, by simply going to KEK's Tokai building 1, which is only 120 meters away from the dormitory.

This system is also useful when you want to access the measurement server from outside J-LAN. Outside access is usually complicated due to the need to submit the IP addresses of all the servers you wish to access, as well as all the port numbers to connect to them. This system, on the other hand, requires only the completion of a J-LAN VPN connection application to access the server. This has made the work on the experiment more convenient.

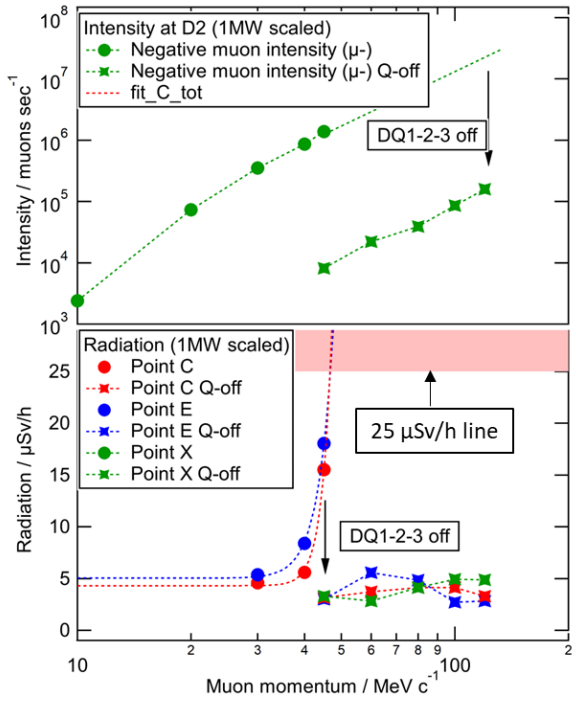

Figure 2. Muon beam momentum dependence of (a) negative muon intensity at D2 area scaled to 1 MW operation and (b) radiation measured at the positions shown in Fig. 1.

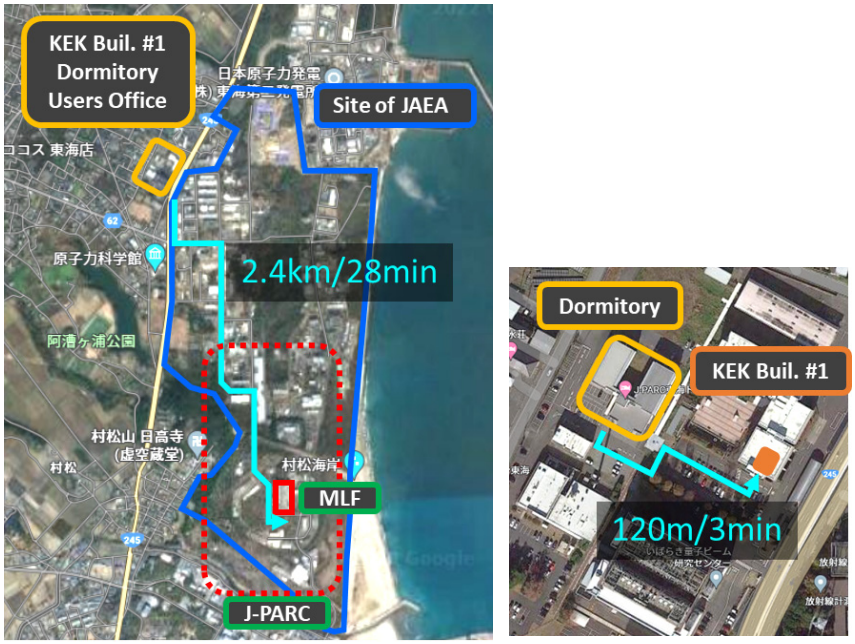

Figure 3. (Left) Route from dormitory to the MLF (~28 min). (Right) Route from dormitory to KEK Building No.1 (~ 3 min).

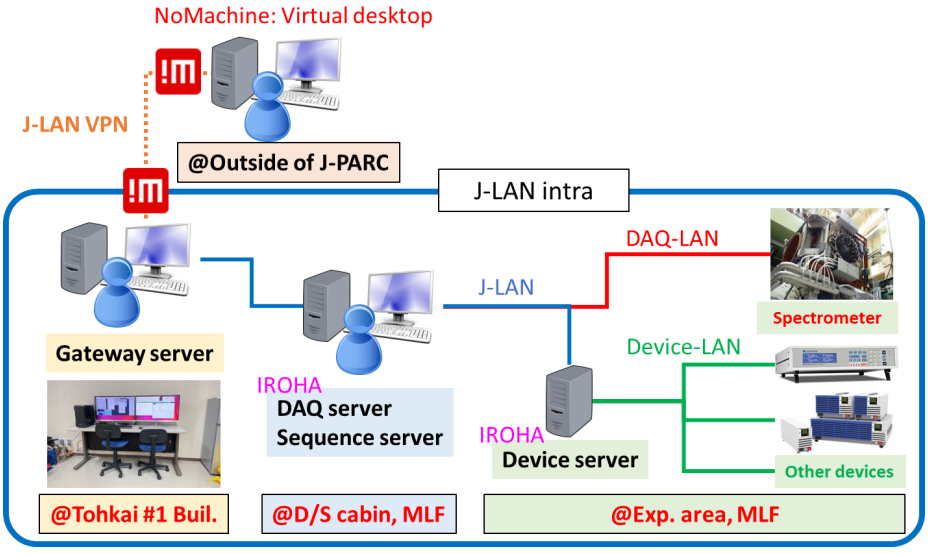

Figure 4. Diagram of the data acquisition system and gateway server for the remote access/experiment.

4. Summary

We have performed basic commissioning to assemble a simple interlock that can utilize high-energy negative muons in the D line while controlling the radiation dose. We have found that the Q magnets in the pion transport section can be not excited in whole or in part without any problem. A system for remote access/experiments was also established.

S. Takeshita[1,2], P. Strasser[1,2], A. Koda[1,2], W. Higemoto[1,3], I. Umegaki[1,2], S. Doiuchi[1,2], A. Hashimoto[1,2], Y. Ishikake[1,2], N. Kawamura[1,2], and K. Shimomura[1,2]

[1]Muon Science Section, Materials and Life Science Division, J-PARC Center; [2]Institute of Materials Structure Science, KEK; [3]Advanced Science Research Center, Sector of Nuclear Science Research, JAEA

Development of D2 (Muonic X-ray Element Analysis) Instrument and Sample Environment

The D2 experimental area provides various momentum of decay muons with a large space of about 4 m × 4.5 m, allowing users to bring in their own equipment or chambers needed to realize their experiments. This has led to the publications and awards of remarkable results in several fundamental physics experiments [1, 2] and elemental analysis [3, 4] in FY2022. Two of the KEK S1 projects led by Prof. Miyake (KEK) and Prof. Takahashi (The Univ. of Tokyo) have conducted experiments at the D2, providing fruitful results and publications. These include an attempt of CT imaging technique of muonic x-rays for analysis of archaeological samples using CdTe detectors [3], an experiment with a TES calorimeter [1], and elemental analysis of the returned samples from Ryugu asteroid by the Hayabusa2[4].

We had 17 theme experiments conducted at the D2 experimental area in FY2022. The largest number of the themes was elemental analysis of muonic x-rays (Fig. 1), which was followed by soft error (2 themes), Atomic Physics (2 themes), μCF(1 theme), and Nuclear capture(1 theme).

In Prof. Miyake's S1 project, we developed a sample chamber to install germanium (Ge) semiconductor detectors. Then, the sample chamber, which was called hemispherical chamber, became available to any user of the D2. The hemispherical chamber was designed by Dr. M. Tampo with a capacity to install 9 Ge detectors to measure muonic x-rays. The goal was to obtain fine data within a shorter time in order to perform effectively larger numbers of interesting research programs in the limited beam time. Therefore, the development of the data taking, and analysis is essential for efficient use of the beamtime. For each experiment, the difficulties of adding up all data immediately after completion of the measurement has been a problem. So, it is desired to add up all data during measurements of muonic x-rays.

One of the major advancements in the D2 experimental area in FY2022 was the development of software to analyze data instantly during measurements. Since we have 9 ports to set Ge detectors in the sample chamber for elemental analysis with muonic x-ray, we need to check data obtained from each detector and to obtain total count of all data from the 9 detectors to know whether the statistics is high enough in the measurement. Figure 2 shows a screenshot of the software to sum data from each Ge detectors and to calibrate the energy of the detectors. On the right side, a run number is set (the number of 204003 can be found in Fig. 2) at first and trigger modes are selected as beam or self-modes. Then, channels corresponding to detectors to analyze are selected by checking a box. The application displays each spectrum with different colors in the center of the window. The summation of all data can also be obtained immediately by clicking the sum bottom. The application is effective even for a still-ongoing run, not only for a run that has already finished. The software was realized by Mr. Y. Ishikake and Mr. S. Doiuchi.

The hemispheric chamber was modified so that nine Ge semiconductor detectors could be mounted, and various elemental analysis experiments were conducted

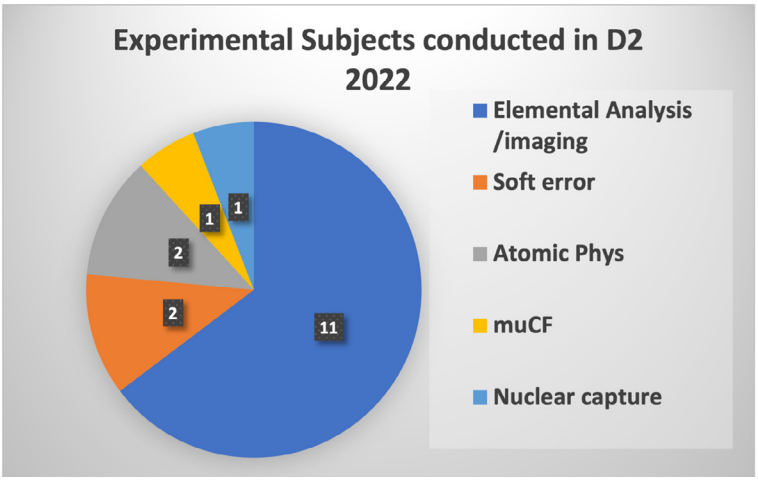

Figure 1. Experimental themes conducted at D2 in FY2022.

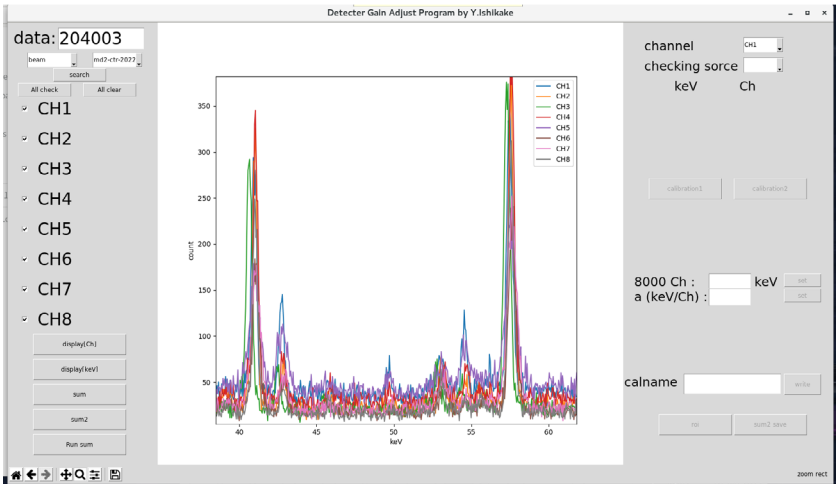

Figure 2. A screenshot of software to sum data from each Ge detectors and to calibrate the energy.

using these detectors in FY2022. As an example, the following elemental analysis experiments were conducted in FY2022:

[2022A0352(P)] Depth profiling of gradient composition in diode-type CeTe X-ray detector by position sensitive muonic atom spectroscopy

[2022A0066] Confirmation of the effect on the loss of metallic Li deposition in a lithium-ion battery using muonic x-rays

[2022B0054] First attempt to apply elemental analysis with muonic x-rays to commercially available LIBs

[2021MS02] Elemental analysis of cultural property

Other than elemental analysis, the hemispherical chamber was also used for experiments, such as muon transmission imaging and muon fusion. Particularly, for investigation of errors caused by muons in an SRAM, the depth to analyze can be confirmed by measuring muonic x-rays during irradiation of muons at the same time. The research attempts to find the momentum dependence of the rate of error occurrences by irradiation of muons in semiconductor devices.

In FY2022, three new low-energy semiconductor Ge detectors (LEGe), which we were preparing last year, have been installed on the hemispherical chamber for experiments and we conducted further fruitful research programs in elemental analysis using muonic x-rays.

Acknowledgments

The development of the software that we showed here was conducted as a part of "integration of arts and sciences" research program promoted by the KEK IMSS MSL and a part of Dr. Miyake's S1 project. It was also supported by the JSPS Grant-in-Aid for Scientific Research on Innovative Areas "Toward new frontiers: Encounter and synergy of state-of-the-art astronomical detectors and exotic quantum beams". The authors appreciate the cooperation of Mr. Shogo Doiuchi, Dr. Akiko Hashimoto, Mr. Yudai Ishikake, Dr. Adam Pant and other members of the Negative Muon Group. The design and production of the hemispherical chamber and the detector adding were managed with great diligence by Dr. Tampo.

References

[1] T. Okumura et al., "Proof-of-Principle Experiment for Testing Strong-Field Quantum Electrodynamics with Exotic Atoms: High precision X-Ray Spectroscopy of Muonic Neon" Phys. Reb. Lett. 130 (2023) 173001 (1-7).

[2] S. Nishimura et al., "Rabi-oscillation spectroscopy of the hyper fine structure of muonium atoms" Nishikawa Prize, Research & Development highlights in 2022.

[3] T. Nakamura et al., "Formation and evolution of carbonaceous asteroid Ryugu: Direct evidence from retuened samples" Science, 379 (2022) 787.

[4] I-H. Chiu et al., "Non-destructive 3D imaging method using muonic X-rays and a CdTe double-sided strip detector" Sc, Rep. 12 (2022) 5261 (1-9).

I. Umegaki, M. Tampo, and Y. Miyake
Muon Science Laboratory, Institute of Materials Structure Science, KEK

Muon Beamline Magnets and Power Supplies Update – Upgrade of D1-triplet and Power Supply –

1. Introduction

The triplet magnet D1-triplet (DQ10-11-12) is installed just before the D1 area of the decay muon beamline (D-line). This D1-triplet can transport muons with momentum up to 67 MeV/c because of the limitation of the temperature rise of cooling water and power supply specifications. But recently, users have requested higher muon momentum, as high as 90 MeV/c. So, we decided to upgrade the D1-triplet and power supply. They were replaced, and new current values that resulted in the same GL product and distance between the magnet centers were determined so that the beam optics would not change before and after the replacement. Commissioning was performed at 30 MeV/c. The current values from the optimization calculations were compared with the current values obtained after the beam commissioning.

2. Old and New D1-triplets

As shown in Fig. 1, the D1-triplet is installed just before the D1 area. The old D1-triplet can only transport muons up to 67 MeV/c. Table 1 shows the parameters that would be needed for transporting muons of 90 MeV/c with the old and new D1-triplets.

To transport 90 MeV/c muons with the old D1-triplet, a current of 504 A would be required, but the existing power supply specification of 375 A is insufficient. Also, even if 504 A could be supplied, the temperature rise of the cooling water in the magnet would exceed 30°C, thus violating the J-PARC regulation (temperature rise of cooling water should be within 25°C). So, we decided to upgrade both the D1-triplet and its power supply. Figure 2 shows the old and new D1-triplets.

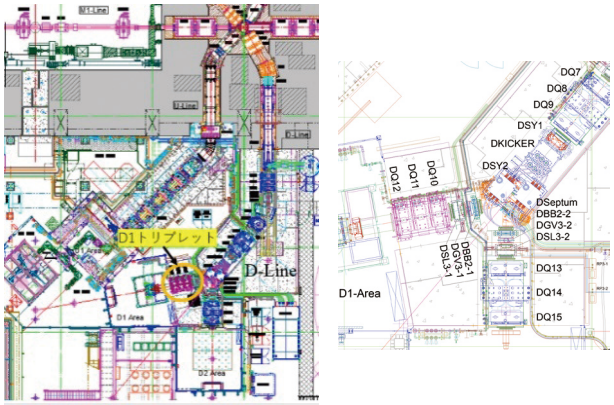

Figure 1. Decay muon beamline (D-line).

Table 1. Parameters of the old and new D1-triplets for transporting muons of 90 MeV/c.

	Old	New
Momentum [MeV/c]	90	
Field gradient [T/m]	2.7	
GL [T]	1.06	1.09
Magnetomotive force [A*Turns]	24170	
Number of coil turns [Turns/coil]	48	72
Bore diameter [mm]	300	
Pole length [mm]	300	
Distance between magnet centers [mm]	500	490
Excitation current [A]	504	336
Excitation voltage [V]	51	51
Water flow [L/min]	10.8	25.6
Flow speed [m/s]	1.6	1.9
Temperature rise of cooling water Δt [°C]	34	10

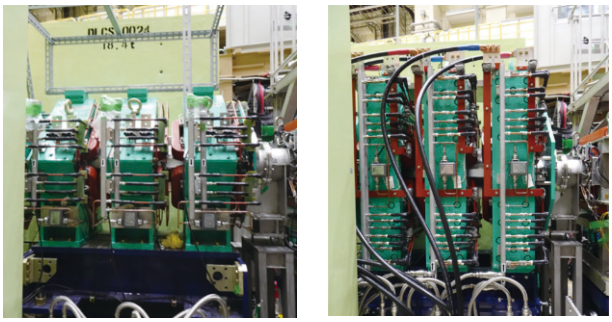

Figure 2. Old D1-triplet (left) and new D1-triplet (right).

3. Upgrade of the D1-triplet and power supply

A quadrupole magnet triplet originally designed for high-momentum muon transport (coil turns N = 72) was rebuilt and used as a new D1-triplet. The pitch of the magnets and the position of the field clamps, also called end guards, were adjusted, and a new support frame was fabricated. In addition, the power supply was upgraded from 40 V/375 A to 75 V/1000 A. The replacement of the D1-triplet made transporting muons up to 120 MeV/c possible. At 120 MeV/c, the excitation current is 448 A, the excitation voltage is 68 A, and the cooling water temperature rise is 17°C, so it meets the J-PARC regulation.

4. Beam optics calculation

After replacing the D1-triplet, it was necessary to optimize the current, considering the magnetic field interference effects and effective length due to changes in magnetomotive force from the increase in the winding number of coil, magnet pitch, and end-guard position. Therefore, the beam transport program Transport was used to optimize the excitation current so that the beam size passing through the D1-triplet does not change downstream. Figure 3 shows the beam envelope of the new D1-triplet at 30 MeV/c when the current values are adjusted so that the GL products are equal. The upper half of the graph shows the vertical beam spread, and the lower half shows the horizontal beam spread.

As a result, when surface muons with a momentum equivalent to 30 MeV/c are transported, the D1-triplet currents shown in Table 2 are required to achieve the same beam envelope as with the old triplet. After the beam commissioning, the optimum current values are also shown in Table 2, and they agree well with the beam optics calculation results.

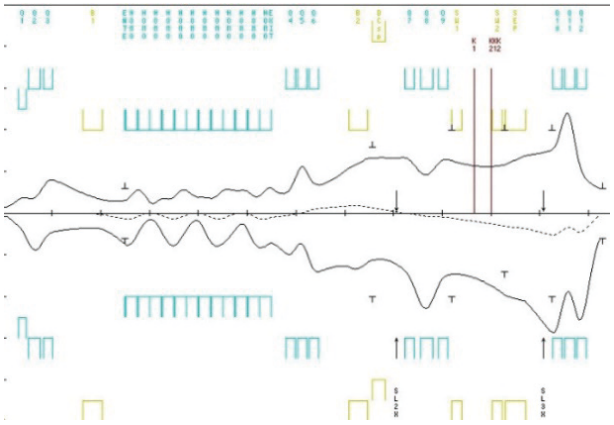

Figure 3. Beam envelope of the new D1-triplet at 30 MeV/c.

Table 2. Comparison of the current values of the D1-triplet for transporting 30 MeV/c muon beam.

D1-triplet	Old	New	Commissioning
DQ10	68.6 A	46.3 A	48.2 A
DQ11	−124.7 A	-84.7 A	-85.5 A
DQ12	124.0 A	83.6 A	89.5 A

5. Summary

The D1-triplet and power supply were upgraded without problems and now operate smoothly. In the future, users can conduct their experiment at the D1 area using a muon beam with a higher momentum of up to 120 MeV/c.

6. Acknowledgments

We thank Dr. Y. Irie for helpful discussions about magnetic field interference.

Reference

[1] T. Yuasa et al., "Upgrade of triplet magnets at J-PARC MUSE" Proceedings of the 19th Annual Meeting of Particle Accelerator Society of Japan (in Japanese).

T. Yuasa[1,2], H. Fujimori[1,2], N. Kawamura[1,2], M. Meguro[3], H. Sunagawa[3], and K. Kawabata[3]
[1]Muon Science Laboratory, Institute of Materials Structure Science, KEK; [2]Muon Science Section, Materials and Life Science Division, J-PARC Center; [3]NAT Corporation

Muon H-Line PPS Interlock System Update

1. Introduction

The muon H-line has been constructed in experimental hall No.1 of the MLF J-PARC. This beamline includes an experimental area named the H1 area, which was completed in 2021. In FY2022, the second experimental area (H2 area) was constructed. The Personnel Protection System (PPS) must be implemented to construct a new experimental area. [1]

This article describes the modification of the PPS done in the H-line to add the H2 area.

2. Experimental areas in the H-Line, the existing H1 area and the newly constructed H2 area

The structure from the muon target installed on the M2 line in the MLF to the existing H1 experimental area and the newly constructed H2 area is shown in Fig. 1.

The muon beam is delivered from the muon target to the experimental areas of the H-line through several bending magnets. The H2 experimental area and the beamline downstream from the exit of the bending magnet named HB2 were newly constructed and accordingly, the PPS system was updated in FY2022.

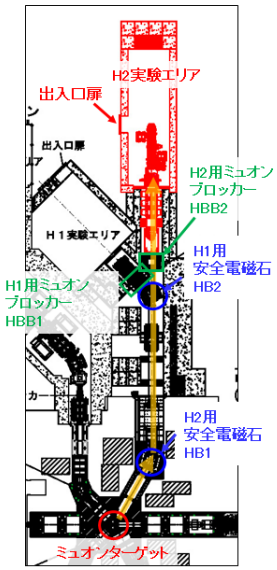

Figure 1. Experimental areas on the H-Line.

2.1. PPS system before the construction of the H2 area

When only the H1 area was operated in the H-line, the supply of muon beams to the H1 area was controlled by a muon blocker HBB1 and a safety magnet HB2.

Figure 2 shows the PPS logic of the H1 area before the update. When the door of the H1 area is opened so that workers can enter the H1 area for sample exchange,

ビーム状態	H1 ON	H1 OFF
HB2	ON	OFF
HBB1	OPEN	CLOSE

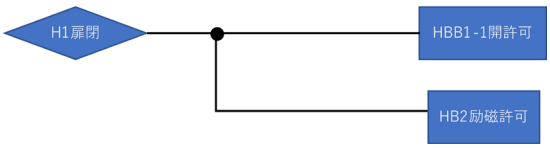

Figure 2. PPS logic of the H1 area before the update.

and so on, it is necessary to prevent muon beam irradiation to the experimental area. Safety is guaranteed by keeping HBB1 closed and by keeping the power supply of the HB2 magnets turned off.

When the work in the experimental area is finished and the door is properly closed, the forced OFF command to the HB2 magnet power supply is released and HB2 excitation is permitted. At the same time, HBB1 is allowed to open, and therefore muon beams can be irradiated to the H1 area.

2.2. Features of the new PPS for the H-line

The updates of the PPS for the H2 area are slightly more complicated than usual because the H2 area is located in the straight section through HB2. When entering the H2 area, beam irradiation to the H2 area must be prevented. However, the safety magnet power supply HB1 for the H2 area cannot be turned off because the muon beam experiments in the H1 area can be conducted. On the other hand, when entering the H1 area and performing muon beam irradiation to the H2 area, the power supply of the safety magnet HB2 for the H1 area can be turned off.

Therefore, it is difficult to construct the PPS for the H-line after the H2 area construction by simply referring to the status of entry to the experimental area. The new PPS of H-line was built to reference the status of the two safety magnets as well as the information of the entry to the experimental areas. In addition, a key switch was installed to select which experimental area is used.

2.2.1 Updated PPS logic for the H1 area

Figure 3 shows the PPS logic of the H1 area after the update. When irradiating the muon beam to the H1 area, the key switch is set to the H1 mode. At the H1 mode, the H1 door is closed, all safety keys for the HBB1 operation are accommodated, and HBB2 is closed, then

運転状態	H1運転 且つ H2常時入域	H1, H2どちらも常時入域	H2運転 且つ H1常時入域
HB1	ON	OFF	ON
HB2	ON	OFF	OFF
HBB1	OPEN	CLOSE	CLOSE
HBB2	CLOSE	CLOSE	OPEN

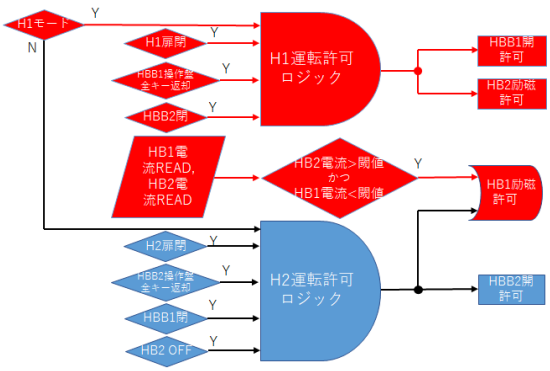

Figure 3. H1 area's PPS logic after the update.

運転状態	H1運転 且つ H2常時入域	H1, H2どちらも常時入域	H2運転 且つ H1常時入域
HB1	ON	OFF	ON
HB2	ON	OFF	OFF
HBB1	OPEN	CLOSE	CLOSE
HBB2	CLOSE	CLOSE	OPEN

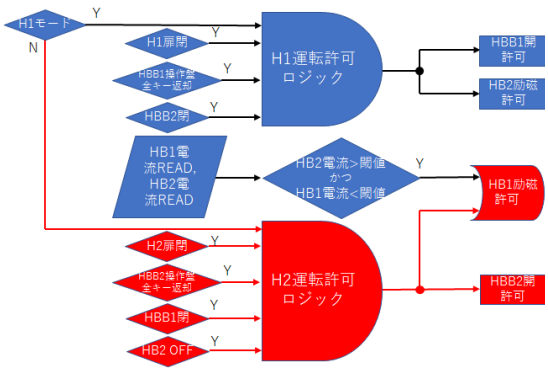

Figure 4. H2 area's PPS logic after the update.

the muon beam can be irradiated in the H1 area. The muon blocker HBB1 is allowed to open. The power supply of the safety magnet HB2 is allowed to be turned on. In order to deliver muon beams to the H1 area, HB1 should be turned on, but the output currents of the HB1 and HB2 are monitored, and HB1 can be turned on only when these currents satisfy certain conditions. Unless the output current of HB2 exceeds a threshold corresponding to the momentum of 12 MeV/c (10% of the rated momentum of the H-line), the HB1 magnet power supply is not allowed to be turned on. This logic is necessary to prevent muon beams from traveling straight through the HB2 magnet and irradiating the H2 area while work is conducted in the experimental area. In addition, if the output current of the HB1 is above a threshold that is determined by the current of the HB2, the HB1 power supply is not allowed to be turned on, so that muon beams with much higher momentum than the HB2 setting will not enter the HB2.

2.2.2 Updated PPS logic for the H2 area

Figure 4 shows the PPS logic of the H2 area after the update. When irradiating the muon beam to the H2 area, the key switch is set to H2 mode. At the H2 mode, the H2 door is closed, all safety keys for the HBB2 operation are accommodated, HBB1 is closed, and the safety magnet HB2 is turned off, then the muon beam can be irradiated in the H2 area. The operation permissions for the safety devices in each experimental area are as follows.

The muon blocker HBB1 is not allowed to open, and HBB2 is allowed to open. For the safety magnet power supplies, the HB1 power supply is allowed to be turned on and the HB2 power supply is not allowed to be turned on. Since the safety magnet for the H1 area is HB2 in H2 mode, the safety of the H1 area is guaranteed by simply prohibiting turning on the power supply of the HB2.

3. Summary

The PPS for the H-line experimental area was updated with the construction of the H2 area, which is located in the straight section through the safety magnet HB2. Because of this positional relationship, more complex logic circuits are required than the PPS for other muon beamlines, such as a key switch to select experimental areas and monitoring the output currents of the safety magnet power supplies.

This PPS logic circuit has passed the operation verification test and started operation in April 2023.

4. Acknowledgements

We would like to thank Dr. Y. Bessho for his continuous support.

Reference

[1] T. Yuasa et al., "Muon Beamlines and Control System (Manufacturing of Spare Coils, and Installation of PPS Equipment for H1 Area)", KEK Prog. Rep. 2021-6 Dec. 2021, 9-11.

Y. Kobayashi[1,2], T. Yamazaki[1,2], N. Kawamura[1,2], Y. Ikedo[1,2], A. Koda[1,2], T. Yuasa[1,2], H. Fujimori[1,2], K. Sakai[3], A. Watanabe[4], and A. Suzuki[4]

[1]Muon Science Laboratory, Institute of Materials Structure Science, KEK; [2]Muon Science Section, Materials and Life Science Division, J-PARC Center; [3]Japan Atomic Energy Agency, JAEA; [4]NAT Co., Ltd.

Commissioning of the Ultra-slow Muon Beamline in FY2022

1. Introduction

The muon spin rotation/relaxation/resonance μSR technique is valuable for investigating the bulk magnetic properties of materials. In many cases, μSR studies employ a surface muon beam. Surface muons exhibit nearly perfect spin polarization and excellent monochromaticity. However, measurements of thin films and tiny samples are challenging due to their kinetic energy of 4 MeV. Low-energy and energy-tunable muon beams expand the applicability of μSR and pave the way for various new potential applications.

At J-PARC MUSE, the generation of ultra-slow muons (USM) through the laser ionization of thermal muonium has been studied with regard to its application in materials science. USM can be implanted into a sample at energies below 30 keV. Furthermore, the time resolution of USM-μSR is several tens of times better than that of conventional μSR using pulsed muons.

2. Present status and tasks

The beamline is under commissioning for the initiation of scientific measurements using USM-μSR. The layout of the facility was described in last year's report [1]. To carry out experiments within a realistic measurement time, it is essential to ensure a certain level of USM flux. The required statistics depends on the experiment, but with a flux of 100 cps at the sample position it would enable the data acquisition of 1 million statistics in half a day, which is sufficient for the initial stages of a scientific campaign.

3. Progress in FY2022

To achieve a sufficient USM flux, enhancing the pulse energy of ionization laser is crucial, and this will be explained in detail in another report. In addition to this, increasing the number of muonium atoms emitted in vacuum also contributes to flux improvement. In the U1 beamline, a joule-heated tungsten foil has been used as a muonium emitter. For a muonium emitted, it is also known that laser-ablated silica aerogel is promising. In FY2022, measurements were made to quantitatively compare the performance of these two emitters.

The flux and profile of USM were measured using a microchannel plate (MCP) with a delay-line detector (DLD). The flux was evaluated based on two measurements: direct counting of muons and counting of decay positrons. The effects of particle pileup in the muon measurement were corrected by assuming a Poisson distribution of USM counts.

In the experiments, the momentum of the surface muon, the wavelength and timing of laser injection, and the voltage of the extraction electrode were varied to assess the number, time, and spatial spread of USM. Figure 1 illustrates the layout from the muonium generation chamber to the USM monitoring position. The measurements were performed at the intermediate focus between the first and second electric bends.

Figure 2 represents a plot of the USM flux with varying laser injection timing. This result contains information about the velocity distribution of muonium and the distance from the muonium emitted to the laser beam position. The differences in the optimal laser timing to maximize the yield and the width of USM time are attributed to differences in the emitter temperatures. The tungsten foil was heated to 2000 K, while the silica aerogel was used at room temperature. The spread of the time width as the delay for laser injection increases is due to the spacial distribution of muonium expanding over time.

Due to the different velocity of muonium, the

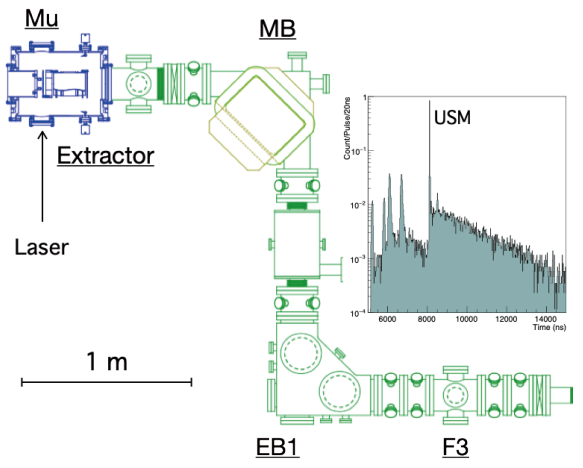

Figure 1. The USM beamline in the U1 area. "Mu" refers to the muonium generation target, "Extractor" represents the electrostatic lens, "MB" stands for the magnetic bend, "EB1" denotes the electrostatic bend, and "F3" indicates the beam monitoring position. The top-right inset shows the time-of-flight spectrum obtained at F3. The four peaks in the early time region correspond, in order, to prompt positrons and degraded muons. Due to the double-pulsed time structure of the primary protons, these peaks appear in pairs as well.

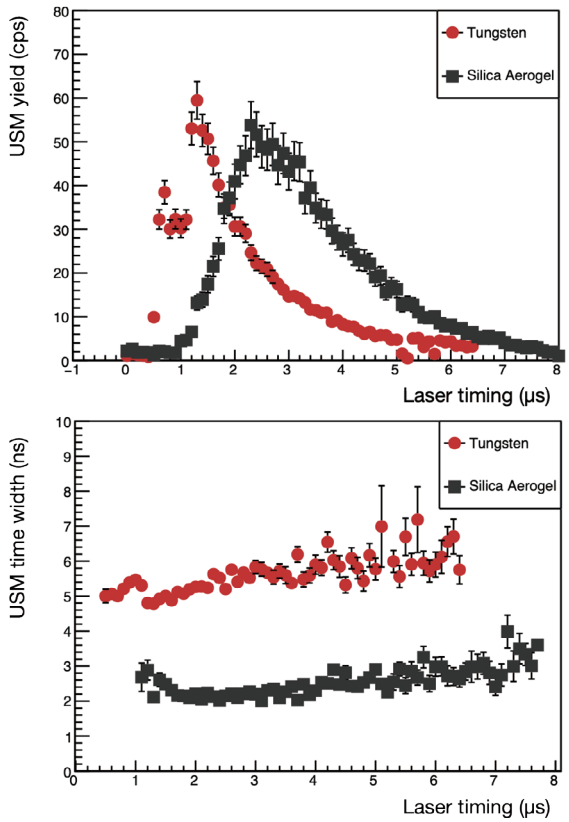

Figure 2. The laser timing dependence of USM yield and time width. Red circles representing the results for tungsten and black squares for silica aerogel. The time width corresponds to the 1$¥sigma$ obtained by fitting the TOF peak with a Gaussian function. Direct comparison of the yield between different emitters is not feasible, because the difference in laser pulse energy is not corrected.

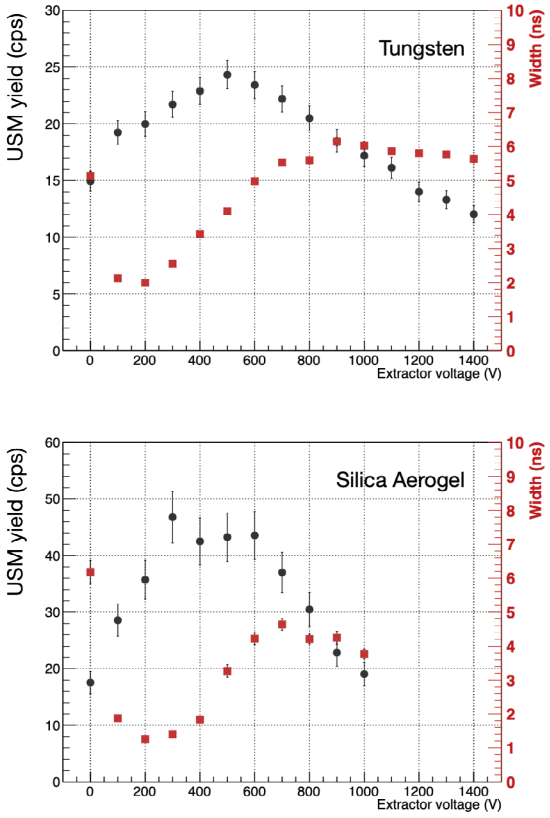

Figure 3. The extraction voltage dependence of USM yield and time width. The upper plot represents the results for tungsten, while the lower corresponds to silica aerogel. The black circles indicate the yield and refer to the left vertical axis, while the red squares represent the time width and refer to the right vertical axis.

optimal voltage for the extractor also varies depending on the emitter. Figure 3 shows the variation of yield and time width with respect to the extraction voltage. Depending on the application, it is possible to optimize either the yield or timing resolution.

Through the commissioning measurements, the maximum yield obtained was 180 cps using the silica aerogel target. Adopting an open area ratio of 0.55 as the upper limit for the MCP detection efficiency, the USM flux becomes 330/s. Even considering losses due to decay during transportation from the intermediate focus F3 to the experimental area, a flux of 100/s or more can be expected at the μSR spectrometer.

4. Summary and prospects

In the FY2022 commissioning, we conducted a study on the comparison of muonium emitters and the optimization of USM generation and transport conditions. The USM flux of 330/s and time width of 1 ns were achieved, which were sufficient beam specifications to initiate a practical measurement of USM-μSR. Next year, we plan to optimize the transportation to the spectrometer and begin experiments using the μSR spectrometer.

The authors would like to express their gratitude to the J-PARC muon g-2/EDM and Mu 1S-2S groups for providing the silica aerogel target. We are thankful for the contributions of S. Kamioka from KEK IPNS to the experiment.

Reference

[1] S. Kanda et al., KEK Prog. Rep. 2022-7, 19 (2023)

S. Kanda[1,2], Y. Ikedo[1,2], Y. Oishi[1,2], N. Teshima[1,2], and K. Shimomura[1,2]

[1]Muon Science Section, Materials and Life Science Division, J-PARC Center; [2]Institute of Materials Structure Science, KEK, [3] Nishina Center for Accelerator-Based Science, RIKEN.

Commissioning of the U1A Spectrometer in FY2022

1. Introduction

Muons find extensive application in materials science as spin-polarized quantum beams. Muon spin rotation/relaxation/resonance (μSR) is an experimental method to implant muons into materials for probing local magnetic fields. The muon beams primarily used in μSR experiments are obtained from pion decays at the surface of the production target. These beams are the so-called surface muons, which exhibit near-perfect polarization and monochromaticity. Nevertheless, due to their high energy of 4 MeV, measurements on thin samples using a surface muon beam are challenging. In this regard, low-energy muons have advantages for measurements with thin-film samples and studies on interfaces.

The ultra-slow muon (USM) beamline at MLF MUSE provides a low-energy muon beam via laser ionization of thermal muonium in a vacuum. At the U1A experimental area, a muon spin spectrom eter is located on a high-voltage platform to control the muon implantation energy. USMs can be selectively implanted on surfaces and interfaces in materials, enabling depth-resolving μSR. Further more, the time width of the beam is much narrower than that of the pulsed proton beam, so the frequency range of observable dynamics is wide. Figure 1 shows the high-voltage platform, transport optics, and the U1A spectrometer.

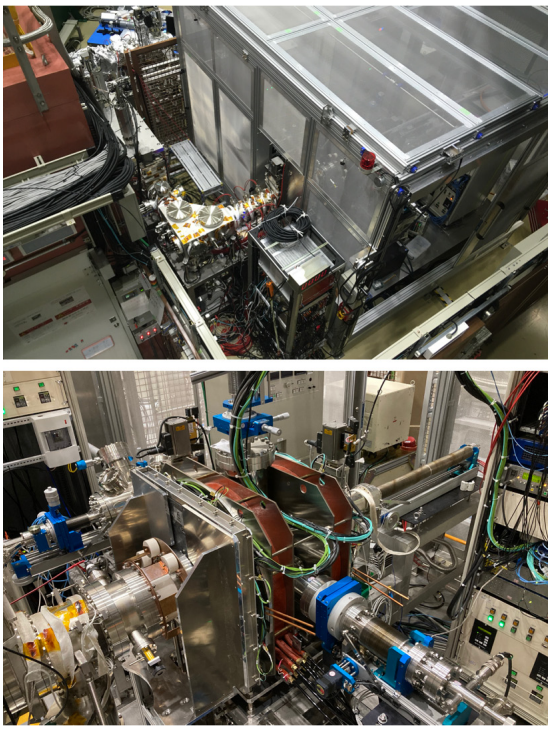

Figure 1. The U1A experimental area: (Top) The high-voltage platform and beamline, (Bottom) The muon spin spectrometer. The platform can be elevated up to 30 kV, controlling the implantation energy of the USM. The spectrometer consists of a positron detector segmented into 512 channels and a pair of coils generating a longitudinal magnetic field of up to 0.14 T.

2. Present status and tasks

The muon spin spectrometer in the U1A experimental area is currently under commissioning in preparation for the commencement of the user programs. Test experiments conducted since 2020 using a multilayered film sample demonstrated the capability to control the beam energy and selectively implant muons at specific depths within materials [1].

The next step required to initiate the user programs is to successfully conduct test experiments with a more practical setup. Specifically, this involves investigating the dependence of physical properties on temperature, magnetic field, and implantation energy using a small thin-film sample.

3. Progress in FY2022

Due to the improvements in beam flux, time width, and spatial profile achieved in the 2022 beam studies, we embarked on a scientific measurement using a thin film sample. While previous test measurements were conducted using relatively large samples at room temperature only, this time we conducted measurements at low temperatures using a thin-film sample with a size of 5 mm and a thickness of 33 nm.

The sample was mounted on a titanium plate using silver paste and was enclosed in a thermal shield, then cooled in a helium flow cryostat. A lowest temperature of 4.2 K was confirmed, demonstrating the applicability of this setup for various applications. Figure 2 displays the sample mounted on the cryostat.

The beam profile at the sample position was measured using a monitor combining a micro channel plate (MCP) and a delay-line detector (DLD). Position calibration was performed by installing an aligned pinhole upstream of the MCP. The MCPDLD and the sample can be moved using linear actuators. After beam adjustment with the MCP, the sample was inserted, and data acquisition was conducted using the spectrometer. Figure 3 shows the positron time spectrum obtained during the commissioning runs using the spectrometer, along

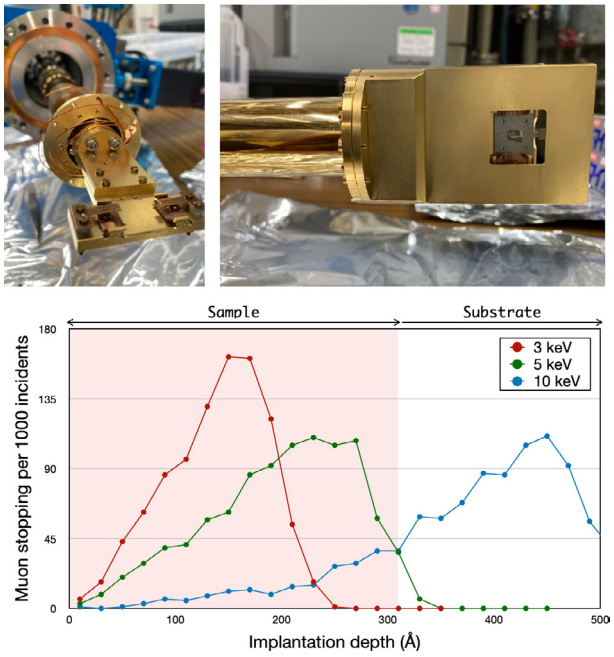

Figure 2. Sample and muon implantation simulation: (Top) Sample mounted on the cryostat and surrounded by the thermal shield, (Bottom) Muon stopping distribution in the sample, calculated by using TRIM.SP.

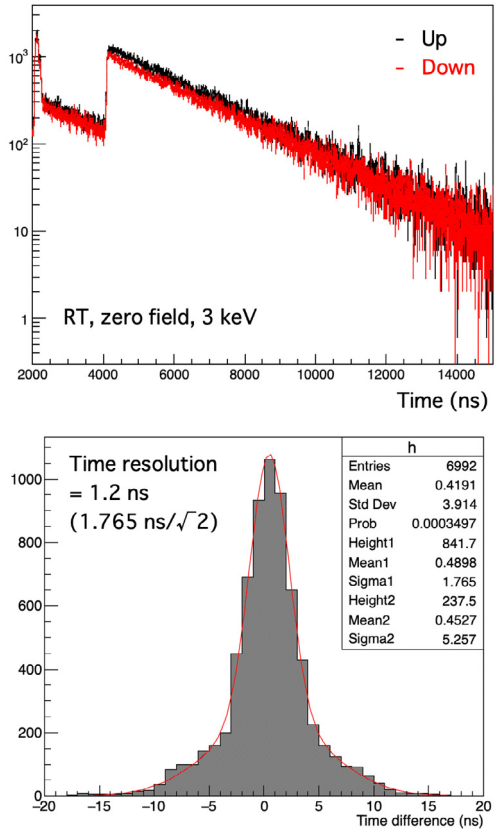

Figure 3. Results from the commissioning run. (Top) Positron time spectrum, (Bottom) Time difference between coincidence hits of the inner and outer layers of the detector. The spectrometer's detector was split into two vertically, with black representing the upper and red the lower. The time difference distribution was fitted with a double Gaussian, and the time resolution for a single layer of the detector was evaluated to be 1.2 ns (1σ).

with the time resolution of the detector. In the FY2022 campaign, statistics were not sufficient to systematically investigate the physical properties of the sample. However, we aim to complete the measurements by continuing the experiments in the next season.

In addition, we enhanced the interlock system of the spectrometer's electromagnet to improve safety and conducted magnetic field measurements. Good agreement was confirmed between the measurements and calculations based on the finite element method. We developed a water-cooling system to improve the stability of the detector by controlling the temperature. Moreover, simulation studies were performed to design a new detector for a larger solid angle and full asymmetry.

4. Summary and prospects

In preparation for initiating the user programs, we have started a demonstration of scientific measurement using the U1A spectrometer. Both the spectrometer and the sample environment operated as expected, indicating the feasibility of scientific measurements in the U1A area.

The next year, we aim to complete the test experiment and focus on improving beam quality and the sample environment to accommodate various user experiments.

The authors are grateful for the sample provided by the T. Adachi's group at Sophia University and for the cooperation in the sample installation by H. Okabe from Tohoku University. We thank T. Yuasa, N. Teshima, H. Fujimori, and Y. Irie of KEK MSL for their contributions for improving and testing the spectrometer's magnet.

Reference

[1] S. Kanda *et al.*, J. Phys.: Conf. Ser. 2462 012030 (2023).

S. Kanda[1,2], Y. Ikedo[1,2], W. Higemoto[2,3], and T. U. Ito[2,3]

[1]Muon Science Laboratory, Institute of Materials Structure Science, KEK; [2]Muon Science Section, Materials and Life Science Division, J-PARC Center; [3]Advanced Science Research Center, JAEA

USM Commissioning at the U1B area

At the U1B area, a transmission muon microscope (TμM) is being constructed. The TμM will visualize thick objects (>10 μm) in nanometer resolution. Its capabilities are powered by the quantum coherence of the ultra-slow muon beam, and the deep-penetration power of the muon beam accelerated to 5 MeV. In this FY, the 5 MeV muon-cyclotron system was completed and installed to the U1B area. The cyclotron is connected to the ultraslow muon beam line (Fig. 1). The commissioning of the cyclotron officially started on June 23, 2023.

For safety operation of the system, we constructed an interlock system which has many inputs and targets. For mutually exclusive and collectively exhaustive (MECE) design and implementation of the interlocking operations, an interlock matrix is employed (Fig. 2). By the interlock matrix, chain-reactions of the interlocking operations are organized and described visually. For example, when the main coil water is short, then the main coil is shut down, magnetic field disappears, then the RF input and the HV input should be also shut down associatively. This associated operation is described by the mark "A" in the matrix.

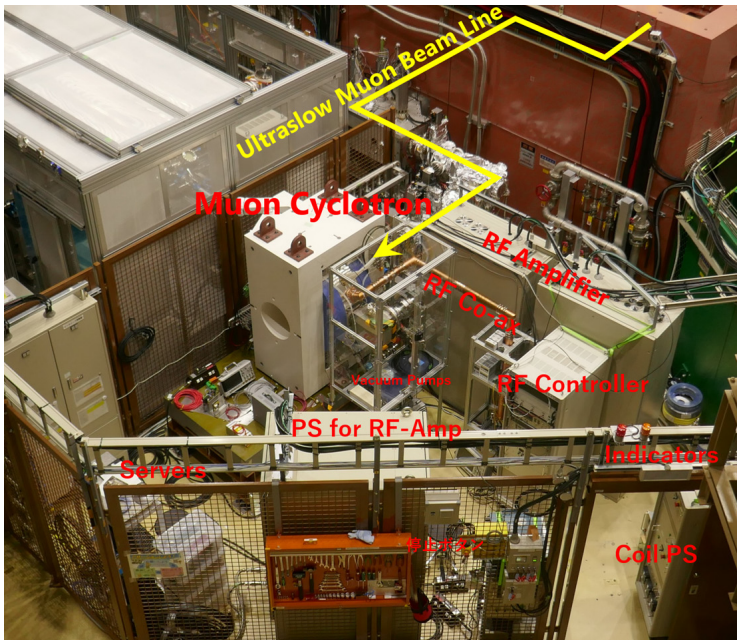

Figure 1. The 5 MeV muon-cyclotron system completed at the U1B area. The RF amplifier provides RF of 108 MHz/20 kW to the cyclotron through the RF coaxial tube. The installation of the RF controller is temporary, the main column of the TμM will be installed into the place of the RF controller. The Ultraslow muon beam enters the cyclotron from its rear, and the accelerated muon beam is ejected diagonally upward and is bended down to the TμM. by a magnet.

		Interlock Inputs																
		EM Stop Button	Earth Quake	Vacuum > 1E-2Pa	Low Magnetic Field	RF Water shortage	Cyclotron Door Open	Main Coil Water shortage	Main Coil Overheat	Glaser Coil Water shortage	Glaser Coil Overheat	Water Leakage	Breaker open	Amp Water shortage	Fan Stop	RF EM stop button	Amp Door Open	Amp Overheat
Targets	RF Amplifire	1	1	1	1	1	A	A	A			1	1	1	1	1	1	1
	Def/Inf HV	1	1	1	1		A	A	A									
	Main Coil	1	1				1	1	1			1						
	Glaser Coil	1	1							1	1	1						
	Tuner/Def Drive	1	1															

Figure 2. Interlock matrix. The mark "1" means that the input stops the target device directly, the mark "A" means that the related target device is associatively stopped.

The RF controller (Fig. 3) for the cyclotron has been completed and installed. Driving of the RF-amplifier and detection of the RF in the cyclotron are fully controlled by a FPGA, thorough complex RF-mixers controlled by DACs and detections by ADCs (Fig. 4). Both continuous wave- and pulsed wave- operations are available by a software directive.

At the next beam time, the cyclotron will be started to accelerate the ultraslow muon beam to 5 MeV.

Reverence

[1] Y.Nagatani, K.Shimomura, Journal of the Crystallographic Society of Japan, Vol 65. 33-41 (2023).

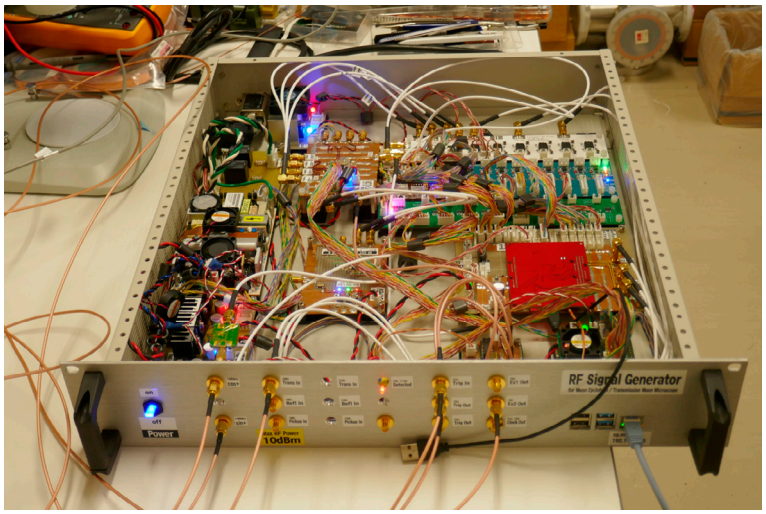

Figure 3. RF low level controller.

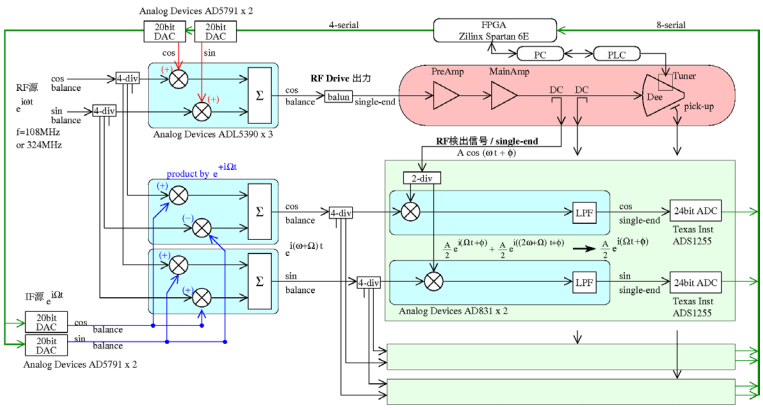

Figure 4. Block diagram of the RF-control system.

Y. Nagatani[1], T. Yamazaki[1], J. Ohnishi[2], A. Goto[1], T. Yuasa[1], Y. Nakazawa[2], T. Adachi[1], and Y. Ikedo[1]
[1]*Muon Science Laboratory, Institute of Materials Structure Science, KEK;* [2]*Nishina Center, RIKEN*

The Progress of Laser System for Ultra-slow Muon Generation

1. Introduction

Ultra-slow Muon Spin Rotation / Relaxation / Resonance (USμSR) for measuring the material properties in thin films and surface/interface has recently begun at J-PARC [1]. The only method to generate ultra-slow muons, with a momentum range limited below ~0.2 eV, is through laser photoionization of thermal muonium (Mu). This method requires coherent Lyman-α light (122.09 nm) to excite an electron from the ground state to the 2 p state of Mu, and coherent light at 355 nm to dissociate the electron from the 2 p state. So far, we have constructed an all-solid-state laser system with a highly stabilized in the wavelength and output pulse energy, and achieved the generation of Lyman-α light pulses exceeding 10 μJ through subsequent wavelength conversions. We have also been working on further increasing the output pulse energy. This fiscal year, we introduced a new concept amplifier into the all-solid-state laser system to enhance the output energy of Lyman-α light.

2. Nd:YSAG end pumped amplifier

The design of the Lyman-α laser system is described in Ref. 2. More than 10 μJ Lyman-α pulse is stably generated in a krypton/argon mixture filled gas-cell by methods of two-photon-resonant four-wave-mixing which method requires intense 212.556 nm and 820 nm pulses. These two wavelength pulses were generated by methods of nonlinear wavelength conversions of one fundamental pulse (1062.78 nm). To generate about 100 mJ fundamental pulses, specially produced Nd:YGAG and Nd:YSAG ceramics rod (ø 4 mm, 80 mm long) are used in diode pumped amplifiers as a gain medium. To achieve amplification up to several hundred mJ while avoiding damage to optical components, the beam diameter must be increased during amplification, which requires a large-aperture (ø > ~10 mm) gain medium. However, it has been difficult to eliminate the optical wavefront distortion caused by the inhomogeneity in the medium using not only well-established single crystal grows but also laser ceramic technology. To compensate for these material shortcomings, we applied a deformable mirror system [3], but such adaptive optics introduced an optical energy loss and some laser beam instability. Thus, we decided to change dramatically the pumping configuration from conventional side pump to end pump geometry to reduce the optical pathlength in the gain medium. Figure 1 shows a comparison between the conventional geometry, in which the pump

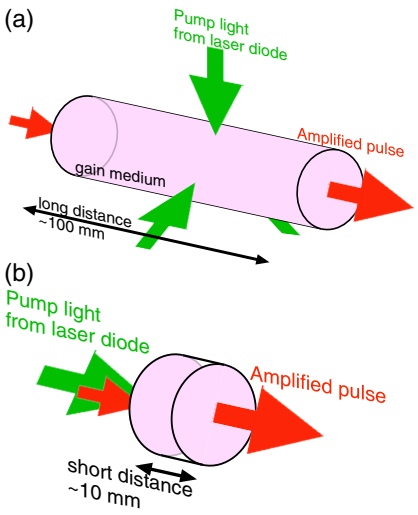

Figure 1. Schematic of the pumping geometry. (a) conventional side pump for long laser rod and (b) end pump for short laser disk.

light from laser diodes (LDs) are injected from the side of the rod, and the new geometry, in which the amplified light and the pump light are injected coaxially. The new pumping geometry requires spatial profile shaping for the pump light beam from LDs, but the wavefront distortion can be dramatically reduced by shortening the crystal length.

3. New amplifier module

In the new method, sapphire substrates are bonded to the light input and output surfaces for efficient cooling of the laser medium and end-face protection. Nd:YSAG and the sapphire plate have different thermal expansion coefficient, the bonding was carried out using room temperature surface activated bonding technology, which has been developed in the Institute for Molecular Science [4]. 9.3 mm cubic Nd:YSAG ceramic with bonded sapphire plates (ø 25.4, t = 2 mm) and water-cooling holder are shown in Fig. 2. We constructed an amplification module using the bonded Nd:YSAG and carried out an optical pulse amplification for 1062.78 nm pulse. The setup of the amplifier module

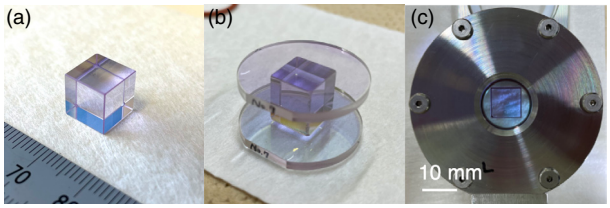

Figure 2. Nd:YSAG ceramic for the power amplifier. (a) polished ceramic cube, (b) bonded ceramic cube with sapphire plates and (c) set in a water-cooling holder.

is shown in Fig. 3. The Nd:YSAG ceramic was pumped by 8.5 mm square shaped beam with the 885 nm wavelength light from two laser diode bar stacks. Since the pump light absorption of a single ceramic was about 51%, two ceramics were placed in series. The horizontally polarized pulse delivered from the intermediate amplifier was injected into the ceramics, and the transmitted pulse was folded back into the same optical path. By rotating the polarization by 90 degrees when folding back, the incident and amplified pulses were separated by the polarizing-beam-splitter. The double pass configuration amplifier module was installed to the laser system and the gain factor measurements were carried out using reduced incident pulse energy of 10 mJ to avoid unexpected optical damage. The function of the gain factor versus the applied current to the LDs is shown in Fig. 4. The maximum gain factor of 2.2 was

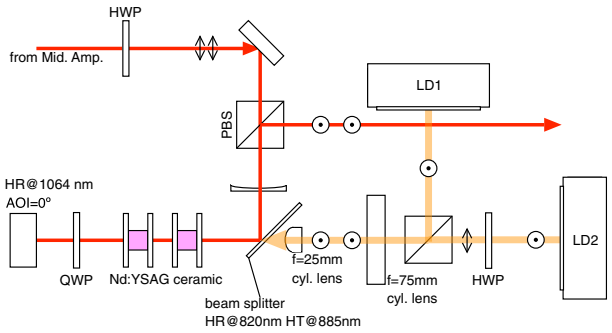

Figure 3. Setup of Nd:YSAG ceramic for the power amplifier module. The pump lights from two LD modules were combined with polarizing-beam-splitter. The pump beam was shaped into about 8.5 mm square intensity profile for square shape Nd:YSAG ceramics.

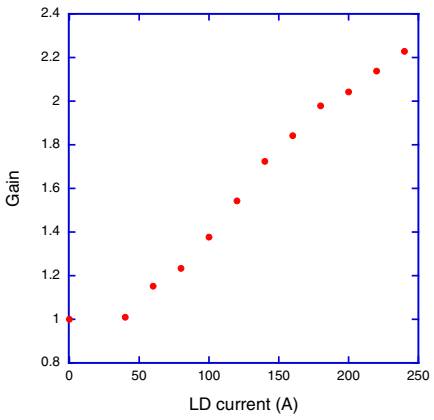

Figure 4. The obtained amplification gain corresponds to the applied current to LDs. The slope shows that the threshold of laser emission of LD is around 45 A.

obtained when the 250 A current was applied to LDs. Since the slope of the graph is not saturated, this amplifier would have a higher amplification gain potential for the current condition. In the next step, we plan to verify whether increasing the input pulse energy causes optical damage to the optics in the amplification module or distortions in the output beam profile and wavefront that affect the efficiency of subsequent nonlinear wavelength conversions.

4. Summary

We have built a new amplification module for further laser power enhancement and integrated it into a laser system to evaluate the fundamental amplification characteristics. The new amplification module uses a pumping method that utilizes a laser medium with a crystal length that is one order of magnitude shorter than the conventional one in order to solve the wavefront distortion of the output beam caused by non-uniformity in the laser medium, which has been a problem up to now. It has been shown that an amplification factor of more than 2.2 times can be achieved using this amplification module, making it possible to increase the output power of the entire laser system. In the future, the aim is to generate a maximum output of 200 mJ or more and, through subsequent wavelength conversion, to increase the intensity of the Lyman-α light by several times.

Acknowledgement

This work was done with Prof. M. Yoshida, Dr. S. Kamioka and member of Muon Science Laboratory in KEK. The author would like to thank Mr. A. Kausas and Prof. T. Taira at Institute of Molecular Science for bonding ceramics.

References

[1] S. Kanda *et al.*, J. Phys. Conf. Ser. 2462(1), 012030 (2023).
[2] Y. Oishi *et al.*, J. Phys. Conf. Ser. 2462(1), 012026 (2023).
[3] KEK-MSL Report2020, 14 (2021). https://lib-extopc.kek.jp/preprints/PDF/2021/2123/2123006.pdf
[4] A. Kausas et al., *2019 6th International Workshop on Low Temperature Bonding for 3D Integration (LTB-3D)*, Kanazawa, Japan, 2019, pp. 6-6.

Y. Oishi[1,2]
[1]*Muon Science Laboratory, Institute of Materials Structure Science, KEK;* [2]*Muon Science Section, Materials and Life Science Division, J-PARC Center*

Present Status of the S-line

In this report on the S-line in 2022, we have to mention three issues that have affected the beamtime of the users of the inter-university experiment program: First, the S1 area experienced a malfunction in the longitudinal field (LF) power supply. The issue was the system halt due to a transformer temperature interlock while operating at 1000 A. The malfunction was traced back to one of the two thyristor banks not functioning correctly. Consequently, the operational thyristor attempted to compensate by outputting a higher current than anticipated, striving to maintain the desired current. One of the authors (TY) and the manufacturer's engineers investigated the cause of the problem. Still, for about two weeks, until the issue was solved, users were asked to conduct their experiments only with another power supply to apply a relatively low LF (maximum 160 gauss).

The second incident that occurred at the end of March 2022, was more critical: it involved the gate valve SGV1 located at the head of the beamline in the S-line, which was discovered to be incapable of closing properly. Upon examining various scenarios, it was assumed that the Kapton foil, which serves as a barrier between the primary and secondary beamlines, had ruptured and consequently became lodged in the gate valve. To repair or replace SGV1, it was necessary to open both the primary and secondary beamlines, and the closest opportunity to schedule such work was during the holiday season in May 2022. Therefore, all planned beamtime for the S-line from the beginning of April through the May holiday season had to be canceled. Five user experiments, corresponding to 13 days of beamtime, were carried over to the 2022B period.

Anticipating the potential release of tritium-containing gases due to the opening of the primary beamline duct, a safety review meeting was convened. This meeting included experts from outside the MLF Division, and its focus was to meticulously evaluate the work procedures and safety precautions necessary for the situation. The work was conducted in a negative-pressure controlled workspace, a "Green House," in which two groups of three workers wearing air-line masks worked in shifts. The work was performed between consecutive holidays. The original plan was to replace SGV1 on May 2. Still, as a result of gas sampling, it was determined that the tritium concentration should be further lowered, so the work schedule was changed to May 6, and the vacuum pumping was continued until the replacement work was resumed.

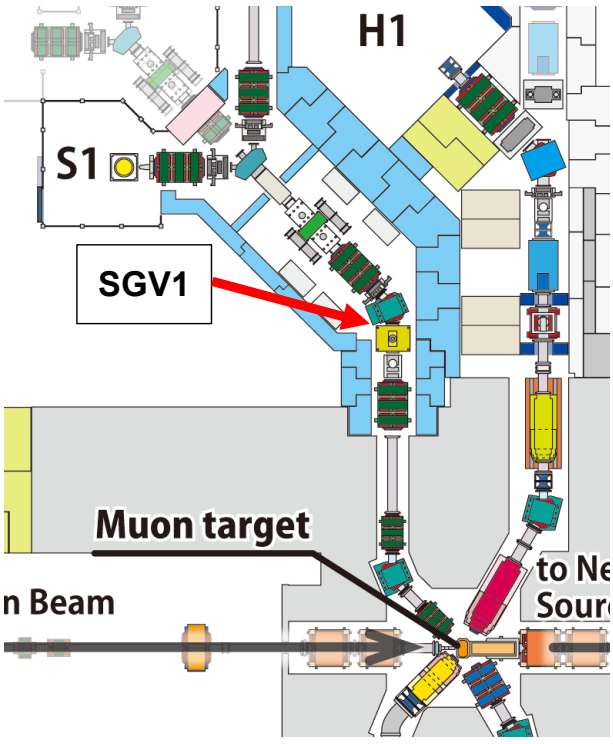

Figure 1. Layout of the S line and location of SGV1.

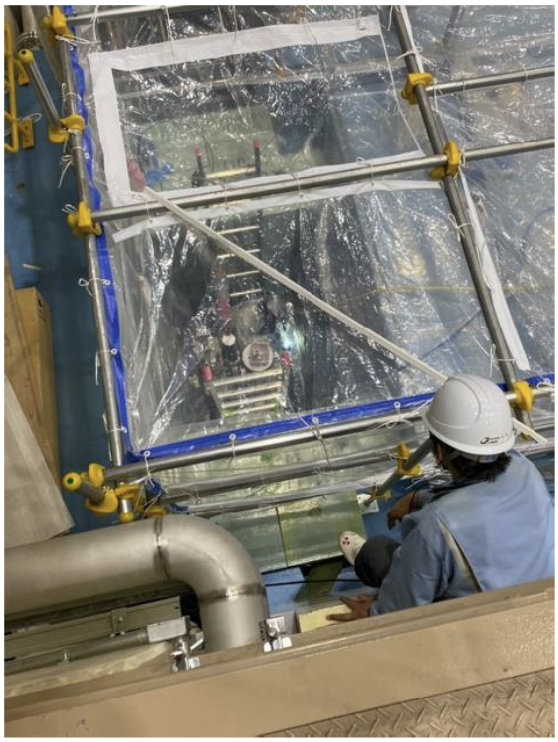

Figure 2. Worksite and the Green House.

On May 6, the SGV1 gate valve was successfully removed, revealing the downstream Kapton foil trapped within it. At the same time, however, it was also discovered that a section of the Kapton foil was caught in the beam blocker located upstream of SGV1. Since removing the Kapton foil from the beam blocker was an unplanned task, we decided to take measures to prevent Kapton foil's dispersion during the beam blocker's operation and refocused on the beamline restoration work. The complete retrieval of the Kapton foils is planned for a future date. The beamline restoration work went smoothly, and the S-line experiments were successfully resumed without any impact on the resumption of the MLF operation on May 11. The inquiry into the cause of the Kapton foil rupture remains unresolved. Additionally, in November 2022, efforts were undertaken to install an observation window. This window enables downstream inspection of the Kapton foil's integrity without the need to open the beam duct, thereby avoiding potential tritium contamination.

Finally, we report the status of the S-line kicker power supply, an essential device for the simultaneous single-pulse operation of the S1 and S2 areas. As mentioned in previous facility reports, unfortunately, there have been times when failures have affected users' experiment schedules. As shown in Fig. 3, the number of failures has clearly increased since the beginning of the 2022B period. Since a trend of increase has already been observed in the 2022A period, MOS-FET degradation was assumed as a possible cause. Therefore, in October 2022, just before the start of the 2022B period, we attempted to verify the effectiveness of preventive replacement by measuring the MOS-FET leakage current. The leakage current was measured to be about 20 μA for most MARX boards, but some showed a leakage current of 140 μA, and these MARX boards were replaced. However, as shown in Fig. 3, many MARX boards with a leakage current of 20 μA failed in the 2022B period. As a next countermeasure, we plan to replace the MOS-FET devices with modern SiC devices; we have already selected SiC devices and verified the operation of the power supplies alone, but we are still discussing the replacement plan and schedule with the manufacturer. The critical technical point is that it is difficult to mix SiC device power supplies with existing MOS-FET power supplies on a unit-by-unit basis. This means that to replace them without affecting the beam operation, power supplies with new SiC devices for replacement must also be prepared.

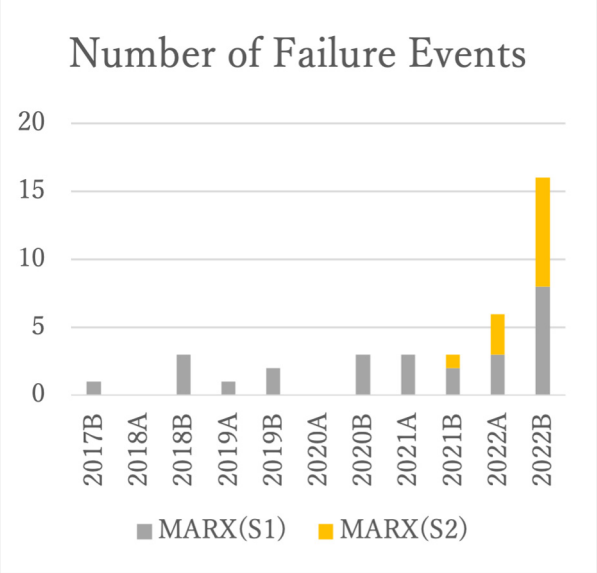

Figure 3. Number of MARX board failures that occurred in each operating period. Gray (yellow) bars represent the number of failures in the circuit that kicks the beam toward S1 (S2), respectively.

A. Koda, T. Yuasa, J.G. Nakamura, S. Nishimura, and P. Strasser
Muon Science Laboratory, Institute of Materials Structure Science, KEK

Present Status of the H-line

The H-line is a muon beamline in the east experimental hall #1 of the MLF. It is a general-purpose and high-intensity muon beamline that can generate both positive and negative muons [1,2]. The first branch of the H-line, named the H1 area, began operation in January 2022. The result of the beam commissioning at the H1 area is summarized in the last progress report [3]. The intensity of surface muons was measured and found to be almost the same as its design value (10^8 muons/s), despite the absence of a DC separator (or Wien filter) and the failure of the power supplies of the capture solenoids. Currently, the H-line is open for users, and a detector run of the DeeMe experiment [4] searching for μ-e conversion is ongoing. The hyperfine splitting measurement of muonium (MuSEUM experiment [5]) will be conducted at the H1 area in FY2023. In FY2022, we worked to resolve the problems of the DC separator and the power supplies and constructed the second branch of the H-line (H2 area). This report describes these updates.

A DC separator is a device used to eliminate positrons/electrons backgrounds in a positive/negative muon beam by applying crossed electric and magnetic fields to select particle velocity. The DC separator to be installed in the H-line was used at another muon beamline. The insulation of its HV power supply had been damaged, causing frequent electrical discharges. We replaced the damaged insulation ceramic with a new one. The repaired power supply was tested at the factory, and it worked normally. The installation of the DC separator in the H-line is scheduled for August 2023.

The power supplies of the capture solenoids adopt phase control using thyristors. The output currents of the power supplies were limited to about half of their rated currents due to the misfiring problem in the trigger boards designed to trigger the thyristors. The insufficient rating current of diodes used in the trigger boards was the cause of the misfiring. These diodes were replaced with other ones with sufficient ratings, and subsequently, the power supplies were adjusted in situ during the beam shutdown. The adjustment was not enough to restore the rated performance, but the maximum currents were recovered to some extent, as shown in Table. 1. Further adjustment is scheduled for the summer shutdown in FY2023.

Another advancement in FY2022 is the construction of the H2 area. The H2 area is the second branch of the H-line. At the H2 area, ultra-slow muons will be produced and then re-accelerated up to 4 MeV. The beamline is planned to be extended further to produce a novel low-emittance muon beam by accelerating muons up to 212 MeV. The low-emittance beam will be used in the measurement of the muon *g-2* and electric dipole moment [6] and the transmission muon microscope (TμM). Adding a new building on the east side of the MLF is necessary to extend the beamline. Figure 1 shows the overall 3D drawing of the beamline. Its engineering design is going to be finalized in FY2023.

Table 1. Status of the maximum currents of the power supplies of the capture solenoids (HS1-1, 2, 3).

	Before repair (A)	Current status (A)	Rated current (A)
HS1-1	1500	2500	3000
HS1-2	1500	2200	3000
HS1-3	900	2100	3000

The radiation shields for the H2 area, composed of concrete and iron, were manufactured and delivered to the MLF during the summer shutdown of FY2022. Partial assembly of these shields occurred during this period as part of the H2 area's construction. The construction was then resumed and finalized in the March 2023 shutdown. Figure 2 is a picture of the H-line after the construction. In addition, the safety interlock system of the H2 area was implemented.

While the H2 area was completed and underwent a self-radiation inspection in April, the installed beamline equipment was minimal and inadequate for commissioning. Beam ducts, vacuum apparatuses, and a quadrupole triplet with a small bore are scheduled to be installed in FY2023. This upgrade will enable the delivery of a low-intensity muon beam to the H2 area, making possible research and development in ultra-slow muon

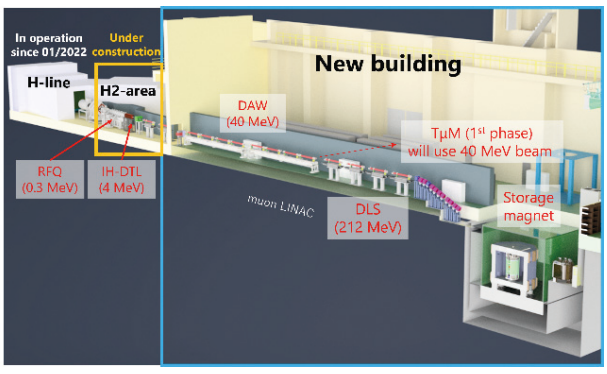

Figure 1. 3D drawing of the H-line.

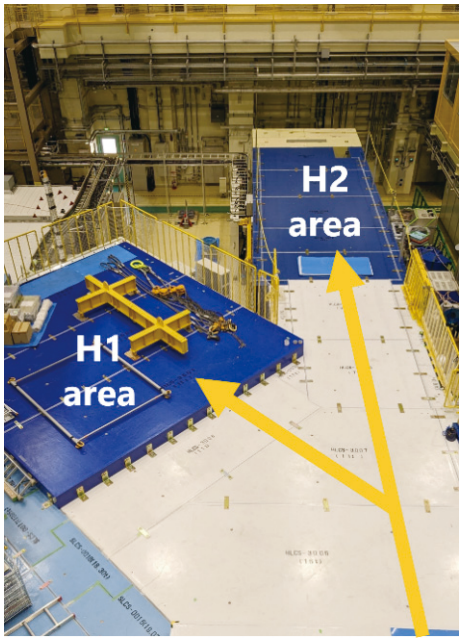

Figure 2. Picture of the H-line after the H2 area construction.

production and its re-acceleration testing.

References

[1] N. Kawamura, *et al.*, Prog. Theor. Exp. Phys. **2018** (2018) 113G01.
[2] T. Yamazaki, *et al.*, EPJ Web of Conferences **282**, 01016 (2023).
[3] T. Yamazaki and N. Kawamura, KEK-MSL Report 2021, pp. 26-27.
[4] H. Natori, *et al.*, Nucl. Phys. B (Proc. Suppl.) **248-250** (2014) 52-57.
[5] K. Shimomura, AIP conf. proc. **1382** (2011) 245.
[6] T. Mibe, *et al.*, Chin. Phys. C **34** (2010) 745.

T. Yamazaki[1,2] and N. Kawamura[1,2]
[1]*Muon Science Section, Materials and Life Science Division, J-PARC Center;* [2]*Muon Science Laboratory, High-Energy Accelerator Research Organization (KEK-IMSS)*

MLF Safety

Research Safety

1. Radiation safety

Radiological license upgrade

The applications for radiological license upgrades in FY2021 were approved on August 24, 2022.

The following items were updated at this application approval:

(1) Extension of the High momentum decay muon instrument (H-line).
(2) Change of the off-gas treatment system.
(3) Change of the quantity of produced radioactive nuclides.
(4) Change of the number of storage tanks at the RAM building.
(5) Refinement of the system diagram of the drainage system.
(6) Permission for use of the muon accelerator instrument.

The permission for use of the muon accelerator instrument has been granted for the first time as a radiation generation instrument license for a muon acceleration. The facility inspection of the muon accelerator instrument will take place in FY2025.

A new application is not planned until FY2024 and the next application to be approved in FY2025 is being prepared.

2. Chemical safety

The total number of chemical substances brought in in FY2022 was the same as in the previous year (Fig. 1). There were no major changes in the types of substances, but the number of battery-related samples and hydrogen storage alloys increased. The use of flammable gases, such as methane and ethane, also increased. As of the usage status of the experimental preparation room, the consumption of inert gas increased after May in response to bringing in of samples that are sensitive to moisture.

3. Crane safety

Also, this year, due to space limitations, only statistics of the crane usage are shown in Fig. 2. As in previous years, its usage was unaffected by the COVID-19 pandemic.

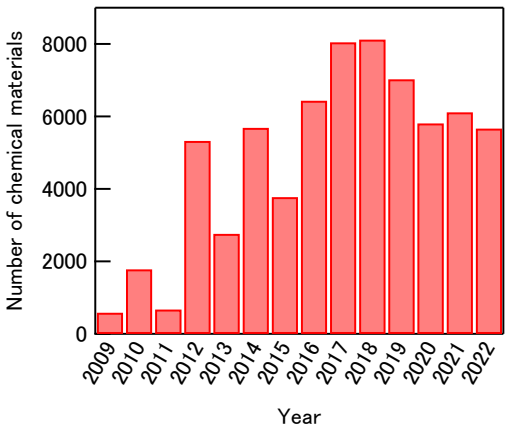

Figure 1. Trend of the amount of user-brought chemical materials for chemical safety check from the start of the MLF operation to the last year.

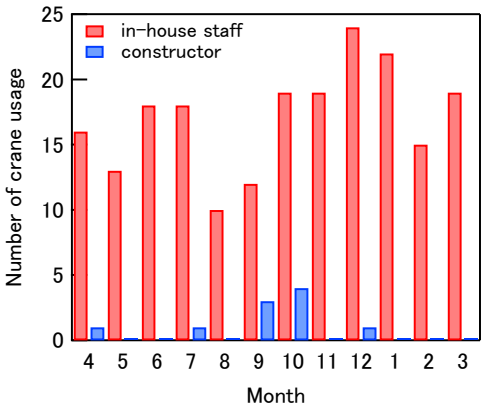

Figure 2. Trend of the total crane usage in one year.

4. COVID-19 pandemic measures

Although there were sporadic cases of COVID-19 among staff and users entering the MLF experimental hall, no clusters or other outbreaks occurred. In order to reduce the burden on those who enter the MLF experimental hall, the daily record of name, temperature, and location in the MLF experimental hall, which had been conducted since FY2020, was abolished on 2/24/2023. However, temperature checks, hand sterilization, and multiple daily sterilization of common areas have continued.

M. Harada[1], T. Ito[1], H. Morikawa[1], N. Hashimoto[2], Y. Watanabe[2], H. Tanaka[2], W. Kambara[2], H. Inoue[2], T. Oku[2], K. Suzuya[3], N. Kawamura[4], Y. Sakaguchi[5], R. Takahashi[2], Y. Yamaguchi[5], and K. Aizawa[2]

[1]Neutron Source Section, Materials and Life Science Division, J-PARC Center, [2]Technology Development Section, Materials and Life Science Division, J-PARC Center, [3]Neutron Science Section, Materials and Life Science Division, J-PARC Center, [4]Muon Science Section, Materials and Life Science Division, J-PARC Center, [5]Neutron Science and Technology Center, CROSS

MLF Operations in 2022

Beam Operation Status at the MLF

1. Overall

In Japanese Fiscal Year (JFY) 2022, the beam operation at the MLF started on April 1, 2022, and ended on March 14, 2023. Despite the influence of the pandemic and steeply raised electrical fees, the beam operation was conducted almost as planned.

The records of the beam power and availability are shown in Fig. 1. In JFY2022, the beam operation started with a power of 730 kW with a double-bunch beam. After April 7, the beam power was increased from 730 kW to 830 kW. During a long holiday called Golden Week, the beam operation was completely stopped in J-PARC from April 29 to May 8. The Main Ring (MR) resumed the beam operation after the improvement of their power supplies for the power upgrade with the increasing MR's duty. Before June, the duty of MR of 3.1% was chosen using slow extraction of MR with a repetition cycle of 5.2 sec. Every 4 shots of the beam are delivered to the MR with the MR cycle out of the beam at 25 Hz. Due to the increase of the duty of MR by decreasing the MR repetition cycle from 5.24 to 1.28 sec, the beam power to the MLF was decreased by 9.5%. After the user operation on June 24, beam operation with 1 MW was demonstrated. Due to the insufficient cooling for the RF cavities in the 3 GeV Rapid Cycling Synchrotron (RCS) in the hot summer, the duration of 1 MW lasted only for a short period of several hours. During the demonstration, RCS RF cavity #10 malfunctioned due to failure of the transformer supplied to the cavity for unknown reasons. Because of the long time required to repair the transformer, cavity #10 cannot be used until April 2024.

During the summer outage, the spent neutron production target #14 was replaced with new target #13, which had been fabricated before target #14. During the replacement, no significant problem was found on the target. Since no severe damage was found on target #13 by the precise inspection, we decided to continue with the 830 kW beam after the outage. Due to the failure of the RCS RF cavity, the beam power after the outage was limited to 830 kW for 25 Hz operation without the loss of duty by the MR operation, as shown in the green line in Fig. 1.

The beam period of 2022A was switched to 2022B on November 17, 2022. Due to concerns about the impact of the insufficient RCS cavity, the beam operation started with a slightly lower power of 780 kW. On December 2, the beam power was increased since no issue on the RCS cavity was found. After December 7, the MR started a continuous beam operation. Although the beam power for 25 Hz was maintained after December 2, the actual beam power to the MLF oscillated as shown in the blue line in Fig. 1, following the change of the MR cycle.

A high-intensity beam with a stable beam for users

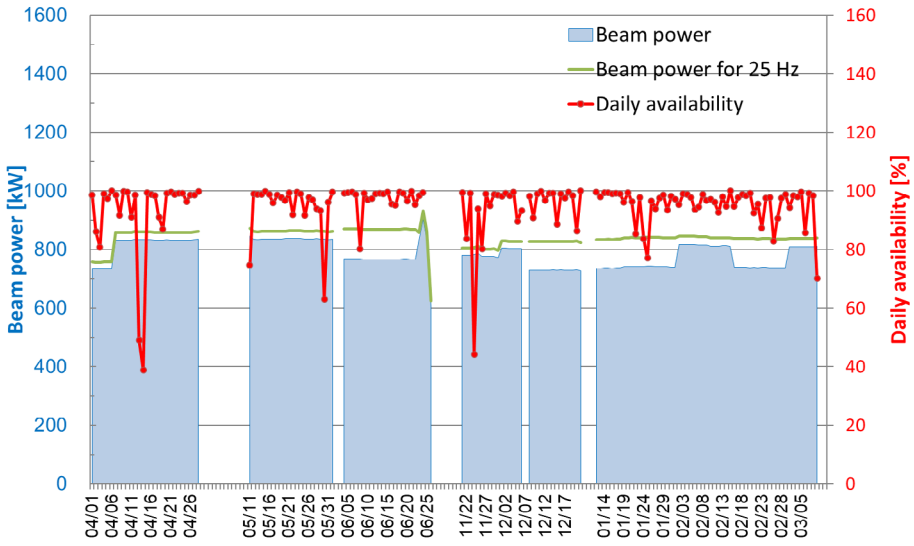

Figure 1. Beam power trend (blue line) at the MLF, beam power for the 25 Hz operation (green line,) i.e., beam power per shot and including the loss of duty for MR delivery), and availability per day (red line).

Table 1. Run cycle, scheduled time, actual beam time, and availability.

Run cycle	Duration	Scheduled time (h)	Beam time (h)	Availability (%)
89	April 1 – June 23	1,485	1,411	95.0
90	November 19 – March 14	1,984	1,887	95.1
2022A	April 1 – June 23	1,485	1,411	95.0
2022B	November 19 – March 14	1,984	1,887	95.1
Overall	April 1 – March 14	3,468	3,298	95.1

Table 2. Events that stopped the beam with a duration longer than 3 hours.

Stop date	Cause of beam stop	Stop duration for each event [h]
May 30	RCS RF11 failure	8.7
November 22	MLF anomaly gas pressure in cooling water	3.9
November 24	MLF PPS	6.7
November 26	MLF anomaly gas pressure in cooling water	4.7
December 20	MR PPS and LINAC quadrupole magnet failure	3.3
January 22	LINAC RF Klystron 8 failure	3.5
January 24	Drop in electricity voltage	3.9
February 26	LINAC RF Klystron 11 failure	4.3
March 6	RCS RF5 failure	7.2

was carried out in JFY2022. Table 1 shows the scheduled time and availability in JFY2022. As shown in Table 1, a stable beam operation with 95% availability was achieved up to June 24 for 2022A. Eventually, the overall availability in JFY2022 was 95.1%. From March 15 to 31, the beam study of LINAC was conducted.

The beam operation was stopped on several occasions due to minor failures. The typical causes of the beam stop with a duration longer than 3 hours are summarized in Table 2 and described below.

2. Causes of the beam stop

LINAC:

During JFY2022, there were no shortages of water flow for the magnet at LINAC, which had been the main reason for beam stops before JFY2019. In JFY2022, there were a few failures related to LINAC RF.

3 GeV Rapid Cycling Synchrotron (RCS):

Due to the failure of RF cavity #10, it took a long time to restart the operation. For the case of all cavities available, the resuming time tends to be shorter because tuning is applied before the cavity malfunctions.

MLF and Personnel Protection System (PPS)

After the summer outage, the water loop systems for cooling the mercury target vessel and the proton beam window at the MLF failed twice. The failures were caused by the gas in the water loop, which exceeded the allowable pressure at the surge tanks. These failures occurred after the last year's outage. We will improve the gas handling to minimize such long interruptions.

The PPS occurred for the MLF and the MR. The PPS has redundancy to observe the failure independently and should register the multiple events of failure. However, both PPS events in JFY2022 observed only one failure event. Failure of detection due to the noise is thought to make the PPS.

S. Meigo
Neutron Source Section, Materials and Life Science Division, J-PARC Center

Users at the MLF

The MLF beam operation for FY2022 started on April 1 with a beam intensity of 730 kW. Then, the beam intensity was increased to 830 kW on April 7. From April 29 to May 8, J-PARC suspended the beam operations entirely for a vacation. Following the user operation on June 24, a demonstration of a beam operating at 1 MW was conducted. It should be noted that the overall availability reached 95%, achieving a very stable beam supply. The total number of users of the neutron and muon experimental facilities in FY2022 was 644, an increase compared to the previous year, indicating a gradual recovery from the impact of the travel restrictions due to COVID-19.

The trend for the number of users at the MLF since the start of the operations in FY2008 is summarized in Table 1 and Fig. 1.

Table 1. The number of domestic and foreign users by fiscal year.

	FY2008		FY2009		FY2010		FY2011		FY2012		FY2013		FY2014		FY2015	
	Domestic Users	Foreign Users	Domestic Users	Foreign Users	Domestic Users	Foreign Users	Domestic Users	Foreign Users	Domestic Users	Foreign Users	Domestic Users	Foreign Users	Domestic Users	Foreign Users	Domestic Users	Foreign Users
Neutron	107		317		476		259		708		449		824		559	
	95	12	303	14	432	44	238	21	628	80	399	50	711	113	476	83
Muon	18		40		50		23		56		61		91		69	
	18	0	38	2	42	8	21	2	46	10	50	11	78	13	59	10

	FY2016		FY2017		FY2018		FY2019		FY2020		FY2021		FY2022	
	Domestic Users	Foreign Users	Domestic Users	Foreign Users	Domestic Users	Foreign Users	Domestic Users	Foreign Users	Domestic Users	Foreign Users	Domestic Users	Foreign Users	Domestic Users	Foreign Users
Neutron	852		927		965		940		489		307		406	
	744	108	742	185	789	176	827	113	448	41	257	50	296	110
Muon	99		179		161		138		92		117		238	
	83	16	149	30	146	15	127	11	88	4	112	5	203	35

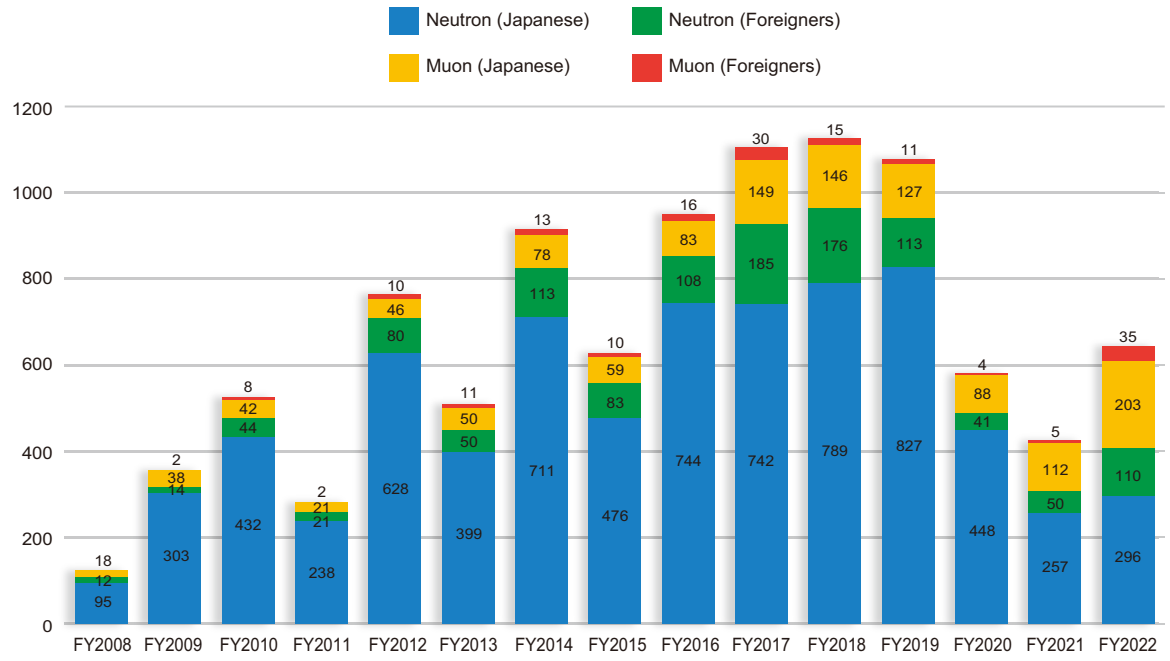

Figure 1. The number of domestic and foreign users by fiscal year.

MLF Proposals Summary – FY2022

Table 1. Number of Proposals by Beamline

Beam-line	Instrument	2022A		2022B		Full Year			
		Submitted	Approved	Submitted	Approved	Submitted		Approved	
		GU	GU	GU	GU	PU/S	IU	PU/S	IU
BL01	4D-Space Access Neutron Spectrometer - ***4SEASONS***	22(0)	8(0)	25(0)	9(0)	0	1	0	1
BL02	Biomolecular Dynamics Spectrometer - ***DNA***	18(2)	12(2)	21(1)	7(1)	2	1	2	2
BL03	IBARAKI Biological Crystal Diffractometer - ***iBIX*** (100-β)‡	2	1	4	1	0	0	0	0
	(β)†	0	0	1	1	24※	0	24※	0
BL04	Accurate Neutron-Nucleus Reaction Measurement Instrument - ***ANNRI***	8	4	4	3	2	1	2	1
BL05	Neutron Optics and Physics - ***NOP***	6	6	7	5	1	0	1	0
BL06	Village of Neutron Resonance Spin Echo Spectrometers - ***VIN ROSE***	3	2	4	2	1	0	1	0
BL08	Super High Resolution Powder Diffractometer - ***SuperHRPD***	11	8	6	5	1	0	1	0
BL09	Special Environment Neutron Powder Diffractometer - ***SPICA***	5	5	1	1	1	0	1	0
BL10	NeutrOn Beam-line for Observation and Research Use - ***NOBORU***	17	3	9	10	2	1	2	1
BL11	High-Pressure Neutron Diffractometer - ***PLANET***	8(0)	7(0)	13(0)	5(0)	0	2	0	2
BL12	High Resolution Chopper Spectrometer - ***HRC***	10	6	7	5	1	0	1	0
BL14	Cold-Neutron Disk-Chopper Spectrometer - ***AMATERAS***	35	8	35	8	1	1	1	1
BL15	Small and Wide Angle Neutron Scattering Instrument - ***TAIKAN***	34(2)	13(2)	36(0)	10(0)	2	4	2	4
BL16	Soft Interface Analyzer - ***SOFIA***	21	12	21	10	1	1	1	1
BL17	Polarized Neutron Reflectometer - ***SHARAKU***	17(2)	14(2)	15(1)	7(1)	3	2	3	2
BL18	Extreme Environment Single Crystal Neutron Diffractometer - ***SENJU***	18(0)	8(0)	17(0)	7(0)	1	1	1	1
BL19	Engineering Materials Diffractometer - ***TAKUMI***	27	12	29	7	2	1	2	1
BL20	IBARAKI Materials Design Diffractometer - ***iMATERIA*** (100-β)‡	3	3	5	5	0	0	0	0
	(β)‡	18	18	13	13	23	0	23	0
BL21	High Intensity Total Diffractometer - ***NOVA***	21	19	14	10	1	0	1	0
BL22	Energy Resolved Neutron Imaging System - ***RADEN***	23(0)	8(0)	18(1)	8(1)	0	2	0	2
BL23	Polarization Analysis Neutron Spectrometer - ***POLANO***	5	4	6	4	1	0	1	0
D1	Muon Spectrometer for Materials and Life Science Experiments - ***D1***	12(0)	6(0)	16(0)	9(0)	0	1	0	1
D2	Muon Spectrometer for Basic Science Experiments - ***D2***	10(4)	5(3)	5(0)	1(0)	1	1	1	1
S1	General purpose μSR spectrometer - ***ARTEMIS***	28(0)	15(0)	37(1)	12(1)	1	1	1	1
S2	Muonium Laser Physics Apparatus - ***S2***	0(0)	0(0)	0(0)	0(0)	0	1	0	1
U1A	Ultra Slow Muon Microscope - ***U1A***	0	0	0	0	0	1	0	1
U1B	Transmission Muon Microscope - ***U1B***	0	0	0	0	0	0	0	0
H1	High-intensity Muon Beam for General Use - ***H1***	0	0	0	0	0	1	0	1
Total		**382**	**207**	**371**	**158**	**65**	**24**	**65**	**24**

GU : General Use **PU :** Project Use or Ibaraki Pref. Project Use **S :** S-type Proposals **IU :** Instrument Group Use
† : Ibaraki Pref. Exclusive Use Beamtime (β = 80% in FY2022) **‡ :** J-PARC Center General Use Beamtime (100−β = 20% in FY2022)
( ) : Proposal Numbers under the New User Promotion (BL01, BL02, BL11, BL15, BL17, BL18, BL22) or P-type proposals (D1,D2, S1) in GU
※ **:** Operations period is held twice per year (for each of the A and B periods), with only the yearly total shown above.
The actual total number of proposals in each beamline named in the table does not match the number shown in the "Total" cell, because some proposals are submitted or approved across multiple beamlines.

Table 2. Number of Long-Term Proposals by Fiscal Year

Application FY	Submitted	Approved
2020	13	3
2021	0	0
2022	5	4

Due to the COVID-19 situation, no Long-Term Proposals were called for FY2021.

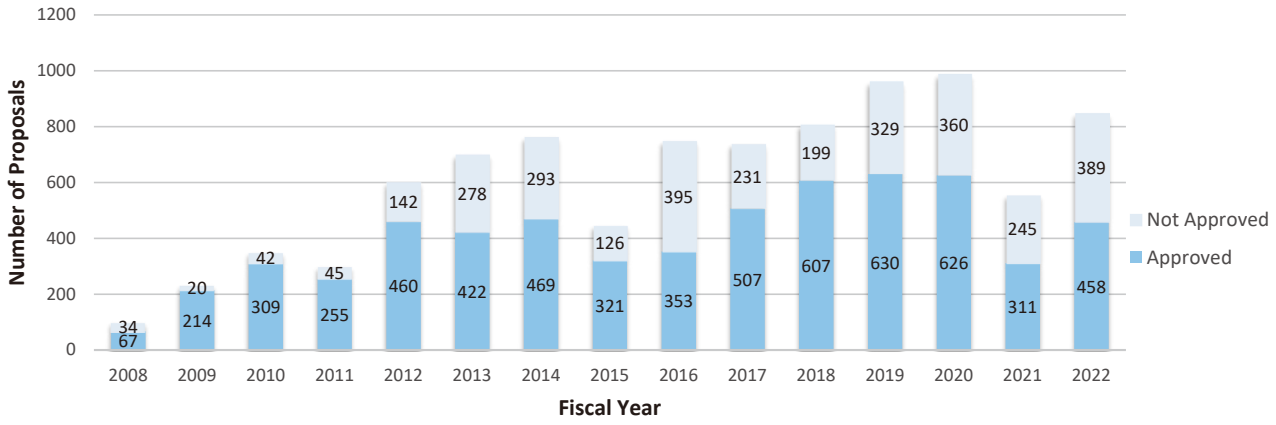

Figure 1. Number of MLF Proposals over Time

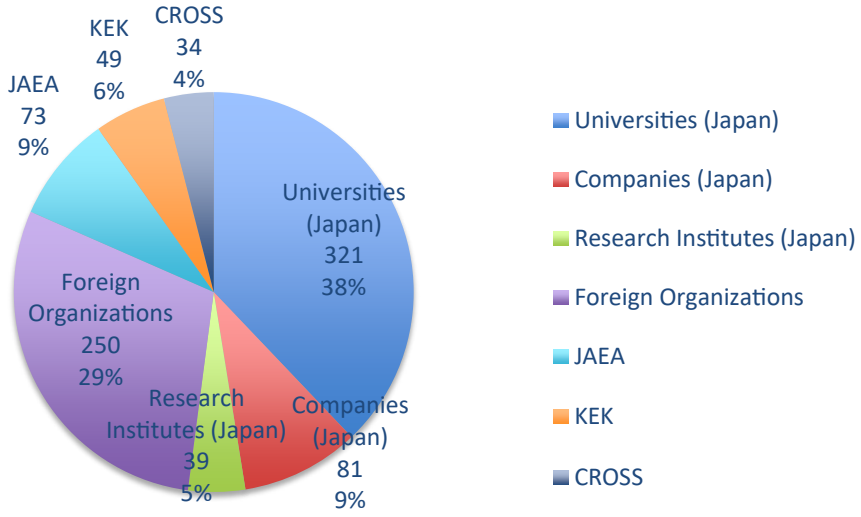

Figure 2. Origin of Submitted Proposals by Affiliation - FY2022

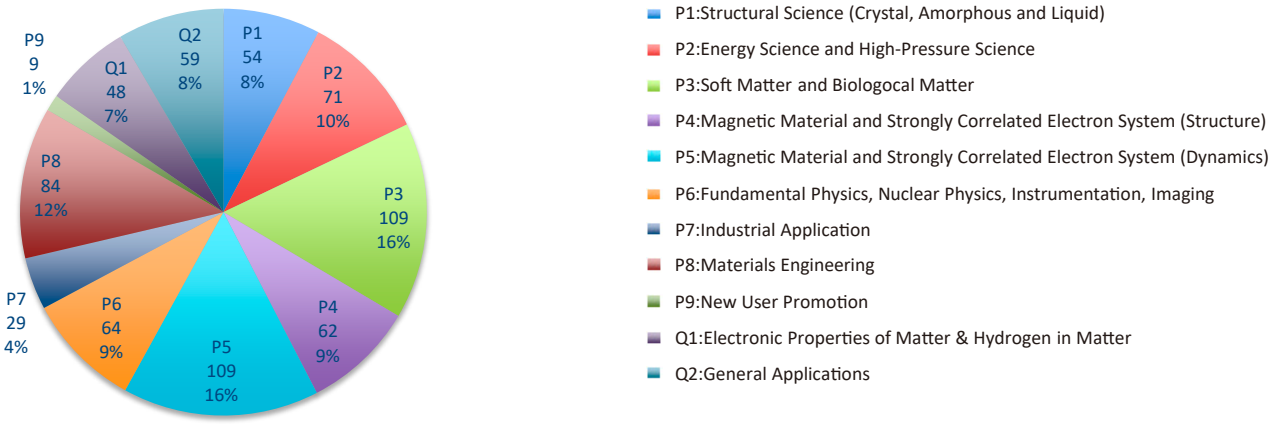

Figure 3. Submitted Proposals by Sub-committee/Expert Panel – FY2022

MLF Division Staff 2022

Toshiya Otomo (Head)
Kazuya Aizawa (Deputy Head)
Hiroshi Takada (Deputy Head)
Koichiro Shimomura (Deputy Head)

Eiichi Wakai
Kyoko Aizawa

Neutron Source Section

*: additional duties

<JAEA>

Katsuhiro Haga (Leader)
Kenji Sakai (Sub-Leader)
Makoto Teshigawara
Masahide Harada
Tomokazu Aso
Hiroyuki Kogawa
Hidetaka Kinoshita
Takashi Wakui
Takashi Naoe
Koichi Saruta
Masakazu Seki
Shiho Masuda
Gen Ariyoshi
Toshiaki Uehara
Hideki Muto
Shigeto Tanaka
Yoshinori Kikuchi
Toshiyuki Yasuhara
Akihiko Watanabe
Masakazu Nakamura
Noriyuki Morikawa
Akiyoshi Futakawa
Taku Ito
Shizuka Yoshinari
Rie Nemoto
Shin-ichiro Meigo *
Tetsuya Kai *
Kenichi Oikawa *
Shoichi Hasegawa *
Hiroyuki Uehara *
Motoki Ooi *
Yuji Yamaguchi *
Shoya Suda *
Midori Yamamoto *

Neutron Science Section

*: additional duties

<JAEA>

Yukinobu Kawakita (Leader)
Mitsutaka Nakamura (Sub-Leader)
Kentaro Suzuya
Ryoichi Kajimoto
Takanori Hattori
Stefanus Harjo
Kenichi Oikawa
Takashi Ohhara
Takenao Shinohara
Hiroyuki Aoki
Asami Sano
Tetsuya Kai
Seiko Kawamura
Shinichi Takata
Ryoji Kiyanagi
Yasuhiro Inamura
Maiko Kofu
Wu Gong
Kosuke Hiroi
Naoki Murai
Yusuke Tsuchikawa
Hiromu Tamatsukuri
Kaoru Shibata
Wenqi Mao
Masami Nirei
Wang Shan
Kotomi Nakamura
Tatsuya Kikuchi
Masashi Harada
Hiroshi Nozaki
Takeshi Harada
Hideaki Isozaki
Keiichi Inoue
Sakai Motonobu
Motohiro Aizawa
Hiroko Uchiki
Keiko Nemoto
Naoko Shimizu
Itaru Tamura *
Koji Kaneko *
Hiroshi Nakagawa *
Atsushi Moriai *
Satoshi Morooka *
Atsushi Kimura *
Shoji Nakamura *
Shunsuke Endo *
Yosuke Toh *
Mariko Segawa *
Masahide Harada *
Masao Watanabe *
Dai Yamazaki *
Takuro Kawasaki *
Kazuo Kurihara *
Tarou Tamada *

Yu Hirano *
Takeshi Hiromoto *
Fumiaki Kono *
Tatsuhito Matsuo *

<KEK>

Testuya Yokoo (Sub-Leader)
Shinichi Ito
Hideki Seto
Toshiya Otomo *
Kazuhiro Mori
Takashi Kamiyama
Hitoshi Endo
Takashi Ino
Takashi Honda
Taichi Ueta
Masako Yamada
Naokatsu Kaneko
Shuki Torii
Kaoru Taketani
Sara Yamauchi
Hiroyuki Aoki *
Asami Sano *
Kenji Mishima
Kazutaka Ikeda
Takashi Saito
Go Ichikawa
Norifumi Yamada
Nur Ika Puji Ayu
Seungyub Song
Hidetoshi Oshita *
Tomohiro Seya *
Setsuo Sato *

Technology Development Section

*: additional duties

<JAEA>

Takayuki Oku (Leader)
Kazuyoshi Tatsumi
Masao Watanabe
Yuhua Su
Ryota Komine
Hiroyuki Hasemi
Takuya Okudaira
The Dang Vu
Wataru Kambara
Yoko Watanabe
Hideaki Takahashi
Ryuta Takahashi
Nirimichi Hashimoto
Hiromichi Tanaka
Hiroyuki Asai
Chie Shibazaki
Yukiko Nagai
Kenji Sakai *
Tetsuya Kai *
Hiroyuki Kogawa *
Motoki Ooi *
Kentaro Suzuya *
Mitsutaka Nakamura *
Shinichi Takata *
Tatsuya Nakamura *
Yasuhiro Inamura *
Masahide Harada *
Tomokazu Aso *
Seiko Kawamura *
Rumi Shimizu *
Satoru Fujiwara *
Motoyasu Adachi *
Shigeki Arai *

<KEK>

Testuya Yokoo *
Shuki Torii *
Takashi Ino *
Naokatsu Kaneko *
Kaoru Taketani *
Naritoshi Kawamura *
Hiroshi Fujimori *
Shunsuke Makimura *

Neutron Instrumentation Section

*: additional duties

<JAEA>

Tatsuya Nakamura (Leader)
Dai Yamazaki
Kentaro Toh
Ryuji Maruyama
Kaoru Sakasai
Masahiro Tobe
Yukio Hishinuma
Takaaki Hosoya
Hiroki Kajihara
Aoi Yanagi
Masumi Ebine *

<KEK>

Hidetoshi Oshita
Tomohiro Seya
Setsuo Sato

Muon Science Section

*: additional duties

<KEK>

Naritoshi Kawamura (Leader)	Jumpei Nakamura	Amba Datt Pant
Akihiro Koda (Sub-Leader)	Shiro Matoba	Yasuhiro Miyake
Koichiro Shimomura *	Takahiro Yuasa	Hiroshi Fujimori
Patrick Strasser	Ryosuke Kadono	Yasunori Bessho
Takayuki Yamazaki	Yu Oishi	Ryoto Iwai
Sohtaro Kanda	Yukinori Nagatani	Hua Li
Soshi Takeshita	Shoichiro Nishimura	Shogo Doiuchi
Izumi Umegaki	Hiroaki Natori	Akiko Hashimoto
Yutaka Ikedo	Sourav Kumar Dey	Yoshinori Ito
Yasuo Kobayashi	Motonobu Tampo	Yuta Ishikake

<JAEA>

Wataru Higemoto *	Takashi Ito *

CROSS Staff 2022

Director Mitsuhiro Shibayama

Science Coordinators

Shamoto Shinichi
Jun Sugiyama
Matahiro Komuro
Kazuhisa Kakurai
Midori Kamimura

Research & Development Division

*: additional duties

Jun-ichi Suzuki (Head)
Kenichi Funakoshi (Deputy Head)
Masato Matsuura (Deputy Head)

<BL01 Group>
Kazuya Kamazawa (Leader)
Kazuki Iida
Kazuhiko Ikeuchi

<BL02 Group>
Masato Matsuura (Leader)
Taiki Tominaga
Takeshi Yamada

<BL11 Group>
Kenichi Funakoshi * (Leader)
Jun Abe
Shinichi Machida

<BL15 Group>
Kazuki Ohishi (Leader)
Hiroki Iwase
Yukihiko Kawamura
Jun-ichi Suzuki *

<BL17 Group>
Noboru Miyata * (Leader)
Kazuhiro Akutsu
Takayasu Hanashima

<BL18 Group>
Akiko Nakao (Leader)
Koji Munakata
Yoshihisa Ishikawa

<BL22 Group>
Hirotoshi Hayashida (Leader)
Joseph Don Parker
Yoshihiro Matsumoto

<Technical Support Group>
Yoshifumi Sakaguchi (Leader)
Nobuo Okazaki (Leader)
Toshiaki Morikawa (Sub-Leader)
Hiroshi Arima
Motoyuki Ishikado
Misaki Ueda
Keiichi Ohuchi
Hiroshi Kira
Masae Sahara
Shuoyuan Zhang
Yuukou Nojiri
Koji Kiriyama *
Satoshi Kasai
Yuuki Nagai
Kentaro Moriyama
Takayoshi Ito *

Safety Division

*: additional duties

Mitsuhiro Shibayama * (Head)
Koji Kiriyama (Leader)
Tazuko Mizusawa *
Masae Sahara *
Yasuhiro Yamaguchi

Utilization Promotion Division

*: additional duties

Takashi Noma (Head)
Kazuki Mita (Deputy Head)
Takayoshi Ito (Leader)
Toshiki Asai (Leader)
Miho Igarashi
Taeko Ishikawa
Tomoko Ishikawa
Maya Endo
Kaoru Ohuchi
Emi Goto
Hideyuki Niitsuma
Tazuko Mizusawa
Nobuo Okazaki *

Administration Division

*: additional duties

Michihiko Murasawa (Head)
Takashi Hikita (Deputy Head)
Junichi Sato (Leader)
Rei Ito (Leader)
Mami Uchida
Rie Kurosawa
Tomoko Sakuma
Mutsumi Shiraishi
Shinobu Matsumoto
Seiya Konishi *

Industrial Collaboration Promotion Division

*: additional duties

Mitsuhiro Shibayama (Head)
Seiya Konishi (Deputy Head)
Noboru Miyata (Leader)
Jun Abe *
Hiroki Iwase *
Yoshihiro Matsumoto *
Kazuki Mita *
Takeshi Yamada *

Ibaraki Neutron Beamline Staff in 2022

Ibaraki Prefectural Government

<Senior Director for Neutron Promotion>
Hideya Anzai

<Neutron Beamline Coordinator>
Michiko Konno
Tetsuroh Minemura

Ibaraki University *

* Trustee of the Beamline operations

<BL03 iBIX Group>
Katsuhiro Kusaka (Leader)
Taro Yamada
Naomine Yano
Ichiro Tanaka
Takaaki Hosoya

<BL20 iMATERIA Group>
Toru Ishigaki (Leader)
Akinori Hoshikawa
Satoshi Koizumi
Takeshi Matsukawa
Kazuaki Iwasa
Tomoki Maeda
Shigeo Sato
Yohei Noda

<Technical Support Group>
Mitsuyuki Fujii
Shinju Shibata
Tomoyuki Nakazawa
Junichi Hiroki

Proposals Review System, Committees and Meetings

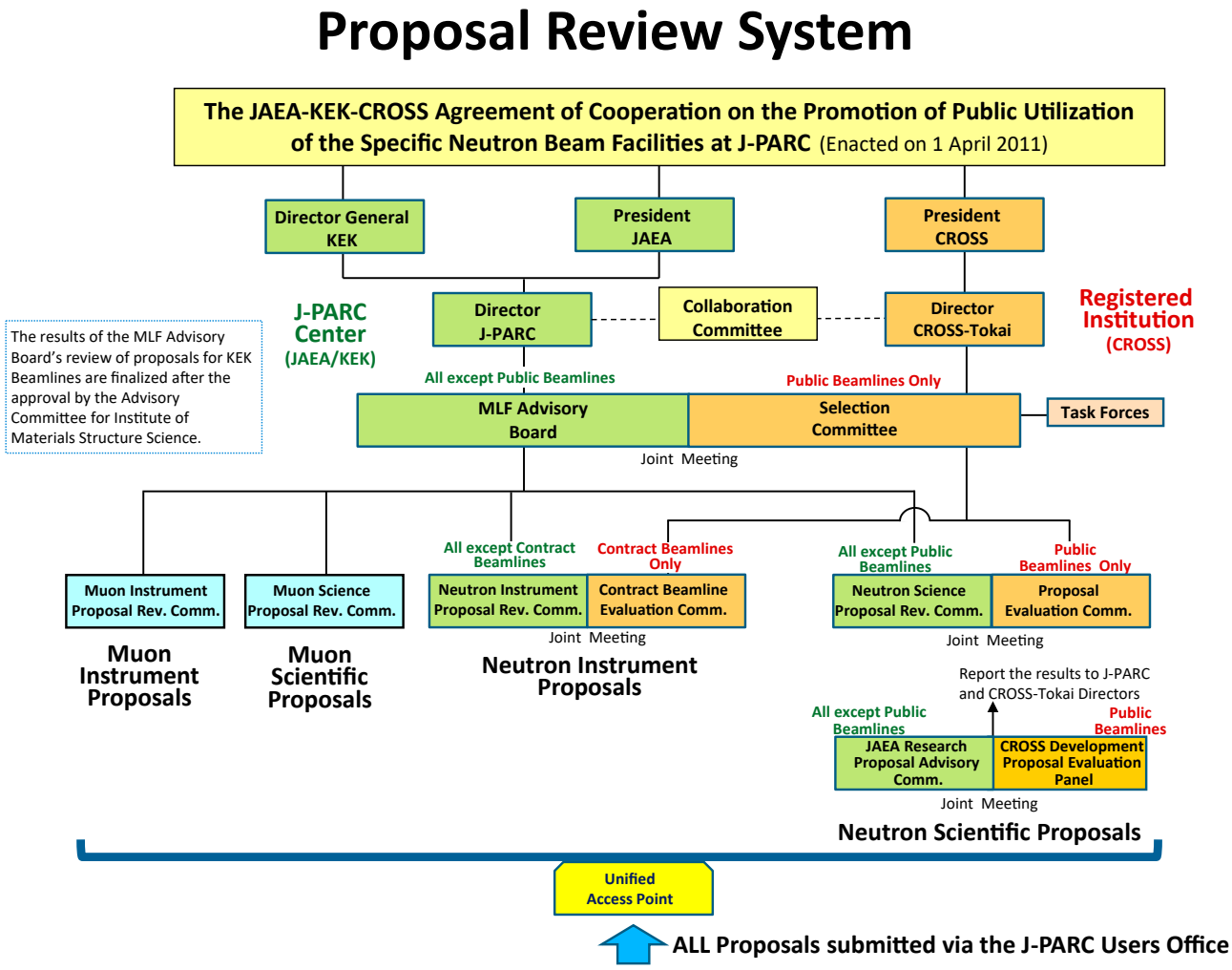

Figure 1. Proposals Review System Framework.

Materials and Life Science Facility Advisory Board

Tadashi Adachi	Sophia University
Kazuya Aizawa	Japan Atomic Energy Agency
Hiroshi Amitsuka	Hokkaido University
Taka-hisa Arima (chair)	The University of Tokyo
Masahiro Hino	Kyoto University
Shinich Itoh	High Energy Accelerator Research Organization
Yasuhiro Iye	Chubu University
Takashi Kamiyama	Hokkaido University
Yukinobu Kawakita	Japan Atomic Energy Agency
Naritoshi Kawamura	High Energy Accelerator Research Organization
Hiroyuki Kishimoto	Sumitomo Rubber Industries, LTD.
Kenji Nakajima	Japan Atomic Energy Agency
Yoshie Otake	RIKEN
Toshiya Otomo	High Energy Accelerator Research Organization
Yoshiharu Sakurai	Japan Synchrotron Radiation Research Institute
Taku Sato	Tohoku University
Koichiro Shimomura	High Energy Accelerator Research Organization
Yoko Sugawara	Toyota Physical and Chemical Research Institute
Jun-ichi Suzuki	Comprehensive Research Organization for Science and Society
Hiroshi Takada	Japan Atomic Energy Agency
Atsushi Takahara	Kyushu University
Masayasu Takeda	Japan Atomic Energy Agency
Osamu Yamamuro	The University of Tokyo

Term: through March 31, 2023

Neutron Science Proposal Review Committee

Hiroshi Abe	National Defense Academy of Japan
Mitsuhiro Hirai	Gunma University
Shinich Itoh	High Energy Accelerator Research Organization
Yukinobu Kawakita	Japan Atomic Energy Agency
Naritoshi Kawamura	High Energy Accelerator Research Organization
Masaaki Kitaguchi	Nagoya University
Takatsugu Masuda	The University of Tokyo
Koichi Mayumi	The University of Tokyo
Kenji Nakajima	Japan Atomic Energy Agency
Toshiya Otomo	High Energy Accelerator Research Organization
Taku Sato	Tohoku University
Toshiyuki Takamuku	Saga University
Noriyuki Tsuchida	University of Hyogo
Satoshi Tsutsui	Japan Synchrotron Radiation Research Institute
Osamu Yamamuro (chair)	The University of Tokyo

Term: through September 30, 2023

Muon Science Proposal Review Committee

Tadashi Adachi	Sophia University
Kenta Amemiya	High Energy Accelerator Research Organization
Hidehito Asaoka	Japan Atomic Energy Agency
Katsuyuki Fukutani	The University of Tokyo
Wataru Higemoto	Japan Atomic Energy Agency
Adrian Hillier	Rutherford Appleton Laboratory
Hiromi Iinuma	Ibaraki University
Katsuya Inoue	Hiroshima University
Shinichi Itoh	High Energy Accelerator Research Organization
Ryosuke Kadono	High Energy Accelerator Research Organization
Yukinobu Kawakita	Japan Atomic Energy Agency
Naritoshi Kawamura	High Energy Accelerator Research Organization
Yasushi Kino	Tohoku University
Akihiro Koda	High Energy Accelerator Research Organization
Kenya Kubo (chair)	International Christian University
Roderick Macrae	Marian University
Kenji Mishima	High Energy Accelerator Research Organization
Takehito Nakano	Ibaraki University

Seiko Ohira-Kawamura	Japan Atomic Energy Agency
Chihiro Ohmori	High Energy Accelerator Research Organization
Toshiya Otomo	High Energy Accelerator Research Organization
Hideki Seto	High Energy Accelerator Research Organization
Tatsushi Shima	Osaka University
Koichiro Shimomura	High Energy Accelerator Research Organization
Takashi Suemasu	University of Tsukuba
Yoko Sugawara	Kitasato University
Toshiyuki Takayanagi	Saitama University

Term: through March 31, 2023

Selection Committee

Tadashi Adachi	Sophia University
Hiroshi Amitsuka	Hokkaido University
Taka-hisa Arima (chair)	The University of Tokyo
Masahiro Hino	Kyoto University
Yasuhiro Iye	Chubu University
Takashi Kamiyama	Hokkaido University
Hiroyuki Kishimoto	Sumitomo Rubber Industries, LTD.
Yoshie Otake	RIKEN
Yoshiharu Sakurai	Japan Synchrotron Radiation Research Institute
Taku Sato	Tohoku University
Yoko Sugawara	Toyota Physical and Chemical Research Institute
Atsushi Takahara	Kyushu University
Osamu Yamamuro	The University of Tokyo

Term: through March 31, 2023

Proposal Evaluation Committee

Hiroshi Abe	National Defense Academy of Japan
Mitsuhiro Hirai	Gunma University
Masaaki Kitaguchi	Nagoya University
Takatsugu Masuda	The University of Tokyo
Koichi Mayumi	The University of Tokyo
Toshiya Otomo	High Energy Accelerator Research Organization
Taku Sato	Tohoku University
Toshiyuki Takamuku	Saga University
Noriyuki Tsuchida	University of Hyogo
Satoshi Tsutsui	Japan Synchrotron Radiation Research Institute
Osamu Yamamuro (chair)	The University of Tokyo

Term: through September 30, 2023

Neutron Advisory Committee (NAC)

NAC convened on 9 and 10 February 2023.

Ken Anderson	Oak Ridge National Laboratory
Taka-hisa Arima	The University of Tokyo
Christiane Alba-Simionesco	Laboratoire Léon Brillouin
Bertrand Blau	Paul Scherrer Institut
Michael Dayton	Oak Ridge National Laboratory
Phillip King	Rutherford Appleton Laboratory
Toyohiko Kinoshita	Japan Synchrotron Radiation Research Institute
Guenter Muhrer	European Spallation Source
Yoshie Otake	RIKEN
Sungil Park	Korea Atomic Energy Research Institute
Jamie Schulz (chair)	Australian Nuclear Science and Technology Organization
Jon Taylor	European Spallation Source

Muon Advisory Committee (MAC)

MAC convened on 20 and 21 February 2023.

Thomas Prokscha (chair)	Paul Scherrer Institut
Hiroshi Amitsuka	Hokkaido University
Klaus Kirch	ETH Zurich and Paul Scherrer Institut
Kenya Kubo	International Christian University
Andrew Macfarlane	The University of British Columbia
Martin Månsson	KTH Royal Institute of Technology
Nori Aoi	Osaka University
Tadayuki Takahashi	The University of Tokyo

Workshops, Conferences, Seminars and Schools in 2022

Conferences held jointly by J-PARC MLF and CROSS

2022 Meeting on J-PARC MLF Industrial Use
14-15 Jul. 2022, Akihabara Convention Hall, Tokyo, Online

Photo of 2022 Meeting on J-PARC MLF Industrial Use
(photo courtesy of J-PARC)

ISSE workshop 2022
11th International Workshop on Sample Environment at Scattering Facilities
28 Aug. - 1 Sep. 2022, Resort Hotel Laforet Nasu, Nasu

Photo of ISSE workshop 2022
(photo courtesy of CROSS)

2022 Workshop on Neutron Imaging
14-15 Sep. 2022, Essam Kanda Hall, Tokyo, Online

J-PARC Workshop, Progress for Fundamental Physics with Neutrons
28-29 Sep. 2022, KEK Tokai Campus and J-PARC Center, Tokai

Photo of Progress for Fundamental Physics with Neutrons
(photo courtesy of J-PARC)

2022 年度中性子実験技術基礎講習会（レベル 1 講習会）
7 Oct. 2022, Online

J-PARC Workshop 2022, Deuterium Science Entering a New Phase
19-20 Dec. 2022, IBARAKI Quantum Beam Research Center, Tokai

Photo of J-PARC Workshop 2022
(photo courtesy of CROSS)

2022 Quantum Beam Science Festa (The 14th MLF Symposium and the 40th PF Symposium)
13-15 Mar. 2023, Tsukuba International Congress Center, Tsukuba

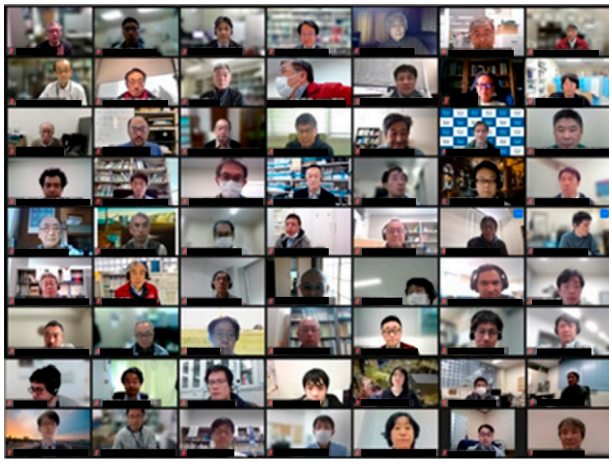

Screenshot of 14th MLF Symposium
(photo courtesy of CROSS)

中性子小角散乱研究会
16 Mar. 2023, KEK, Tsukuba

2022 Z-Code Intermediate level Training Course
6 Dec. 2022-28 Feb. 2023, On-demand

Conferences held by KEK

第 7 回文理融合シンポジウム " 量子ビームで歴史を探る ー加速器が紡ぐ文理融合の地平ー "
2-3 Nov. 2022, KEK Tsukuba Campus, Ibaraki, Online

Workshops held by KEK

2022 年度物構研コロキウム
" 放射光および中性子を用いた次世代二次電池の開発 "
6 June 2022, Online

2022 年度物構研コロキウム
" 中性子ビーム利用の有効性を定量的に記述する方法の模索 "
3 Oct. 2022, Online

Analysis of ordered/disordered structure in functional materials with high intensity neutron total scattering technique (BL21)
28 Nov. 2022, Online

Study on Cross-correlated Physics by Polarized Neutron Spectrometer, POLANO (BL23)
30 Nov. 2022, Online

Studies on Dynamics in Condensed Matters by using the High Resolution Chopper Spectrometer (BL12)
2 Dec. 2022, Online

Study on slow dynamics by the neutron resonance spin echo spectrometers VIN ROSE (BL06)
6 Dec. 2022, Online

Fundamental Physics with Pulsed Cold Neutrons (BL05)
15-16 Dec. 2022, Nagoya University, Nagoya

Workshop on Neutron Powder Diffraction using SuperHRPD (BL08)
17 Dec. 2022, Online

Workshop on Neutron Powder Diffraction using SPICA (BL09)
16 Dec. 2022, Online

Workshops and Seminars held by CROSS and other organizations

Workshop on Battery Materials
10 May 2022, Online

第 77 回 Spring-8 先端利用技術ワークショップ / 第 2 回放射光・中性子連携利用研究会 / 第 1 回量子ビームを用いた構造材料研究会
20 May 2022, Online

CBI 研究機構 量子構造生命科学研究所 中性子産業利用推進協議会 生物・生体材料研究会 合同シンポジウム
" 生体分子の動的挙動解析への挑戦　試料調製から解析まで　III "
27 Jul. 2022, Online

8th Symposium on the Collaborative Use of Large Research Institutions and the Super Computer
30 Sep. 2022, Akihabara UDX, Tokyo

The 26th CROSSroads Workshop
" データ解析ソフトウェアの紹介パート 2 "
14 Oct. 2022, Online

Screenshot of 26th CROSSroads Workshop
(photo courtesy of CROSS)

Workshop on Organic materials and Polymers
“ 有機・高分子材料への反射率法の展開（第 4 回）”
17 Oct. 2022, Online

CBI 研究機構 量子構造生命科学研究所 中性子産業利用推進協議会 生物・生体材料研究会 合同シンポジウム
“ MicroED の現状と未来 ”
6 Dec. 2022, Online

2022 Workshop on Magnetic Materials
11 Jan. 2023, Online

6th Joint Workshop for Complementary Use of Synchrotron Radiation and Neutrons
“ 小角散乱測定研修会 ”
2 Feb. 2023, IBARAKI Quantum Beam Research Center, Tokai

7th Joint Workshop for Complementary Use of Synchrotron Radiation and Neutrons
“ 粉末回折測定研修会 ”
17 Nov. 2022, JRR-3, IBARAKI Quantum Beam Research Center, Tokai

ものづくり基盤研究会
“ ー接合・加工における課題解決に向けた評価技術ー ”
6 Mar. 2023, Online

2022 Workshop on Liquids and Amorphous Materials
16 Mar. 2023, KEK, Tsukuba

Workshops and Seminars held by Ibaraki Neutron Beamline and other organizations

2022 1st Workshop on iMATERIA
21-22 Apr. 2022, Hokkaido University, Sapporo, Online

第 4 回中性子産業利用の研究会（茨城県中性子利用研究会　令和 4 年度第 2 回 iMATERIA 研究会　合同開催）
12 Sep. 2022, Essam Kanda Hall, Tokyo, Online

2022 3rd Workshop on iMATERIA
29 Nov. 2022, Online

2022 1st Workshop on iBIX
20 Sep. 2022, Online

2022 2nd Workshop on iBIX
22 Dec. 2022, Online

2022 4th Workshop on iMATERIA
18 Jan. 2023, Online

2022 年度 iBIX-JAXA-KEK 物構研 -QST 合同タンパク質研究会
“「酵素反応の中間体」の観測は可能か ”
27 Feb. 2023, Online

2022 5th Workshop on iMATERIA
8 Mar. 2023, University of Tokyo, Tokyo

2022 6th Workshop on iMATERIA
24 Mar. 2023, Essam Kanda Hall, Tokyo, Online

Schools in 2022

Hello Science from J-PARC
“ Form and Motion of Giant Molecules ”
29 Jul. 2022, IBARAKI Quantum Beam Research Center, Tokai, Online

Hello Science from J-PARC
“ What can we do with the Ibaraki Prefectural device iBIX? ”
30 Sep. 2022, IBARAKI Quantum Beam Research Center, Tokai, Online

Hello Science from J-PARC
"Artisans' Techniques in Making Elementary Particles - From Site of Muon Production Targets -"
23 Dec. 2022, IBARAKI Quantum Beam Research Center, Tokai, Online

The 6th Neutron and Muon School
12-16 Dec. 2021, J-PARC Center, Tokai

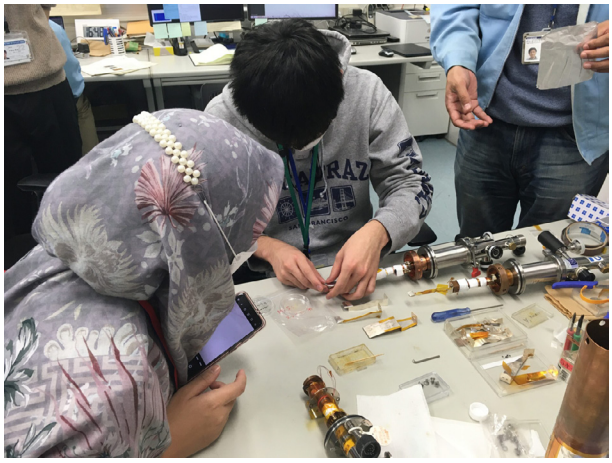

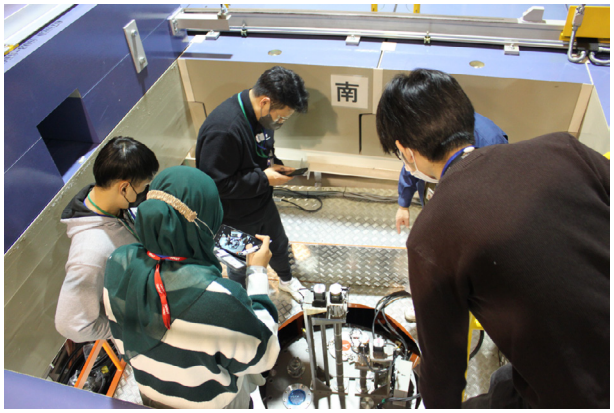

Photo of Neutron and Muon School
(photo courtesy of CROSS)

Award List

2022 JMMS Outstanding Achievement Prize
Construction of the high intensity pulsed muon facility and development of interdisciplinary muon science
Y. Miyake (2023-03-29)

2022 JMMS Young Researcher Prize
層状カルコゲナイドに関するμSR研究
J. Nakamura (2023-03-29)

2022 JMMS Technology Prize
J-PARC 物質・生命科学実験施設におけるミュオン回転標的の開発と安全な運用・保守
S. Makimura, S. Matoba (2023-03-29)

Young Scientist Award of the Physical Society of Japan
Establishment of techniques using muon beam to detect Li diffusion and metallic Li deposition in a Li-ion battery
I. Umegaki (2023-03)

SAT Technology Showcase 2023 ベスト産業実用化賞
最先端加速器技術で産業を革新する―超耐熱高靭性・高電気抵抗率タングステン合金
S. Makimura (2023-01-26)

J-PARC Center, Workshop 2022, Deuterium Science Entering a New Phase, Poster Award
Development of a new analytical method for deuterium-labeled compounds using NMR techniques
M. Ueda, K. Akutsu, M. Shibayama, T. A. Darwish, T. Yamada, T. Ikawa, H. Sajiki (2023-01-20)

The JSNS Poster Prize
Feasibility Study of Magnetic Scattering Holography using Polarized Neutrons
T. Kanno (2022-10-27)

The JSNS Poster Prize
Study of local atomic fluctuation in RB_6 with cage type structure by neutron holography
Y. Kobayashi (2022-10-27)

The JSNS Poster Prize
Effect of grain refinement on deformation-induced martensitic transformation
W. Mao (2022-10-27)

The JSNS President's Choice
Application of Muon Beam for Li-ion Battery Research
I. Umegaki (2022-10-26)

The JSNS President's Choice
Development of Spin-Contrast-Variation Neutron Reflectometry for Structural Analyses of Multilayer Films
T. Kumada, D. Miura, K. Akutsu, J. Suzuki, N. Torikai (2022-10-26)

The JSNS Young Researcher Prize
Research on Microstructure Control and Mechanical Properties of Advanced Structural Materials using Pulsed Neutron Diffraction
W. Gong (2022-10-26)

Student Presentation Award of the Physical Society of Japan
Neutron lifetime measurement at J-PARC/BL05: Status of the neutron lifetime analysis until 2022
T. Mogi (2022-10-15)

The Japan Institute of Metals and Materials The Metals Best Poster Award
Deformation microstructure and recrystallization behavior of $Co_{20}Cr_{40}Ni_{40}$ medium entropy alloy
K. Yamamoto (2022-09-29)

The JSNS President's Choice
Neutron Imaging for Observation of Grease Fluidity in Ball Bearings
N. Kimura, K. Sakai, Y. Ayame, Y. Iwanami Y. Matsumoto (2022-09-28)

The Japan Institute of Metals and Materials Murakami Young Researcher Award
金属材料を対象としたAdditive Manufacturingに関する研究
K. Yamanaka (2022-09-21)

JAMS Research Paper Award
Neutron diffraction study of hydrogen site occupancy in $Fe_{0.95}Si_{0.05}$ at 14.7 GPa and 800 K
Y. Mori H. Kagi S. Kakizawa K. Komatsu A. Sano-Furukawa (2022-09-17)

The JLCS Best Paper Award B
Structural and Dynamical Studies on Liquid Crystalline Ionic Liquids by Thermal Analysis and Neutron Scattering
F. Nemoto (2022-09-15)

SPSJ Showa Denko Materials Award 2022
Effects of Interfacial Structure and Physical Properties on Functions in Polymer Thin Films
D. Kawaguchi (2022-09-06)

Acta/Scripta Materialia's Outstanding Reviewers in 2021
S. Harjo (2022-08)

Nishikawa Prize, the Foundation for High Energy Accelerator Science for 2021
Rabi-oscillation Spectroscopy in Accurate Measurement of Hyperfine Structure of Muonium Atoms
S. Nishimura, S. Kanda, K. Shimomura, H. Torii, K. Tanaka (2022-05-30)

The 21th Intelligent Cosmos Encouragement Prize
耐摩耗性と耐食性に優れた鉄鋼材料の開発
K. Yamanaka (2022-05-09)

Progress Award of Japan Oil Chemists' Society
自己組織体内部の特異な環境を利用した超分子機能の発現と応用
M. Akamatsu (2022-04-20)

Ibaraki UNIV. President Award
太陽電池材料SnドープSi, Ge薄膜の活性サイト位置のSn量の定量評価
S. Hoshi (2022-03-30)

The JSNS Poster Prize
太陽電池材料SnドープSi, Ge薄膜の活性サイト位置のSn量の定量評価
S. Hoshi (2021-12-03)

JAMS: Japan Association of Mineralogical Sciences
JLCS: The Japanese Liquid Crystal Society
JMMS: Society of Muon and Meson Science of Japan
JSNS: The Japanese Society for Neutron Science
SAT: Science Academy of Tsukuba
SPSJ: The Society of Polymer Science, Japan

MLF Publication 2022

1 K. Ohishi, D. Igarashi, R. Tatara, I. Umegaki, A. Koda, S. Komaba, J. Sugiyama
Operando Muon Spin Rotation and Relaxation Measurement on $LiCoO_2$ Half-Cell
ACS Appl. Energy Mater., **5** 12538–12544 (2022).

2 H. Kawaura, M. Harada, Y. Kondo, M. Mizutani, N. Takahashi, N. L. Yamada
Effects of Lithium Bis(oxalate)Borate Electrolyte Additive on the Formation of a Solid Electrolyte Interphase on Amorphous Carbon Electrodes by Operando Time-Slicing Neutron Reflectometry
ACS Appl. Mater. Interfaces, **14** 24526–24535 (2022).

3 T. T. Chuong, T. Ogura, N. Hiyoshi, K. Takahashi, S. Lee, K. Hiraga, H. Iwase, A. Yamaguchi, K. Kamagata, E. Mano, S. Hamakawa, H. Nishihara, T. Kyotani, G. D. Stucky, T. Itoh
Giant Carbon Nano-Test Tubes as Versatile Imaging Vessels for High-Resolution and in situ Observation of Proteins
ACS Appl. Mater. Interfaces, **14** 26507–26516 (2022).

4 W. Yoshimune, N. Kikkawa, H. Yoneyama, N. Takahashi, S. Minami, Y. Akimoto, T. Mitsuoka, H. Kawaura, M. Harada, N. L. Yamada, H. Aoki
Interfacial Distribution of Nafion Ionomer Thin Films on Nitrogen-Modified Carbon Surfaces
ACS Appl. Mater. Interfaces, **14** 53744–53754 (2022).

5 M. Inutsuka, H. Watanabe, M. Aoyagi, N. L. Yamada, C. Tanaka, T. Ikehara, D. Kawaguchi, S. Yamamoto, K. Tanaka
Effect of Oligomer Segregation on the Aggregation State and Strength at the Polystyrene/Substrate Interface
ACS Macro Lett., **11** 504–509 (2022).

6 E. Saiki, Y. Nohara, H. Iwase, T. Shikata
Evidence of Long Two-Dimensional Folding Chain Structure Formation of Poly(vinylidene fluoride) in N -Methylpyrrolidone Solution: Total Form Factor Determination by Combining Multiscattering Data
ACS Omega, **7** 22825–22829 (2022).

7 E. Saiki, M. Yoshida, K. Kurahashi, H. Iwase, T. Shikata
Elongated Rodlike Particle Formation of Methyl Cellulose in Aqueous Solution
ACS Omega, **7** 28849–28859 (2022).

8 K. Ohishi, D. Igarashi, R. Tatara, S. Nishimura, A. Koda, S. Komaba, J. Sugiyama
Na Diffusion in Hard Carbon Studied with Positive Muon Spin Rotation and Relaxation
ACS Phys. Chem. Au, **2** 98–107 (2022).

9 T. Kawasaki, M. Takahashi, R. Kiyanagi, T. Ohhara
Rearrangement of Hydrogen Bonds in Dehydrated Raffinose Tetrahydrate: A Time-of-Flight Neutron Diffraction Study
Acta Crystallogr. Sect. C Struct. Chem., **78** 743–748 (2022).

10 T. Chatake, I. Tanaka, K. Kusaka, S. Fujiwara
Protonation States of Hen Egg-White Lysozyme Observed Using D/H Contrast Neutron Crystallography
Acta Crystallogr. Sect. Struct. Biol., **78** 770–778 (2022).

11 Y. Terasawa, T. Ohhara, S. Sato, S. Yoshida, T. Asahi
Single-Crystal Structure Analysis of Non-Deuterated Triglycine Sulfate by Neutron Diffraction at 20 and 298 K: A New Disorder Model for the 298 K Structure
Acta Crystallogr. Sect. E Crystallogr. Commun., **78** 306–312 (2022).

12 K. Okada, A. Shibata, W. Gong, N. Tsuji
Effect of Hydrogen on Evolution of Deformation Microstructure in Low-Carbon Steel with Ferrite Microstructure
Acta Mater., **225** 117549 (2022).

13 D. Wei, L. Wang, Y. Zhang, W. Gong, T. Tsuru, I. Lobzenko, J. Jiang, S. Harjo, T. Kawasaki, J. W. Bae, W. Lu, Z. Lu, Y. Hayasaka, T. Kiguchi, N. L. Okamoto, T. Ichitsubo, H. S. Kim, T. Furuhara, E. Ma, H. Kato
Metalloid Substitution Elevates Simultaneously the Strength and Ductility of Face-Centered-Cubic High-Entropy Alloys
Acta Mater., **225** 117571 (2022).

14 M. Liu, W. Gong, R. Zheng, J. Li, Z. Zhang, S. Gao, C. Ma, N. Tsuji
Achieving Excellent Mechanical Properties in Type 316 Stainless Steel by Tailoring Grain Size in Homogeneously Recovered or Recrystallized Nanostructures
Acta Mater., **226** 117629 (2022).

15 K. Sakaki, H. Kim, E. H. Majzoub, A. Machida, T. Watanuki, K. Ikeda, T. Otomo, M. Mizuno, D. Matsumura, Y. Nakamura
Displacement of Hydrogen Position in Di-Hydride of V-Ti-Cr Solid Solution Alloys
Acta Mater., **234** 118055 (2022).

16 R. Zheng, W. Gong, J. Du, S. Gao, M. Liu, G. Li, T. Kawasaki, S. Harjo, C. Ma, S. Ogata, N. Tsuji
Rediscovery of Hall-Petch Strengthening in Bulk Ultrafine Grained Pure Mg at Cryogenic Temperature: A Combined in-situ Neutron Diffraction and Electron Microscopy Study
Acta Mater., **238** 118243 (2022).

17 R. S. Ramadhan, D. Glaser, H. Soyama, W. Kockelmann, T. Shinohara, T. Pirling, M. E. Fitzpatrick, A. S. Tremsin
Mechanical Surface Treatment Studies by Bragg Edge Neutron Imaging
Acta Mater., **239** 118259 (2022).

18 Q. Li, Y. Onuki, A. Ahadi, Q. Sun
Large Tunable Thermal Expansion in Ferroelastic Alloys by Stress
Acta Mater., **240** 118350 (2022).

19 B. Guo, W. Mao, Y. Chong, A. Shibata, S. Harjo, W. Gong, H. Chen, J. J. Jonas, N. Tsuji
Unexpected Dynamic Transformation from α Phase to β Phase in Zirconium Alloy Revealed by in-situ Neutron Diffraction during High Temperature Deformation
Acta Mater., **242** 118427 (2022).

20 T. Sawaguchi, Y. Tomota, F. Yoshinaka, S. Harjo
Evidence Supporting Reversible Martensitic Transformation under Cyclic Loading on Fe–Mn–Si–Al Alloys Using in situ Neutron Diffraction
Acta Mater., **242** 118494 (2022).

21 M. Ohira, T. Katashima, M. Naito, D. Aoki, Y. Yoshikawa, H. Iwase, S. Takata, K. Miyata, U. Chung, T. Sakai, M. Shibayama, X. Li
Star-Polymer–DNA Gels Showing Highly Predictable and Tunable Mechanical Responses
Adv. Mater., **34** 2108818 (2022).

22 T. Odaira, S. Xu, K. Hirata, X. Xu, T. Omori, K. Ueki, K. Ueda, T. Narushima, M. Nagasako, S. Harjo, T. Kawasaki, L. Bodnárová, P. Sedlák, H. Seiner, R. Kainuma
Flexible and Tough Superelastic Co–Cr Alloys for Biomedical Applications
Adv. Mater., **34** 2202305 (2022).

23 X. Xu, T. Odaira, S. Xu, K. Hirata, T. Omori, K. Ueki, K. Ueda, T. Narushima, M. Nagasako, R. Kainuma, S. Harjo, T. Kawasaki, L. Bodnarova, P. Sedlak, H. Seiner
Tough Yet Flexible Superelastic Alloys Meet Biomedical Needs
Adv. Mater. Process., **180** 35–37 (2022).

24 K. Okamoto, F. Takeiri, Y. Imai, M. Yonemura, T. Saito, K. Ikeda, T. Otomo, T. Kamiyama, G. Kobayashi
Impact of Na Concentration on the Phase Transition Behavior and H^- Conductivities in the Ba–Li–Na–H–O Oxyhydride System
Adv. Sci., **10** 2203541 (2022).

25 E. Nomura, M. Chiba, S. Matsuo, C. Noda, S. Kobayashi, J. Manjanna, Y. Kawamura, K. Ohishi, K. Hiroi, J. Suzuki
Magnetization Process of Cubic Fe_3O_4 Submicron Particles Studied by Polarized Small-Angle Neutron Scattering
AIP Adv., **12** 035034 (2022).

26 T. Ohashi, T. Sakamaki, K. Funakoshi, T. Hattori, N. Hisano, J. Abe, A. Suzuki
Structure of Basaltic Glass at Pressures up to 18 GPa
Am. Mineral., **107** 325–335 (2022).

27 M. Segawa, Y. Toh, T. Kai, A. Kimura, S. Nakamura
Investigation of Radioactive Samples for Neutron Capture Reaction Measurements Using Energy-Resolved Neutron Imaging
Ann. Nucl. Energy, **167** 108828 (2022).

28 K. Kino, T. Itoh, T. Fujiwara, R. Kuroda, N. Oshima, M. Tanaka, A. Watazu, T. Kamiyama, M. Yonemura, Y. Ishikawa
Nondestructive Quantitative Imaging for Spatially Nonuniform Degradation in a Commercial Lithium-Ion Battery Using a Pulsed Neutron Beam
Appl. Phys. Express, **15** 027005 (2022).

29 K. Hayashi, M. Lederer, Y. Fukumoto, M. Goto, Y. Yamamoto, N. Happo, M. Harada, Y. Inamura, K. Oikawa, K. Ohoyama, P. Wellmann
Determination of Site Occupancy of Boron in 6H–SiC by Multiple-Wavelength Neutron Holography
Appl. Phys. Lett., **120** 132101 (2022).

30 K. Akutsu-Suyama, N. L. Yamada, Y. Ueda, R. Motokawa, H. Narita
New Design of a Sample Cell for Neutron Reflectometry in Liquid–Liquid Systems and Its Application for Studying Structures at Air–Liquid and Liquid–Liquid Interfaces
Appl. Sci., **12** 1215 (2022).

31 Y. Hirota, T. Tominaga, T. Kawabata, Y. Kawakita, Y. Matsuo
Hydrogen Dynamics in Hydrated Chitosan by Quasi-Elastic Neutron Scattering
Bioengineering, **9** 599 (2022).

32 T. Sogabe, H. Nakagawa, T. Yamada, S. Koseki, K. Kawai
Effect of Water Activity on the Mechanical Glass Transition and Dynamical Transition of Bacteria
Biophys. J., **121** 3874–3882 (2022).

33 Y. Kameda, N. Arai, Y. Amo, T. Usuki, J. Han, H. Watanabe, Y. Umebayashi, S. Tsuzuki, K. Ikeda, T. Otomo
Neutron Diffraction with $^{34}S/^{nat}S$ Isotopic Substitution Method on the Solvation Structure of S_8 Molecule in Concentrated CS_2 Solutions
Bull. Chem. Soc. Jpn., **95** 1481–1485 (2022).

34 S. H. Song, S. Hong, M. Cho, J.-G. Yoo, H. Min Jin, S.-H. Lee, M. Avdeev, K. Ikeda, J. Kim, S. C. Nam, S.-H. Yu, I. Park, H. Kim
Rational Design of Li Off-Stoichiometric Ni-Rich Layered Cathode Materials for Li-Ion Batteries
Chem. Eng. J., **448** 137685 (2022).

35 A. Hoshikawa, A. Hachikubo
Observation of Hydrogen Bonding Network in Hydrogen Sulfide Hydrate Using Neutron Diffraction
Chem. Phys. Lett., **812** 140274 (2022).

36 L. Zheng, Z. Liu, Q. Zhang, S. Li, J. Huang, L. Zhang, B. Zan, M. Tyagi, H. Cheng, T. Zuo, V. G. Sakai, T. Yamada, C. Yang, P. Tan, F. Jiang, H. Chen, W. Zhuang, L. Hong
Universal Dynamical Onset in Water at Distinct Material Interfaces
Chem. Sci., **13** 4341–4351 (2022).

37 C. Tsutsumi-Arai, K. Akutsu-Suyama, Y. Iwamiya, C. Terada-Ito, Z. Hiroi, M. Shibayama, K. Satomura
Antimicrobial Surface Processing of Polymethyl Methacrylate Denture Base Resin Using a Novel Silica-Based Coating Technology
Clin. Oral Investig., **27** 1043–1053 (2022).

38 M. Akamatsu, T. Morita, K. Kobayashi, H. Iwase, K. Sakai, H. Sakai
Controlled Recombination Rate of Lophyl Radicals in Cationic Surfactant Micelles
Colloids Surf. Physicochem. Eng. Asp., **638** 128319 (2022).

39 N. V. Mdlovu, K.-S. Lin, M.-T. Weng, Y.-S. Lin
Design of Doxorubicin Encapsulated pH-/Thermo-Responsive and Cationic Shell-Crosslinked Magnetic Drug Delivery System
Colloids Surf. B Biointerfaces, **209** 112168 (2022).

40 Y. Furuike, D. Ouyang, T. Tominaga, T. Matsuo, A. Mukaiyama, Y. Kawakita, S. Fujiwara, S. Akiyama
Cross-Scale Analysis of Temperature Compensation in the Cyanobacterial Circadian Clock System
Commun. Phys., **5** 75 (2022).

41 K. Komatsu
Neutrons Meet Ice Polymorphs
Crystallogr. Rev., **28** 224–297 (2022).

42 S. Kanda
A Search for Atomic Parity Violation in Muonic Atoms Using a High-Intensity Pulsed Muon Beam at J-PARC
EPJ Web Conf., **262** 01010 (2022).

43 S. Fukumura, P. Strasser, T. Ino, T. Oku, T. Okudaira, S. Kanda, M. Kitaguchi, K. Shimomura, H. M. Shimizu, H. A. Torii, S. Nishimura
Proposal for New Measurements of Muonic Helium Hyperfine Structure at J-PARC
EPJ Web Conf., **262** 01012 (2022).

44 T. Higuchi, on behalf of the TUCAN collaboration
Prospects for a Neutron EDM Measurement with an Advanced Ultracold Neutron Source at TRIUMF
EPJ Web Conf., **262** 01015 (2022).

45 Y. Kawakita, M. Matsuura, T. Tominaga, T. Yamada, H. Tamatsukuri, H. Nakagawa, K. Ohuchi
Recent Progress on DNA ToF Backscattering Spectrometer in MLF, J-PARC
EPJ Web Conf., **272** 02002 (2022).

46 R. Kajimoto, M. Nakamura, K. Kamazawa, Y. Inamura, K. Iida, K. Ikeuchi, M. Ishikado
Possible Future Upgrades of the Direct-Geometry Chopper Spectrometer 4SEASONS
EPJ Web Conf., **272** 02007 (2022).

47 K. Nakajima, T. Kikuchi, S. Ohira-Kawamura, W. Kambara
Possible Options for Efficient Wide-Band Polychromatic Measurements Using Chopper Spectrometers at Pulsed Sources
EPJ Web Conf., **272** 02012 (2022).

48 M. Shibata, T. Terashima, T. Koga
Micellar Aggregation and Thermogelation of Amphiphilic Random Copolymers in Water Hierarchically Dependent on Chain Length
Eur. Polym. J., **168** 111091 (2022).

49 N. Kitamura, K. Kimura, N. Ishida, C. Ishibashi, Y. Idemoto
Effects of Ca Substitution on the Local Structure and Oxide–Ion Behavior of Layered Perovskite Lanthanum Nickelate
Front. Mater., **9** 954729 (2022).

50 D. Gong, M. Yi, M. Wang, T. Xie, W. Zhang, S. Danilkin, G. Deng, X. Liu, J. T. Park, K. Ikeuchi, K. Kamazawa, S.-K. Mo, M. Hashimoto, D. Lu, R. Zhang, P. Dai, R. J. Birgeneau, S. Li, H. Luo
Nematic Fluctuations in the Non-Superconducting Iron Pnictide $BaFe_{1.9-x}Ni_{0.1}Cr_xAs_2$
Front. Phys., **10** 886459 (2022).

51 K. Yamashita, K. Komatsu, T. Ohhara, K. Munakata, T. Irifune, T. Shinmei, K. Sugiyama, T. Kawamata, H. Kagi
Improvement of Nano-Polycrystalline Diamond Anvil Cells with Zr-Based Bulk Metallic Glass Cylinder for Higher Pressures: Application to Laue-TOF Diffractometer
High Press. Res., **42** 121–135 (2022).

52 T. Hattori, S. Ohira-Kawamura, T. Kawasaki
Development of a Hybrid Piston Cylinder Cell for Quasielastic Neutron Scattering Experiments up to 1 GPa
High Press. Res., **42** 226–235 (2022).

53 S. Machida, S. Nakano
Investigation of Null-Matrix Alloy Gaskets for a Diamond-Anvil-Cell on High Pressure Neutron Diffraction Experiments
High Press. Res., **42** 303–317 (2022).

54 K. Sasaki, M. Sugita, M. Abe, H. Iinuma, C. Ogane, T. Mibe, K. Shimomura, T. Ogitsu
Development of Precise Shimming Technique With Materials Having Low Saturation Magnetization
IEEE Trans. Appl. Supercond., **32** 9002107 (2022).

55 H. Tada, F. Yoshizu, S. Oyama, T. Tanaka, K. Sasaki, K. Shimomura
Development of Magnetic Field Mapping System for the MuSEUM Experiment With High Precision Using CW-NMR Probes
IEEE Trans. Appl. Supercond., **32** 9002205 (2022).

56 Y. Iwamiya, D. Nishio-Hamane, K. Akutsu-Suyama, H. Arima-Osonoi, M. Shibayama, Z. Hiroi
Photocatalytic Silica–Resin Coating for Environmental Protection of Paper as a Plastic Substitute
Ind. Eng. Chem. Res., **61** 6967–6972 (2022).

57 K. Takaya, M. Hagiwara, S. Matoba, M. Takaya, N. Shibata
A Real-Time Gas Monitoring System Based on Ion Mobility Spectrometry for Workplace Environmental Measurements
Ind. Health, **60** 40–46 (2021).

58 T. Yajima, K. Takahashi, H. Nakajima, T. Honda, K. Ikeda, T. Otomo, Z. Hiroi
High-Pressure Synthesis of Transition-Metal Oxyhydrides with Double-Perovskite Structures
Inorg. Chem., **61** 2010–2016 (2022).

59 M. K. Sugumar, T. Yamamoto, K. Ikeda, M. Motoyama, Y. Iriyama
Preparation of Li-Excess and Li-Deficient Antiperovskite Structured $Li_{2+x}OH_{1-x}Br$ *and Their Effects on Total Ionic Conductivity*
Inorg. Chem., **61** 4655–4659 (2022).

60 Y. Yasuda, F. Nabeshima, K. Horiuchi, H. Nagai
Visualization of the Working Fluid in a Flat-Plate Pulsating Heat Pipe by Neutron Radiography
Int. J. Heat Mass Transf., **185** 122336 (2022).

61 D. Wei, W. Gong, T. Tsuru, T. Kawasaki, S. Harjo, B. Cai, P. K. Liaw, H. Kato
Mechanical Behaviors of Equiatomic and Near-Equiatomic Face-Centered-Cubic Phase High-Entropy Alloys Probed Using in situ Neutron Diffraction
Int. J. Plast., **158** 103417 (2022).

62 D. Wei, W. Gong, T. Tsuru, I. Lobzenko, X. Li, S. Harjo, T. Kawasaki, H.-S. Do, J. W. Bae, C. Wagner, G. Laplanche, Y. Koizumi, H. Adachi, K. Aoyagi, A. Chiba, B.-J. Lee, H. S. Kim, H. Kato
Si-Addition Contributes to Overcoming the Strength-Ductility Trade-off in High-Entropy Alloys
Int. J. Plast., **159** 103443 (2022).

63 S. Yoshida, R. Fu, W. Gong, T. Ikeuchi, Y. Bai, Z. Feng, G. Wu, A. Shibata, N. Hansen, X. Huang, N. Tsuji
Grain Orientation Dependence of Deformation Microstructure Evolution and Mechanical Properties in Face-Centered Cubic High/Medium Entropy Alloys
IOP Conf. Ser. Mater. Sci. Eng., **1249** 012027 (2022).

64 Y. Oba, S. Morooka, K. Ohishi, J. Suzuki, T. Tsuchiyama
Characterization of Deformation by Cold Rolling in Ferritic Steel Containing Cu Particles Using Neutron Transmission Analysis
ISIJ Int., **62** 173–178 (2022).

65 H. Uchima, M. Kumagai, J. Shimbe, A. Tanabe, Y. Mizuno, Y. Onuki
Impact of Dislocation Density and Mobility on Yielding Behavior in Quenched Medium-Carbon Martensitic Steel Tempered at Low Temperature
ISIJ Int., **62** 998–1003 (2022).

66 S. Harjo, W. Gong, T. Kawasaki, S. Morooka, T. Yamashita
Revisit Deformation Behavior of Lath Martensite
ISIJ Int., **62** 1990–1999 (2022).

67 M. Koyama, T. Yamashita, S. Morooka, T. Sawaguchi, Z. Yang, T. Hojo, T. Kawasaki, S. Harjo
Microstructure and Plasticity Evolution During Lüders Deformation in an Fe-5Mn-0.1C Medium-Mn Steel
ISIJ Int., **62** 2036–2042 (2022).

68 M. Koyama, T. Yamashita, S. Morooka, Z. Yang, R. S. Varanasi, T. Hojo, T. Kawasaki, S. Harjo
Hierarchical Deformation Heterogeneity during Lüders Band Propagation in an Fe-5Mn-0.1C Medium Mn Steel Clarified through in situ *Scanning Electron Microscopy*
ISIJ Int., **62** 2043–2053 (2022).

69 H. Sato, A. Kusumi, Y. Shiota, H. Hayashida, Y. Su, J. Don Parker, K. Watanabe, T. Kamiyama, Y. Kiyanagi
Visualising Martensite Phase Fraction in Bulk Ferrite Steel by Superimposed Bragg-Edge Profile Analysis of Wavelength-Resolved Neutron Transmission Imaging
ISIJ Int., **62** 2319–2330 (2022).

70 T. Murakawa, K. Kurihara, M. Adachi, K. Kusaka, K. Tanizawa, T. Okajima
Re-Evaluation of Protein Neutron Crystallography with and without X-Ray/Neutron Joint Refinement
IUCrJ, **9** 342–348 (2022).

71 S. Sasada, Y. Takahashi, K. Takeuchi, K. Hiroi, Y. Su, T. Shinohara, K. Watanabe, A. Uritani
Strain Distribution Visualization of Punched Electrical Steel Sheets Using Neutron Bragg-Edge Transmission Imaging
Jpn. J. Appl. Phys., **61** 046004 (2022).

72 Z. Deng, Q. Li, Y. Onuki, Q. Sun
Multifunctional Nanostructured NiTi Alloy with Invar, Elinvar and Rinvar Properties
J. Alloys Compd., **909** 164682 (2022).

73 D. Yun, H. Chae, T. Lee, D.-H. Lee, H. J. Ryu, R. Banerjee, S. Harjo, T. Kawasaki, S. Y. Lee
Stress Contribution of B2 Phase in $Al_{0.7}$*CoCrFeNi Eutectic High Entropy Alloy*

J. Alloys Compd., **918** 165673 (2022).

74 F. Malamud, J. R. Santisteban, Y. Gao, T. Shinohara, K. Oikawa, A. Tremsin
Non-Destructive Characterization of the Spatial Variation of γ/γ′ Lattice Misfit in a Single-Crystal Ni-Based Superalloy by Energy-Resolved Neutron Imaging
J. Appl. Crystallogr., **55** 228–239 (2022).

75 K. Tatsumi, Y. Inamura, M. Kofu, R. Kiyanagi, H. Shimazaki
Optimization and Inference of Bin Widths for Histogramming Inelastic Neutron Scattering Spectra
J. Appl. Crystallogr., **55** 533–543 (2022).

76 T. Kumada, D. Miura, K. Akutsu-Suyama, K. Ohishi, T. Morikawa, Y. Kawamura, J. Suzuki, T. Oku, N. Torikai, T. Niizeki
Structure Analysis of a Buried Interface between Organic and Porous Inorganic Layers Using Spin-Contrast-Variation Neutron Reflectivity
J. Appl. Crystallogr., **55** 1147–1153 (2022).

77 K. Ikeda, H. Ohshita, T. Otomo, K. Sakaki, H. Kim, Y. Nakamura, A. Machida, R. B. Von Dreele
Pressure Cells for in situ Neutron Total Scattering: Time and Real-Space Resolution during Deuterium Absorption
J. Appl. Crystallogr., **55** 1631–1639 (2022).

78 T. Kawasaki, T. Fukuda, S. Yamanaka, T. Sakamoto, I. Murayama, T. Katou, M. Baba, H. Hashimoto, S. Harjo, K. Aizawa, H. Tanaka, M. Takeda, T. Sekino, T. Nakayama, Y. Kim
Operando Structure Observation of Pyroelectric Ceramics during Power Generation Cycle
J. Appl. Phys., **131** 134103 (2022).

79 M. Hiraishi, H. Okabe, A. Koda, R. Kadono, H. Hosono
Ambipolarity of Diluted Hydrogen in Wide-Gap Oxides Revealed by Muon Study
J. Appl. Phys., **132** 105701 (2022).

80 Y. Sakuda, J. R. Hester, M. Yashima
Improved Oxide-Ion and Lower Proton Conduction of Hexagonal Perovskite-Related Oxides Based on $Ba_7Nb_4MoO_{20}$ by Cr^{6+} Doping
J. Ceram. Soc. Jpn., **130** 442-447 (2022).

81 Y. Mitsuya, K. Shimazoe, T. Fujiwara, H. Takahashi
Energy-Resolved Neutron Imaging with Glass Gas Electron Multiplier and Dynamic Time-over-Threshold Method
J. Instrum., **17** C01006 (2022).

82 N. Muto, H. Abele, T. Ariga, J. Bosina, M. Hino, K. Hirota, G. Ichikawa, T. Jenke, H. Kawahara, S. Kawasaki, M. Kitaguchi, J. Micko, K. Mishima, N. Naganawa, M. Nakamura, S. Roccia, O. Sato, R. I. P. Sedmik, Y. Seki, H. M. Shimizu, S. Tada, A. Umemoto
A Novel Nuclear Emulsion Detector for Measurement of Quantum States of Ultracold Neutrons in the Earth's Gravitational Field
J. Instrum., **17** P07014 (2022).

83 W. Gong, R. Zheng, S. Harjo, T. Kawasaki, K. Aizawa, N. Tsuji
In-situ Observation of Twinning and Detwinning in AZ31 Alloy
J. Magnes. Alloys, **10** 3418–3432 (2022).

84 K. Okamoto, F. Takeiri, Y. Imai, M. Yonemura, T. Saito, K. Ikeda, T. Otomo, T. Kamiyama, G. Kobayashi
Stabilization of a High H^--Conducting Phase via *K Doping of Ba–Li Oxyhydride*
J. Mater. Chem. A, **10** 23023–23027 (2022).

85 J. Yang, W. Ren, X. Zhao, T. Kikuchi, P. Miao, K. Nakajima, B. Li, Z. Zhang
Mictomagnetism and Suppressed Thermal Conduction of the Prototype High-Entropy Alloy CrMnFeCoNi
J. Mater. Sci. Technol., **99** 55–60 (2022).

86 D. Wei, W. Gong, L. Wang, B. Tang, T. Kawasaki, S. Harjo, H. Kato
Strengthening of High-Entropy Alloys via Modulation of Cryo-Pre-Straining-Induced Defects
J. Mater. Sci. Technol., **129** 251–260 (2022).

87 H. Abe, F. Nemoto, K. Hiroi, K. Ohishi, S. Takata
Spontaneous Formations of Nanoconfined Water in Ionic Liquids by Small-Angle Neutron Scattering
J. Mol. Liq., **346** 117035 (2022).

88 W. Q. Zhang, T. Yamaguchi, C. H. Fang, K. Yoshida, Y. Q. Zhou, F. Y. Zhu, S. Machida, T. Hattori, W. Li
Structure of an Aqueous RbCl Solution in the Gigapascal Pressure Range by Neutron Diffraction Combined with Empirical Potential Structure Refinement Modeling
J. Mol. Liq., **348** 118080 (2022).

89 T. Yamaguchi, K. Yoshida, S. Machida, T. Hattori
Neutron Scattering on an Aqueous Sodium Chloride Solution in the Gigapascal Pressure Range
J. Mol. Liq., **365** 120181 (2022).

90 K. Yoshida, Y. Sanada, T. Yamaguchi, M. Matsuura, H. Tamatsukuri, H. Uchiyama
The Translational, Rotational, and Phonon Dynamics of Water in ZrO_2 /Water Nanofluid
J. Mol. Liq., **366** 120218 (2022).

91 S. Sato, R. Kajimoto, Y. Inamura
Development of a Pulse-Width-Discriminating ^{3}He Position-Sensitive Detector System
J. Neutron Res., **24** 427–434 (2022).

92 R. Motokawa, K. Kaneko, Y. Oba, T. Nagai, Y. Okamoto, T. Kobayashi, T. Kumada, W. T. Heller
Nanoscopic Structure of Borosilicate Glass with Additives for Nuclear Waste Vitrification
J. Non-Cryst. Solids, **578** 121352 (2022).

93 D. Ito, H. Sato, N. Odaira, Y. Saito, J. D. Parker, T. Shinohara, T. Kai, K. Oikawa
Spatial Distribution and Preferred Orientation of Crystalline Microstructure of Lead-Bismuth Eutectic
J. Nucl. Mater., **569** 153921 (2022).

94 G. Rovira, T. Katabuchi, K. Tosaka, S. Matsuura, Y. Kodama, H. Nakano, O. Iwamoto, A. Kimura, S. Nakamura, N. Iwamoto
KeV-Region Analysis of the Neutron Capture Cross-Section of ^{237}Np
J. Nucl. Sci. Technol., **59** 110–122 (2022).

95 S. Endo, A. Kimura, S. Nakamura, O. Iwamoto, N. Iwamoto, G. Rovira, K. Terada, S. Meigo, Y. Toh, M. Segawa, M. Maeda, M. Tsuneyama
Neutron Capture and Total Cross-Section Measurements and Resonance Parameter Analysis of Niobium-93 below 400 EV
J. Nucl. Sci. Technol., **59** 318–333 (2022).

96 G. Rovira, A. Kimura, S. Nakamura, S. Endo, O. Iwamoto, N. Iwamoto, T. Katabuchi, Y. Kodama, H. Nakano, Y. Sato, J. Hori, Y. Shibahara, K. Terada
KeV-neutron capture cross-section measurement of ^{197}Au with a Cr-filtered neutron beam at the ANNRI beamline of MLF/J-PARC
J. Nucl. Sci. Technol., **59** 647-655 (2022).

97 H. Nakano, T. Katabuchi, G. Rovira, Y. Kodama, K. Terada, A. Kimura, S. Nakamura, S. Endo
Development of a neutron beam monitor with a thin plastic scintillator for nuclear data measurement using spallation neutron source
J. Nucl. Sci. Technol., **59** 1499-1506 (2022).

98 G. Rovira, A. Kimura, S. Nakamura, S. Endo, O. Iwamoto, N.

Iwamoto, T. Katabuchi, Y. Kodama, H. Nakano
^{241}Am Neutron Capture Cross Section in the KeV Region Using Si and Fe-Filtered Neutron Beams
J. Nucl. Sci. Technol., **60** 489–499 (2022).

99 A. Kimura, S. Nakamura, S. Endo, G. Rovira, O. Iwamoto, N. Iwamoto, H. Harada, T. Katabuchi, K. Terada, J. Hori, Y. Shibahara, T. Fujii
Neutron Total and Capture Cross-Section Measurements of ^{155}Gd and ^{157}Gd in the Thermal Energy Region with the Li-Glass Detectors and NaI(Tl) Spectrometer Installed in J-PARC·MLF·ANNRI
J. Nucl. Sci. Technol., **60** 678–696 (2022).

100 M. Uyama, A. Takahara, Y. Higaki, N. L. Yamada, H. Iwase
Neutron Reflectometry & Simultaneous Measurements of Rheology and Small Angle Neutron Scattering Studies for Polyether Modified Silicone Vesicle Systems
J. Oleo Sci., **71** 1625–1637 (2022).

101 S. Shimono, H. Ishibashi, Y. Nagayoshi, H. Ikeno, S. Kawaguchi, M. Hagihala, S. Torii, T. Kamiyama, K. Ichihashi, S. Nishihara, K. Inoue, Y. Ishii, Y. Kubota
Structural Phase Transition in Cobalt Oxyfluoride $Co_3Sb_4O_6F_6$ Observed by High-Resolution Synchrotron and Neutron Diffraction
J. Phys. Chem. Solids, **163** 110568 (2022).

102 T. Yamanaka, S. Rahman, Y. Nakamoto, T. Hattori, B. G. Jang, D. Y. Kim, H. Mao
Enhancement of Electrical Conductivity to Metallization of $Mn_{3-x}Fe_xO_4$ Spinel and Postspinel with Elevating Pressure
J. Phys. Chem. Solids, **167** 110721 (2022).

103 C. Kim, J. Jeong, G. Lin, P. Park, T. Masuda, S. Asai, S. Itoh, H.-S. Kim, H. Zhou, J. Ma, J.-G. Park
Antiferromagnetic Kitaev Interaction in J_{eff} = 1/2 Cobalt Honeycomb Materials $Na_3Co_2SbO_6$ and $Na_2Co_2TeO_6$
J. Phys. Condens. Matter, **34** 045802 (2022).

104 K. Kataoka, D. Hirai, A. Koda, R. Kadono, T. Honda, Z. Hiroi
Pyrochlore Oxide $Hg_2Os_2O_7$ on Verge of Metal–Insulator Boundary
J. Phys. Condens. Matter, **34** 135602 (2022).

105 T. Xie, C. Liu, R. Kajimoto, K. Ikeuchi, S. Li, H. Luo
Spin Fluctuations in the 112-Type Iron-Based Superconductor $Ca_{0.82}La_{0.18}Fe_{0.96}Ni_{0.04}As_2$
J. Phys. Condens. Matter, **34** 474001 (2022).

106 T. D. Vu, H. Shishido, K. Aizawa, T. Oku, K. Oikawa, M. Harada, K. M. Kojima, S. Miyajima, K. Soyama, T. Koyama, M. Hidaka, S. Y. Suzuki, M. M. Tanaka, A. Malins, M. Machida, T. Ishida
Narrow-Area Bragg-Edge Transmission of Iron Samples Using Superconducting Neutron Sensor
J. Phys. Conf. Ser., **2323** 012028 (2022).

107 H. Shishido, T. D. Vu, K. Aizawa, K. M. Kojima, T. Koyama, K. Oikawa, M. Harada, T. Oku, K. Soyama, S. Miyajima, M. Hidaka, S. Y. Suzuki, M. M. Tanaka, S. Kawamata, T. Ishida
Neutron Imaging toward Epithermal Regime Using a Delay Line Current-Biased Kinetic-Inductance Detector
J. Phys. Conf. Ser., **2323** 012029 (2022).

108 M. Nasu, H. Yanai, N. Hirayama, H. Adachi, Y. Kakizawa, Y. Shirase, H. Nishiyama, T. Kawamoto, J. Inukai, T. Shinohara, H. Hayashida, M. Watanabe
Neutron Imaging of Generated Water inside Polymer Electrolyte Fuel Cell Using Newly-Developed Gas Diffusion Layer with Gas Flow Channels during Power Generation
J. Power Sources, **530** 231251 (2022).

109 M. Kitaguchi
T-violation in neutron scattering
JPS Conf. Proc., **37** 011010 (2022).

110 H. Akatsuka, T. Higuchi, S. Hansen-Romu, K. Hatanaka, T. Hayamizu, M. Hino, G. Ichikawa, S. Imajo, B. Jamieson, S. Kawasaki, M. Kitaguchi, R. Matsumiya, K. Mishima
Study of Thin Iron Films for Polarization Analysis of Ultracold Neutrons
JPS Conf. Proc., **37** 020801 (2022).

111 T. Ino, S. Fukumura, P. Strasser, M. Fujita, Y. Ikeda, S. Kanda, M. Kitaguchi, S. Nishimura, T. Oku, T. Okudaira, H. M. Shimizu, K. Shimomura
Optically Polarized Alkali Metal Cell for Muonic Helium Measurements
JPS Conf. Proc., **37** 021208 (2022).

112 K. Saito, K. Fujii, M. Yashima
Oxide-Ion and Proton Conductivity of the Ordered Perovskite $BaY_{1/3}Ga_{2/3}O_{2.5}$
J. Solid State Chem., **306** 122733 (2022).

113 K. Fukui, S. Iimura, A. Iskandarov, T. Tada, H. Hosono
Room-Temperature Fast H^- Conduction in Oxygen-Substituted Lanthanum Hydride
J. Am. Chem. Soc., **144** 1523–1527 (2022).

114 K. Kakimoto, S. Takada, H. Ohta, Y. Haraguchi, M. Hagihala, S. Torii, T. Kamiyama, H. Mitamura, M. Tokunaga, A. Hatakeyama, H. A. Katori
Magnetism of $Al_xFe_{2-x}GeO_5$ with Andalusite Structure
J. Phys. Soc. Jpn., **91** 054704 (2022).

115 K. Kakimoto, H. Ohta, Y. Haraguchi, M. Hagihala, S. Torii, T. Kamiyama, H. A. Katori
Sinusoidal Magnetic Structure of Andalusite-Type $Al_x Fe_{2-x}GeO_5$ with x = 0.09 and 0.1
J. Phys. Soc. Jpn., **91** 054707 (2022).

116 N. Metoki, K. Shibata, M. Matsuura, H. Kitazawa, H. S. Suzuki, H. Yamauchi, M. Hagihala, M. D. Frontzek, M. Matsuda
Hyperfine Splitting and Nuclear Spin Polarization in $NdPd_5Al_2$ and $Nd_3Pd_{20}Ge_6$
J. Phys. Soc. Jpn., **91** 054710 (2022).

117 T. Matsumura, M. Tsukagoshi, Y. Ueda, N. Higa, A. Nakao, K. Kaneko, M. Kakihana, M. Hedo, T. Nakama, Y. Ōnuki
Cycloidal Magnetic Ordering in Noncentrosymmetric $EuIrGe_3$
J. Phys. Soc. Jpn., **91** 073703 (2022).

118 D. Ueta, R. Kobayashi, H. Sawada, Y. Iwata, S. Yano, S. Kuniyoshi, Y. Fujisawa, T. Masuda, Y. Okada, S. Itoh
Anomalous Magnetic Moment Direction under Magnetic Anisotropy Originated from Crystalline Electric Field in van Der Waals Compounds $CeTe_3$ and $CeTe_2Se$
J. Phys. Soc. Jpn., **91** 094706 (2022).

119 M. Soda, M. Kofu, S. Ohira-Kawamura, S. Asai, T. Masuda, H. Yoshizawa, H. Kawano-Furukawa
Magnetic Diffuse and Quasi-Elastic Scatterings in Frustrated Magnet $YBaCo_4O_7$
J. Phys. Soc. Jpn., **91** 094707 (2022).

120 K. Yamaoka, N. L. Yamada, K. Hori, Y. Fujii, N. Torikai
Interfacial Selective Study on the Gelation Behavior of Aqueous Methylcellulose Solution via a Quartz Crystal Microbalance
Langmuir, **38** 4494–4502 (2022).

121 D. Ihara, Y. Higaki, N. L. Yamada, F. Nemoto, Y. Matsuda, K. Kojio, A. Takahara
Cononsolvency of Poly[2-(methacryloyloxy)ethyl phosphorylcholine] in Ethanol–Water Mixtures: A Neutron Reflectivity Study
Langmuir, **38** 5081–5088 (2022).

122 Y. Xie, J. Iwata, T. Matsumoto, N. L. Yamada, F. Nemoto, H. Seto, T. Nishino
Hydrophobicity of the Pentafluorosulfanyl Group in Side Chains of Polymethacrylates by Evaluation with Surface Free Energy and Neutron Reflectivity
Langmuir, **38** 6472–6480 (2022).

123 Y. Higaki, R. Furusawa, T. Otsu, N. L. Yamada
Zwitterionic Poly(carboxybetaine) Brush/Albumin Conjugate Films: Structure and Lubricity
Langmuir, **38** 9278–9284 (2022).

124 K. Shimokita, K. Yamamoto, N. Miyata, H. Arima-Osonoi, Y. Nakanishi, M. Takenaka, M. Shibata, N. L. Yamada, H. Seto, H. Aoki, T. Miyazaki
Neutron Reflectivity Study on the Suppression of Interfacial Water Accumulation between a Polypropylene Thin Film and Si Substrate Using a Silane-Coupling Agent
Langmuir, **38** 12457–12465 (2022).

125 T. Tominaga, H. Nakagawa, M. Sahara, T. Oda, R. Inoue, M. Sugiyama
Data Collection for Dilute Protein Solutions via a Neutron Backscattering Spectrometer
Life, **12** 675 (2022).

126 S. Imai, M. Arakawa, Y. Nakanishi, M. Takenaka, H. Aoki, M. Ouchi, T. Terashima
Water-Assisted Microphase Separation of Cationic Random Copolymers into Sub-5 Nm Lamellar Materials and Thin Films
Macromolecules, **55** 9113–9125 (2022).

127 N. R. Jaladurgam, A. Lozinko, S. Guo, S. Harjo, M. H. Colliander
Load Redistribution in Eutectic High Entropy Alloy $AlCoCrFeNi_{2.1}$ during High Temperature Deformation
Materialia, **22** 101392 (2022).

128 Y. Wang, Y. Tomota, T. Ohmura, W. Gong, S. Harjo
Evolution of Austenite Lattice Parameter during Isothermal Transformation in a 0.4 C Low Alloyed Steel
Materialia, **27** 101685 (2022).

129 M. Kumagai, M. Kuroda, T. Matsuno, S. Harjo, K. Akita
In situ Neutron Diffraction Analysis of Microstructural Evolution-Dependent Stress Response in Austenitic Stainless Steel under Cyclic Plastic Deformation
Mater. Des., **221** 110965 (2022).

130 K. S. N. Sesha, K. Yamanaka, M. Mori, Y. Onuki, S. Sato, D. Fabrègue, A. Chiba
Demonstrating a Duplex TRIP/TWIP Titanium Alloy via the Introduction of Metastable Retained β-Phase
Mater. Res. Lett., **10** 754–761 (2022).

131 H. Dannoshita, H. Hasegawa, S. Higuchi, H. Matsuda, W. Gong, T. Kawasaki, S. Harjo, O. Umezawa
Evolution of Dislocation Structure Determined by Neutron Diffraction Line Profile Analysis during Tensile Deformation in Quenched and Tempered Martensitic Steels
Mater. Sci. Eng. A, **854** 143795 (2022).

132 P. Thirathipviwat, S. Nozawa, M. Furusawa, Y. Onuki, M. Hasegawa, K. Matsumoto, S. Sato
In-situ Neutron Diffraction Study on a Dislocation Density in a Correlation with Strain Hardening in Al–Mg Alloys
Mater. Sci. Eng. A, **855** 143956 (2022).

133 T.-N. Lam, A. Lee, Y.-R. Chiu, H.-F. Kuo, T. Kawasaki, S. Harjo, J. Jain, S. Y. Lee, E.-W. Huang
Estimating Fine Melt Pool, Coarse Melt Pool, and Heat Affected Zone Effects on the Strengths of Additive Manufactured AlSi10Mg Alloys
Mater. Sci. Eng. A, **856** 143961 (2022).

134 D. Egusa, R. Manabe, T. Kawasaki, S. Harjo, S. Sato, E. Abe
Quantitative X-Ray Diffraction Analysis of Solute-Enriched Stacking Faults in Hcp-Mg Alloys Based on Peak Asymmetry Analysis
Mater. Today Commun., **31** 103344 (2022).

135 R. Miyazaki, K. Ikeda, N. Kitamura, Y. Takabayashi, K. Kimura, K. Hayashi, T. Hihara
Reverse Monte Carlo Analysis of NaI-LiI Solid Electrolyte Based on the Neutron Total Scattering Data
Mater. Today Commun., **32** 104014 (2022).

136 S. M. Suturin, P. A. Dvortsova, L. A. Snigirev, V. A. Ukleev, T. Hanashima, M. Rosado, B. Ballesteros
Structural Peculiarities of ε-Fe_2O_3/GaN Epitaxial Layers Unveiled by High-Resolution Transmission Electron Microscopy and Neutron Reflectometry
Mater. Today Commun., **33** 104412 (2022).

137 E. Rathore, R. Juneja, D. Sarkar, S. Roychowdhury, M. Kofu, K. Nakajima, A. K. Singh, K. Biswas
Enhanced Covalency and Nanostructured-Phonon Scattering Lead to High Thermoelectric Performance in n-Type PbS
Mater. Today Energy, **24** 100953 (2022).

138 H. Sasaki, S. Akiya, Y. Oba, M. Onuma, A. D. Giddings, T. Ohkubo
Characterization of Precipitated Phase in Cu–Ni–Si Alloy by Small-Angle X-Ray Scattering, Small Angle Neutron Scattering and Atom Probe Tomography
Mater. Trans., **63** 1384–1389 (2022).

139 T. Yamada
Quasi Elastic Neutron Scattering Study on Water Dynamics in Nafion Membrane
MEMBRANE, **47** 207–212 (2022).

140 M.-M. Schiavone, Y. Zhao, H. Iwase, H. Arima-Osonoi, S. Takata, A. Radulescu
On the Proton Conduction Pathways in Polyelectrolyte Membranes Based on Syndiotactic-Polystyrene
Membranes, **12** 143 (2022).

141 Y. Onuki, K. Umemura, K. Fujiwara, Y. Tanaka, T. Tomida, K. Kawano, S. Sato
Microstructure Formation and Carbon Partitioning with Austenite Decomposition during Isothermal Heating Process in Fe-Si-Mn-C Steel Monitored by in situ Time-of-Flight Neutron Diffraction
Metals, **12** 957 (2022).

142 K. Yamanaka, M. Mori, Y. Onuki, S. Sato, A. Chiba
Dislocation Density of Electron Beam Powder Bed Fusion Ti–6Al–4V Alloys Determined via Time-Of-Flight Neutron Diffraction Line-Profile Analysis
Metals, **13** 86 (2022).

143 Q. Li, J. Sun, Y. Zhang, T. Li, H. Liu, Y. Cao, Q. Zhang, L. Gu, T. Honda, K. Ikeda, T. Otomo, K. Lin, J. Deng, X. Xing
Ferroelectric Ordering in Nanosized $PbTiO_3$
Nano Lett., **22** 9405–9410 (2022).

144 R. Takagi, N. Matsuyama, V. Ukleev, L. Yu, J. S. White, S. Francoual, J. R. L. Mardegan, S. Hayami, H. Saito, K. Kaneko, K. Ohishi, Y. Ōnuki, T. Arima, Y. Tokura, T. Nakajima, S. Seki
Square and Rhombic Lattices of Magnetic Skyrmions in a Centrosymmetric Binary Compound
Nat. Commun., **13** 1472 (2022).

145 P. Luo, Y. Zhai, P. Falus, V. García Sakai, M. Hartl, M. Kofu, K. Nakajima, A. Faraone, Y. Z
Q-Dependent Collective Relaxation Dynamics of Glass-Forming Liquid $Ca_{0.4}K_{0.6}(NO_3)_{1.4}$ Investigated by Wide-Angle Neutron Spin-Echo
Nat. Commun., **13** 2092 (2022).

146 Y. Yu, C. Yang, M. Baggioli, A. E. Phillips, A. Zaccone, L. Zhang, R. Kajimoto, M. Nakamura, D. Yu, L. Hong
The ω^3 Scaling of the Vibrational Density of States in Quasi-2D Nanoconfined Solids
Nat. Commun., **13** 3649 (2022).

147 L. Chen, C. Mao, J.-H. Chung, M. B. Stone, A. I. Kolesnikov, X. Wang, N. Murai, B. Gao, O. Delaire, P. Dai
Anisotropic Magnon Damping by Zero-Temperature Quantum Fluctuations in Ferromagnetic $CrGeTe_3$
Nat. Commun., **13** 4037 (2022).

148 S. Xu, T. Odaira, S. Sato, X. Xu, T. Omori, S. Harjo, T. Kawasaki, H. Seiner, K. Zoubková, Y. Murakami, R. Kainuma
Non-Hookean Large Elastic Deformation in Bulk Crystalline Metals
Nat. Commun., **13** 5307 (2022).

149 F. Takeiri, A. Watanabe, K. Okamoto, D. Bresser, S. Lyonnard, B. Frick, A. Ali, Y. Imai, M. Nishikawa, M. Yonemura, T. Saito, K. Ikeda, T. Otomo, T. Kamiyama, R. Kanno, G. Kobayashi
Hydride-Ion-Conducting K_2NiF_4-Type Ba–Li Oxyhydride Solid Electrolyte
Nat. Mater., **21** 325–330 (2022).

150 A. D. Hillier, S. J. Blundell, I. McKenzie, I. Umegaki, L. Shu, J. A. Wright, T. Prokscha, F. Bert, K. Shimomura, A. Berlie, H. Alberto, I. Watanabe
Muon Spin Spectroscopy
Nat. Rev. Methods Primer, **2** 4 (2022).

151 K. Horie, K. Kamada, A. Kobayashi, M. Mihara, S. Shimizu, A. Yamaji, A. Yoshikawa
Measurement of Residual μ^+ Polarization in Various Scintillating Materials to Search for T-Violating μ^+ Polarization in $K^+ \rightarrow \pi^0\mu^+\nu$ Decay
Nucl. Instrum. Methods Phys. Res. Sect. Accel. Spectrometers Detect. Assoc. Equip., **1037** 166932 (2022).

152 F. Nemoto, N. L. Yamada, S. Satoh
Performance of Position-Sensitive Flat-Panel and Resister Type Photomultiplier Tube Detector on Neutron Reflectometer SOFIA at J-PARC
Nucl. Instrum. Methods Phys. Res. Sect. Accel. Spectrometers Detect. Assoc. Equip., **1040** 166988 (2022).

153 K. Isegawa, D. Setoyama, Y. Higuchi, Y. Matsumoto, Y. Nagai, T. Shinohara
Fast Phase Differentiation between Liquid–Water and Ice by Pulsed Neutron Imaging with Gated Image Intensifier
Nucl. Instrum. Methods Phys. Res. Sect. Accel. Spectrometers Detect. Assoc. Equip., **1040** 167260 (2022).

154 M. Kawano, A. Tashiro, Y. Imamura, M. Yamada, K. Sadakane, H. Iwase, M. Matsugami, B. A. Marekha, A. Idrissi, T. Takamuku
Effects of Self-Hydrogen Bonding among Formamide Molecules on the UCST-Type Liquid–Liquid Phase Separation of Binary Solutions with Imidazolium-Based Ionic Liquid, $[C_nMim][TFSI]$, Studied by NMR, IR, MD Simulations, and SANS
Phys. Chem. Chem. Phys., **24** 13698–13712 (2022).

155 K. Yamaguchi, D. Kawaguchi, N. Miyata, T. Miyazaki, H. Aoki, S. Yamamoto, K. Tanaka
Kinetics of the Interfacial Curing Reaction for an Epoxy–Amine Mixture
Phys. Chem. Chem. Phys., **24** 21578–21582 (2022).

156 H. Kadowaki, M. Wakita, B. Fåk, J. Ollivier, S. Ohira-Kawamura
Spin and Quadrupole Correlations by Three-Spin Interaction in the Frustrated Pyrochlore Magnet $Tb_{2+x}Ti_{2-x}O_{7+y}$
Phys. Rev. B, **105** 014439 (2022).

157 K. Ikeuchi, S. Wakimoto, M. Fujita, T. Fukuda, R. Kajimoto, M. Arai
Spin Excitations Coupled with Lattice and Charge Dynamics in $La_{2-x}Sr_xCuO_4$
Phys. Rev. B, **105** 014508 (2022).

158 Y. Kojima, N. Kurita, H. Tanaka, K. Nakajima
Magnons and Spinons in Ba_2CoTeO_6: A Composite System of Isolated Spin-1/2 Triangular Heisenberg-like and Frustrated Honeycomb Ising-like Antiferromagnets
Phys. Rev. B, **105** L020408 (2022).

159 Y. Imai, K. Nawa, Y. Shimizu, W. Yamada, H. Fujihara, T. Aoyama, R. Takahashi, D. Okuyama, T. Ohashi, M. Hagihala, S. Torii, D. Morikawa, M. Terauchi, T. Kawamata, M. Kato, H. Gotou, M. Itoh, T. J. Sato, K. Ohgushi
Zigzag Magnetic Order in the Kitaev Spin-Liquid Candidate Material $RuBr_3$ with a Honeycomb Lattice
Phys. Rev. B, **105** L041112 (2022).

160 M. Watanabe, N. Kurita, H. Tanaka, W. Ueno, K. Matsui, T. Goto, M. Hagihala
Contrasting Magnetic Structures in $SrLaCuSbO_6$ and $SrLaCuNbO_6$: Spin- 1/2 Quasi-Square-Lattice J_1–J_2 Heisenberg Antiferromagnets
Phys. Rev. B, **105** 054414 (2022).

161 M. Saito, R. Takagishi, N. Kurita, M. Watanabe, H. Tanaka, R. Nomura, Y. Fukumoto, K. Ikeuchi, R. Kajimoto
Structures of Magnetic Excitations in the Spin- 1/2 Kagome-Lattice Antiferromagnets $Cs_2Cu_3SnF_{12}$ and $Rb_2Cu_3SnF_{12}$
Phys. Rev. B, **105** 064424 (2022).

162 K. Matan, T. Ono, S. Ohira-Kawamura, K. Nakajima, Y. Nambu, T. J. Sato
Breakdown of Linear Spin-wave Theory and Existence of Spinon Bound States in the Frustrated Kagome-Lattice Antiferromagnet
Phys. Rev. B, **105** 134403 (2022).

163 M. Fujihala, Y. Sakuma, S. Mitsuda, A. Nakao, K. Munakata, R. A. Mole, S. Yano, D. H. Yu, K. Takehana, Y. Imanaka, M. Akaki, S. Okubo, H. Ohta
Relief of Spin Frustration through Magnetic Anisotropy in the Quasi-One-Dimensional S = 1/2 Antiferromagnet $Na_2CuSO_4Cl_2$
Phys. Rev. B, **105** 144410 (2022).

164 S.-H. Do, K. Kaneko, R. Kajimoto, K. Kamazawa, M. B. Stone, J. Y. Y. Lin, S. Itoh, T. Masuda, G. D. Samolyuk, E. Dagotto, W. R. Meier, B. C. Sales, H. Miao, A. D. Christianson
Damped Dirac Magnon in the Metallic Kagome Antiferromagnet FeSn
Phys. Rev. B, **105** L180403 (2022).

165 M. Micoulaut, I. Pethes, P. Jóvári, L. Pusztai, M. Krbal, T. Wágner, V. Prokop, Š. Michalik, K. Ikeda, I. Kaban
Structural Properties of Chalcogenide Glasses and the Isocoordination Rule: Disentangling Effects from Chemistry and Network Topology
Phys. Rev. B, **106** 014206 (2022).

166 K. Tomiyasu, Y. P. Mizuta, M. Matsuura, K. Aoyama, H. Kawamura
Observation of Topological Z_2 Vortex Fluctuations in the Frustrated Heisenberg Magnet $NaCrO_2$
Phys. Rev. B, **106** 054407 (2022).

167 R. Tripathi, D. T. Adroja, C. Ritter, S. Sharma, C. Yang, A. D. Hillier, M. M. Koza, F. Demmel, A. Sundaresan, S. Langridge, W. Higemoto, T. U. Ito, A. M. Strydom, G. B. G. Stenning, A. Bhattacharyya, D. Keen, H. C. Walker, R. S. Perry, F. Pratt, Q. Si, T. Takabatake
Quantum Critical Spin-Liquid-like Behavior in the S = 1/2 Quasikagome-Lattice Compound $CeRh_{1-x}Pd_xSn$ Investigated Using Muon Spin Relaxation and Neutron Scattering
Phys. Rev. B, **106** 064436 (2022).

168 B. Gao, T. Chen, H. Yan, C. Duan, C.-L. Huang, X. P. Yao, F. Ye, C. Balz,

J. R. Stewart, K. Nakajima, S. Ohira-Kawamura, G. Xu, X. Xu, S.-W. Cheong, E. Morosan, A. H. Nevidomskyy, G. Chen, P. Dai
Magnetic Field Effects in an Octupolar Quantum Spin Liquid Candidate
Phys. Rev. B, **106** 094425 (2022).

169 Y. Ishii, A. Yamamoto, N. Sato, Y. Nambu, S. Ohira-Kawamura, N. Murai, K. Ohara, S. Kawaguchi, T. Mori, S. Mori
Partial Breakdown of Translation Symmetry at a Structural Quantum Critical Point Associated with a Ferroelectric Soft Mode
Phys. Rev. B, **106** 134111 (2022).

170 T. Hattori, M. Nakamura, K. Iida, A. Machida, A. Sano-Furukawa, S. Machida, H. Arima, H. Ohshita, T. Honda, K. Ikeda, T. Otomo
Hydrogen Vibration Excitations of $ZrH_{1.8}$ and $TiH_{1.84}$ up to 21 GPa by Incoherent Inelastic Neutron Scattering
Phys. Rev. B, **106** 134309 (2022).

171 Z. Jin, B. Hu, Y. Liu, Y. Li, T. Zhang, K. Iida, K. Kamazawa, A. I. Kolesnikov, M. B. Stone, X. Zhang, H. Chen, Y. Wang, I. A. Zaliznyak, J. M. Tranquada, C. Fang, Y. Li
Chern Numbers of Topological Phonon Band Crossing Determined with Inelastic Neutron Scattering
Phys. Rev. B, **106** 224304 (2022).

172 M. Hiraishi, H. Okabe, A. Koda, R. Kadono, T. Ohsawa, N. Ohashi, K. Ide, T. Kamiya, H. Hosono
Local Electronic Structure of Dilute Hydrogen in β–Ga_2O_3 Probed by Muons
Phys. Rev. B, **107** L041201 (2022).

173 J. Koga, S. Takada, S. Endo, H. Fujioka, K. Hirota, K. Ishizaki, A. Kimura, M. Kitaguchi, Y. Niinomi, T. Okudaira, K. Sakai, T. Shima, H. M. Shimizu, Y. Tani, T. Yamamoto, H. Yoshikawa, T. Yoshioka
Angular Distribution of γ Rays from the p-Wave Resonance of ^{118}Sn
Phys. Rev. C, **105** 054615 (2022).

174 S. Endo, T. Okudaira, R. Abe, H. Fujioka, K. Hirota, A. Kimura, M. Kitaguchi, T. Oku, K. Sakai, T. Shima, H. M. Shimizu, S. Takada, S. Takahashi, T. Yamamoto, H. Yoshikawa, T. Yoshioka
Measurement of the Transverse Asymmetry of γ Rays in the $^{117}Sn(n,\gamma)^{118}Sn$ Reaction
Phys. Rev. C, **106** 064601 (2022).

175 S.-M. Chang, C. Y. Yu, Y.-F. Chen
Mechanism of Endosomal Escape by pH -Responsive Nucleic-Acid Vectors
Phys. Rev. E, **106** 034408 (2022).

176 W. Yao, K. Iida, K. Kamazawa, Y. Li
Excitations in the Ordered and Paramagnetic States of Honeycomb Magnet $Na_2Co_2TeO_6$
Phys. Rev. Lett., **129** 147202 (2022).

177 M. Fujihala, H. O. Jeschke, K. Morita, T. Kuwai, A. Koda, H. Okabe, A. Matsuo, K. Kindo, S. Mitsuda
Birchite $Cd_2Cu_2(PO_4)_2SO_4 \cdot 5H_2O$ as a Model Antiferromagnetic Spin-1/2 Heisenberg J_1–J_2 Chain
Phys. Rev. Mater., **6** 114408 (2022).

178 S. Shamoto, M. Akatsu, M. Matsuura, S. Ohira-Kawamura, K. Harii, M. Ono, L.-J. Chang, T. U. Ito, Y. Nemoto, J. Ieda
Magnetic Bragg Peak Enhancement under Ultrasound Injection
Phys. Rev. Res., **4** 013245 (2022).

179 Y. Ohmasa, S. Takagi, K. Toshima, K. Yokoyama, W. Endo, S. Orimo, H. Saitoh, T. Yamada, Y. Kawakita, K. Ikeda, T. Otomo, H. Akiba, O. Yamamuro
Rotation of Complex Ions with Ninefold Hydrogen Coordination Studied by Quasielastic Neutron Scattering and First-Principles Molecular Dynamics Calculations
Phys. Rev. Res., **4** 033215 (2022).

180 M. Matsuura, T. Sasaki, M. Naka, J. Müller, O. Stockert, A. Piovano, N. Yoneyama, M. Lang
Phonon Renormalization Effects Accompanying the 6 K Anomaly in the Quantum Spin Liquid Candidate K–(BEDT-TTF)$_2$Cu$_2$(CN)$_3$
Phys. Rev. Res., **4** L042047 (2022).

181 S. Bao, W. Wang, Y. Shangguan, Z. Cai, Z.-Y. Dong, Z. Huang, W. Si, Z. Ma, R. Kajimoto, K. Ikeuchi, S. Yano, S.-L. Yu, X. Wan, J.-X. Li, J. Wen
Neutron Spectroscopy Evidence on the Dual Nature of Magnetic Excitations in a van Der Waals Metallic Ferromagnet $Fe_{2.72}GeTe_2$
Phys. Rev. X, **12** 011022 (2022).

182 X. Li, Y. Gu, Y. Chen, V. O. Garlea, K. Iida, K. Kamazawa, Y. Li, G. Deng, Q. Xiao, X. Zheng, Z. Ye, Y. Peng, I. A. Zaliznyak, J. M. Tranquada, Y. Li
Giant Magnetic In-Plane Anisotropy and Competing Instabilities in $Na_3Co_2SbO_6$
Phys. Rev. X, **12** 041024 (2022).

183 T. Yamanaka, N. Hirao, Y. Nakamoto, T. Mikouchi, T. Hattori, K. Komatsu, H. Mao
Magnetic and Structure Transition of $Mn_{3-x}Fe_xO_4$ Solid Solutions under High-Pressure and High-Temperature Conditions
Phys. Chem. Miner., **49** 41 (2022).

184 M. Yoshida, H. Iwase, T. Shikata
Conformation and Structure of Hydroxyethyl Cellulose Ether with a Wide Range of Average Molar Masses in Aqueous Solutions
Polymers, **14** 4532 (2022).

185 M. Kamibayashi, K. Kobayashi, M. Hashimoto
Single Bit Upsets Versus Burst Errors of Stacked-Capacitor DRAMs Induced by High-Energy Neutron -SECDED Is No Longer Effective-
Proc. Eur. Conf. Radiat. Its Eff. Compon. Syst. RADECS (2022).

186 F. Suekane, Y. Hino, W. Noguchi, T. Tokuraku, T. Konno, T. Kawasaki, Y. Hoshino, M. Watanabe
A Plan for Decay at Rest ν_e + Pb Cross Section Measurement: DaRveX
PoSNuFACT2021, **402** 194 (2022).

187 S. Kanda
Toward a High-Precision Measurement of the Muon Lifetime with an Intense Pulsed Muon Beam at J-PARC
PoSNuFACT2021, **402** 215 (2022).

188 A. Koda, H. Okabe, M. Hiraishi, R. Kadono, K. A. Dagnall, J. J. Choi, S.-H. Lee
Organic Molecular Dynamics and Charge-carrier Lifetime in Lead Iodide Perovskite $MAPbI_3$
Proc. Natl. Acad. Sci., **119** e2115812119 (2022).

189 K. Yamashita, K. Komatsu, S. Klotz, O. Fabelo, M. T. Fernández-Díaz, J. Abe, S. Machida, T. Hattori, T. Irifune, T. Shinmei, K. Sugiyama, T. Kawamata, H. Kagi
Atomic Distribution and Local Structure in Ice VII from in situ Neutron Diffraction
Proc. Natl. Acad. Sci., **119** e2208717119 (2022).

190 W. Higemoto, M. Yokoyama, T. U. Ito, T. Suzuki, S. Raymond, Y. Yanase
Direct Measurement of the Evolution of Magnetism and Superconductivity toward the Quantum Critical Point
Proc. Natl. Acad. Sci., **119** e2209549119 (2022).

191 J. Sheng, L. Wang, A. Candini, W. Jiang, L. Huang, B. Xi, J. Zhao, H. Ge, N. Zhao, Y. Fu, J. Ren, J. Yang, P. Miao, X. Tong, D. Yu, S. Wang, Q. Liu, M. Kofu, R. Mole, G. Biasiol, D. Yu, I. A. Zaliznyak, J.-W. Mei, L. Wu
Two-Dimensional Quantum Universality in the Spin-1/2 Triangular-Lattice Quantum Antiferromagnet $Na_2BaCo(PO_4)_2$
Proc. Natl. Acad. Sci., **119** e2211193119 (2022).

192 M. Nishida, S. Harjo, T. Kawasaki, T. Yamashita, W. Gong
Neutron Stress Measurement of W/Ti Composite in Cryogenic Temperatures Using Time-of-Flight Method
Quantum Beam Sci., **7** 8 (2022).

193 T. Fujiwara, H. Miyoshi, Y. Mitsuya, N. L. Yamada, Y. Wakabayashi, Y. Otake, M. Hino, K. Kino, M. Tanaka, N. Oshima, H. Takahashi
Neutron Flat-Panel Detector Using In–Ga–Zn–O Thin-Film Transistor
Rev. Sci. Instrum., **93** 013304 (2022).

194 J. Abe, T. Kawasaki, S. Harjo
Development of Triaxial Compressive Apparatus for Neutron Experiments with Rocks
Rev. Sci. Instrum., **93** 025103 (2022).

195 K. Akutsu-Suyama, H. Sajiki, M. Ueda, M. Asamoto, Y. Tsutsumi
Heavy Water Recycling for Producing Deuterium Compounds
RSC Adv., **12** 24821–24829 (2022).

196 N. Okita, E. Iwama, Y. Takami, S. Abo, W. Naoi, P. Rozier, P. Simon, M. T. H. Reid, K. Naoi
The Origin of Stability and High $Co^{2+/3+}$ Redox Utilization for $FePO_4$-Coated $LiCo_{0.90}Ti_{0.05}PO_4$/MWCNT Nanocomposites for 5 V Class Lithium Ion Batteries
RSC Adv., **12** 26192–26200 (2022).

197 T. Nakamura, M. Matsumoto, K. Amano, Y. Enokido, M. E. Zolensky, T. Mikouchi, H. Genda, S. Tanaka, M. Y. Zolotov, K. Kurosawa, S. Wakita, R. Hyodo, H. Nagano, D. Nakashima, Y. Takahashi, Y. Fujioka, M. Kikuiri, E. Kagawa, M. Matsuoka, A. J. Brearley, A. Tsuchiyama, M. Uesugi, J. Matsuno, Y. Kimura, M. Sato, R. E. Milliken, E. Tatsumi, S. Sugita, T. Hiroi, K. Kitazato, D. Brownlee, D. J. Joswiak, M. Takahashi, K. Ninomiya, T. Takahashi, T. Osawa, K. Terada, F. E. Brenker, B. J. Tkalcec, L. Vincze, R. Brunetto, A. Aléon-Toppani, Q. H. S. Chan, M. Roskosz, J.-C. Viennet, P. Beck, E. E. Alp, T. Michikami, Y. Nagaashi, T. Tsuji, Y. Ino, J. Martinez, J. Han, A. Dolocan, R. J. Bodnar, M. Tanaka, H. Yoshida, K. Sugiyama, A. J. King, K. Fukushi, H. Suga, S. Yamashita, T. Kawai, K. Inoue, A. Nakato, T. Noguchi, F. Vilas, A. R. Hendrix, C. Jaramillo-Correa, D. L. Domingue, G. Dominguez, Z. Gainsforth, C. Engrand, J. Duprat, S. S. Russell, E. Bonato, C. Ma, T. Kawamoto, T. Wada, S. Watanabe, R. Endo, S. Enju, L. Riu, S. Rubino, P. Tack, S. Takeshita, Y. Takeichi, A. Takeuchi, A. Takigawa, D. Takir, T. Tanigaki, A. Taniguchi, K. Tsukamoto, T. Yagi, S. Yamada, K. Yamamoto, Y. Yamashita, M. Yasutake, K. Uesugi, I. Umegaki, I. Chiu, T. Ishizaki, S. Okumura, E. Palomba, C. Pilorget, S. M. Potin, A. Alasli, S. Anada, Y. Araki, N. Sakatani, C. Schultz, O. Sekizawa, S. D. Sitzman, K. Sugiura, M. Sun, E. Dartois, E. De Pauw, Z. Dionnet, Z. Djouadi, G. Falkenberg, R. Fujita, T. Fukuma, I. R. Gearba, K. Hagiya, M. Y. Hu, T. Kato, T. Kawamura, M. Kimura, M. K. Kubo, F. Langenhorst, C. Lantz, B. Lavina, M. Lindner, J. Zhao, B. Vekemans, D. Baklouti, B. Bazi, F. Borondics, S. Nagasawa, G. Nishiyama, K. Nitta, J. Mathurin, T. Matsumoto, I. Mitsukawa, H. Miura, A. Miyake, Y. Miyake, H. Yurimoto, R. Okazaki, H. Yabuta, H. Naraoka, K. Sakamoto, S. Tachibana, H. C. Connolly, D. S. Lauretta, M. Yoshitake, M. Yoshikawa, K. Yoshikawa, K. Yoshihara, Y. Yokota, K. Yogata, H. Yano, Y. Yamamoto, D. Yamamoto, M. Yamada, T. Yamada, T. Yada, K. Wada, T. Usui, R. Tsukizaki, F. Terui, H. Takeuchi, Y. Takei, A. Iwamae, H. Soejima, K. Shirai, Y. Shimaki, H. Senshu, H. Sawada, T. Saiki, M. Ozaki, G. Ono, T. Okada, N. Ogawa, K. Ogawa, R. Noguchi, H. Noda, M. Nishimura, N. Namiki, S. Nakazawa, T. Morota, A. Miyazaki, A. Miura, Y. Mimasu, K. Matsumoto, K. Kumagai, T. Kouyama, S. Kikuchi, K. Kawahara, S. Kameda, T. Iwata, Y. Ishihara, M. Ishiguro, H. Ikeda, S. Hosoda, R. Honda, C. Honda, Y. Hitomi, N. Hirata, N. Hirata, T. Hayashi, M. Hayakawa, K. Hatakeda, S. Furuya, R. Fukai, A. Fujii, Y. Cho, M. Arakawa, M. Abe, S. Watanabe, Y. Tsuda
Formation and Evolution of Carbonaceous Asteroid Ryugu: Direct Evidence from Returned Samples
Science, **379** eabn8671 (2022).

198 Y. Hanazono, Y. Hirano, K. Takeda, K. Kusaka, T. Tamada, K. Miki
Revisiting the Concept of Peptide Bond Planarity in an Iron-Sulfur Protein by Neutron Structure Analysis
Sci. Adv., **8** eabn2276 (2022).

199 H. Kwon, S. Harjo, T. Kawasaki, W. Gong, S. G. Jeong, E. S. Kim, P. Sathiyamoorthi, H. Kato, H. S. Kim
Work Hardening Behavior of Hot-Rolled Metastable $Fe_{50}Co_{25}Ni_{10}Al_5Ti_5Mo_5$ Medium-Entropy Alloy: in situ Neutron Diffraction Analysis
Sci. Technol. Adv. Mater., **23** 579–586 (2022).

200 Y. Qin, Y. Shen, C. Liu, H. Wo, Y. Gao, Y. Feng, X. Zhang, G. Ding, Y. Gu, Q. Wang, S. Shen, H. C. Walker, R. Bewley, J. Xu, M. Boehm, P. Steffens, S. Ohira-Kawamura, N. Murai, A. Schneidewind, X. Tong, G. Chen, J. Zhao
Field-Tuned Quantum Effects in a Triangular-Lattice Ising Magnet
Sci. Bull., **67** 38–44 (2022).

201 H. Hashimoto, Y. Onodera, S. Tahara, S. Kohara, K. Yazawa, H. Segawa, M. Murakami, K. Ohara
Structure of Alumina Glass
Sci. Rep., **12** 516 (2022).

202 I.-H. Chiu, S. Takeda, M. Kajino, A. Shinohara, M. Katsuragawa, S. Nagasawa, R. Tomaru, G. Yabu, T. Takahashi, S. Watanabe, S. Takeshita, Y. Miyake, K. Ninomiya
Non-Destructive 3D Imaging Method Using Muonic X-Rays and a CdTe Double-Sided Strip Detector
Sci. Rep., **12** 5261 (2022).

203 M. Maeda, M. Segawa, Y. Toh, S. Endo, S. Nakamura, A. Kimura
Effect of Sample Density in Prompt γ-Ray Analysis
Sci. Rep., **12** 6287 (2022).

204 K. Iida, K. Kodama, Y. Inamura, M. Nakamura, L.-J. Chang, S. Shamoto
Magnon Mode Transition in Real Space
Sci. Rep., **12** 20663 (2022).

205 E. Nocerino, C. Witteveen, S. Kobayashi, O. K. Forslund, N. Matsubara, A. Zubayer, F. Mazza, S. Kawaguchi, A. Hoshikawa, I. Umegaki, J. Sugiyama, K. Yoshimura, Y. Sassa, F. O. Von Rohr, M. Månsson
Nuclear and Magnetic Spin Structure of the Antiferromagnetic Triangular Lattice Compound $LiCrTe_2$ Investigated by μ^+SR, Neutron and X-Ray Diffraction
Sci. Rep., **12** 21657 (2022).

206 M.-Y. Luo, T.-N. Lam, P.-T. Wang, N.-T. Tsou, Y.-J. Chang, R. Feng, T. Kawasaki, S. Harjo, P. K. Liaw, A.-C. Yeh, S. Y. Lee, J. Jain, E.-W. Huang
Grain-Size-Dependent Microstructure Effects on Cyclic Deformation Mechanisms in CoCrFeMnNi High-Entropy-Alloys
Scr. Mater., **210** 114459 (2022).

207 D. Wei, W. Gong, T. Kawasaki, S. Harjo, H. Kato
Regulation of Strength and Ductility of Single-Phase Twinning-Induced Plasticity High-Entropy Alloys
Scr. Mater., **216** 114738 (2022).

208 N. Tsuchida, R. Ueji, W. Gong, T. Kawasaki, S. Harjo
Stress Partitioning between Bcc and Cementite Phases Discussed from Phase Stress and Dislocation Density in Martensite Steels
Scr. Mater., **222** 115002 (2022).

209 W. Gong, T. Kawasaki, R. Zheng, T. Mayama, B. Sun, K. Aizawa, S. Harjo, N. Tsuji
Compressive Deformation Behavior of AZ31 Alloy at 21K: An in-situ Neutron Diffraction Study
Scr. Mater., **225** 115161 (2022).

210 E. Zhao, K. Wu, Z. Zhang, Z. Fu, H. Jiang, Y. Ke, W. Yin, K. Ikeda, T. Otomo, F. Wang, J. Zhao

Quantifying the Anomalous Local and Nanostructure Evolutions Induced by Lattice Oxygen Redox in Lithium-Rich Cathodes
Small Methods, **6** 2200740 (2022).

211 F. Nemoto, N. L. Yamada, M. Hino, H. Aoki, H. Seto
Neutron Reflectometry-Based in situ Structural Analysis of an Aligning Agent Additive for the Alignment of Nematic Liquid Crystals on Solid Substrates
Soft Matter, **18** 545–553 (2022).

212 F. Song, H. Chen, H. Hayashida, T. Kai, T. Shinohara, T. Yabutsuka, T. Yao, S. Takai
Tracer Diffusion Coefficients Measurements on $LaPO_4$-Dispersed LATP by Means of Neutron Radiography
Solid State Ion., **377** 115873 (2022).

213 T. Tominaga, M. Hishida, D. Murakami, Y. Fujii, M. Tanaka, H. Seto
Experimental Evidence of Slow Mode Water in the Vicinity of Poly(ethylene oxide) at Physiological Temperature
J. Phys. Chem. B, **126** 1758–1767 (2022).

214 S. Hori, R. Kanno, O. Kwon, Y. Kato, T. Yamada, M. Matsuura, M. Yonemura, T. Kamiyama, K. Shibata, Y. Kawakita
Revealing the Ion Dynamics in $Li_{10}GeP_2S_{12}$ by Quasi-Elastic Neutron Scattering Measurements
J. Phys. Chem. C, **126** 9518–9527 (2022).

215 I. Umegaki, K. Ohishi, T. Nakano, S. Nishimura, S. Takeshita, A. Koda, K. Ninomiya, M. K. Kubo, J. Sugiyama
Negative Muon Spin Rotation and Relaxation Study on Battery Anode Material, Spinel $Li_4Ti_5O_{12}$
J. Phys. Chem. C, **126** 10506–10514 (2022).

216 T. Sato, K. Ikeda, T. Honda, L. L. Daemen, Y. Cheng, T. Otomo, H. Sagayama, A. J. Ramirez–Cuesta, S. Takagi, T. Kono, H. Yang, W. Luo, L. Lombardo, A. Züttel, S. Orimo
Effect of Co-Substitution on Hydrogen Absorption and Desorption Reactions of $YMgNi_4$-Based Alloys
J. Phys. Chem. C, **126** 16943–16951 (2022).

217 M. Nakano, H. Nakao, S. Yoshida, M. Fukuda, M. Imai, K. Ikeda
Energetic and Structural Insights into Phospholipid Transfer from Membranes with Different Curvatures by Time-Resolved Neutron Scattering
J. Phys. Chem. Lett., **13** 6024–6030 (2022).

218 R. Akiyama, R. Ishikawa, K. Akutsu-Suyama, R. Nakanishi, Y. Tomohiro, K. Watanabe, K. Iida, M. Mitome, S. Hasegawa, S. Kuroda
Direct Probe of the Ferromagnetic Proximity Effect at the Interface of SnTe/Fe Heterostructure by Polarized Neutron Reflectometry
J. Phys. Chem. Lett., **13** 8228–8235 (2022).

219 M. Aizawa, H. Iwase, T. Kamijo, A. Yamaguchi
Protein Condensation at Nanopore Entrances as Studied by Differential Scanning Calorimetry and Small-Angle Neutron Scattering
J. Phys. Chem. Lett., **13** 8684–8691 (2022).

220 W. Shen, T. Hirayama, N. Yamashita, M. Adachi, T. Oshio, H. Tsuneoka, K. Tagawa, K. Yagishita, N. L. Yamada
Relationship between Interfacial Adsorption of Additive Molecules and Reduction of Friction Coefficient in the Organic Friction Modifiers-ZDDP Combinations
Tribol. Int., **167** 107365 (2022).

221 N. Yamashita, T. Hirayama, N. L. Yamada, Y. Shimizu, K. Oda, H. Kawamoto
Interfacial Structure and Tribological Property of Adsorbed Layer Formed by Dibasic Acid Ester Derivative
Tribol. Online, **17** 246–256 (2022).

222 崔烘福, 向井智久, 菖蒲敬久, 有木克良, 衣笠秀行
中性子イメージング技術を用いた接着系あと施工アンカーにおける接着剤未充填部の特定手法
日本地震工学会・大会 2022, (2022).

Editorial Board - MLF Annual Report 2022

Chief Editor
Shoichiro Nishimura
Muon Science Section

Takashi Ino
Neutron Science Section

Yoshihiro Matsumoto
CROSS

Kosuke Hiroi
Neutron Science Section

Akiko Nakao
CROSS

Kaoru Sakasai
Neutron Instrumentation Section

Terutoshi Sakakura
CROSS

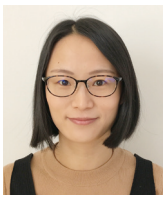

Yuhua Su
Technology Development Section

Takashi Naoe
Neutron Source Section

Misono Fujii
Muon Science Section

J-PARC

JAPAN PROTON ACCELERATOR RESEARCH COMPLEX

High Energy Accelerator Research Organization (KEK)
Japan Atomic Energy Agency (JAEA)

http://j-parc.jp/

Materials and Life Science Division
J-PARC Center

https://mlfinfo.jp/en

Comprehensive Research Organization for Science and Society
https://neutron.cross.or.jp/en

J-PARC 23-02